HARVARD UNIVERSITY

THE GRADUATE SCHOOL OF ARTS AND SCIENCES

THESIS ACCEPTANCE CERTIFICATE

(To be placed in Original Copy)

The undersigned, appointed by the

Division

Department of Physics

Committee

have examined a thesis entitled
"Single Electron Transport and Charge Quantization in Coupled Quantum Dots"

presented by Catherine Louise Hirshfeld Crouch

candidate for the degree of Doctor of Philosophy and hereby certify that it is worthy of acceptance.

Signature R. M. Westervelt

Typed name Robert M. Westervelt, Chair

Signature M. Tinkham

Typed name Michael Tinkham

Signature E. J. Heller

Typed name Eric J. Heller

Date September 10, 1996

SINGLE ELECTRON TRANSPORT AND CHARGE QUANTIZATION IN COUPLED QUANTUM DOTS

A thesis presented

by

Catherine Louise Hirshfeld Crouch

to

the Department of Physics

in partial fulfillment of the requirements

for the degree of

Doctor of Philosophy

in the subject of

Physics

Harvard University

Cambridge, Massachusetts

September, 1996

ABSTRACT

This thesis presents results on the breakdown of charge quantization in single and coupled quantum dots as the strength of tunneling between dots or between a dot and its environment is increased. Ordinarily, single-electron transport is studied in systems in which the number of electrons is well-defined. However, increasing the strength of tunneling between two dots or between a dot and its environment allows an electron to be shared between the two locations in the same fashion as electrons are shared between atoms in forming molecular bonds. Thus it is no longer meaningful to assign a particular number of electrons to a given dot.

In single quantum dots which are sufficiently small that the energy of adding a single electron is large, there are two signatures of charge quantization in very low temperature transport: sharp peaks in the linear conductance and a region of current suppression in the current-voltage characteristic. In a double quantum dot with adjustable interdot tunneling rate, the linear conductance peaks split into pairs with the separation between the pairs depending on the rate of interdot tunneling. The temperature dependence of these peaks indicates that each member of the pair results from a single electron tunneling into the entire double dot system. The region of current suppression, known as the Coulomb gap, narrows as interdot tunneling increases, and secondary regions grow until the gate voltage period of the Coulomb gap doubles and the size has shrunk to that of one large composite dot. The dependence of these nonlinear transport signatures on interdot tunneling rate is in agreement with theories describing the breakdown of charge quantization by tunneling.

In single quantum dots in which the tunneling rate between the dot and its environment is allowed to grow, we find that oscillations in the conductance which are periodic in the total charge on the dot are visible even in the presence of strong tunneling, except when there is exactly one channel available for transport at the Fermi level.

However, increased tunneling decreases the peak-to valley ratio of the oscillations and also decreases the temperature to which these oscillations persist.

Finally, we observe excited states in the nonlinear conductance of a well-defined single quantum dot. These states remain at the same energies even as the total number of electrons in the dot is increased by about twenty out of approximately 750 electrons total. This suggests that the excitation spectrum of the dot is surprisingly independent of the exact shape of the dot and of the number of electrons.

SINGLE ELECTRON TRANSPORT AND CHARGE QUANTIZATION IN COUPLED QUANTUM DOTS

Magna opera Domini exquisita in omnes voluntates eius[1]
("Great are the works of the Lord, studied by all who delight in them")
Psalms 111:2

Soli Deo Gloria[2]
("For the glory of God alone")

[1]This quotation appears in Latin on the doors of the original Cavendish Laboratory at Cambridge University, Cambridge, U. K., and in English over the doors of the new building. James Clerk Maxwell, the first director of the Cavendish Laboratory, had those words placed there as a motto and guide to all of his scientific work. With Maxwell, Kepler, Newton, and many other physicists as role models, I have sought to remember that the universe is the work of the Lord and to delight in it as I have studied physics.

[2]J. S. Bach began the manuscript of every one of his compositions with this statement. Likewise I offer this work of my hands and mind to the glory of God.

ACKNOWLEDGMENTS

A Ph.D. thesis, like any other large undertaking, relies not only on the determination and abilities of its author, but also on the support and encouragement of numerous people. My many physics teachers are the most obvious people to thank. I am particularly grateful to Bill Sweeney of Strath Haven High School for making physics fun; Bill Wootters of Williams College, for befriending me and encouraging my enjoyment of physics; Stuart Crampton of Williams College, for patiently guiding me through my undergraduate thesis project; Michael Seul, my mentor in the 1989 AT&T Summer Research Program, who devoted endless time and energy to both training me as a researcher and introducing me to his colleagues at Bell Labs; and Frank Stillinger and Cherry Murray, my official and unofficial mentors through the AT&T Graduate Research Program for Women, for their concern and advocacy for me.

Mark Eriksson and Rich Finlay, my study partners throughout our coursework, helped me through numerous problem sets with patience and good humor, and have continued to be important friends and colleagues. Carol Livermore has been a wonderful collaborator for the last two years. I am grateful for her cheerful enthusiasm and encouragement at every stage of the research process. All three have helped me learn what it means to be a physicist.

I wish to thank everyone in the Westervelt and Tinkham groups for their part in my progress. I am grateful to Doug Mar for providing my early training; Fred Waugh for getting me started on the coupled dot project; Jack Hergenrother and Jia Lu, for their friendly and considerate cooperation in running and maintaining the Oxford Model 200; and Jordan Katine and Aram Adourian, for being available when the SEM or the fridge confounded me. Rex Beck and Junmin Hu have been an important part of the collegial Westervelt group dynamic. I wish all the best to Mark, Rex, and Carol, as well as Mark Topinka, Marija Drndic, and David Duncan, as they continue the group tradition.

Experimental physics at Gordon McKay Laboratories depends on both excellent facilities and outstanding people. I am grateful to Yuan Lu and Steve Shepard for their fine care of the SEM and cleanroom, respectively. Louis DeFeo and his outstanding team of machinists have taught me drawing and designing as well as fixing numerous parts of the dilution refrigerator top-loading system with patience and courtesy.

Bob Westervelt has been an exemplary advisor in many ways. His seemingly endless patience, his dedication to effective communication, his ability to keep the big picture in mind while solving day-to-day problems, his careful management of the group research budget, and his creation of a cooperative group atmosphere, have all served me well. I am grateful that his priority for me has always been that I do what interests me most. I am particularly grateful for his support of my interest in teaching.

Because I am as much a teacher as a researcher, graduate school has been an opportunity to grow in teaching experience and ability. I thank David Layzer for the opportunities he has provided for me through Chemistry 8, and for his respect and encouragement of me as a teacher. Likewise I thank Eric Mazur for all I learned working with him in Physics 11a. I look forward to working with Eric as a postdoctoral fellow.

I am grateful to the people who have encouraged me day-to-day, through both the routine frustrations of research and the times when I felt that it would be too difficult or costly to finish this degree. My sisters Amy and Mary Ann Hirshfeld and my parents-in-law Joyce and Wayne Crouch have helped me remember that I like physics and teaching and have repeated their confidence in me when my self-confidence ebbed. Kristen Lynch has helped me adjust to graduate school and keep my priorities straight while in it. Laura and Peter Brown, Marguerite and Brian Taylor, Tim Shah, Ericka and Tim Benson, Francis Su, and Anne and Steve Barr, as well as my housemates, my church family, and other friends too numerous to mention, have listened to me, encouraged me, and prayed for me. Mark Eriksson, Rich Finlay, Carol Livermore, and Fred Waugh have provided an essential colleague's and friend's perspective on my work.

Finally, there are four people whom I particularly wish to thank. Howard Georgi has gone out of his way to advise and encourage me, and his encouragement has come at many critical times. My parents, John and Barbara Hirshfeld, likewise have helped me remember why I came here and what I intended to accomplish. Their love of me and confidence in me sustained me through difficult times. My husband Andy has walked the road step by step with me and kept my eyes on Jesus.

To these four, and everyone else who has shared my last five years, I am grateful.

TABLE OF CONTENTS

CHAPTER 1
INTRODUCTION

1.1 Quantum Dots and Single-Electron Charging Effects

Professor Michael Tinkham gave a talk at Harvard University in the fall of 1995 about single-electron charging effects which was subtitled, "When one electron in a billion makes a difference." Indeed, one of the most remarkable features of the study of nanoelectronics is that even though there are hundreds (in the case of this thesis) or thousands or even more electrons present in the tiny circuit elements studied, the presence or absence of one electron is significant. Single electron charging effects are phenomena in which the number of electrons in a confined region of a nanostructure can be controlled by the experimenter because the energy cost of adding or removing a single electron from the device is significant compared to other energies in the problem, and because the nanostructure is designed in such a way that the number of electrons in its confined region is well defined. This can be experimentally realized because of the strength of the Coulomb interaction, the small size of these devices, and the low temperatures achievable with ^{3}He/^{4}He dilution refrigerators.

What does it mean for the number of electrons to be well-defined? Consider a conducting island which is connected to its environment by so-called weak links or tunnel junctions, pathways which contain energy barriers substantially higher in energy than the ambient temperature of the electrons. Such an island is shown schematically in Fig. 1.1. Transport through these pathways only takes place by either quantum mechanical tunneling through the barriers or thermal activation over the barrier. If the tunneling rate is very weak, the quantum mechanical lifetime of an electron on the island is sufficiently long that the energy uncertainty associated with that lifetime is substantially smaller than the energy cost of adding a single electron (the "single-electron charging energy" or just the "charging

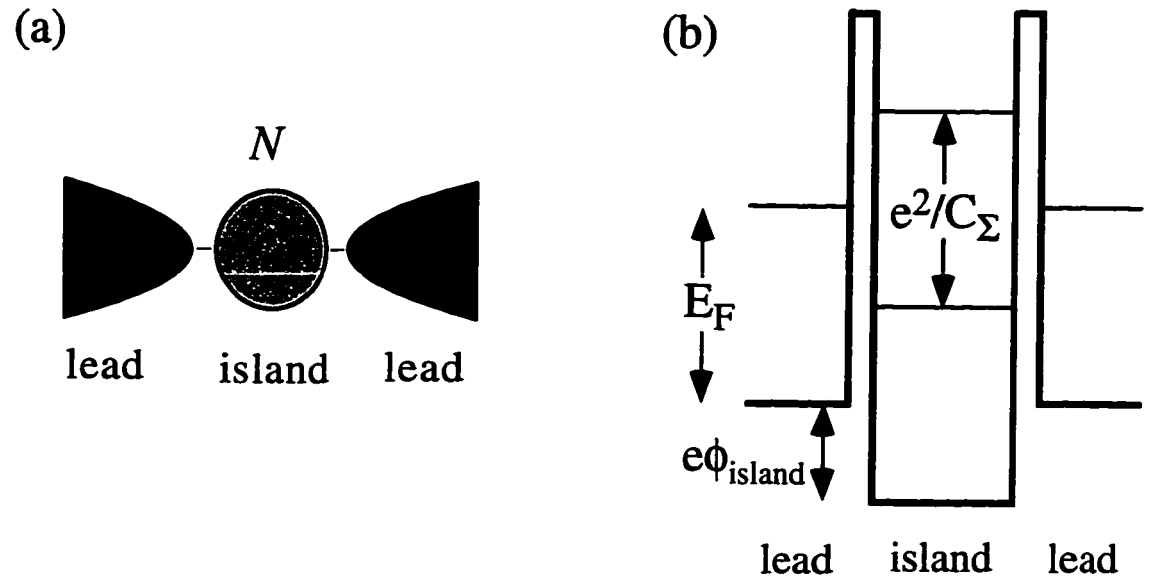

Figure 1.1 (a) Single island between two leads; thin lines connecting island to leads represent tunnel junctions. (b) Energy diagram of electrons in this system; a Fermi level exists in the two leads which is not necessarily the same as the electrochemical potential of the island (depending on environmental factors). Shaded areas represent bands of filled electron states. Tunnel barriers separate the island from its leads.

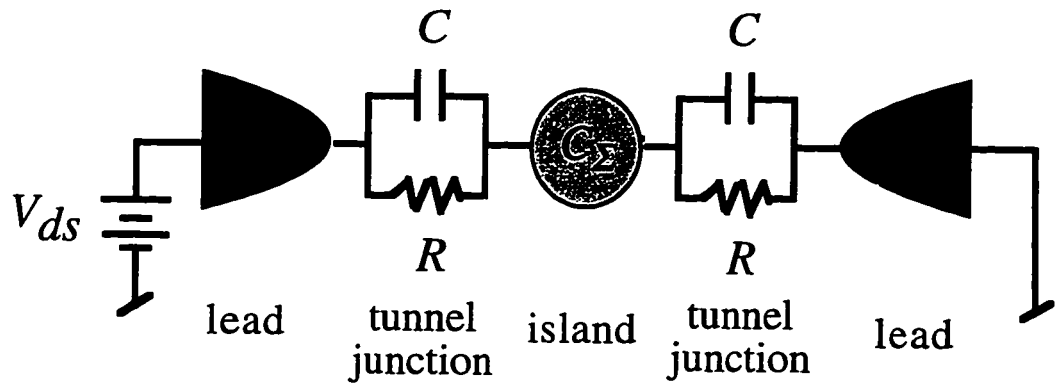

Figure 1.2 Rudimentary circuit corresponding to single island shown in Fig. 1.1. The tunnel junctions have a tunneling resistance R and a capacitance C. The total capacitance of the island C_Σ includes the tunnel junction capacitances and any additional stray capacitance to ground C_0.

energy", equal to e^2/C_Σ)[1]. In other words, the number of electrons on the island is sufficiently well-defined for the presence or absence of one electron to be energetically significant. If the temperature is also substantially smaller than the charging energy, thermally activated transport and thermal fluctuations in the total charge present on the island will also be negligible.

These conditions for well-defined island charge can be summarized mathematically as follows: The lifetime τ of an electron on an island with total capacitance C_Σ and resistance to its environment R, as shown in Fig. 1.2, is simply the RC time for charge to leak off the island, RC_Σ; the energy uncertainty is thus $h/2\pi\tau = h/2\pi RC_\Sigma$. Thus requiring this energy uncertainty to be much less than the charging energy amounts to

$$\frac{e^2}{C_\Sigma} >> \frac{h}{2\pi RC_\Sigma} \quad \Rightarrow \quad R >> \frac{h}{e^2} \tag{1.1}$$

This condition is often described as requiring the tunnel junction resistance to exceed the "resistance quantum" $R_Q \equiv h/e^2$, or, conversely, for the junction conductance to be far less than the "conductance quantum" $g_Q \equiv 2e^2/h$. The reason for defining this particular quantity as the quantum of transport will be discussed further in Chapter 4.[2] Likewise, the temperature condition can be summarized as

---

[1] There are unfortunately two different ways to determine the charging energy, depending on the particular ensemble chosen. The total electrostatic energy F which is calculated in Chapters 2 and 5 (for the single and double dot respectively) is the energy cost of adding an electron when the ground state of the system has a fixed number of electrons N. The change in F on adding an electron can be determined by thinking about the energy involved in adding a unit charge e to a conductor of total capacitance C_Σ. Integrating the work done to bring the charge from infinity and deposit it on the conductor, which can also be thought of the work required to rearrange the charges on the conductor to accommodate the charge e, gives a total energy $e^2/2C_\Sigma$. Unfortunately, in linear conductance measurements (as opposed to nonlinear measurements), N for the ground state is not well defined when transport occurs (transport with zero bias occurs precisely because N can fluctuate) and thus the relevant energy change is not the change in F but the change in electrochemical potential, $\Omega = F - E_F N$. As is also discussed in Chapter 2, the energy cost of adding one electron to the system when N can fluctuate is the change in Ω, e^2/C_Σ. For another exposition of this, see van Houten, Beenakker, and Staring [1992]. For simplicity, in this thesis, when we say "the charging energy," we will mean e^2/C_Σ.

[2] At this point it should be noted that in certain European countries, h/e^2 is actually considered a unit of resistance, and is called the von Klitzing, after one of the discoverers of the quantum Hall effect, in which the Hall resistance of two-dimensional electron systems is quantized in units of h/e^2. A logical question is

$$\frac{e^2}{C_\Sigma} >> k_B T \tag{1.2}$$

If the charge on the island must be well-defined, then for current to flow through an island which initially contains N electrons requires the number of electrons on the island to oscillate between N and $N + 1$ (or N and $N - 1$). For this to occur the energy of the system must be nearly the same for N and N $\pm$ 1 electrons on the island. Otherwise, no current will flow – there is an energy gap against changing the number of electrons, because to add another electron will cost some fraction of the charging energy e^2/C_Σ. This is known as the "Coulomb blockade" of transport, and was first observed in tunneling microscopy through metallic grains several decades ago [for a review see Grabert and Devoret, 1992]. Current will flow if the energy supplied by an applied bias voltage exceeds the charging energy.

Now consider adding another control to the system. Shown schematically in Fig. 1.3 is the device of Fig. 1.1 with a third electrode coupled to the island. However, this electrode, called the "gate" electrode, is only capacitively coupled to the island; no tunneling can occur between island and gate. Applying a voltage to the gate electrode changes the electrostatic potential of the island according to the energy stored in the gate-island capacitance. Thus, the island potential can be tuned with the gate voltage such that at certain gate voltages, the energies with N and with $N + 1$ electrons on the island are degenerate. (This will be discussed more extensively in Ch. 2.) Current will then flow at those gate voltages even with no voltage bias present.

Both of these phenomena are referred to as single-electron transport effects, because the number of electrons present (along with the gate voltage or the bias voltage) controls the flow of current. In the well-established "orthodox" theory of single-electron

---

to ask what the unit e^2/h should be called in such countries. Given that most people rarely remember that the inverse ohm is technically called a Siemen and refer to it as a mho instead, perhaps e^2/h should be called the gniztilk nov.

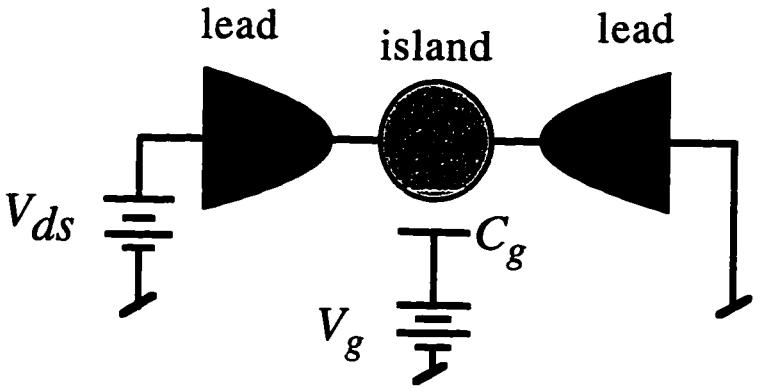

Figure 1.3 Three-terminal device: a single island with a capacitively coupled gate electrode. A gate voltage V_g can be applied to the gate to modulate the electrostatic potential of the island. Tunnel junctions are again depicted by thin lines connecting the leads to the island.

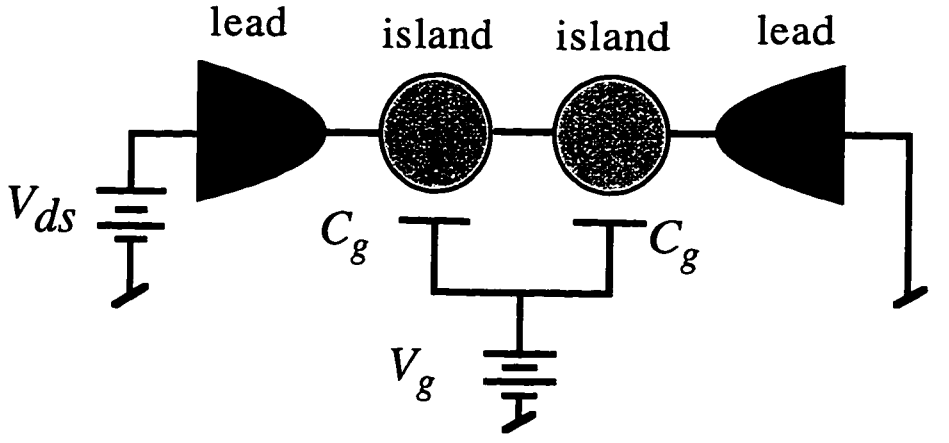

Figure 1.4 Double-island device with tunneling between the two islands as well as from the island to the leads. The gate voltage is applied to two identical gate electrodes which each have capacitance C_g to the nearer island (and a smaller capacitance to the farther island).

transport [see for example van Houten, Beenakker, and Staring, 1992], the tunneling rate between the island and its leads is assumed to be very weak; the system can then be modeled with an equivalent circuit and the energetics of the circuit can be determined from classical electrostatics. This thesis studies how stronger tunneling – the intrusion of quantum mechanics into the system – relaxes the constraints which exist for a purely classical system. This can be studied in a single quantum dot (as in the work presented in Chapter 4) or in a coupled dot system, the subject of the next section.

1.2 Tunnel-Coupled Quantum Dots

The same physics described previously applies to two islands coupled to one another by tunnel junctions, as shown schematically in Fig. 1.4.[3] Now in addition to the energies of each island, there is an energy associated with the inter-island coupling. Consider a system in which the two islands are identical and have the same electrostatic environment. If the number of electrons on each of the two islands is well-defined (in the same fashion as previously discussed), and there are different numbers of electrons N_1 and N_2 on the two islands, there exists a potential difference between the two islands. The interdot charging energy is determined by the strength of the capacitive coupling between the islands; as the capacitance increases, this energy decreases.

If the inter-island tunneling rate is significant, so that N_1 and N_2 are no longer required to be integers (although the total number of electrons on the double-island system, $N_{tot} = N_1 + N_2$, is still well-defined because the tunneling rate to the leads is low), the interdot potential difference and hence the total energy of the system decreases as N_1 and N_2 approach $(N_1 + N_2)/2$. This process is analogous to molecular bond formation between atoms. The primary work of this thesis (presented in Chapter 5) consists of measurements

[3]It also applies to dots which are only capacitively coupled, with no tunneling allowed, and some interesting studies of such systems have been done, but this work is outside the scope of this thesis. See for example M. Field *et al.*, 1993.

of how the energy of the system depends on the strength of inter-island tunneling as the quantization of N_1 and N_2 is lifted. It is like watching a bond form between the two islands. In the language of Coulomb blockade physics, we study the erosion of inter-island Coulomb blockade as the tunneling rate between the islands increases. The double-island system is convenient for studying this because Coulomb blockade still determines transport between the leads and the double island as a whole; thus we can use the Coulomb blockade to probe the ground state energy of the system.

1.3 Experimental System

Many research groups have studied Coulomb blockade physics with almost as many different experimental systems [for reviews see Kouwenhoven and McEuen, 1996; Tinkham, 1996; Grabert and Devoret, 1992; Averin and Likharev, 1991]. In this thesis, we have studied quantum dots formed in a GaAs/AlGaAs two-dimensional electron gas (2DEG) by electrostatic depletion of the gas from voltages applied to surface metal gates. Such devices are known as split-gate semiconductor quantum dots. The split-gate technique was demonstrated ten years ago by two different research groups [Thornton *et al.*, 1986; Zheng *et al.*, 1986]. This technique will be discussed in detail in Ch. 3; here we will give a brief overview. Because of the different band gaps of GaAs and AlGaAs, an electrostatic potential well forms at the interface between the two materials. Electrons from Si donors placed in the AlGaAs then move to this potential well, and if the right concentration of donors is present, a continuous layer of electrons is confined to the interface. These electrons are localized within nanometers along the direction perpendicular to the GaAs/AlGaAs interface, but are free to move parallel to the interface; thus they exist in an essentially two-dimensional potential. With modern molecular beam epitaxy techniques, the interface can be made sufficiently smooth and the neighboring materials sufficiently free of defects that these electrons are like free electrons in two dimensions with mean free path length up to several microns at cryogenic temperatures.

If the 2DEG is located sufficiently near the surface of the wafer, the electron distribution can be sharply modulated by voltages applied to metal gates on the wafer surface. This process is shown schematically in Fig. 1.5. A negative voltage on a surface gate produces an electric field which depletes electrons from the 2DEG directly underneath and somewhat to the side; thus gates which do not actually touch (hence "split gates") can be used to deplete a continuous region of the 2DEG, as shown in the figure. This allows the gates which define an island to be electrically isolated from one another, so that different voltages can be applied to different gates, and if desired, some subset of the gates can be left grounded and thus not used. For example, one such gate can be used as the capacitively coupled gate of Fig. 1.3 and the voltage on it can be swept, while other gates can be used to define narrow potential barriers in the 2DEG which serve as tunnel junctions between the neighboring electrodes and the island.

One of the devices used for the experiments presented in this thesis (KC7EE) is shown in Fig. 1.6. Figure 1.6(a) shows a scanning electron micrograph of the active region of the actual device; bright areas are metal gates, and dark areas are the surface of the GaAs/AlGaAs wafer.[4] In Fig. 1.6(b) the electrical wiring of the device is shown. The rectangular gates labeled V_{gi} are side gates and couple capacitively to the dot. The pointed gates labeled V_{qi} are quantum point contact gates; the regions of 2DEG between the tips are depleted by the field from the tips and form tunnel barriers for electrons crossing that region. The crossed boxes represent ohmic contacts to the ungated regions of 2DEG to the left and right of the device; these ungated regions serve as electrical leads to the device. To use just one dot of the two-dot device, only the shaded gates are energized. This device is

[4]The chip on which the device is fabricated is 3 x 5 mm^2, substantially larger than the active area shown, which is about 16 μm^2; each gate shown in the micrograph extends all the way to the edge of the chip so that it cuts off the ungated region of the 2DEG from the device. These gates become substantially larger as they travel further from the device. There are also two ohmic contacts from the surface to the 2DEG at the left and right ends of the chip which are not shown in Fig. 1.6(a) but are shown in Fig. 1.6(b).

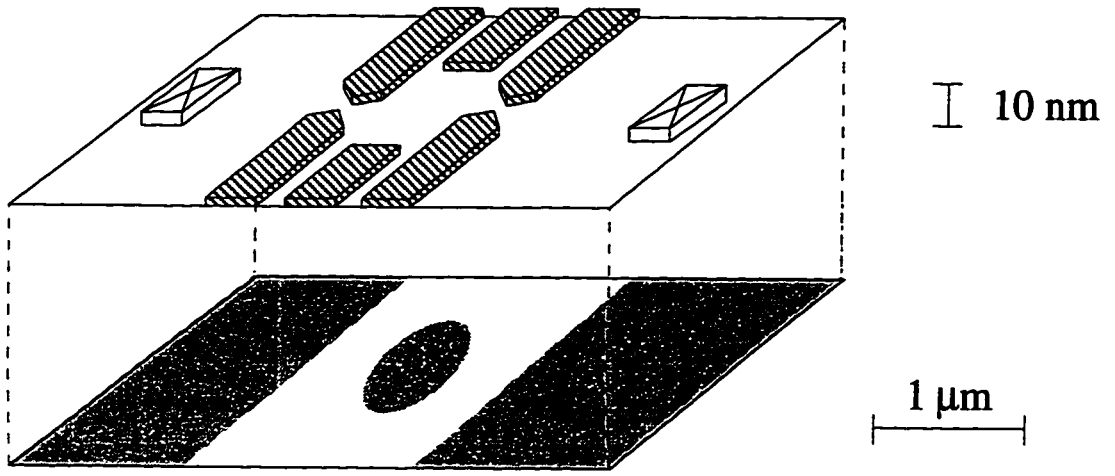

Figure 1.5 Split-gate device schematic: negative voltages applied to surface gates deplete the electron gas underneath in a larger area than the footprint of the gates, so that gates which do not touch can still deplete a continuous area. Vertical and horizontal scales differ: confined electron gas (quantum dot) length is of order 1 μm, while surface-to-gas distance is about 57 nm.

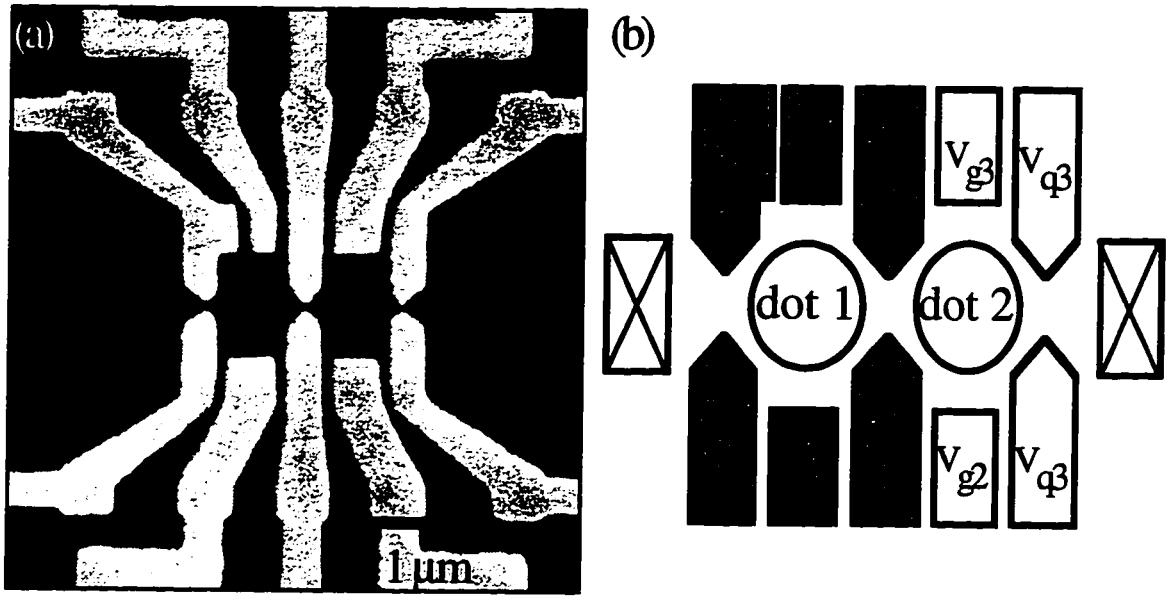

Figure 1.6 (a) SEM micrograph of the device used for most of the measurements of this thesis. Bright areas are metal gates; dark areas are the surface of the GaAs/AlGaAs wafer. The electron gas is depleted beneath and about 150 nm out surrounding the gates, forming the device shown schematically in Fig. 1.4. (b) Wiring diagram of the device with the two dots also represented. Gates with a common symbol (representing an applied voltage) are electrically connected. Crossed boxes are ohmic contacts. If only one dot is to be used, the shaded gates are energized and the others are grounded.

thus equivalent to the schematic double island structure of Fig. 1.4, and can also be used as the single-island structure of Fig. 1.3.

The primary advantage of a split-gate structure for the work of this thesis is that the tunnel conductance through the barriers formed by the quantum point contact gates can be tuned by adjusting the point contact voltage; thus we can study the device physics as the tunneling rate either from one dot to the lead or between the two dots is changed continuously. Such tuning of tunnel rates is not presently possible in metal structures. An additional advantage of GaAs devices is that the low effective mass of electrons in the 2DEG ($m^* = 0.06\ m_e$) and correspondingly long Fermi wavelength ($\lambda_F \sim 40$ nm for typical 2DEG sheet densities $n_s \sim 4 \times 10^{11}/cm^2$) means that individual quantum eigenstates of the electrons in the dots can be detected at device sizes and temperatures which are fairly readily attainable. In metals the wavelength of the conduction electrons is much too short to reach this regime with conventional devices.[5]

1.4 Summary of the Thesis

The methods and results of this thesis are presented in four chapters and four appendices. Chapter 2 describes the well-established phenomena of single-electron transport in a single quantum dot in the limit described by orthodox theory, showing both theoretical and experimental results. While most of the measurements presented in this chapter are similar to work previously published by other groups, they are presented because they characterize the device and also provide background for understanding the novel results of Chapters 4 and 5. (All the measurements presented were performed by this author with the samples used for the results of Chs. 4 and 5.) Chapter 3 summarizes the experimental methods used, and Appendices B and C supply further technical details on

[5]Recently Black and Ralph [1996] have fabricated gated single metal islands small enough to observe single quantum states using state-of-the-art fabrication technology, but this technology has not yet been refined as needed to make double island structures.

electron beam lithography and operation of the Oxford Model 200 ^{3}He/^{4}He dilution refrigerator. In Chapter 4 we examine how the Coulomb blockade is eroded by strong tunneling with some studies of single quantum dots with strong tunneling between the dot and leads. Finally, Chapter 5 presents the heart of the thesis, experiments and calculations studying the breakdown of Coulomb blockade by increasing interdot tunneling in a double quantum dot. The measurements in Chapter 5, consisting of current-voltage characteristics and temperature dependence of linear conductance peaks, are augmented by Appendix A, which presents the full charging diagram measurements of the double dot linear conductance. Appendix D presents the details of a self-consistent calculation of the Coulomb gap within a model which accounts for interdot charge sharing.

1.5 Acknowledgment of Collaborators

Several collaborators have been essential to the work presented in this thesis, and I wish to acknowledge their contributions. Fred Waugh began the double quantum dot project in the Westervelt group and spent a great deal of time preparing me to work on it as he was about to graduate. He has also continued to discuss results with me. Carol Livermore has worked with me on the measurements presented in this thesis (as well as others not presented here). Both Carol and Fred have been outstanding colleagues and collaborators for the past two years. John Golden, Bert Halperin, Konstantin Matveev, and Michael Stopa have done many of the calculations[6] used to interpret the measurements in this thesis, arising from ongoing conversations between them and our research group. It has been a great pleasure to work with each of them, because each has been patient and pleasant to work with as well as scientifically stimulating.

[6]The electrostatic calculations of Chapters 2 and 5 were done by this author, following orthodox theory as reviewed in Grabert and Devoret, 1991; Section 5.4.3 is also the work of this author following lengthy discussions with John Golden about how their theory could be applied to the finite-bias case.

CHAPTER 2
SINGLE QUANTUM DOTS[1]

2.1 Introduction

In Chapter 1 we sketched a brief overview of single-electron transport. In this chapter we will present experimental results and theory on single-electron transport through a single semiconductor quantum dot influenced by a capacitively coupled gate voltage, shown schematically in Fig. 2.1. For the work of this chapter, tunneling between the dot and its leads is kept weak; thus the number of electrons N on the dot is quantized, and the dot energetics are dominated by its total capacitance $C_\Sigma \equiv 2C_L + C_g + C_0$ and the capacitances to its leads (C_L) and to the gate (C_g). We will present both equilibrium (V_{ds} ~ 0) and nonequilibrium ($V_{ds} \neq 0$) measurements. The device used is one dot of the device shown in Fig. 1.6.

The most striking feature of transport through such a quantum dot is shown in Figure 2.2. These data are a measurement of the two-terminal zero-bias conductance through the device, G_{dot}, vs. V_g, measured at dilution refrigerator base temperature (mixing chamber temperature T_{mix} ~ 15 mK, electron temperature $T_{electron}$ ~ 80 mK, as will be discussed in section 2.2.3). We see that as the gate voltage is changed, very sharp periodic peaks in conductance occur, with near-zero conductance in between (the peak conductance corresponds to resistance ~ 1 MΩ, whereas the conductance in between is approximately three orders of magnitude less). Although the spacing of these peaks is nearly constant, the height is not. In Figure 2.2(a) we see that over about 250 mV in gate voltage, the peak heights vary by a factor of five in a non-monotonic fashion. Part (b)

[1]Data equivalent to Figures 2.4 and 2.11(a), and results from analyzing those data, were originally measured by the author and Carol Livermore and presented in Waugh *et al.* (1996). We have subsequently improved those measurements, so the actual data shown in this thesis are of better quality (though taken with a somewhat more temperamental sample). Data from section 2.3.4. has been included in the manuscript submitted to *Applied Physics Letters* which contains the primary results of Ch. 5.

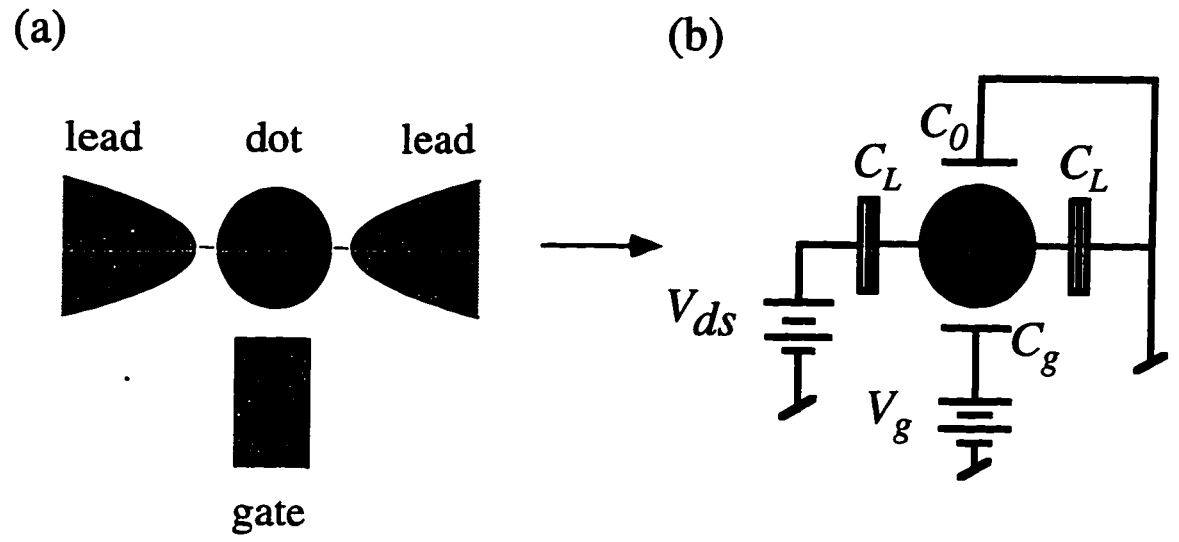

Figure 2.1 (a) Schematic of a single quantum dot between two leads with a capacitively coupled gate electrode. (b) Equivalent circuit with capacitances C_g from dot to gate, C_L from dot to each lead, and C_0 to ground. Split boxes connecting dot to leads represent tunnel junctions. The number of electrons N on the dot must be quantized in this model.

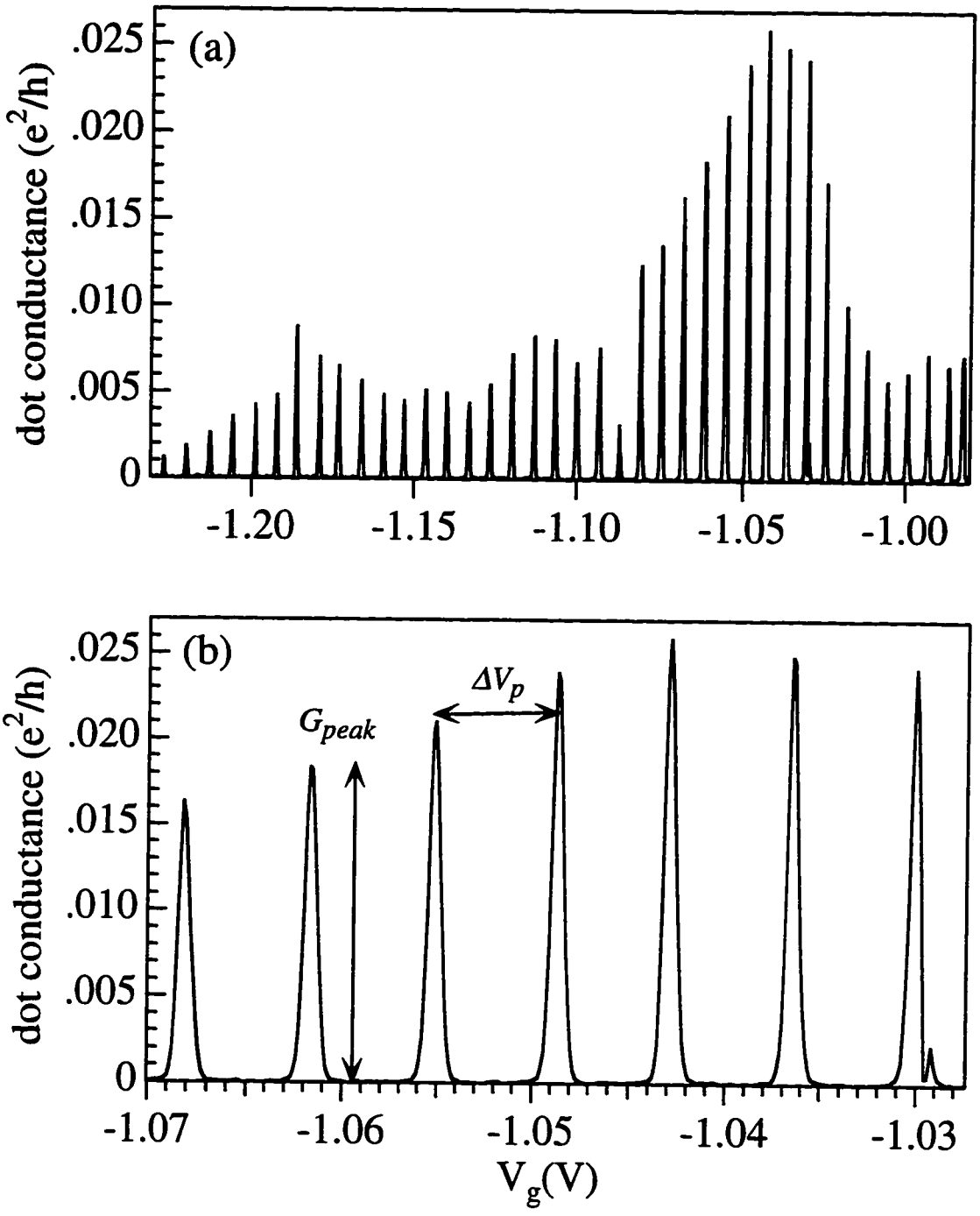

Figure 2.2 (a) Zero-bias conductance through a single quantum dot vs. gate voltage V_g, measured with dot 2 of the device shown in Fig. 1.6. (b) Expanded view of a few of the conductance peaks shown in (a). The leftmost peak is disrupted by a charging event. The peak height G_{peak} and the gate voltage period of the peaks ΔV_p are illustrated.

shows a detailed view of a few peaks; we see that the peaks are symmetric and cleanly shaped, except for the rightmost peak which has been disrupted by a charging event.[2]

What causes these peaks in conductance? First observed in metal samples with the same basic design [Fulton and Dolan, 1987], and subsequently studied by many workers in different contexts, these peaks are one of the best-known signatures of single-electron transport.[3] [For a general review see Grabert and Devoret, 1992; for results in semiconductor split-gate quantum dots see Kastner, 1992; van Houten, Beenakker, and Staring, 1992; and Kouwenhoven and McEuen, 1996.] Each peak occurs at a gate voltage position such that the number of electrons on the island can change by one with zero energy cost; this allows current to flow, whereas at other gate voltages a certain number of electrons is lowest in energy and thus current flow is "blockaded" by the energy cost of changing the number of electrons. Let us examine the energetics of this system to understand why the energy of the island depends on electron number and gate voltage in this fashion.

2.2 Zero-Bias Transport in Single Quantum Dots

2.2.1 Single Dot Electrostatic Energy: Capacitive Circuit Model

The total electrostatic energy of a quantum dot system at zero temperature can be determined from an equivalent circuit. In this particular model of quantum dots, known informally[4] as the orthodox theory, capacitive coupling is assumed to dominate; tunneling between the dot and the leads is assumed to be very weak ($R_{leads} << h/e^2$), so the number of electrons on the dot is quantized; and quantum states are considered as a term in the Hamiltonian separable from the electrostatics [Grabert and Devoret, 1992; Tinkham, 1996].

---

[2]Charging events will be discussed in Chapter 3, section 2; the disrupted peak is included as an illustration.
[3]These effects in semiconductors were first observed accidentally in studies of narrow wires [Scott-Thomas *et al.*, 1989].
[4]A number of publications, including van Houten, Beenakker, and Staring (1992), use this "informal" term, and there does not seem to exist a more formal name for it, so this author will refer to the "orthodox theory" throughout the thesis to mean the model presented here.

Hamiltonian separable from the electrostatics [Grabert and Devoret, 1992; Tinkham, 1996]. At very low temperature, in devices with weak dot-to-lead tunneling, this model works very well.

Consider the circuit shown in Fig. 2.1(b), corresponding to the schematic quantum dot of Fig. 2.1(a). The metallic island in the middle of the circuit, which corresponds to the quantum dot, is capacitively coupled to the left and right leads through capacitance C_L and to a gate electrode by capacitance C_g. The total capacitance of the island C_Σ is defined as

$$C_\Sigma \equiv 2C_L + C_g + C_0 \tag{2.1}$$

with C_0 the total capacitance of the island to ground (to anything other than the leads and the gate).

To determine the total electrostatic energy[6] F of the circuit of Fig. 2.1 (b), we simply calculate the total energy stored in all of the capacitors, and subtract the work done on the circuit by the batteries in charging the capacitors [Tinkham, 1996][7]. The internal energy U stored in the capacitors is given by

$$U = \frac{1}{2}\sum_i C_i(\Delta V_i)^2 \tag{2.2}$$

where ΔV_i denotes the voltage across the i^{th} capacitor. The work W done by the batteries is

$$W = \sum_j Q_j V_j \tag{2.3}$$

---

[6] Tinkham [1996] properly points out that this "energy" F ought to be called an enthalpy, since it includes both the energies stored in the capacitors, which constitute the internal energy of the circuit, and the work done by the batteries. Technically speaking this energy is not truly the free energy of the system since it does not include an entropy term. However, in semiconductor quantum dots at low temperatures the entropy term does not affect transport, so many authors, including van Houten, Beenakker, and Staring [1992] refer to this energy as a "free energy" and designate it F. Others, such as Tinkham [1996] and Kouwenhoven and McEuen [1996] refer to it as simply an "energy" E. This author has used F to try to avoid confusion with the energies of the single-particle states E_p, but will resist referring to the energy as a "free energy" and will instead call it the "total electrostatic energy."

[7] In Tinkham the algebra is done in a somewhat different fashion but the approach and the results are the same.

where Q_j is the charge placed by the j^{th} battery on its neighboring capacitor plate and V_j is the voltage of the battery. Since the charge on a capacitor is

$$Q_i = C_i \Delta V_i \tag{2.4}$$

we can rewrite the work done by the batteries as

$$W = \sum_i C_i V_i \Delta V_i - eN_t V_{ds} \tag{2.5}$$

understanding that in the first term, the sum i runs over all capacitors which are adjacent to a battery, V_i refers to the voltage of that battery, and ΔV_i is as defined above. The second term accounts for the work done by the bias voltage V_{ds} on any electrons that have tunneled onto the island: N_t is the number of electrons which have tunneled onto the island from the left lead, and the term is negative because e, the elementary charge, is taken to be positive. Finally, we obtain for the total electrostatic energy

$$F = U - W = \frac{1}{2}\sum_i C_i\left[(\Delta V_i)^2 - V_i \Delta V_i\right] + eN_t V_{ds} \tag{2.6}$$

To calculate this for the circuit of Fig. 2.1(b), we need to determine the electrostatic potential of the dot itself, ϕ_{dot}, which is done most easily by superposing the potentials due to each battery. We arrive at

$$\phi_{dot} = \frac{C_L V_{ds} + C_g V_g - Ne}{C_\Sigma} \tag{2.7}$$

where N is the number of excess electrons residing on the dot. We find that the free energy of the single dot, as a function of N, is

$$F(N) = \frac{e^2}{2C_\Sigma}\left[N - \left(\frac{C_g V_g}{e} + \frac{C_L V_{ds}}{e}\right)\right]^2 + N_t e V_{ds} - C_L {V_{ds}}^2 - C_g {V_g}^2 \tag{2.8}$$

For the study of single-electron charging effects, we are primarily concerned with how F depends on N; as we will see later, terms independent of N do not affect transport. Thus for the remainder of this section we will use a simpler form of the energy, F_0, in which we neglect the N-independent final terms:[8]

$$F_0(N) = \frac{e^2}{2C_\Sigma}\left[N - \left(\frac{C_g V_g}{e} + \frac{C_L V_{ds}}{e}\right)\right]^2 + NeV_{ds} \tag{2.9}$$

2.2.2 *Zero-Bias Conductance Peaks*

What are the consequences of the energy expression (2.9)? Consider initially the linear response of this circuit for $V_{ds} \cong 0$.[9] Then (2.9) simplifies to

$$F_0(N, V_{ds} = 0) = \frac{e^2}{2C_\Sigma}\left[N - \frac{C_g V_g}{e}\right]^2 \tag{2.10}$$

Curves of F_0 vs. $C_g V_g/e$ for $N = 0$ and 1 are shown in Fig. 2.3(a). For a given V_g, there is a certain N which is lowest in energy, except at half-integer values of the gate voltage. Other than at the crossing points of the parabolas, N is fixed. As a result, current through the dot is strongly suppressed except at the crossing points, giving rise to the peaks in G_{dot} shown schematically in Fig. 2.3(b). These peaks correspond to the measured peaks shown in Fig. 2.2. They are periodic in gate voltage with period ΔV_p,

$$\Delta V_p = \frac{e}{C_g} \tag{2.11}$$

This period is represented in Fig. 2.2.

In the notation of this thesis, N refers to the net charge of the island measured in units of the electron charge e (and e is positive). The island actually consists of both

---

[8]The term $N_t eV_{ds}$ in Eqn. 2.6b becomes just NeV_{ds} in Eqn. 2.7 because only those electrons which are currently on the dot matter for N-dependent properties.

[9]In a real measurement of linear transport, though V_{ds} must be nonzero in order to measure anything, its magnitude is chosen to be negligibly small compared with other energies in the system.

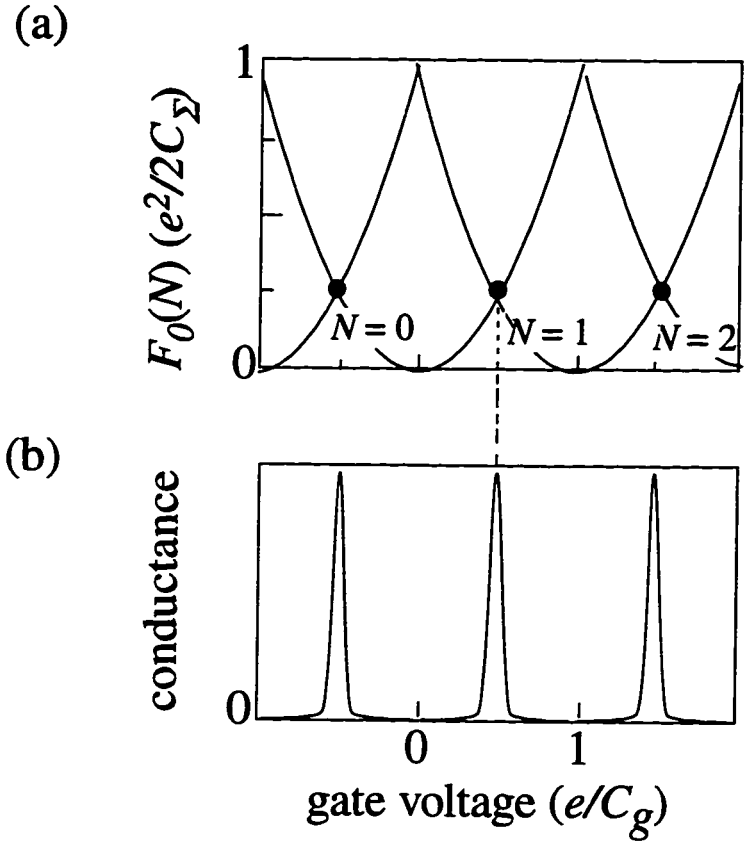

Figure 2.3 (a) Single dot electrostatic energy F_0 with zero drain-source bias vs. gate voltage V_g for N = -1, 0, 1, and 2. (b) Schematic zero-bias dot conductance G_{dot} vs. V_g; conductance peaks occur at gate voltages at which $F_0(N) = F_0(N \pm 1)$.

positive and negative charges, so there are far more than N electrons in the physical island. Some authors choose to make this explicit by referring to the net (or excess) number of electrons as $N - N_0$. The experimental consequences of N being an excess number of electrons will be discussed more in Chapter 3.

2.2.3 *Effects of Single-Particle States on Conductance Peaks*

Since semiconductor quantum dots are not simply ideal circuits, we must introduce additional subtleties to our model. The same conditions of small size and low temperature which allow single-electron charging effects to be observed also give rise to quantum confinement effects. A simple model for the effects of quantum confinement is to approximate it as independent of the electrostatics [Kouwenhoven and McEuen, 1996].

A hard-walled box in two dimensions has eigenstates which are on average evenly spaced.[10] If we model the level spacing, δE, as a constant, then in zero magnetic field[11] δE is simply the Fermi energy divided by the total number of (spin-degenerate) states,

$$\delta E = \frac{2E_F}{N} \tag{2.12}$$

The Fermi energy of the electrons in the GaAs/AlGaAs 2DEG used for the measurements of this thesis is 14 meV; thus if electron temperatures $T_e = 75$ mK are attainable, $T < 4\ \delta E$ and thus single-particle states can be resolved under the following conditions:

$$\delta E = \frac{2E_F}{N} = \frac{325\ \text{K}}{N} \quad \text{so} \quad \delta E > 4(75)\ \text{mK} \quad \text{if} \quad N < 1100\ \text{electrons} \tag{2.13}$$

For a quantum dot formed in a typical 2DEG with electron sheet density $n_s \sim 4 \times 10^{11}/\text{cm}^2$, the maximum dot area for which $4T < \delta E$. is the area corresponding to 1100 electrons,

---

[10]Since the density of states in two dimensions, when smoothed over some energy scale, is constant, and since slight irregularities in the shape of the dot destroy any symmetries of the dot which would tend to select particular eigenstates, the single-particle level spacing in a moderate-size quantum dot is often approximated as constant. However, it is not truly constant even in a chaotic system in which level repulsion tends to compress the statistical distribution of level spacings.

[11]In the presence of a magnetic field, the spin degeneracy of levels is removed, so the level spacing is halved.

$$A_{dot} = \frac{N}{n_s} = \frac{1100}{4x10^{11}/\text{cm}^2} = 2.75 \text{ x } 10^{-9} \text{ cm}^2 = 0.275 \ \mu\text{m}^2 \qquad (2.14)$$

(The lithographic area of the dot is substantially larger than the actual area of the 2DEG in the dot because the 2DEG depletes laterally out from the gates, as will be discussed in Chapter 3.)

We can estimate the range of dot areas for which Coulomb charging is significant as follows: The total capacitance C_Σ of a conducting disc of diameter d is approximately $C_\Sigma(d) \approx \pi\varepsilon_0\varepsilon_s d$, where ε_s is the dielectric constant of the material surrounding the disc [Glattli *et al.*, 1991]. For quantum dots in GaAs/AlGaAs heterostructures, this relation reduces numerically to

$$C_\Sigma(d) \approx 4.49x10^{-18}(\text{F}/\text{nm})d \qquad (2.15)$$

For the disc capacitance to be less than 1.5 fF (corresponding to charging energy ~ 1 K), we require a diameter less than 350 nm, corresponding to an area of 0.123 μm^2. We see that sub-micron-size dots which exhibit Coulomb charging will also have a level spacing which is significant at dilution refrigerator temperatures: a dot of area ~ 0.12 μm^2 should have $N \sim 500$ electrons and thus $\delta E/4 \sim 165$ mK.

To include single-particle levels in the total energy of the dot F_0, we add a term to Eq. (2.9) [van Houten, Beenakker, and Staring, 1992] which sums over levels p:

$$F_0(N) = \frac{e^2}{2C_\Sigma}\left[N - \left(\frac{C_g V_g}{e} + \frac{C_L V_{ds}}{e}\right)\right]^2 + NeV_{ds} + \sum_p E_p \qquad (2.16)$$

where E_p is the energy of the p^{th} electron in the dot, measured from the bottom of the conduction band. (Note that at zero magnetic field there will be pairs of spin-degenerate levels so that $E_p = E_{p+1}$ for odd p.) Again this result simplifies for zero-bias conductance because the terms containing V_{ds} drop out.

Calculations analogous to those shown above for the circuit model have been done which include the effect of single-particle states [Averin, Korotkov, and Likharev, 1991; Averin and Likharev, 1991]. A good sense of the physics can be gained by considering energy diagrams as in Fig. 2.4.[12] Figures 2.4 (a) and (b) show the energy landscape for a single quantum dot with $\delta E = 0$ and Figs. 2.4 (c) and (d) modify the landscape to include discrete energy levels. In both cases we consider infinitesimally small dc bias voltage. As shown in Eq. 2.7, for $V_{ds} \equiv 0$, ϕ_{dot} depends on gate voltage and number of electrons; in this figure we assume N electrons on the dot and $\phi_{dot} = \phi_{dot}(N)$. We see in both (a) and (c) that the energy cost of adding an electron ("addition energy") means that current does not flow through the dot for most gate voltages (as previously discussed). When the electrostatic potential ϕ_{dot} of the island is such that the electrochemical potential of the leads μ_{lead} is aligned with the electrochemical potential of the dot μ_{dot} corresponding to the lowest unoccupied state, current will flow, as shown in (b) and (d). Thus this alignment is accomplished for specific gate voltage values V_g at which $\mu_{lead} = \mu_{dot}(N + 1)$.

So how do we determine the addition energy? The electrochemical potential of the leads μ_{lead} is simply equal to the Fermi energy of the 2DEG; the dot electrochemical potential μ_{dot} is given by [Kouwenhoven and McEuen, 1996]

$$\mu_{dot}(N) \equiv F_0(N) - F_0(N-1) = \frac{e^2}{C_\Sigma}\left[N + \frac{1}{2}\right] - e\frac{C_g V_g}{C_\Sigma} + E_N \qquad (2.17)$$

Thus the addition energy at constant V_g is

$$\mu_{dot}(N+1) - \mu_{dot}(N) = \frac{e^2}{C_\Sigma} + (E_{N+1} - E_N) = \frac{e^2}{C_\Sigma} + \delta E \qquad (2.18)$$

where the second expression is for the case of constant level spacing. Note that the addition energy of an electron (2.18) reduces to the single-electron charging energy e^2/C_Σ in the

[12]This approach to discussing the role of single-particle states is similar to that used in the Ph.D. thesis of Nijs van der Vaart (1995).

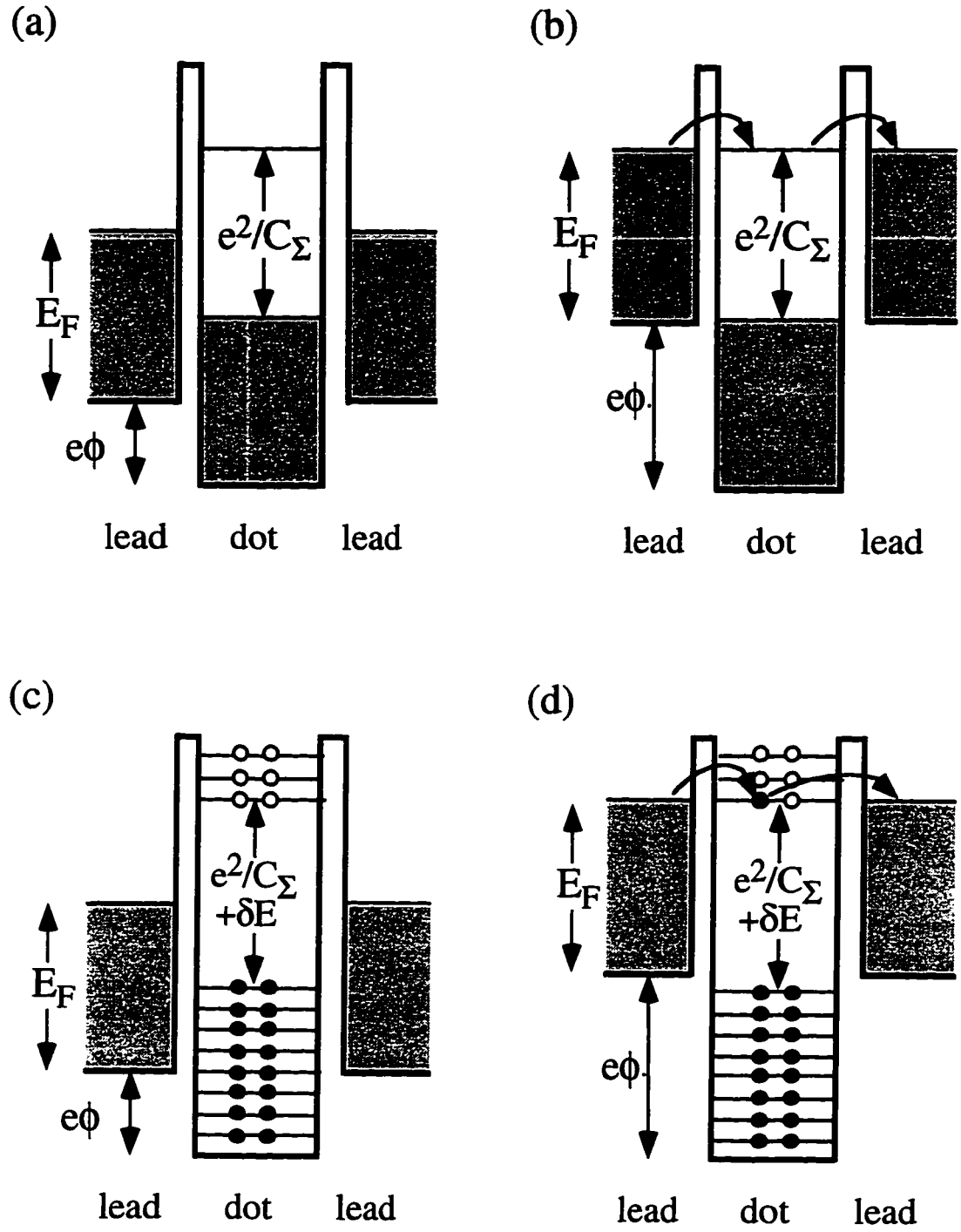

Figure 2.4 Energy diagrams of a quantum dot showing conditions for tunneling. Shaded areas represent continuous bands of energy states which are filled with electrons. Arrows represent tunneling. (a) Transport is blocked by the addition energy e^2/C_Σ; (b) the potential ϕ of the dot relative to the leads overcomes the blockade. In (c) and (d) the same physics is shown except that in the presence of discrete single-particle states, the addition energy is $e^2/C_\Sigma + \delta E$, as discussed in the text. [After van Houten *et al.*, 1992.]

limit of continuous level spacing ($E_{N+1} - E_N \to 0$), and is modified by the single-particle level spacing if that spacing is significant. Current will thus flow (for $V_{ds} = 0$) when $\mu_{lead} = \mu_{dot}(N+1)$ with N electrons in the dot. Since μ_{dot} depends on V_g, sweeping V_g will produce a sequence of peaks in conductance spaced by

$$\Delta V_p = \frac{C_\Sigma}{eC_g}\left[\frac{e^2}{C_\Sigma} + E_{N+1} - E_N\right] \tag{2.19}$$

The primary impact of single-particle levels on zero-bias conductance is thus to modify the conductance peak spacing, so that a peak occurs when the dot addition energy is supplied by the change in gate voltage since the most recent conductance peak. Consider the case of zero magnetic field, in which energy levels are spin-degenerate. If uniformly spaced levels with spacing δE are assumed, we obtain an alternating peak spacing,

$$\Delta V_{p1} = \left(\frac{\delta E}{e} + \frac{e}{C_g}\right)\frac{e^2 / C_\Sigma}{e^2 / C_\Sigma + \delta E / 2} \tag{2.20a}$$

$$\Delta V_{p2} = \left(\frac{\delta E}{e} + \frac{e}{C_g}\right)\frac{e^2 / C_\Sigma + \delta E}{e^2 / C_\Sigma + \delta E / 2} \tag{2.20b}$$

The average spacing is $e/C_g + \delta E/2$.

If we measure the peak spacings from the data of Fig. 2.2(a), we do not see this alternating peak spacing; rather there is a fair amount of scatter in the peak spacings.[13] This shows that either the level spacing is not constant, or transport is taking place through several levels rather than one (likely if $T > \delta E/4$). As stated previously, the approximation of constant level spacing is not at all exact. Charging events can also disrupt the peak spacing, as will be discussed in Chapter 3.

[13]There is a slow monotonic decrease in the average peak spacing as the side gate voltage becomes less negative; this is most likely due to the dot becoming slightly larger and slightly closer to the gate as the depletion around the gate decreases, thus increasing C_g and decreasing the period e/C_g.

The other significant effect of quantum confinement on conductance peaks is the modulation of peak heights. We see in Fig. 2.2 that the heights of the conductance peaks G_{peak} at base temperature vary substantially.[14] If there were a continuum of levels in the dot (or just a very large number of levels within k_BT of the Fermi level) the peak heights would all be the same. The explanation commonly invoked in the literature for peak height variation [see, for example, van Houten, Beenakker, and Staring, 1992] is that tunneling through a series of single quantum states with dramatically different coupling to the leads would give different peak heights. Indeed, electrostatic simulations of conductance peaks [Stopa, 1996] indicates that for a dot with ~100 electrons, there is significant variation of tunneling matrix elements from state to state in the presence of some ordering in the donor layer. Thus the variation in G_{peak} confirms that tunneling is taking place through one or a few single-particle states.

Another approach to modeling transport through a single quantum dot uses the Anderson Hamiltonian for a single impurity site coupled to leads [Gruner and Azwadowski, 1974; Kulik and Shekhter, 1975; Meir, Wingreen, and Lee, 1991, 1993; Wang, Zhang, and Bishop, 1994] and modifying it appropriately for the single quantum dot:

$$H = \sum_n E_n c_n^+ c_n + \frac{1}{2} UN(N-1) + \sum_{k \in L,R} E_k a_k^+ a_k + \sum_{\substack{n \\ k \in L,R}} \left[V_{kn} a_k^+ c_n + h.c. \right] \qquad (2.21)$$

The operators c_n^+ and a_k^+ create electrons on the dot and in the leads respectively (L, R refer to the right and left leads), and their hermitian conjugates (h.c.) are the appropriate

[14] An alternative explanation for not having all peak heights the same would be that as the side gate voltage is swept, the conductance of the tunnel barrier between the dot and the leads changes due to the capacitive influence of the side gate on the tunnel barriers. There certainly is some amount of influence of the side gate on the conductance of the tunnel barriers, as will be discussed in Chapter 3. However, such influence is too small to cause the dramatic modulation we observe, and it also ought to produce a monotonic decrease in the peak heights as the gate voltage is made more negative. We do observe this at the extreme negative end of the gate voltage range over which conductance peaks can be observed, but there is a wide range of gate voltage over which the effect is insignificant.

annihilation operators. $U = e^2/C_\Sigma$ is the Coulomb interaction energy, $E_{n,k}$ the energy levels on the dot and in the leads, and V_{kn} the matrix elements for tunneling between the k^{th} lead level and the n^{th} dot level. The advantage this treatment has over the orthodox theory presented earlier is that it accounts for the matrix elements for transport between the dot and leads. This model becomes fairly intractable, however, with more than a few levels.

2.2.4. Temperature Dependence of Zero-Bias Conductance Peaks

The most common model used to determine the zero-bias conductance peak shape is linear response treatment of the orthodox theory [Kulik and Shekhter, 1975; Beenakker, 1991; for a review see van Houten, Beenakker, and Staring, 1992]. When it is assumed that the tunneling rates Γ between the dot and its leads are very low, so that lifetime broadening $h\Gamma$ is insignificant compared to other energies, and that those tunneling rates are energy-independent (i.e. that all tunneling matrix elements are the same), the peak shape simply comes from the derivative of the Fermi function. This model has three distinct temperature regimes. In the first, in which k_BT exceeds the charging energy e^2/C_Σ, charging effects are not seen, so only the other two regimes are relevant to our measurements.

In the "classical Coulomb blockade" regime [van Houten, Beenakker, and Staring, 1992], $\delta E << k_BT << e^2/C_\Sigma$, the temperature is substantially smaller than the charging energy, so that charging effects are important, and it is significantly greater than the level spacing, so that the dot is effectively metallic and tunneling takes place through a continuum of states at the Fermi level. In this regime, the peak heights G_{peak} are essentially temperature-independent, and the widths increase with increasing temperature according to the following peak shape:

$$G = G_0 \frac{(\varepsilon_{dot} - \varepsilon_0)/k_BT}{\sinh\left((\varepsilon_{dot} - \varepsilon_0)/k_BT\right)} \approx G_0 \cosh^{-2}\left(\frac{\varepsilon_{dot} - \varepsilon_0}{2.5k_BT}\right) \tag{2.22}$$

with $\varepsilon_{dot} - \varepsilon_0$ measuring the distance between the dot potential and resonance,

$$\varepsilon_{dot} - \varepsilon_0 = \frac{e^2}{C_\Sigma}\left[\frac{C_g}{e}\left(V_g - V_{g0}\right)\right] \tag{2.23}$$

where V_{g0} is the gate voltage location of a conductance peak (as determined in the preceding section). The constant peak height $G_{peak} = G_0$ is determined by the tunneling rates through the leads,

$$G_0 = \frac{e^2}{2\delta E}\left[\frac{\Gamma_l \Gamma_r}{\Gamma_l + \Gamma_r}\right] \tag{2.24}$$

with $\Gamma_{l(r)}$ the total tunneling rate between the dot and the left (right) lead.[15]

In the resonant tunneling or "quantum Coulomb blockade" regime, $h\Gamma << k_B T << \delta E$, only one state is involved in transport, which changes both the peak shapes and heights [van Houten, Beenakker, and Staring, 1992]. The peak shape in the resonant tunneling regime is the derivative of the Fermi function:

$$G = G_0 \cosh^{-2}\left(\frac{\varepsilon_{dot} - \varepsilon_0}{2k_B T}\right) \tag{2.25}$$

If we approximate the tunneling matrix elements between the leads and the dot states as constant, so that the tunneling rates Γ between the dot and its leads are independent of the particular ground state, the peak heights are proportional to $1/T$:

$$G_{peak} = G_0 = \frac{e^2}{4k_B T}\left[\frac{\Gamma_l \Gamma_r}{\Gamma_l + \Gamma_r}\right] \tag{2.26}$$

In the samples we study, the tunneling rates are different for the different ground states, and thus we see peak height variation as previously discussed. These energy-dependent tunneling rates do not affect the peak shape or width, however.

[15]For future students of Coulomb oscillations who are puzzled about the factor of 2.5 in Eq. (2.50), it comes from approximating $x/\sinh(x)$ as $1/\cosh^2(x/2.5)$; the peak shape is not simply the derivative of the Fermi function for one state since multiple states are involved.

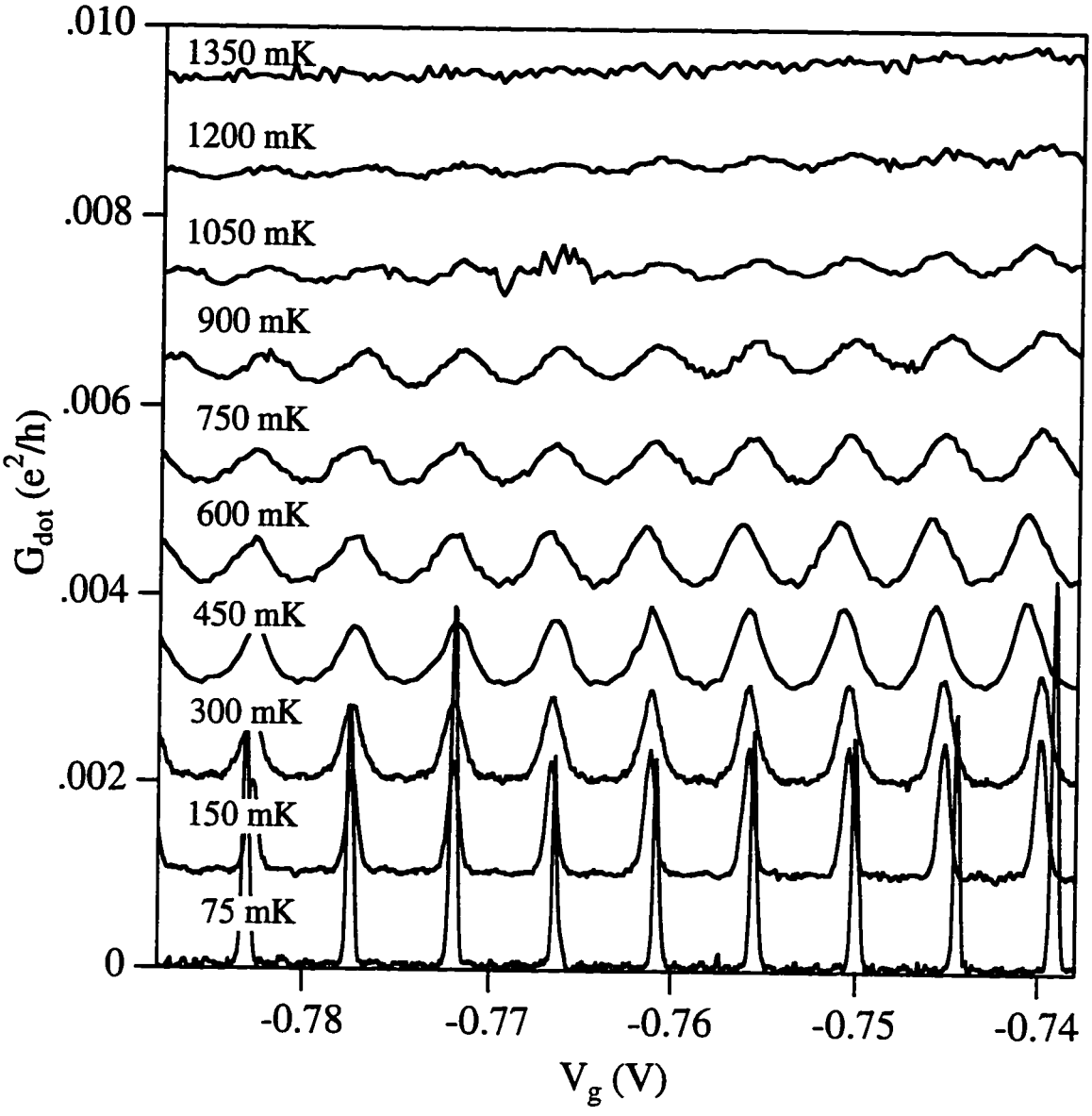

Figure 2.5 Single quantum dot conductance G_{dot} as a function of temperature. Traces have been offset vertically for clarity (by a constant amount) and horizontally to align the peaks (charging events between measurements cause horizontal offsets).

Figure 2.5 shows a series of conductance peaks measured for increasing values of the temperature, vertically offset for clarity. Qualitatively, we can see that the peaks measured at base temperature vary in height from one peak to the next, while those measured at 150 mK and higher have essentially constant height over the range of gate voltage used. This suggests that at base temperature transport is by resonant tunneling, while at 150 mK we enter the classical Coulomb blockade regime . This is consistent with the expected value of $\delta E \sim 400$ mK for our dots, which contain about 750 electrons;[16] once $T > 4\delta E$, we expect multiple states to be involved in transport. The peak heights decrease and the widths increase with increasing temperature.

The peaks of Fig. 2.5 are fit very well by (2.22) and (2.25) from base temperature to 600 mK; Fig. 2.6 shows these fits at (a) base temperature and (b) 450 mK. The dot conductance G_{dot} is shown on a logarithmic scale (open circles) and the fit is drawn as a solid line. The three parameters of the fit are the peak position V_{g0}, the peak height G_0, and the peak width (equal to $2.5C_\Sigma k_B T/C_g e$ in (2.22) and $2C_\Sigma k_B T/C_g e$ in (2.25)). In Fig. 2.7, we see that the peak widths obtained from these fits are proportional to temperature from 150 mK to ~ 600 mK. With $C_\Sigma = 342$ aF and $C_g = 39$ aF (determined from the differential conductance measurements presented in section 2.3.2), we expect the slope of the widths vs. temperature to be 1.94×10^{-3} mV/mK in the classical regime. (We do not expect to measure a slope corresponding to the resonant tunneling regime since we expect only the base temperature widths to reflect resonant tunneling.) We measure a slope which is approximately 2.5×10^{-3} mV/mK, in reasonable agreement. If we assume the base temperature point should lie on a line with slope corresponding to the resonant tunneling

[16]This number is determined from the electrostatic simulations presented in Chapter 5, and is in reasonable agreement with the number obtained from simply multiplying the 2DEG sheet density by the estimated area of the device after accounting for depletion and that obtained from measurements of the single-particle excitation spectrum presented at the end of this chapter. The estimate from the measured excitations gives a slightly larger number (~1000 electrons, corresponding to $\delta E \sim 300$ mK) but very few excitations are measured. Also, as discussed later in this section, the electron temperature appears to be about 70 mK, and the fact that our base temperature measurements seem to be well into the quantum regime is more consistent with the slightly larger δE and smaller number of electrons.

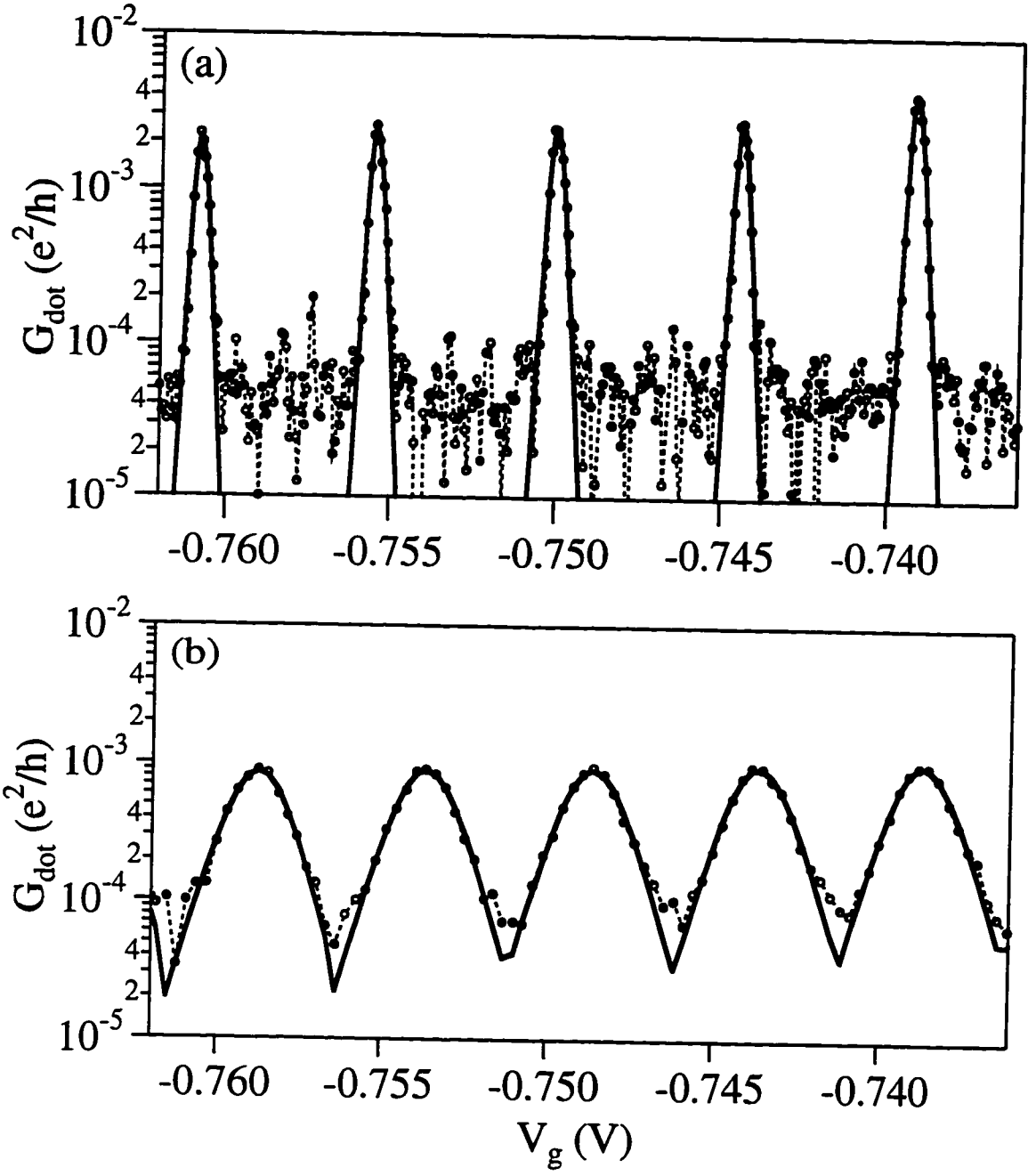

Figure 2.6 Conductance data from Fig. 2.5 (open circles and dashed lines) and fits to thermally broadened lineshape (solid line) at two different temperatures. Conductance is shown on a logarithmic scale. (a) Base temperature ($T_{electron}$ ~ 70 mK, T_{mix} ~ 15 mK) (b) T = 450 mK.

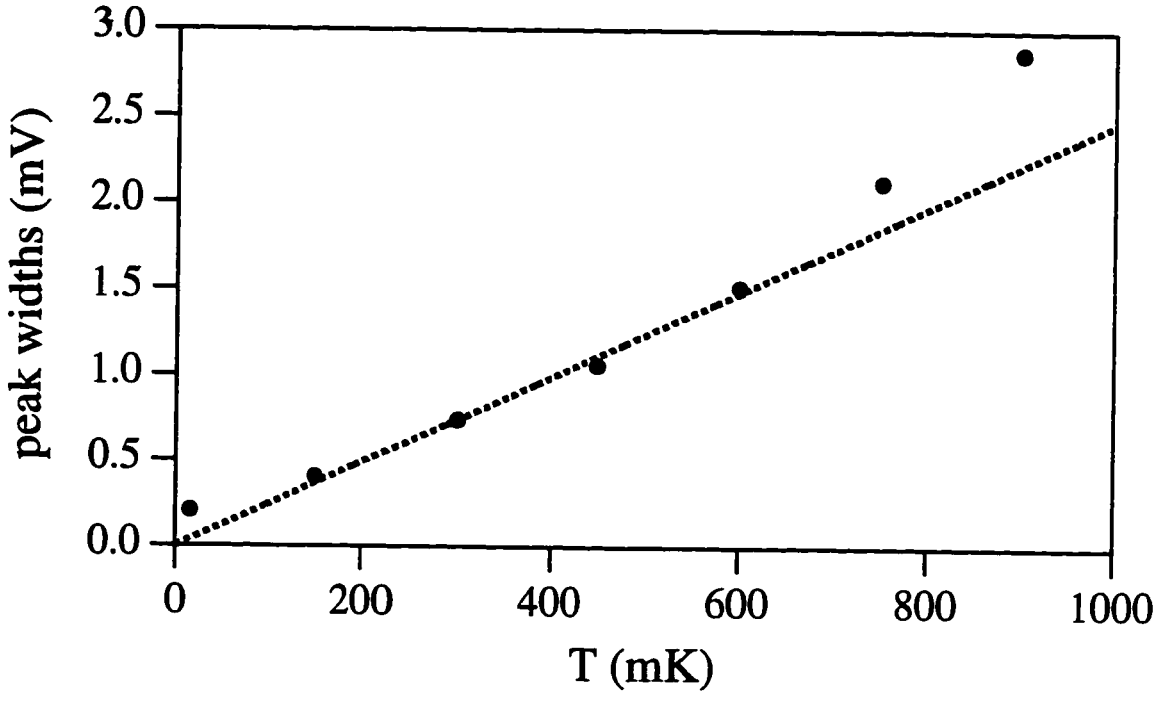

Figure 2.7 Conductance peak widths (from fits to Eq. 2.22 as shown in Fig. 2.6) vs. T (solid circles). The dashed line is the best fit to the data for 150 mK $\leq T \leq$ 600 mK.

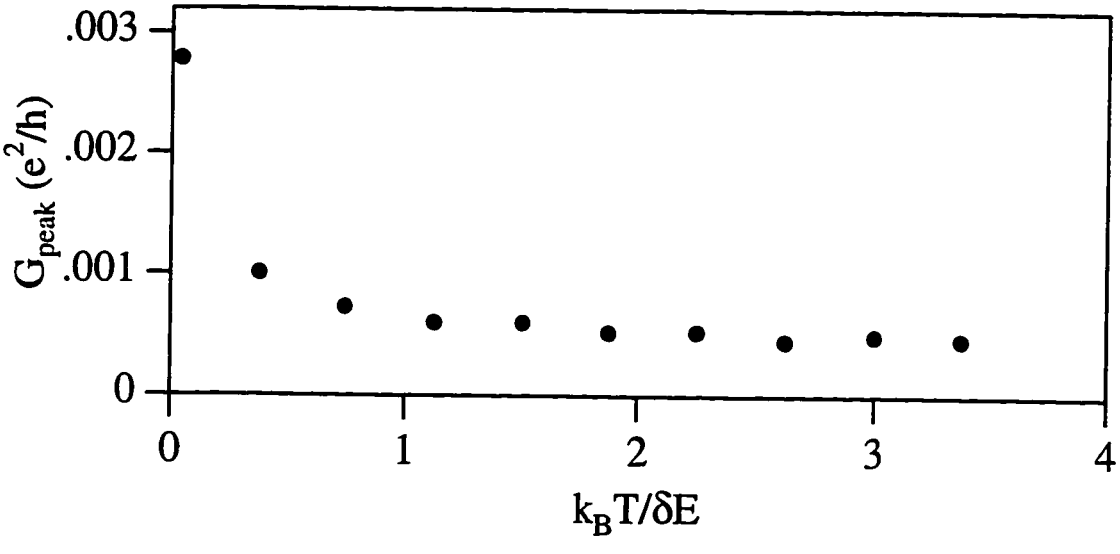

Figure 2.8 Conductance peak heights G_{peak} vs. $k_BT/\delta E$ measured from Fig. 2.5. Heights become nearly constant for $k_BT \geq \delta E$.

regime, we obtain an electron temperature of about 70 mK for those peaks. It is not clear why points taken at higher temperatures do not seem to fit with this trend; at 750 mK, the temperature should still be substantially less than the dot charging energy.

The peak heights G_{peak} vs. T are shown in Fig. 2.8. The peak heights depend sharply on T at the lowest temperatures and then become roughly independent of T for T substantially greater than $\delta E/4k_B$ ~ 100 mK. Indeed, Fig. 2.8 is in good qualitative agreement[17] with a calculation by van Houten, Beenakker, and Staring [1992, Fig. 8, p. 182], which assumes $h\Gamma << k_BT$ and treats the Fermi function exactly (which is important in the regime where δE and k_BT are the same order of magnitude).

The results of Figs. 2.5 to 2.8 are in good agreement with previous measurements [Foxman *et al.*, 1993, 1994]. They demonstrate that in our device, lifetime broadening is unimportant compared to temperature broadening, and at base temperature we are in the resonant tunneling regime, moving into the classical Coulomb blockade regime for $T > 150$ mK. More accurate information on the dot total capacitance and the single-particle level spacing is obtained from the nonlinear measurements of section 2.3.4.

Finally we consider the cotunneling processes which dominate off-peak transport. With weak tunneling between dot and leads, the primary means of transport is through first-order tunneling processes. These processes are activated and are strongest at gate voltage resonance positions; the peaks die off exponentially to the sides. Second-order tunneling, or inelastic cotunneling, processes also occur; electrons tunnel from the right to the left lead through virtual states on the dot, creating electron-hole pairs on the dot. The cotunneling conductance is proportional to T^2 [Furusaki and Matveev, 1995]:

$$G = \frac{G_L G_R}{6e^2/h}\left(\frac{k_B T}{4E_C\left(X - X^*\right)}\right)^2 \qquad (2.27)$$

[17]The calculation cannot be expected to agree quantitatively becaues it is a numerical calculation assuming particular values of the conductances of the left and right tunnel junctions.

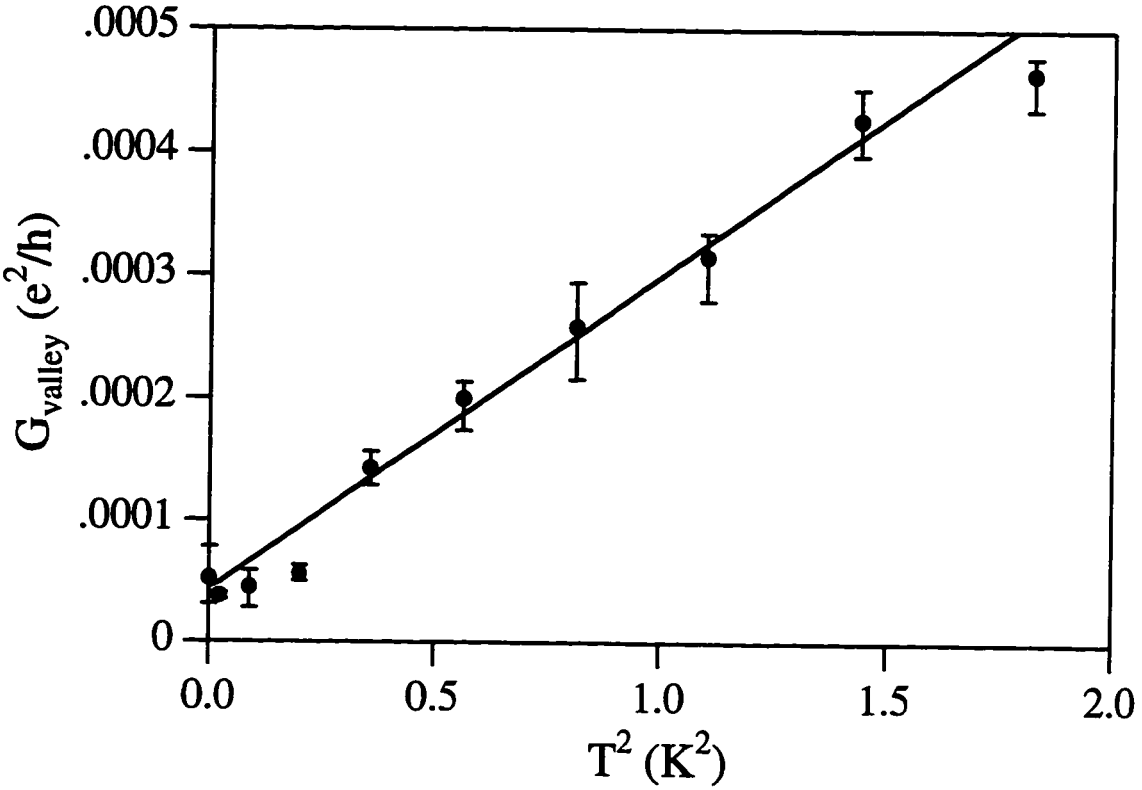

Figure 2.9 Conductance valley heights G_{valley} (from data shown in Fig. 2.4) vs. T^2 (solid circles). Error bars indicate the range of valley heights measured. The dashed line is the best linear fit to the data for $T \leq 600$ mK.

Inelastic cotunneling dominates the conductance between peaks, although it gives only a small correction to the peak value. Figure 2.9 shows valley conductance G_{valley} from the data of Fig. 2.5 vs. T^2 measured at the lowest point between peaks and averaged over several such measurements (error bars reflect range of measurements). We see that valley conductance is roughly proportional to T^2. The best fit line crosses the G_{valley} axis at 4.3 x 10^{-5} e^2/h; we would not expect it to go through zero since there are some noise sources in the measurement.

2.3 Nonequilibrium Single Dot Transport

So far we have discussed linear conductance measurements, which give information primarily about the ground state of the quantum dot. The non-linear current-voltage characteristics give additional information about the ground state but also probe excited states.

2.3.1 Conditions for Coulomb Blockade

The sequence of periodic peaks in linear conductance arise because the energy cost of adding a single electron to the quantum dot is significant, blocking the transport of current except when the ground state energy is degenerate for N and $N+1$ electrons. This phenomenon is also called the "Coulomb blockade" of transport. The Coulomb blockade can be lifted by applying a finite source-drain bias voltage. Returning to the capacitive circuit model, consider the change in free energy which occurs when an electron tunnels from the battery to the island in the tunneling process shown in Fig. 2.10(a), increasing the number of electrons on the island from N to $N+1$. In the presence of finite V_{ds}, this free energy change can be written

$$\Delta F_L(N \to N+1) \equiv F_0(N+1) - F_0(N) = \frac{e^2}{C_\Sigma}\left[N + \frac{1}{2} - \frac{C_g V_g}{e} + \frac{(C_\Sigma - C_L)V_{ds}}{e}\right] \tag{2.28a}$$

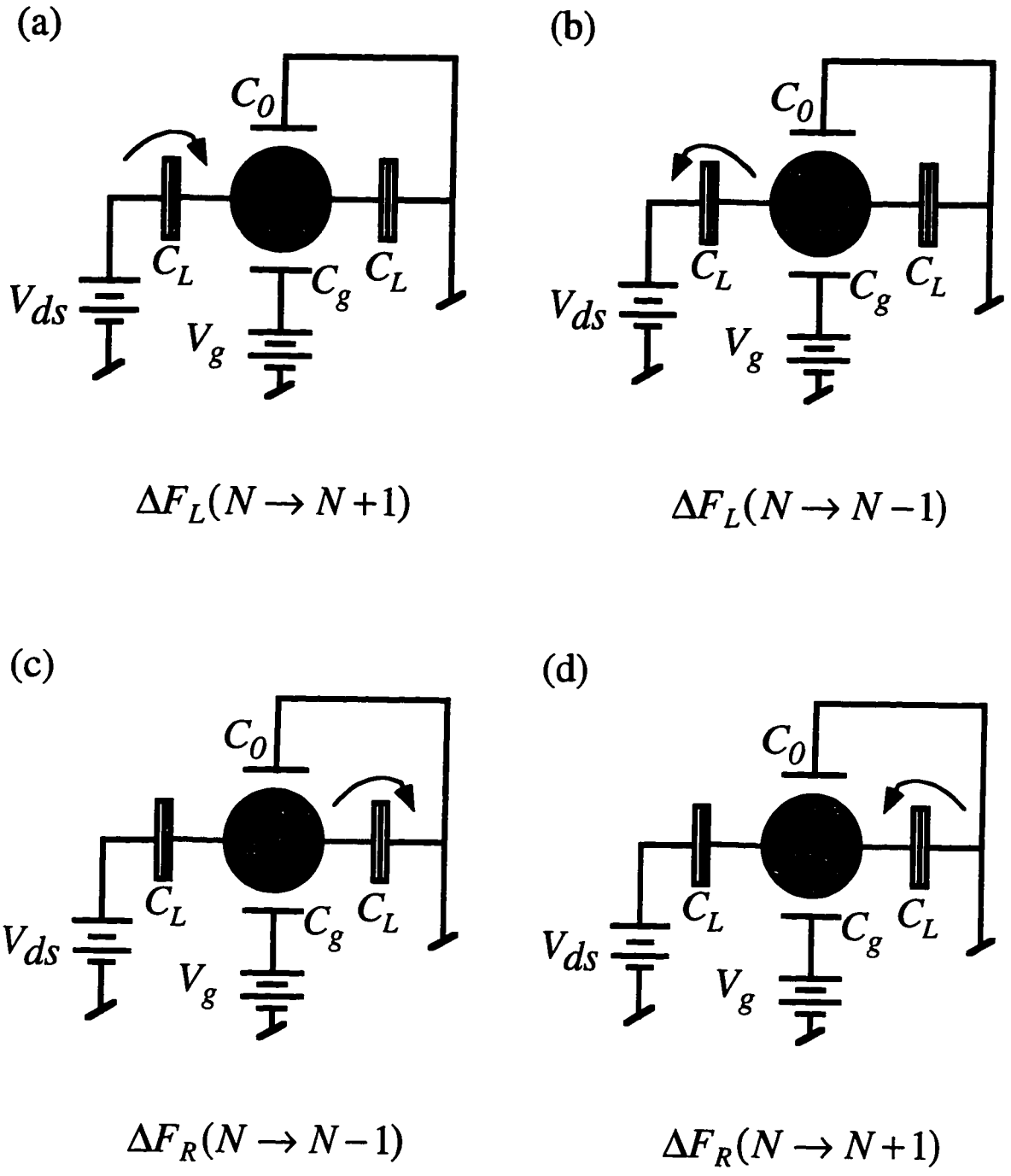

Figure 2.10 (a)-(d) Possible single-electron tunneling processes for a single quantum dot with N electrons initially, represented within the equivalent circuit formalism. The arrow indicates the tunneling process, with the back of the arrow at the point of origin of the tunneling electron and the arrowhead at the destination of the electron. Each process shown has a free energy change given by the corresponding member of Eqs. 2.28.

where $\Delta F_L(N \rightarrow N+1)$ indicates that the number of electrons on the island has changed from N to $N+1$ by an electron tunneling on from the left lead. (When electron number changes because of electrons tunneling through the right lead, the drain-source voltage contribution to the energy change is different; thus it is necessary to keep track of which leads are involved.)

To determine conditions under which current can and cannot flow through the quantum dot, we note that this tunneling event will occur even at zero temperature if $\Delta F_L(N \rightarrow N+1)$ is negative and will not if it is positive. We can write analogous expressions for the three other ways that an electron can be added to or removed from the island, corresponding to Figs. 2.10(b-d); they are

$$\Delta F_L(N \rightarrow N-1) = -\frac{e^2}{C_\Sigma}\left[N - \frac{1}{2} - \frac{C_g V_g}{e} + \frac{(C_\Sigma - C_L)V_{ds}}{e}\right] \tag{2.28b}$$

$$\Delta F_R(N \rightarrow N-1) = -\frac{e^2}{C_\Sigma}\left[N - \frac{1}{2} + \frac{C_g V_g}{e} + \frac{C_L V_{ds}}{e}\right] \tag{2.28c}$$

$$\Delta F_R(N \rightarrow N+1) = \frac{e^2}{C_\Sigma}\left[N + \frac{1}{2} + \frac{C_g V_g}{e} + \frac{C_L V_{ds}}{e}\right] \tag{2.28d}$$

In Figure 2.11(a) we show model $I(V_{ds})$ curves that result from these energy conditions at fixed V_g [after Averin and Likharev, 1991]. We consider $C_g V_g/e = N$ (black solid line), $N + 1/4$ (dashed line), and $N + 1/2$ (gray solid line). Substituting those values into Eqs (2.8) and setting the free energy change which results equal to zero, we solve for V_{ds}, the voltage at which current begins to flow for a particular gate voltage. We also determine V_{ds} values at which states with $N \pm 1$ electrons are degenerate with states with $N \pm 2$ electrons, and so on.[18] What do we expect to happen at these values of V_{ds}? We note

[18] Note that unless a drain-source voltage can be applied wtih infinite speed, the number of electrons must change successively by 1, so that the m^{th} step in the Coulomb staircase is *not* the voltage at which the free energy cost of adding m electrons to a dot with N electronsbecomes zero, but rather at which adding 1 electron to a dot with $N + m - 1$ electrons becomes zero.

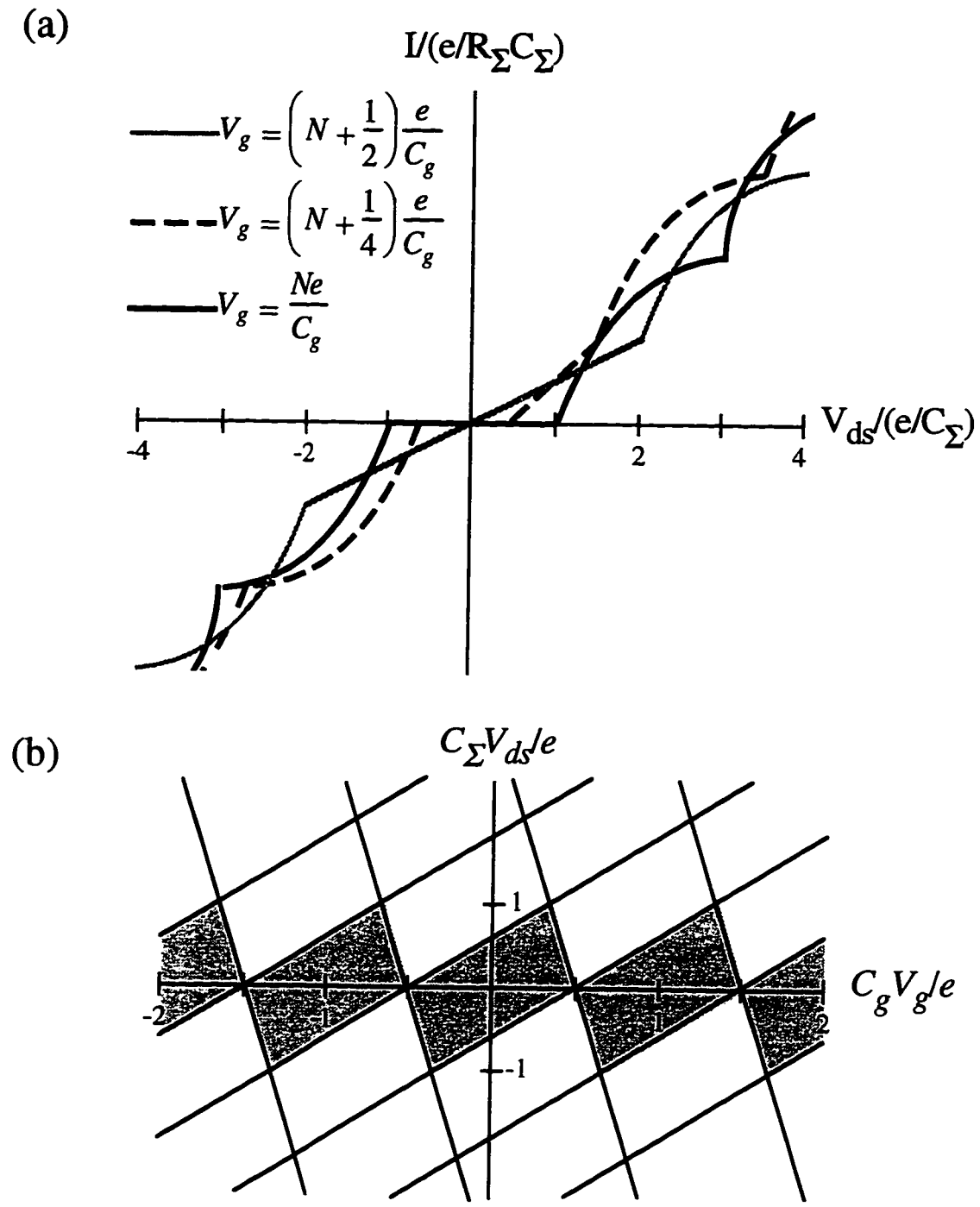

Figure 2.11 (a) Schematic I-V characteristics for a single dot with equal capacitances from the dot to the left and right leads but different tunnel conductances through the two tunnel junctions, for three different values of gate voltage and $T = 0.01\ e^2/C_\Sigma$ (R_Σ = total resistance from island to leads). After Averin and Likharev (1991), Fig. 19. (b) Schematic of region of Coulomb blockade as a function of both V_{ds} and V_g. Shaded region corresponds to Coulomb blockade; boundary of shaded region corresponds to threshold for current flow (peaks in differential conductance). Additional lines correspond to higher Coulomb steps.

that for given values of V_g and V_{ds}, the ground state of the island has a specific number of electrons, except for certain V_{ds} values (for fixed V_g) such that states with N and $N \pm 1$ electrons are degenerate. At these V_{ds} values, there is an abrupt increase in the current which can pass through the device since the degeneracy opens up a new channel for current flow. For $V_g \neq N + 1/2$, we see a region of zero current around $V_{ds} = 0$, surrounded by a series of steps in the current corresponding to the ability to change the number of electrons on the dot by one. This series of steps is known as the Coulomb staircase, and the region of zero current is referred to as Coulomb blockade. For $V_g = N + 1/2$, there is no region of zero current – the other features of the I-V_{ds} characteristic collapse around the onset of current at $V_{ds} = 0$.

The exact shape of the I-V_{ds} characteristic of a single dot depends on the relative magnitude of all the capacitances and conductances of the system, particularly of the tunnel junctions; thus actual simulation of the I-V_{ds} characteristic requires this information [see Tinkham, 1996, for a thorough exposition of the process of calculating an I-V characteristic; also see Averin and Likharev, 1991]. This exposition and the model curves of Fig. 2.11(a) are intended only to motivate the Coulomb staircase physically.

Now let us determine the regions of Coulomb blockade in (V_{ds}, V_g) space – those regions in which the system is stable against changing the total number of electrons on the island, in which all four energy changes (2.28) are positive. Algebraic manipulation of Eqs. (2.28a) to (d) shows that the Coulomb blockade of transport is effective under the following conditions:

$$N + \frac{1}{2} > \frac{C_g V_g}{e} + \frac{C_L V_{ds}}{e} > N - \frac{1}{2} \tag{2.29a}$$

$$N + \frac{1}{2} > \frac{C_g V_g}{e} - \frac{(C_\Sigma - C_L) V_{ds}}{e} > N - \frac{1}{2} \tag{2.29b}$$

We show these regions graphically in Fig. 2.11(b). We define the following normalized voltage coordinates:

$$x \equiv \frac{C_g V_g}{e} \quad \text{and} \quad y \equiv \frac{C_\Sigma V_{ds}}{e} \tag{2.30}$$

and define $\gamma \equiv C_L / C_\Sigma$. Making these substitutions in Eqs. (2.29), we then find that the region of Coulomb blockade forms a parallelogram in the (x,y) plane. The boundaries of this parallelogram, which correspond to zero free energy change required for a tunneling event, are given by

$$y = \frac{1}{1-\gamma} x \pm \frac{1}{2(1-\gamma)} \tag{2.31a}$$

$$y = -\frac{1}{\gamma} x \pm \frac{1}{2\gamma} \tag{2.32b}$$

These parallelograms are the shaded regions of Fig. 2.11(b). Note that the slopes of the sides of the parallelogram and its height and width are completely determined by the island capacitances C_g, C_Σ, and C_L.

The two-dimensional regions of Coulomb blockade shown in Fig. 2.11(b) reduce to two familiar phenomena when their behavior along just one axis is examined. If we fix $V_{ds} = 0$ and look along the V_g axis, we see that transport is blockaded except at half-integer values of $C_g V_g / e$, corresponding to the linear conductance peaks in previously derived. If we fix V_g to some constant value (other than half-integer) and look at a slice through the diagram parallel to the y axis, we see a region of no current flow around $V_{ds} = 0$, surrounded by the onset of current, corresponding to the I-V_{ds} characteristic previously shown in Fig. 2.11(a).

2.3.2 Experimental Results – Finite-Bias Differential Conductance

In a measurement of current as a function of V_{ds} and V_g, the area inside the parallelograms of Fig. 2.11(b) is the region of Coulomb blockade, the boundaries of the

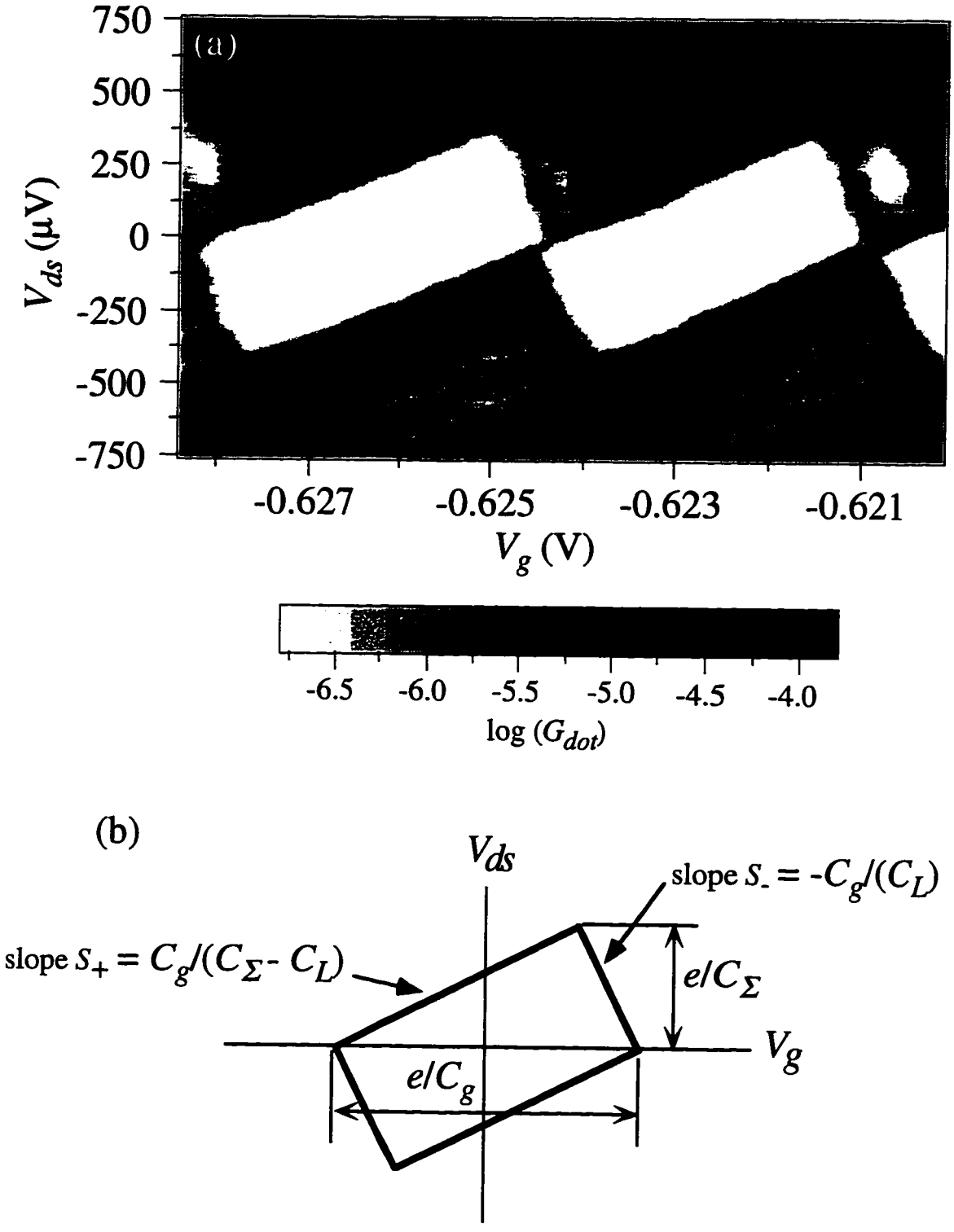

Figure 2.12 (a) Measured differential conductance (logarithmic grayscale shown above) $G_{dot}(V_{ds}, V_g)$ through a single dot. (b) Schematic of one region of Coulomb blockade illustrating how dot capacitances (as defined in Fig. 2.1(b)) are determined.

parallelogram correspond to the threshold voltages for current flow, and outside the parallelogram current can flow.[19] We have measured differential conductance dI/dV rather than current; thus the boundaries of the parallelogram correspond to peaks in the differential conductance surrounding a region of zero conductance, and the higher Coulomb steps also appear as peaks.

Figure 2.12 (a) shows the two-probe voltage-biased differential conductance of a single quantum dot as a function of both gate voltage and drain-source voltage, measured with ac lockin techniques. (The measurement technique is discussed in more detail in Chapter 3.). The magnitude of the conductance G_{dot} in Fig. 2.12(a) is represented by the (logarithmic) inverted grayscale, with black the highest conductance and white the lowest conductance. We can easily see light parallelograms of Coulomb blockade outlined by dark lines corresponding to the onset of current.[20] We can also see the second step of the Coulomb staircase, which corresponds to extending the boundary from an adjacent parallelogram into the gate voltage region of interest. The intervening lines of peaks are due to quantum confinement and will be discussed in section 2.3.3.

As was explained in section 2.3.1, the slopes of the boundaries and the dimensions of the parallelograms are determined by the capacitances of the equivalent circuit shown in Fig. 2.1(b). In terms of the actual gate voltage and drain-source voltage (rather than renormalized quantities), the total height of the parallelogram, as indicated in Fig. 2.12(b),

---

[19]These boundaries are determined from the threshold voltages for an electron to tunnel across one tunnel junction. Is it necessarily energetically favorable for an electron to tunnel through the other junction, allowing current to flow as another electron undergoes the original tunneling event and so on? It can be shown readily [Tinkham, 1996; also this author has done the calculations for both single and double dots, but will not bore the reader with the details] that after the first tunneling event occurs, the energetics are such that it is also favorable for current to flow by having an electron tunnel in the same direction through the other junction.

[20]The steeper (negative slope) boundaries are less pronounced than the positive slope boundaries, which is also true of the double dot nonlinear conductance measurements (Ch. 5). Most likely this is because these data are taken scanning drain-source voltage at a fixed value of side gate voltage, then incrementing the gate voltage and repeating the scan, and the negative-sloped boundaries are thus nearly parallel to the direction of the scan. It is not possible to measure this pattern sweeping gate voltage and incrementing drain-source voltage; too many charging events (discussed further in Ch. 3) render the pattern unrecognizable.

is $2e/C_\Sigma$ (in volts). This allows us to measure the charging energy e^2/C_Σ. For the slopes of the boundaries, we have

$$S_+ = \frac{C_g}{C_\Sigma - C_L} \tag{2.32}$$

$$S_- = -\frac{C_g}{C_L} \tag{2.33}$$

where S_+ and S_- refer to the positive and negative boundary slopes respectively. These quantities are indicated in Fig. 2.12(b).

Performing fits to the boundaries for several periods of the measurement shown in Fig. 2.12(a) gives the following values for the capacitances of a single dot (as defined in Fig. 2.1(b) and Eq. 2.1):

$C_\Sigma = 342 \pm 15$ aF

$C_L = 75 \pm 10$ aF

$C_g = 39 \pm 2$ aF (previously determined from conductance peak spacing)

These measurements were made on dot 1 of sample KC7EE; numbers which agree within the error bars of the measurement were obtained for the other dot and for other samples.

2.3.3 Role of Quantum Confinement in Nonequilibrium Transport

The orthodox theory [van Houten, Beenakker, and Staring, 1992] includes single-particle levels as a separate term in the total energy (2.16). To understand the effect of single-particle levels in nonequilibrium transport, Fig. 2.13 shows the energy landscape of Fig. 2.4 generalized to include finite V_{ds}. Current flows when $\mu_L \geq \mu_{dot}(N+1)$.

The simplest effect of single-particle levels on nonlinear transport is to change the energy cost of adding a single electron by the single-particle level spacing, as described in Eq. (2.18). Thus, all of the conditions (2.28) would be modified by adding the term $E_{N+1} - E_N$, slightly distorting the parallelograms. For quantum dots in which the energy level spacing is much smaller than the charging energy, such as those studied in this thesis, the

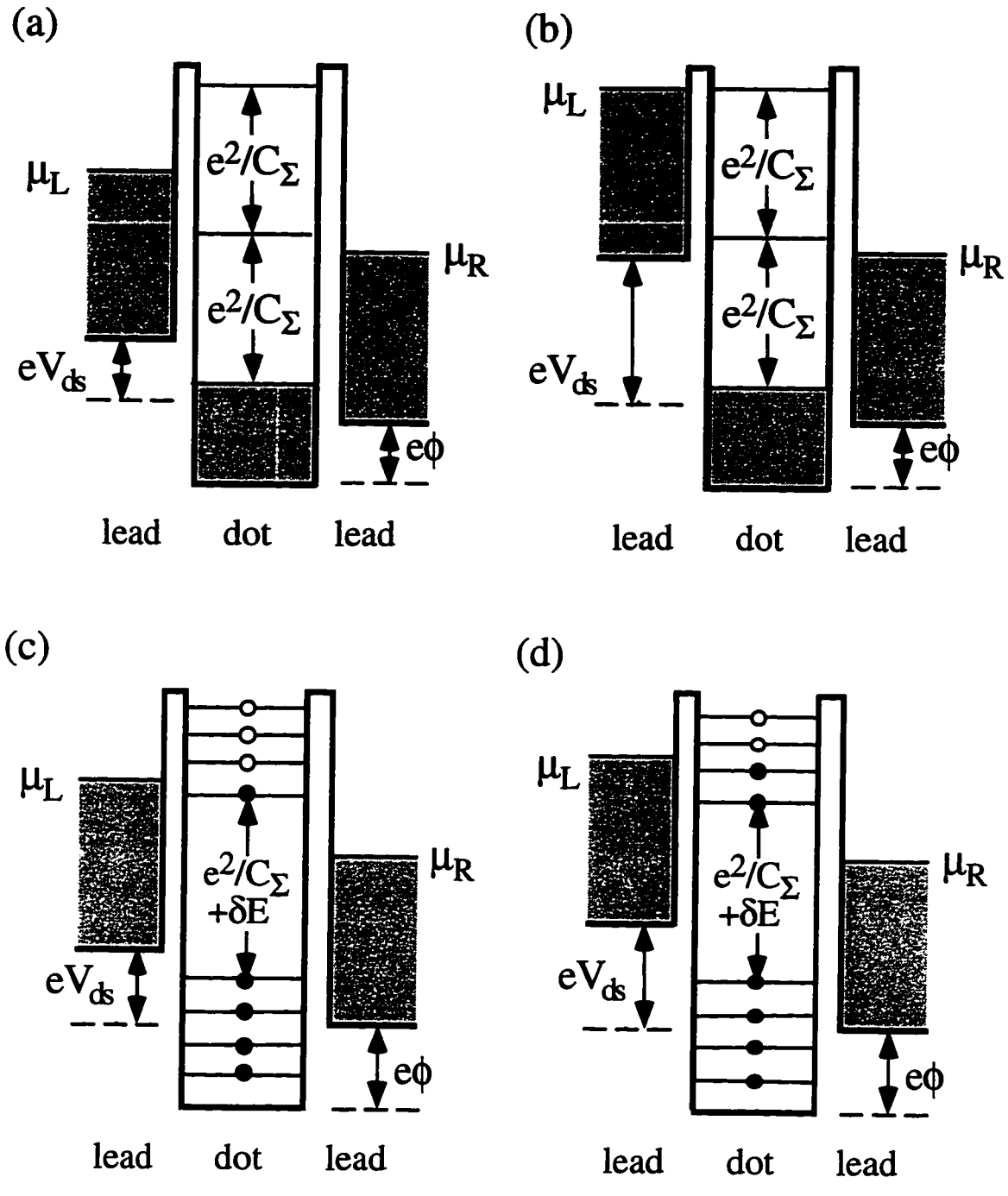

Figure 2.13 Energy diagrams of a quantum dot showing tunneling conditions with finite drain-source bias V_{ds}. Shaded areas represent continuous bands of energy states which are filled with electrons. (a) With continuous dot states, transport is possible when μ_L exceeds the addition energy e^2/C_Σ; (b) the second Coulomb step will be visible if a second electron can then be added. (c) With discrete states spaced by δE, the addition energy becomes $e^2/C_\Sigma + \delta E$ as previously discussed; (d) excited states become visible when multiple states lie between μ_L and μ_R. (Part (c): After van der Vaart, Ph.D. thesis.)

primary effect of the single-particle states is not on transport through the ground state, however; the main difference from a system with a continuum of levels is that now discrete excited states of the system can be detected.

Essentially, the change introduced by adding a source-drain bias is that the chemical potential of the source lead μ_L (taken to be the left lead throughout this thesis) is raised above the Fermi energy by eV_{ds}, and the chemical potential of the dot is correspondingly raised by $eC_L V_{ds}/C_\Sigma$. Because the electrostatic contribution to the potential ϕ_{source} exceeds that of the dot ϕ_{dot} (or, in the case of negative drain-source voltage, $\phi_{drain} > \phi_{dot}$), there are two effects on transport. We have already discussed the effect on transport through the dot ground state: transport can occur at gate voltages for which there is no zero-bias conductance because V_{ds} supplies the energy needed to overcome the Coulomb blockade. This gives the parallelograms of blockade shown in Fig. 2.11(b).

Adding a source-drain bias enables probing excited states of the dot in addition to the ground state. As shown in Fig. 2.13(d), when μ_L is raised sufficiently above μ_{dot} that the first excited state of the $N+1^{st}$ electron is below μ_L in energy, transport can occur not only through the $N+1$-electron ground state but the first excited state with $N+1$ electrons. The probability of tunneling through the dot increases when more than one single-particle state is available for transport, and the total amount of current carried increases. This leads to a secondary step structure in the I-V_{ds} characteristic, which manifests itself as a series of smaller resonances in the differential conductance between those corresponding to the first and second Coulomb steps. Thus transport through excited states is visible as additional resonances within the region of allowed current flow.

2.3.4 Observation of Excited States

In Fig. 2.12(a), we can see lines corresponding to single-particle states quite easily for $V_{ds} < 0$. The V_{ds} spacing between successive lines is 90 μV, 110 μV, and 150 μV. The average spacing is 117 μV, which corresponds to an average energy level spacing $\delta E = 26$

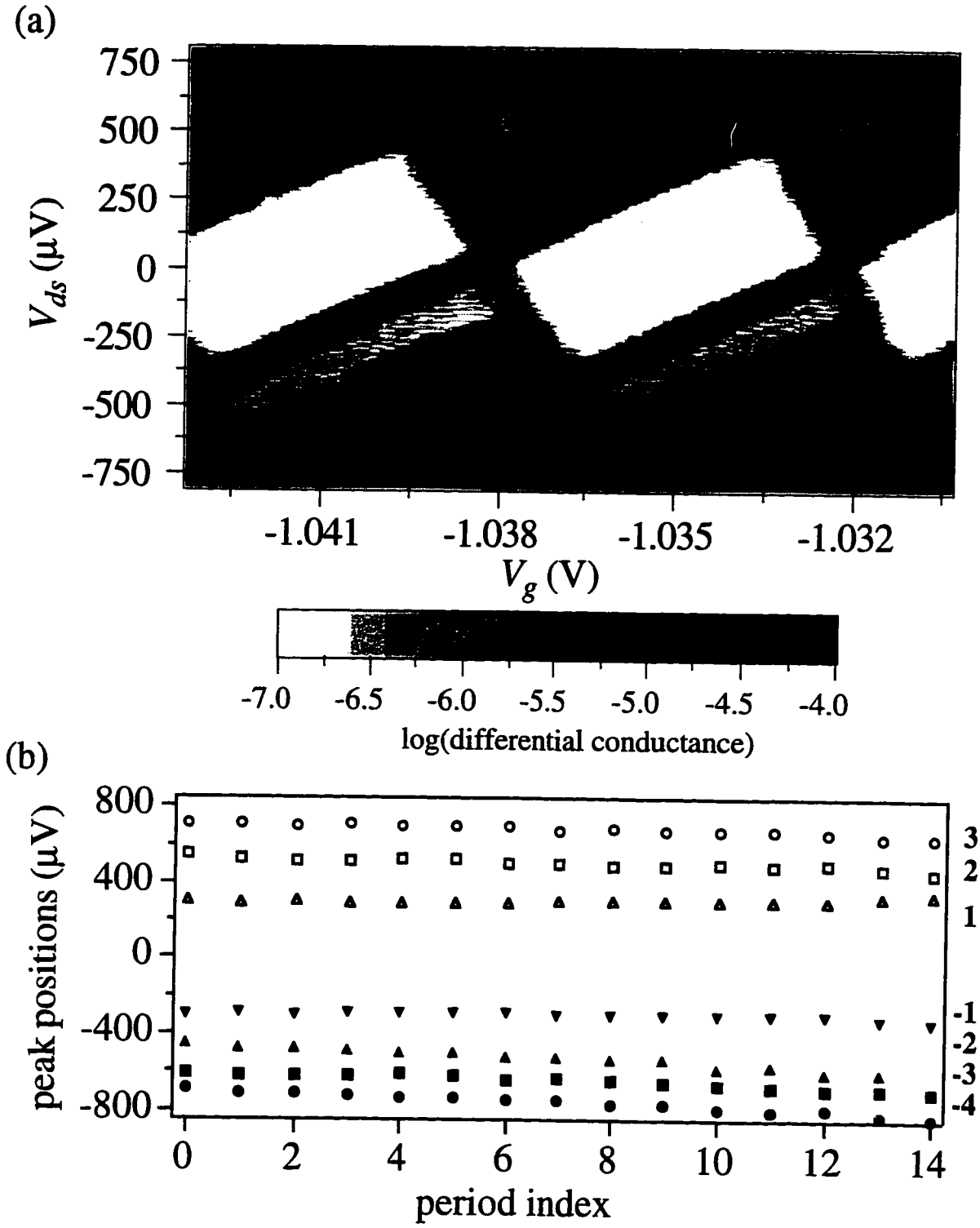

Figure 2.14 (a) Measured differential conductance (logarithmic color scale shown above) through a single dot vs. side gate and drain-source voltage. For this measurement care was taken to match the conductances of the two point contacts so that excited states could be observed for both positive and negative V_{ds}. (b) Positions of differential conductance resonances measured for each of fifteen periods in gate voltage at the gate voltage at which the gap is centered around $V_{ds} = 0$.

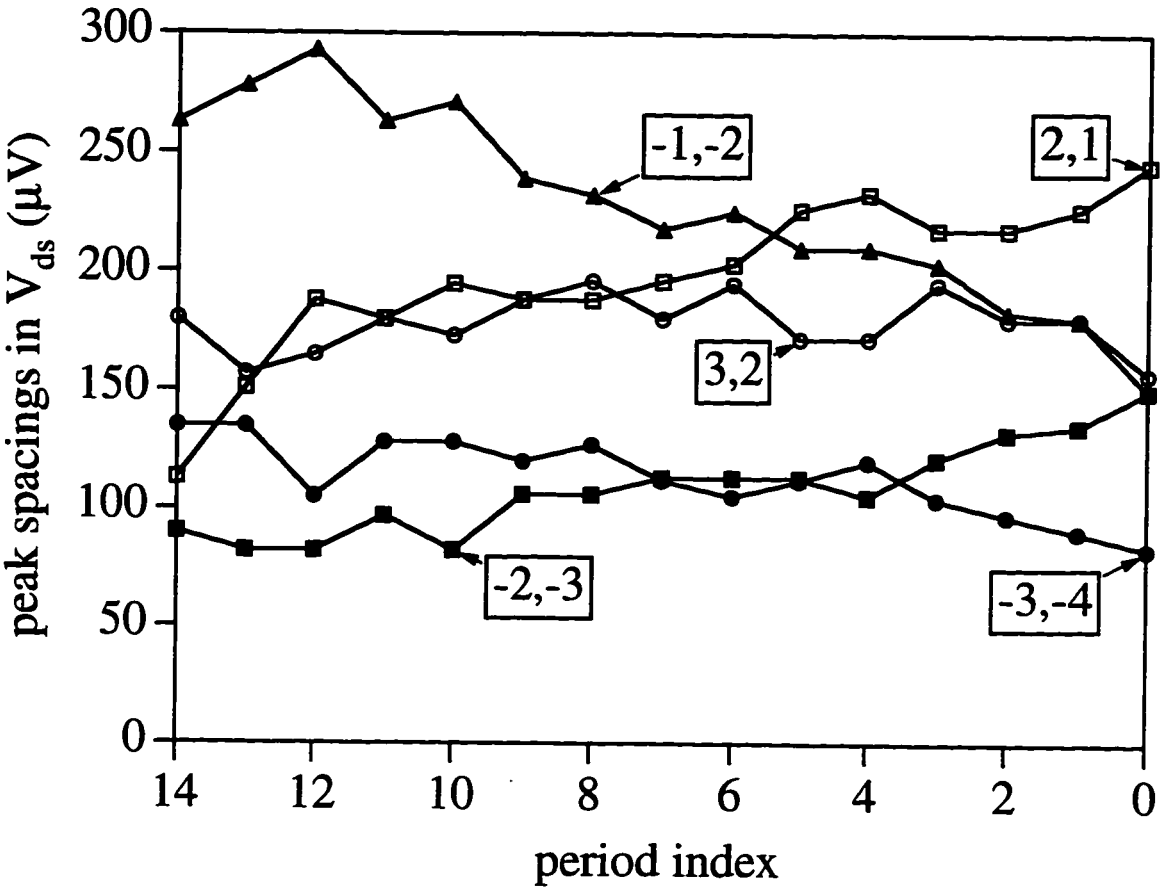

Figure 2.15 Evolution of spacings between excited states of Fig. 2.14 with gate voltage period. Each symbol corresponds to the spacing betwen a particular pair of resonances and is labeled with the numbers given to those resonances in Fig. 2.14.

μeV and a range of observed spacings from 20 to 33 μeV.[21] Solving $\delta E = 2E_F/N$ for N gives about 1000 electrons on the island, corresponding to T = 300 mK. As will be discussed in Chapter 5, electrostatic simulations suggest there are 750 to 800 electrons, which would correspond to an average level spacing of 35-37 μeV, similar to that observed (especially since we do not observe a statistical number of excited states).

An interesting feature of the data shown in Fig. 2.12(a) is that the two adjacent periods of Coulomb blockade shown have essentially identical excited states, which are not evenly spaced. This seems inconsistent with the simple single-particle picture in which the first excited state of a dot with N electrons is the same as the ground state of the dot with N + 1 electrons and the second excited state of a dot with N - 1 electrons. To investigate this further, we carefully balanced the conductances through the two tunnel junctions of the dot so that we could see excited states clearly for both positive and negative V_{ds}, and measured fifteen successive periods of $G_{dot}(V_{ds}, V_g)$.[22] A few periods of this measurement are shown in Fig. 2.14(a), with conductance represented as inverted grayscale as in Fig. 2.12(a). Figure 2.14(b) shows the V_{ds} positions of the excited states in each period, measured at the point at which the gap is symmetric about $V_{ds} = 0$.

These data show clearly that the excited states do not have the naive successive correspondence of the second excited state of N electrons corresponding to the first excited state of $N + 1$, and so on. Rather, the excited state spacing seems to stay roughly the same over all 15 periods, and the changes we do see occur very gradually. Figure 2.15 plots the separation between each pair of states vs. period index, with the first period corresponding to the most negative gate voltage in Fig. 2.14(b). The consistent yet irregular spacing of

---

[21]The energy level positions are determined by determining the change in the dot potential due to the applied voltage using Eq. 2.6(a).

[22]It is difficult to get the conductances well matched when both junctions are conducting only weakly, because in the weak tunneling regime, the junction conductance is very sensitive to the voltage applied to the gate which forms the junction. This will be made clearer in the dicussion of quantum point contacts in Chapter 4. It is also difficult to measure more than about 15 successive periods of this phase diagram, corresponding to 100 mV in gate voltage, because over that range the overall conductance of the device drops substantially and it becomes difficult to see the excitations well, which are generally of lower conductance than the Coulomb steps.

excited states is most evident in the states seen for $V_{ds} < 0$, in which the separation between the first and second excited state is substantially larger than the separation between second and third (compare filled triangles and filled squares in Fig. 2.15).

Is it possible that the excited states of Fig. 2.14(a) correspond to a collective excitation of the electron gas rather than single-particle eigenstates of the dot potential? It seems unlikely, because the center-of-mass plasmon excitations have energies in the infrared, corresponding to millivolt energy separations between states [Meurer et al, 1992]. If some other sort of excitation were responsible for these resonances, that would explain why the excitation energies appear nearly independent of the number of electrons.

From these measurements we conclude that at base temperature tunneling takes place through one single-particle state (or possibly a few), since we can observe individual resonances between the Coulomb steps. Furthermore, the I-V_{ds} characteristics give us values for the capacitances of the dots which will be valuable for analyzing the double dot data later on. Finally, intriguing questions are raised about the nature of the excited states.

2.4 Summary

This chapter presents a detailed introduction to single-electron transport, illustrated with measurements made on a single dot of our double dot sample. These measurements also serve to characterize our sample; from them we determine the capacitances of the individual dots and the single-particle level spacing. We also demonstrate that the primary source of broadening in our weak tunneling measurements is thermal. This information will be useful in interpreting the experimental results of Chapters 4 and 5. Finally, we observe the excited states of the single dot and observe that the spacing of these states is insensitive to the number of electrons on the dot.

CHAPTER 3
EXPERIMENTAL METHODS[1]

3.1 Introduction

In the past twenty years or so, the study of semiconductor nanostructures has grown from infancy into maturity. The modulation-doped GaAs/AlGaAs heterostructure was introduced in 1978 [Dingle *et al.*, 1978]; in 1986 the split-gate confinement technique was demonstrated [Thornton *et al.*, 1986; Zheng *et al.*, 1986]. Since then, the techniques of fabricating split-gate devices on GaAs/AlGaAs heterostructures have been refined by increasing numbers of groups. The Westervelt group is no exception; the members of our group have been developing expertise in wafer processing and electron beam lithography (EBL) for a number of years now, and those techniques have been enumerated in many theses preceding this one [Berry, 1994; Yang, 1995; Katine, 1996; Adourian, 1996]. Likewise, the Oxford Model 200 dilution refrigerator was installed before the chilled water system in Gordon McKay[2], in 1983, and its features have been described extensively in other theses [Tighe, 1993; Hopkins, 1990; Rimberg, 1992; Baskey, 1994; Hergenrother, 1995] and in the annotated Harvard manual (kept in a black binder in Room 202). General principles of design and operation of ^{3}He/^{4}He dilution refrigerators have been understood for much longer [see for example Richardson and Smith, 1988]. Finally, low-noise measurements of multiple-tunnel-junction devices have been done by many groups for some time. General low-noise techniques have been discussed extensively in many sources [for example see Ott, 1976; Mar, 1994] and particular techniques used for single-electron charging effect measurements have been reported in a number of Harvard theses [for example see Waugh, 1994, and Hergenrother, 1995].

---

[1]The author is grateful for guidance in writing this section – namely, what level of detail to use – from Fred Waugh.

[2]This is actually a relevant remark – see Appendix C.

This chapter will therefore not elaborate things which have been explained very well by previous authors; instead the author seeks to give a brief overview of the techniques used which will be helpful to a reader who is not already familiar with them, and then give more technical details only in those areas which this author has participated in developing, or which are particularly pertinent to coupled semiconductor quantum dot studies. Most of the details related to electron beam lithography and Model 200 dilution refrigerator operation are sufficiently technical that they are recorded in Appendices B and C respectively.

3.2 GaAs/AlGaAs Heterostructures and 2DEG Physics

The GaAs/AlGaAs heterostructures our group uses are grown by Art Gossard's research group in the Materials Department at UC-Santa Barbara (and the particular wafers used in the experiments for this thesis were grown by Ken Campman). They are grown in an ultra-high vacuum molecular beam epitaxy (MBE) chamber. This apparatus allows material to be deposited on a substrate one atomic layer at a time, so that atomically clean interfaces separate the various materials in the heterostructure. A layer may consist of a mixture of different elements in precise proportions, or it may be a pure element. The elements used in our wafers are Al, Ga, As, and Si (other common materials for MBE include In and Be).

Figure 3.1 shows a cross-section of the heterostructure (KC7) used for the experiments described here; the extreme right is the substrate, and right to left is the direction in which the wafer is grown, with the leftmost layer the top surface of the wafer. Beginning with the substrate, the composition of wafer KC7 is as follows: 100 nm GaAs; 100 nm AlGaAs; a 30-period superlattice of GaAs/AlGaAs (120 nm total thickness); 1000 nm GaAs; the "spacer layer", 22 nm AlGaAs; the dopant layer, an AlGaAs monolayer with Si concentration 8×10^{12} cm^{-2}; the barrier layer, 30 nm AlGaAs; and the 5 nm GaAs cap layer. AlGaAs is shorthand for $Al_xGa_{1-x}As$, where x is the mole fraction of Al; in this

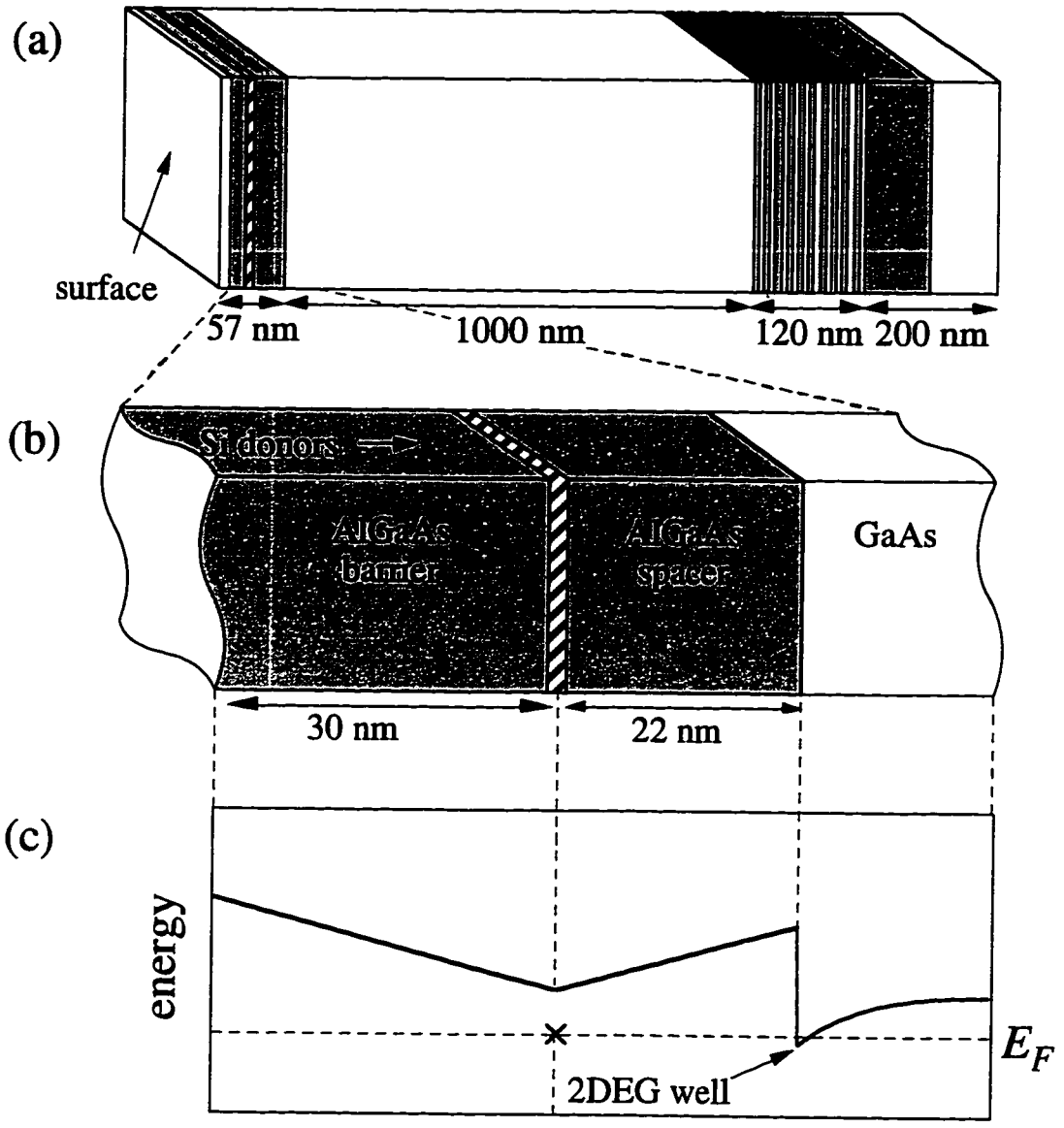

Figure 3.1 (a) Composition profile of GaAs/AlGaAs heterostructure used for the devices studied in this thesis. The growth direction is from right to left. White regions, GaAs; shaded regions, AlGaAs; hatched region, Si donors. (b) Expanded view of region in which 2DEG forms. (c) Schematic conduction band energy vs. position for region shown in (b). 2DEG forms at the triangular well which is the sum of the GaAs/AlGaAs conduction band discontinuity and the electrostatic potential of the ionized donors. After Waugh, Ph.D. thesis (1994).

wafer $x = 0.31$. In the figure GaAs is shown as white and AlGaAs as shaded, with the doping layer hatched. This wafer structure is referred to as "delta doped" because the Si dopants are deposited in a monolayer of AlGaAs, rather than growing a layer of some thickness containing the dopants. The region where the 2DEG is formed is expanded and shown in 3.1(b), and 3.1(c) shows the self-consistent conduction band structure resulting from this composition.

As shown in Fig. 3.1(c), a potential drop is present at the interface between AlGaAs and GaAs because of the conduction band offset between the two materials. Electrons from the Si donors move to this lower potential region, and the self-consistent electrostatic potential resulting from the band offset and the ionized donors produces a roughly triangular well approximately 5 nm wide at the AlGaAs/GaAs interface, where the 2DEG forms. The mobility of electrons in this well can be orders of magnitude higher than in typical Si MOSFETs primarily because GaAs and AlGaAs are almost perfectly lattice-matched, and thus there is much less boundary roughness [Beenakker and van Houten, 1991]. The low effective mass of the electrons ($m^* = 0.067\ m_e$) in GaAs also enhances the mobility. The wafer used in this experiment (KC7) has sheet density $n_s = 3.5 \times 10^{11}$ cm^{-2} and mobility 5×10^5 cm^2/Vs at 10 K, as measured by Ken Campman. At 0.4 K, the mobility of wafer KC3 increases to 7×10^5 cm^2/Vs, as measured by Jordan Katine without illumination. (The growth profile of wafer KC3 is identical to KC7 except that the AlGaAs barrier width is 20 nm instead of 30 nm.) For more detail on 2DEG physics, the reader is referred to Beenakker and van Houten [1991], and other Westervelt group theses including Katine [1996].

For coupled dot experiments, ultrahigh mobility (i.e. several million cm^2/Vs) is not critical as it is for ballistic measurements; however, it does seem that samples made with high-quality wafer perform better in a number of ways. Coupled dot experiments rely on being able to fix the conductances of several point contacts in series to desired values and simultaneously have all the dots be essentially the same size and contain the same number

of electrons. In other words, they rely on identical lithography translating into identical (or nearly identical) dots. This is most easily realized if the 2DEG is highly uniform, without bald spots or local potential wells. It is also easiest to control the point contact conductances simultaneously if all the point contacts have comparable characteristics, so that the effects of cross-capacitance are comparable for all point contacts. (Further discussion of point contacts is found in Chapter 4.) Again this requires the 2DEG to be essentially uniform across the entire active area of the device.

The most critical consideration for quantum dot experiments, however, is that the conductance of a point contact be stable over time when a fixed gate voltage is applied to it. We have had numerous problems in the past with point contacts exhibiting substantial telegraph noise, in which the conductance of the point contact would change by ten percent or more every few seconds to a minute. Presumably this comes from impurities near the point contact charging and discharging. Such frequent switching makes a sample essentially unusable; as a result we now monitor the stability of point contact conductances as part of diagnosing a sample. (A slow drift in the conductance is not unusual and is to be tolerated, especially when the point contact is well in the tunneling regime.) Generally switching seems to worsen as a wafer ages.[3] Such switching seems to be intrinsic to the wafer (see Katine, 1996, for further discussion), and the best strategy is to make a new sample.

A few remarks are in order about real quantum dot samples (as opposed to the idealized drawings of Chapter 2). First of all, the discussion of charging effects in the previous chapter emphasized N, "the number of excess electrons." The *total* charge on the dot obviously must consist of both the positive background charge in the semiconductor and the electrons. Thus the total number of electrons on the dot will be much larger than the number of excess electrons. In charging effects, however, the quantity of interest is the

[3]For example, many very stable samples were made with wafer KC3 in the summer of 1994, but then when the remaining wafer was used the following spring, the samples made from it showed frequent switching.

number of electrons contributing to the net charge of the dot, i.e. the number of excess electrons. For the rest of this thesis, in discussing semiconductor quantum dots, we will take N to refer to the number of excess electrons in the dot.

One of the difficulties in doing single-electron charging experiments in semiconductor quantum dots is that the positive donor charge (the ionized Si atoms) is not perfectly stable, but undergoes abrupt shifts in response to a variety of environmental factors. These shifts are called "charging events" by the Westervelt group, and manifest themselves in data as a sudden jump in the gate voltage dependence of the transport. Figure 2.2(b) shows a set of conductance peaks with the rightmost peak disrupted by a charging event. (It is somewhat rare to see such charging events which actually break a peak, since the peaks take up only a small fraction of the gate voltage range of a measurement. It is more common to see a substantially shorter or longer space between two adjacent peaks.) The frequency of such charging events seems to depend on the quality of the heterostructure material, the quality of radiation shielding in the cryostat, and the length of time for which the device has been cold. As a result, when cooling a new device, its conductance is monitored, and if charging events disrupt the transport less often than every twenty minutes, the device is considered good quality. More frequent charging events make it difficult (though not impossible) to do measurements (at least until a way is devised to make low-noise measurements at kHz rates).

3.3 Split-Gate Device Fabrication and Wiring

3.3.1 Wafer Preparation

After the wafers are received from UCSB, they are stored in a nitrogen-filled cabinet in the Class 10000 region ("outer room") of the Harvard cleanroom until they are to be used, because over time the wafer degrades on exposure to oxygen.[4] When a sample is

[4]For more details on wafer degradation and the extensive problems this caused the Westervelt group during 1995, see Katine [1996].

to be made, a piece of desired size (usually 3 mm x 5 mm) is cleaved and cleaned by successively boiling in TCE (10 minutes), soaking with ultrasound in acetone (15 minutes) and methanol (15 minutes), and blowing dry with dry ultrapure N_2 gas. Care should be taken in cleaving to obtain crisp, clean edges, since gouges at the edge of the surface can perhaps lead to split gates being shorted to the gas; furthermore, pieces with rough edges are difficult to handle. The piece should then be inspected under a high-power optical microscope before further processing. While a few surface defects are to be expected, greasy streaks on the surface of the wafer or numerous defects may be cause for concern, because a bad surface suggests the gas underneath may be patchy or metal may not stick well. More cleaning, including swabbing gently with a cotton swab soaked in solvents, can be attempted.

3.3.2 Contacts

Two contacting procedures are used in the Westervelt group: Au/Ni/Ge contacts and In contacts. The Au/Ni/Ge process produces lower-resistance, nondiodic contacts (typically around 50 Ω, whereas In contacts are typically 300-600 Ω and may be substantially diodic) and is more reliable and robust toward accidental minor variations in the procedure (if one contact works, usually all work, and failed contacts can usually be successfully re-annealed). These contacts also take up less area and are nearly flush with the chip surface, making subsequent processing easier, and can be wired using the wirebonder, whereas In contacts must be hand-wired. However, in the past problems have arisen with "micro-contacts" forming in other parts of the wafer at some stage of the Au/Ni/Ge contacting process, shorting surface gates to the gas [for a thorough discussion see Katine, 1996]. It is not certain whether this problem arose during the actual contacting process or if the gate metallization process had been contaminated with Ge, though the former seems more likely. Procedures have been developed [Katine, 1996] which seem to avoid such microcontacts, but it is good to be aware that it can happen, and sometimes these problems may be unavoidable. Furthermore, if one is skilled in working with a

scalpel under a microscope, the In contacting process is faster for one or two pieces. Thus either procedure may be useful, depending on the situation.

The Au/Ni/Ge contact process was refined for this group by Carol Livermore and Rex Beck, based on the process developed by Kulkarni and Lukowski [1985]. First windows of the desired size and location are defined in a resist layer (using either photolithography or EBL) on the surface of the GaAs/AlGaAs chip. Then a series of metal layers are evaporated onto those windows, and the sample is annealed (the metal forms a eutectic mixture and penetrates the wafer to the electron gas) so that the metal makes ohmic contact to the 2DEG. This process is shown schematically in Figure 3.2. The contacts are usually placed on an edge or corner of the wafer to avoid current circulating around the contact in a magnetic field [Katine, 1996]. Contacts can be as small as the experimenter's skill in connecting to them with the wirebonder or hand wiring can manage. Generally for hand wiring contacts should be at least 200 x 200 μm^2 with at least 150 μm gaps between adjacent contacts; with the wirebonder 75 x 75 μm^2 contacts separated by 50 μm gaps are manageable. If the contacts are in the middle of the chip rather than on the edge, larger contacts may be needed. If possible, contacts should be made significantly larger to provide extra area in case a wire bond fails or indium refuses to stick on part of the contact surface.

Contacts are large enough that in principle EBL is unnecessary and photolithography should be used; photolithography is cheaper and faster, especially with multiple samples. Furthermore, the photoresist layer is substantially thicker than the PMMA used for EBL (several μm rather than 150 nm), and thus was thought likely to be better protection against contact material reaching the surface in unwanted places. However, it seems that photolithography leaves the surface of the wafer dirtier than EBL, and although the contacts seem to anneal properly, they do not stick strongly enough for wirebonding. We have not tried very hard yet to find a way around this,[5] because we have found that using a PMMA trilayer (bottom two layers 496K, top layer 950 K) and EBL is

[5]For example, one could avoid using the primer and see what happens.

(a) top view: open windows in resist

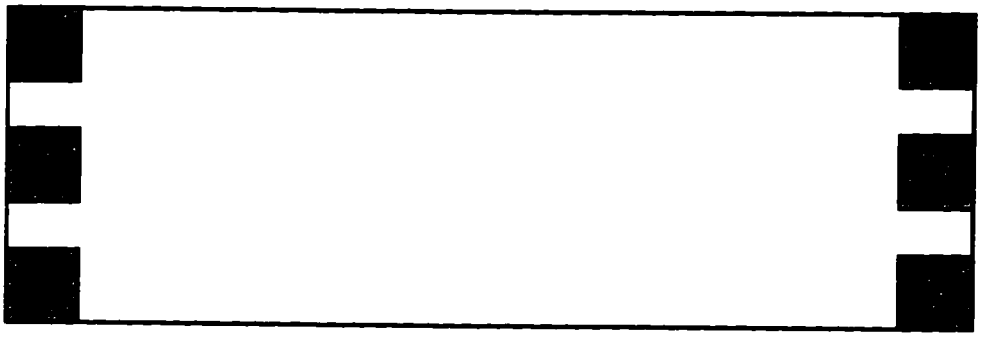

(b) side view: metal layers after liftoff

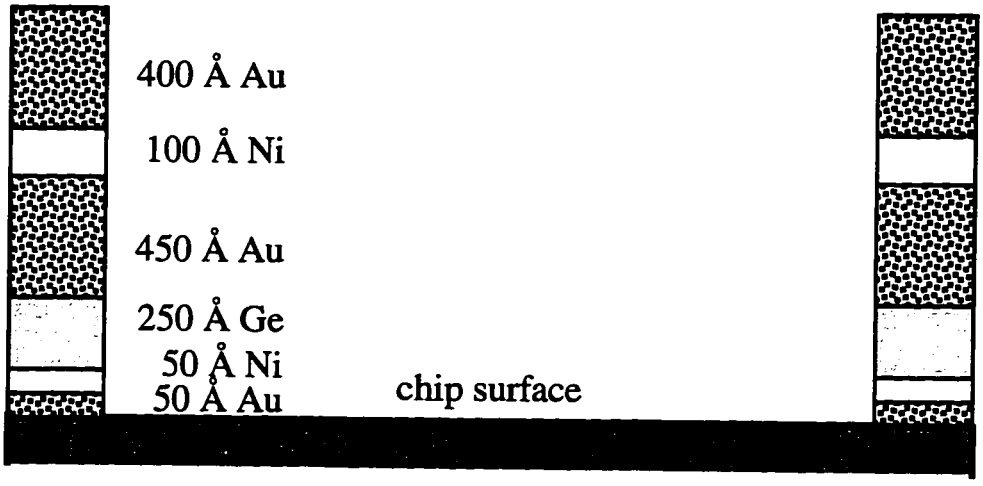

(c) side view: contacts after annealing

Figure 3.2 Au/Ni/Ge contacting process. (a) Openings ("windows") are defined in a resist layer where contacts are desired; (b) after evaporation and liftoff, sequence of metal layers remains where openings were; (c) after annealing, metal forms eutectic and tendrils penetrate semiconductor to contact 2DEG.

effective. Using a trilayer rather than a bilayer prevents cracks in neighboring layers forming a channel all the way to the wafer surface for unwanted contact material.

After developing the lithography, the sample is mounted in the thermal evaporator and the following sequence of metal layers evaporated: 50 Å Ni, 50 Å Au, 250 Å Ge, 450 Å Au, 100 Å Ni, ~ 400 Å Au. (The top layer of Au primarily provides protection and a surface to which to bond, so it can be made as thick as desired.) The stage is usually air-cooled in this process (LN_2 cooling is not necessary and is more likely to cryopump junk into the contacts). Liftoff is accomplished by placing the chips in acetone for an hour or so. Ultrasound should be avoided because before annealing the contacts do not stick very well. The chips are then rinsed with methanol, blown dry with dry N_2 gas, and inspected carefully for unwanted metal clinging to the surface. Such bits of metal, unless they are between contacts which do not need to be electrically isolated, should be removed if at all possible, since they can cause a short from a surface gate to the gas.

When the chip is free of debris, the contacts are annealed by placing the chip on a strip heater in a sealed chamber filled with flowing forming gas (80% He/20% H_2), flushing the chamber with gas for one minute or more at room temperature, and then heating to the following sequence of temperatures: 110° C for one minute to drive off water vapor, 10 seconds at 250° C to form the eutectic, and 15 seconds at 410° C for the metal to penetrate the wafer and for the contacts to anneal. The sample is then returned to room temperature. The chip is mounted on a chip carrier with carbon paint (for easy removal later) and immersed in a LHe storage dewar, and the contact resistances are measured with a two-probe, 1 μA current bias. If all the contacts work, the chip is cleaned thoroughly in the same fashion as after cleaving (after proper annealing the contacts should be insensitive to ultrasound) and it is ready for the next stage of processing. Otherwise, failed contacts can be re-annealed (after cleaning the chip thoroughly without ultrasound).

Indium contacting involves pressing pieces of clean In onto the surface of a clean chip in the same manner as for hand wiring (discussed in section 3.3.4), noting that for In

to stick to and diffuse into GaAs, the In and GaAs must be extremely clean. Typically these contacts are close to 1 mm^2 in area because it is difficult to handle smaller pieces of In and because larger area contacts tend to be lower resistance. This limits the number of contacts that can be made and the places they can be located, though this tends not to be an issue for two-probe samples. Furthermore, the contact resistance seems to depend inversely on how much In surface area actually touches the chip surface, so it is critical to get as much of the In as possible actually stuck to the chip. Using a clean scalpel blade to cut, clean, and place the In, but then using metal tools which have been touched lightly to one's skin (so that they are slightly oily and stick less well to the In) to actually press the In down, seems to work best.[6] After pressing the In down, the contacts are annealed in the same fashion as the Au/Ni/Ge contacts but with a slightly different protocol : 110° C for 3 minutes to drive off water vapor, 180 C for 5 minutes, 405° to 410° C for 1 minute 20 seconds (15 seconds of which is spent ramping from 180° to 410°) for the In to penetrate to the 2DEG, and back to 180° C for 5 minutes to anneal the contacts. The contacts are then tested in the same fashion as Au/Ni/Ge contacts, and can also be reannealed if they fail (though reannealing is less likely to succeed). Finally, the chip is cleaned for the next use, though ultrasound should be used sparingly since bits of In can come off and stick to the chip surface in unwanted places.

3.3.3 Electron Beam Lithography and Metallization

The EBL process is shown schematically in Fig. 3.3. The procedure is as follows:

a) First a PMMA (polymethylmethacrylate) bilayer is spun onto the sample. The clean chip is placed on the spinner inside the Class 100 region of the cleanroom, a drop of 496K PMMA in chlorobenzene is dispensed onto it from a new, clean pipet,[7] and the chip is spun at 4000 rpm for 60 seconds and then baked on a hotplate at 180° C for 20 minutes.

---

[6]Teflon tools work well for the first use or two, but the Teflon coating tends to crack and leave bits behind in the In.

[7]Pipets should not be reused even for the same chip, and should be rinsed two or three times with fresh methanol before use.

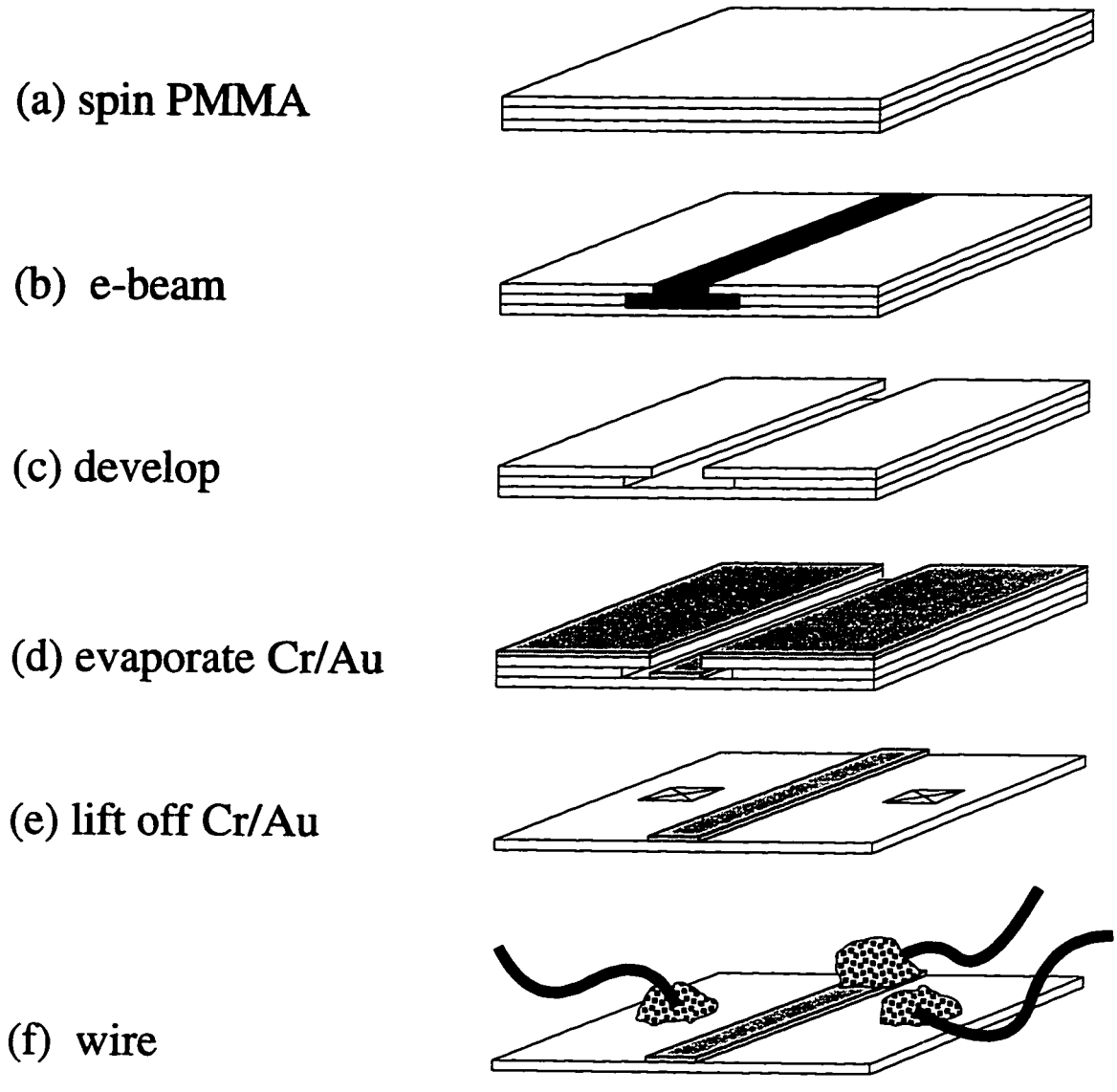

Figure 3.3 Electron beam lithography and metallization (steps described in detail in the text). In this figure the chip already has contacts and lithography is being used to put down split gates. Steps (a)-(e) are also used to put down contacts (though sometimes photolithography rather than electron beam lithography is used). After Waugh, Ph.D. thesis [1994].

The chip is then repositioned on the spinner and set spinning slowly (1000 rpm) while a drop of 950K PMMA is applied; the spin speed is then increased to 4000 rpm and the spin-and-bake procedure repeated.

Essential things to be careful about: Avoid reaching over the chip at any time (always grip from the side with tweezers) so that particles from your hands do not fall into the wet or baking PMMA. Use only one large drop (or if the layers are not covering the chip completely, two small drops), or excess PMMA which collects on the underside of the chip will cause problems in mounting later. Be sure the spinner chuck is clean; any encrustation of old PMMA or photoresist will degrade the vacuum seal between chip and spinner, allowing PMMA to collect on the underside of the chip. It seems that good results can be obtained with or without using a dropper bulb on the pipet. Do not bring acetone into the spinner hood, and if someone else is using acetone in the other hood, keep the cover down while samples are baking.

It is not a problem if the PMMA layer has a few defects, unless they are located where they will interfere with the pattern. If the layer does not cover the chip completely and lacks a large, uniformly thick area in which to write the device, it is best to clean the chip (acetone and methanol with ultrasound remove PMMA) and start over.

There is disagreement over how long PMMA can be left on a chip and still used. The Tinkham group spins PMMA on an entire Si wafer, then cleaves the wafer and writes on a piece at a time, frequently using six-month-old PMMA. The Westervelt group has occasionally had bad results which might have been attributable to old PMMA (though perhaps were just bad luck). It is probably best to use PMMA within a few days, but older PMMA can be used depending on one's willingness for the results to fail.

b) The desired pattern is exposed on the chip with EBL, using the Nanometer Pattern Generation System software (J. Nabity Lithography Systems) with a JEOL 6400 scanning electron microscope (SEM). The PMMA serves as a positive electron beam resist (although very high doses will turn it into a negative resist), so it is exposed in the regions

where metal is desired. Exposure propagates slightly beyond the boundaries of the region directly under the beam, with the distance depending on dosage, magnification, and exposure time. The exposure in the 496K layer propagates further than in the 950K layer, leading to the undercut shown in Fig. 3.3(c) which facilitates liftoff.

Appendix B contains detailed techniques for mounting the chip on a SEM mount and operating the SEM for lithography. A few generalizations are worth mentioning here, all of which can be found in the NPGS manual, but which can be missed on a first reading.

Pattern design: When designing patterns, it is best to work in the lower third of a given decade of magnification (1000x to 3000x, 100x to 300x, etc.) if possible, because in that range the microscope behavior is the most reproducible. It is also best not to use the entire field of view at a given magnification because the pattern will start to bend near the edges of the field of view.

The proximity effect: Regions of PMMA near the beam are partially exposed when the region directly underneath the beam is being exposed. This is of paramount importance in writing small features. For example, writing a single dot requires substantially larger doses (375 vs. 275 $\mu C/cm^2$) in the fine regions than does a double dot pattern consisting of two such adjacent single dots with a common point contact. Thus doses must be set taking the amount of writing in a small region in consideration, and large, heavily exposed areas should be kept as far removed as possible from fine features. Presumably the proximity effect is one of the limits on EBL feature size. The samples used in this thesis have feature sizes as small as 150 nm, which require skill in using the SEM but definitely are not the limit of what is possible; thus future students are likely to have success if they design samples with smaller features.

EBL reproducibility: The key to reproducibility is using the same beam current with the same combination of magnification and condenser lens each time (for fine features). Thus a filament which is at the end of its life should be avoided because it may not be possible to achieve the same currents as in previous SEM work with the same

condenser lens. If the beam currents are measured using a hole bored in the sample mount rather than the PCD cup (see Appendix B for more details), doses and shifts will reproduce from filament to filament. Shifts will, however, change after the biannual cleaning and realignment of the SEM column. Before embarking on a substantial lithography project, it is probably worth asking when the next such maintenance is due.

c) After lithography, the sample is removed from the SEM mount, and care is taken to trim and brush most of the carbon paint from it. It is then developed by immersing in 1:3 methyl isobutyl ketone (MIBK): isopropanol (IPA) for 60 seconds, and rinsed quickly in IPA and then methanol to stop the developing. The sample is blown dry with dry N_2 gas and examined under a high-power optical microscope. If there is any dirt (such as carbon paint) on the exposed surface of the chip, further cleaning should be attempted by spritzing vigorously with methanol[8] and blowing dry again. If the lithography has been successful, the sample should be placed in the thermal evaporator for metallization as soon as possible (waiting overnight is OK, but the longer the wait, the more likely the surface is to become dirty); so it is often best to delay developing until just before the evaporator is available. (If multiple samples have been written, but only one will be metallized immediately, the exposed but undeveloped sample can be stored for several days (up to a week) and then developed for metallization.) The undercut in the PMMA layer, shown schematically in Fig. 3.3, is not generally visible under the optical microscope. Appendix B discusses the procedure for viewing PMMA under the SEM when writing test patterns to check doses.

d) The sample should be dipped for one or two seconds in a 1:5 solution of concentrated (30%) aqueous sodium hydroxide (NaOH): distilled water, then blown dry with ultrapure N_2 gas immediately before placement in the thermal evaporator. The NaOH solution removes an oxide layer from the surface which degrades adhesion of metal films; within an hour or two in an oxygen-containing atmosphere, the oxide layer forms again, so if placing the sample in the evaporator is subsequently delayed, no harm is done, but the

[8]Methanol is the only solvent used for processing which will neither develop nor dissolve the PMMA.

sample should be dipped again. This step can be skipped if the sample is to be hand-wired rather than wire-bonded (see section 3.4.4).

The sample is clipped to the stage in the thermal evaporator directly over the gold and chrome sources,[9] and the evaporator is pumped out. When the evaporator pressure has reached the low 10^{-6} to high 10^{-7} torr range, LN_2 cooling of the stage should begin. While the cooling is being started, the sources (first gold and then chrome) are heated to clean them; once the stage is cold (-20° to -40° C), 100 Å Cr is evaporated onto the sample. The gold layer is then evaporated. In order to wire-bond to the gates, 400 to 450 Å Au is needed. We have had liftoff problems in the past with films of this thickness on quantum dot samples, and have had to evaporate only 200 to 250 Å Au and hand-wire the samples. Atomic force microscope (AFM) measurements of our samples suggest that the film may be substantially thicker than the thickness monitor in the evaporator indicates.

e) The excess metal is lifted off by soaking the sample in a beaker of acetone for several hours. Standing the sample on its side in the beaker seems to aid liftoff. We have frequently had difficulty with liftoff, and have needed to use a great deal of ultrasound. It seems to be good to start with ten seconds of ultrasound and then put the sample in a petri dish filled with acetone to look at it under a microscope and see whether the gold has lifted off (generally the greatest difficulties have been with the medium-size features). Then, if some gold is still sticking to the surface, the best strategy seems to be returning the sample to the beaker and increasing the amount of ultrasound gradually. It is best to keep the sample immersed in acetone until liftoff is complete.

3.3.4 Wiring

There are two methods for wiring samples. The ultrasonic wedge bonder, or "wire bonder", can be used to stitch gold pads on the sample to gold pads on a sample mount

[9]By the creative efforts of an anonymous member of the Westervelt group, the arms have been customized so that the alumina-coated molybdenum boat for the gold and the Cr-coated rod can be positioned parallel to one another, directly beneath the stage.

(either a chip carrier or a piece of gold-plated PC board). Alternatively, gold wires can be pressed by hand into indium pads on a piece of PC board and then attached to gate pads on the sample with more indium. Wire bonding should be used if possible, because when the wire bonder is working properly it is much faster than hand wiring, it is electrostatically safer because there is no sticky indium involved, and gate pads can be made substantially smaller and closer together and can still be successfully wire-bonded. However, there are occasions when hand wiring is necessary. Sometimes wire bonding consistently fails on a given sample (the gate or contact metal tears off the chip when the bonding wedge is brought up), because the chip surface under the gates is not clean or the metal film is too thin. Also, the Oxford Model 200 sample mount (the slug) is not presently wire-bond compatible. (Efforts to change this will be discussed in Appendix C.)

Wire bonding is described elsewhere [Katine, 1996]. Hand wiring really has to be learned from a demonstration. The basic procedure is that, after the sample is cleaned in TCE and rinsed in acetone and methanol (ultrasound is not really necessary since the main concern is to remove all grease from the sample surface), small pieces of indium are scraped clean on one side with a scalpel and pressed, clean side down, onto gold gate pads. Gold wires are then pressed into those indium blobs, as shown in Fig. 3.3(f). Typically the wiring pads are about 200 x 500 μm^2 and separated by spaces of 150 to 200 μm, and the wires used are a few thousandths of an inch in diameter, so this work requires great patience and steady hands.

I list here a few precautions which I have found essential. The main danger in hand-wiring the sample to a PC board mount is destroying the sample with static electricity.[10] Before pressing indium onto gate pads, a long, flexible gold wire should be attached at one

[10]Wire-bonding is not vulnerable to this, as long as the entire wire-bonding armature is electrically connected to a common ground, since the sample is mounted with conducting tape onto a gold-covered surface, and before attaching the sample the user wire-bonds the gold ground plane to one of the leads. The entire chip is conducting at room temperature and thus all the gates are shorted together through the chip to the gold ground plane, which can be grounded to the apparatus through the chip carrier lead. Furthermore, getting tools stuck in indium and having to pull them out is a major source of static in hand wiring.

end to one of the current contacts (with indium) and at the other to a large aluminum plate which is grounded to the same point as all the tools (this connection can be made with tape). All tools should be grounded, and the wirer should wear a grounding strap and remove his or her shoes. Only metal tools should be used (no Teflon-coated tools); to prevent metal tools from sticking to freshly cut indium, the tools can be touched briefly to the wirer's skin. A humidifier running in the room is also important.

Indium should be applied to all gate pads first (and current contacts, if the contacts are Au/Ni/Ge); then, the gate pads should be touched with a grounded tool and very fine wires should be pressed into the indium to connect the two halves of each point contact. Before the sample is placed on the PC board mount, the leads on the mount should be shorted together with a gold wire which will be removed once the PC board mount is attached to the fridge slug. The end of this gold wire should be taped to the aluminum grounding sheet. The sample can then be stuck down to the mount with sticky conducting tape and the wires on the sample connected to the wires on the sample mount.

Finally, wires are placed in the PC board on the fridge slug which are more than long enough to reach the sample once it is in position, and the fridge slug is held in a vise with grounded copper gauze contacting the rings of the slug from underneath. Thus the entire slug is grounded while the sample mount is brought into place, the slug wires are attached to the sample mount, and the grounding wire removed from the sample mount. Only after all wiring is finished is the slug removed from the grounded gauze.

3.4 Low-Temperature, Low-Noise Measurements

Low temperatures are required to probe dot interactions because the energy scale of the interactions is at most half the charging energy of a single dot, or 1 K (100 μeV), and varies over the range of interest all the way to zero. Furthermore, to probe the quantum limit of these interactions requires a temperature comparable to or less than the level spacing, which is approximately 25 μeV in these dots. Consequently, these experiments

are best performed in a $^3He/^4He$ dilution refrigerator (hereafter "fridge"), in which an electron temperature of approximately 70 mK (7 μeV) can be achieved. Likewise the currents involved are very small (as low as a few hundred fA) and must be detected with high-quality low-noise electronics; low temperatures also reduce the noise level.

3.4.1 Cryogenics

The $^3He/^4He$ dilution refrigerator used, the Oxford Model 200, is a top-loading model, which allows samples to be changed without warming up the fridge (at least when the top-loading process is working). Top-loaded samples are limited to eight electrical leads, so there are no extra wires available for the double dot sample (wiring diagram shown in Fig. 5.1(b)) and the measurement is limited to a two-probe measurement. Also, top-loading can be perilous for samples; occasionally samples thought to be intact before loading have proved nonfunctioning by the time they were cooled and tested, most likely from static electric shock (see Appendix C for further discussion). However, when it is working, top-loading seems a blessing rather than a curse, since one sample can be removed and the next ready for measuring within eight hours (on an average day).[11]

When everything is working properly, the Model 200 achieves a base temperature of around 15-18 mK. This appears to correspond to an electron temperature in the 2DEG of $T_{electron} \sim 70$ mK (as discussed in Chapter 2). The fridge is equipped with an automatic temperature controller, but all of the temperature studies reported in this thesis have been done by manually setting the mixing chamber heater to an appropriate power such that the mixing chamber temperature stabilizes at the desired value. (This is discussed further in Appendix C.) The superconducting magnet was not used for the experiments reported in this thesis.[12]

---

[11]This assumes only average success in keeping the fridge cold while loading and unloading but also assumes cooperation from the occupant of the upstairs office. Trying to accommodate his schedule often introduces an additional time lag.

[12]It has, however, always been next on our list to study the magnetic field dependence of these phenomena.

Radiation shielding is very important for studying single-electron transport, since the previously discussed charging events seem more frequent in equipment with a lack of shielding (such as in our ^{3}He evaporation refrigerator).[13] It is also important since microwave photon-assisted tunneling can lead to spurious resonances in the tunnel current and raise the background level. Shielding is required against both radiation traveling on the leads and against ambient blackbody radiation from warmer parts of the fridge. The leads pass through microwave filters consisting of a mixture of epoxy and fine-grain copper powder, which dissipates radiation by the skin effect, and through 1 kΩ metal-film resistors, which reflect microwave radiation [Tighe, 1993]. Shielding against ambient radiation is provided both by reflecting shields surrounding the mixing chamber which are heat-sunk to other parts of the refrigerator and by the sample slug shielding. A brass shield protects most of the open part of the slug, but one large gap must be filled with microwave-absorbing sponge (EquiSorb) and closed with copper tape.[14] Further discussion of the Model 200 radiation shielding can be found in recent theses [Hergenrother, 1995; Tighe, 1993]. [Shielding and photon-assisted tunneling are discussed further in Martinis, Devoret, and Clarke, 1987; Cleland, Schmidt, and Clarke, 1992; Martinis and Nahum, 1993; Martinis, Nahum, and Jensen, 1994; Dresselhaus *et al.*, 1994.]

3.4.2 Electronics

Two different kinds of measurements are made in this thesis: two-probe zero-bias conductance measurements, in which a 10 μV ac voltage bias is applied across the sample and a lockin measurement of the current through the sample is recorded, typically as a function of gate voltage; and two-probe nonequilibrium conductance, in which a dc bias voltage is applied in addition to the small ac bias and the current is measured in the same fashion. The lockin measurement effectively takes the derivative of current with respect to

[13]This piece of equipment is also affectionately known as the "Shubi" dewar.
[14]There has been discussion of modifying the slug to fill in those gaps, which is an excellent idea that should be implemented when the slug is not in use.

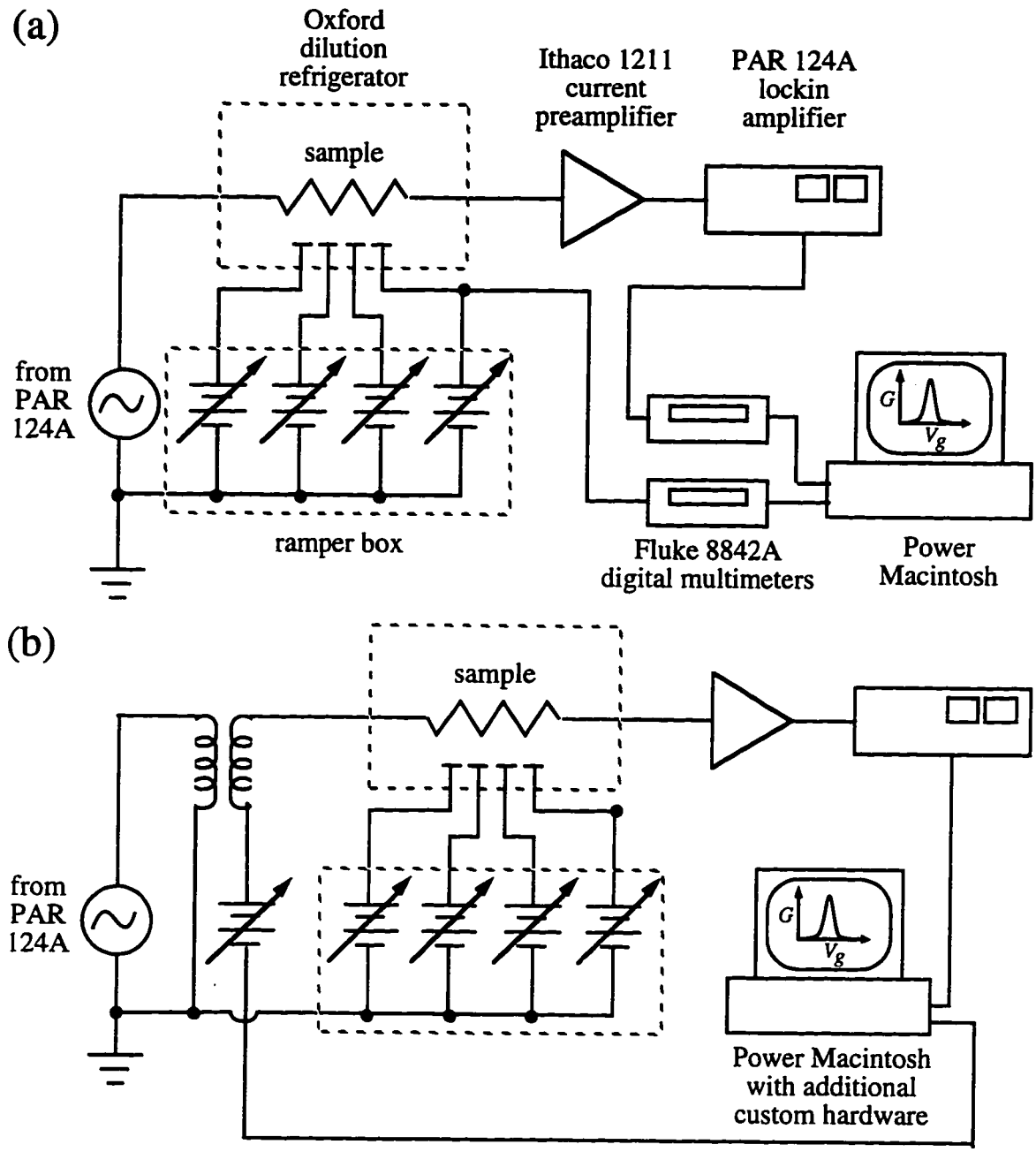

Figure 3.4 (a) Circuit for two-probe zero-bias conductance measurement using digital multimeters to digitize data. Voltage bias (ac only) supplied by PAR 124 reference channel, constant and ramped gate voltages supplied by analog voltage source built by Jordan Katine, data recorded by LabView program written by Doug Mar via GPIB interface to Macintosh II. (b) Circuit for two-probe nonequilibrium conductance measurement using A/D board in computer to digitize data. PAR 124 reference channel supplies ac bias, dc bias and variable gate voltage supplied by computer, constant gate voltages supplied by same analog voltage source. Controlling LabView program written and accompanying hardware (not shown) built by Carol Livermore ("fast data-taker").

bias voltage, so both measurements record differential (small-signal) conductance. In the case of zero-bias conductance, differential conductance and conductance are the same. A voltage-biased measurement rather than a current-biased measurement is made in these experiments because the conductance of the sample can change by three orders of magnitude within a given measurement [Foxman *et al.*, 1993]; two-probe measurements are made because there are not enough leads to make a four-probe measurement.[15]

The measurement circuits are shown in Figs. 3.4(a) and (b) respectively. The 104 Hz ac bias is supplied by the reference channel of an EG&G Princeton Applied Research (PAR) 124A analog lockin amplifier. In the zero-bias measurement, the 124A supplies 1 V rms which is divided down to 10 μV with a $1{:}10^5$ resistive divider, while in the nonlinear measurement the 124A supplies 20 mV rms which is divided down with a 1:2000 divider to 10 μV.[16] A 10 μV ac bias gives a sufficiently large signal that it can be detected cleanly without causing excessive electron heating [Rimberg, 1992]; in the nonlinear measurements, 10 μV is substantially smaller than the features of interest. The output current from the sample is amplified by an Ithaco 1211 battery-operated current preamplifier (with the low-pass filter time constant τ set at 3 ms) and then detected and amplified by the same PAR 124A. The PAR 124A output is recorded digitally by one of two means (which will be described shortly). Finally, constant gate voltages are applied to the sample from a battery-powered voltage source built by Jordan Katine [Katine, 1996]. The same voltage source can supply a ramped voltage for either a dc voltage bias or a gate voltage, or the variable voltages can be supplied by the data-taking computer (as discussed shortly). In the nonlinear measurement, the dc and ac biases are combined using a

[15]Future measurements could take advantage of the 24 leads per sample mount on the new Kelvinox 100 dilution refrigerator.

[16]To get a 20 mV signal from the 124A reference channel requires turning the calibration knob, so the level must be set with an oscilloscope.

Magnetek A67-J 1:1 transformer as shown in the figure.[17] The transformer 3 dB point is at 30 Hz, so the signal is somewhat attenuated at 104 Hz.

In "slow" data collection mode (shown in Fig. 3.4(a)), the 124A signal is read by a Fluke 8842A digital voltmeter, and the value is recorded by a LabView program called "Read N DMMs"[18] running on a Power Macintosh personal computer, which is connected to the multimeter via a GPIB interface. This method acquires one data point approximately every 300 ms[19] with high accuracy (the multimeters can distinguish values within 10 μV and are very low-noise). The "fast data taker," the handiwork of Carol Livermore, uses a Power Macintosh equipped with two National Instruments boards, a digital-to-analog (D/A) board to put out two voltages which are rastered, and an analog-to-digital (A/D) board to read in the PAR 124A output directly. (This data collection mode is shown in Fig. 3.4(b).) The two voltages can be used as two gate voltages or one gate voltage and dc bias voltage, and the sample current is measured as a function of these two voltages. At present, a 100 x 100 array of conductance values can be measured in roughly 15 minutes, which greatly increases our ability to acquire data which is undisrupted by switching events. (It would be good to be able to run about five times faster, however!)

The fast data taker can record data substantially faster than we have been able to get the analog circuit which precedes it to work. At present we take data points every 30 ms (taking data points faster would require running the lockin at higher frequency or eliminating the lockin altogether), and the total time needed to acquire a 2D data scan is increased somewhat by program setup and closing times. Speed is an obvious asset of the

---

[17] This transformer was purchased by the Westervelt group a long time ago, and is no longer commercially available. This is unfortunate, because no other transformer is marketed which can operate at such low frequencies with little distortion and has such good magnetic shielding (the transformer in its Pomona box weighs several pounds). Essentially, there is no replacement comnmercial transformer which has such good characteristics for low-frequency, ultra-low-noise measurements.

[18] This program was originally written by Doug Mar and was subsequently adapted for a new version of LabView by Carol Livermore. "Read N DMMs" describes its function: it simultaneously records the ouputs of up to four digital multimeters (DMMs). For further information on this program see Mar, 1994.

[19] This corresponds to a setting of "medium" for the Fluke DMMs in the LabView program. This is approximately three times faster than reported in Fred Waugh's thesis; the increased speed comes from some combination of using a Power Macintosh (rather than a Mac II) and using the new version of LabView.

fast data taker; the corresponding disadvantage is that it is noisier than the digital voltmeters.[20] Thus generally the slow data collection method is used if peak shapes are to be recorded, whereas if the positions of peaks (and perhaps rough estimates of heights) are the only information desired, the fast data taker can make the same measurement much faster and eliminate the labor of controlling analog voltage sources.[21] The fast data taker is also useful in searching large regions of parameter space for good operating combinations of gate voltages. Further information on the fast data taker (including details of the filtering and the controlling software) can be found in the manual written for it by Carol Livermore.

Standard low-noise techniques must be implemented to make these measurements. The fridge is inside a shielded room, and everything inside the shielded room which is part of the measurement circuit runs on batteries except the PAR 124A. The computer is kept outside the shielded room. The fridge body is grounded to the shielded room to provide further protection from electrical pickup. All signals are carried on shielded coaxial cables which are kept short and are taped to the frame which supports the fridge, so that the cables do not swing around, and all unused wires going into the dewar are terminated with grounding caps. The voltage divider for the bias voltage is attached directly to the signal leads going into the dewar, and the current preamplifier is set less than a foot away from the return signal line. We have avoided using the automatic temperature controller, and we unplug the LN_2 jacket level meter while making measurements, because both seem to introduce noise into the system (apparently from a ground loop somewhere in the former and poor design of the latter). Any electronics used to set up but not actually used in the measurement should be turned off. Strangely enough, the fluorescent lights inside the screen room do not seem to be a source of noise. With all of these precautions, we routinely achieve signal:noise ratios between 100:1 and 1000:1 (peak signal level around 10^{-2} e^2/h) in slow data collection mode (sampling at ~0.3 Hz) and somewhat poorer ratios

[20] I cringe to imagine how noisy it would be without its heroic amounts of shielding.
[21] Note the similarities between this measurement device and the recommendations made in Fred Waugh's thesis (p. 176).

in fast data collection mode (sampling at ~ 33 Hz). The one logical low-noise measure to add, if even smaller currents were to be measured, would be to use triaxial rather than coaxial cable.

3.5 Summary

This chapter has given an overview of the techniques used in the measurements presented in this thesis. Further information can be found in Appendices B and C.

CHAPTER 4
SINGLE DOT TRANSPORT IN THE PRESENCE OF STRONG TUNNELING[1]

4.1 Introduction

Classical charging models for the Coulomb blockade of transport through a quantum dot assume that the conductance of each lead to the dot is much less than $g_Q = 2e^2/h$, the conductance of a quantum point contact carrying one spin-degenerate transverse mode. This amounts to assuming that tunneling between the dot and its leads is very weak and capacitive interactions are dominant. Recently, there has been much theoretical [Matveev, 1995; Furusaki and Matveev, 1995; Flensberg, 1993 and 1994] interest in the effect of strong tunneling on the Coulomb blockade, and a number of experiments in semiconductor quantum dots have been performed [for example Molenkamp *et al.*, 1995; Pasquier *et al.*, 1993; van der Vaart *et al.*, 1993]. In particular, theory which models the dot-to-lead tunnel junctions as perfect one-dimensional channels [Matveev, 1995] predicts that Coulomb blockade oscillations should vanish when the conductance of one lead to the dot equals or exceeds g_Q. However, differing experimental results have been previously obtained; van der Vaart *et al.* [1993] report that the Coulomb oscillations vanish when the conductance in the point contact connecting the dot to one lead exceeds g_Q, whereas Pasquier *et al.* [1993] observe persistence of Coulomb oscillations with dot-to-lead conductance up to several g_Q.

In this chapter we will present measurements of the linear conductance of a single quantum dot when one lead is weakly tunneling and the conductance of the other is varied up to many times g_Q. Section 4.2 introduces quantum point contacts, the devices used to form tunnel barriers between the dot and its leads, and explains the waveguide model of

[1] Parts of this chapter have appeared in *Superlattices and Microstructures* (1996).

transport through them. Section 4.3 summarizes our experimental results and some of the theories of Coulomb blockade in the presence of strong tunneling. Finally, section 4.4 discusses possible interpretations of the results.

4.2 Quantum Point Contacts

The model we will use to discuss quantum charge fluctuations is based in the Landauer-Büttiker formalism of conductance as transmission of electron waves [reviewed in Beenakker and van Houten, 1991, and van Houten and Beenakker, 1996; Büttiker, 1988; Landauer, 1988]. We summarize this approach briefly (the reader is referred to the literature for more detail). Ballistic electron transport through a one-dimensional constriction in a 2DEG is modeled as the propagation of transverse electron waves in a waveguide.[2] When there exists a constriction in the conductor of size comparable to the electron Fermi wavelength λ_F, only a few modes can propagate through that constriction. This is shown schematically in Fig. 4.1(a). In the Landauer-Büttiker model, the constriction is of uniform width along the entire length of the sample; in real samples, if the constriction tapers smoothly, as shown in the figure, so that transport is adiabatic, the width of the constriction at its narrowest point is all that matters.

The modes allowed in the constriction are like one-dimensional subbands of the potential formed by the constriction; a diagram of subband energy as a function of position is shown in Fig. 4.1(b). Since the wavevector of transport electrons is the Fermi wavevector k_F, allowed transverse modes must have $k_x \leq k_F$ (with k_x the component of the wavevector which must fit in the constriction). Thus the number of propagating modes in two dimensions in a lateral confining square-well potential of width W is

$$N_{modes} = \mathrm{int}\left[\frac{k_F W}{\pi}\right]. \tag{4.1}$$

[2] This model assumes that the transverse modes can be separated from the other components of the motion in the Hamiltonian. It also assumes that the constriction has hard walls so that the transverse modes do not penetrate beyond the width of the constriction. This proves to be an excellent approximation.

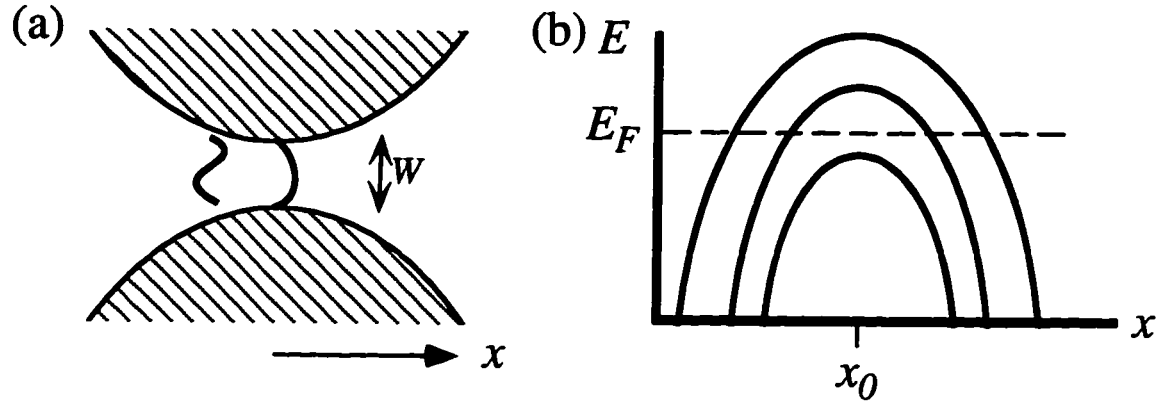

Figure 4.1 (a) Schematic of the constriction formed in a 2DEG by a quantum point contact showing two allowed transverse modes of the electron density propagating through the constriction. (b) Schematic diagram of the energies of different modes as a function of position. At the narrowest point of the constriction x_0, the energy of a mode is greatest because the confinement is greatest. Modes are transmitting if they are at or below E_F everywhere; they are available for tunneling only if they are above E_F at x_0.

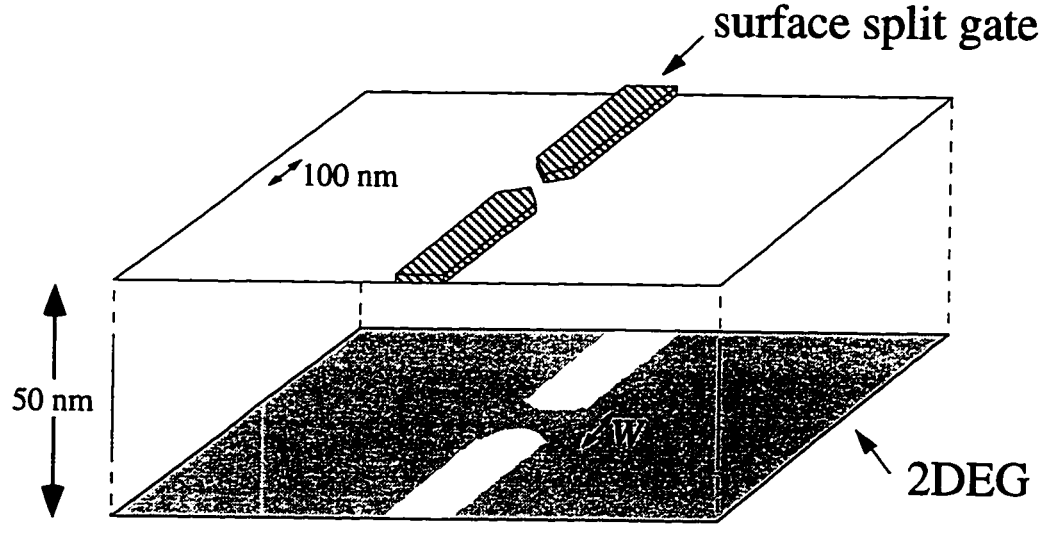

Figure 4.2 Schematic of a split-gate quantum point contact formed in a 2DEG in a GaAs/AlGaAs heterostructure ($\lambda_F \sim 40$ nm for 2DEG electrons). The metal gate is on the heterostructure surface; a negative voltage applied to it depletes the 2DEG below. White area in 2DEG represents depletion. Width of non-depleted area W depends on voltage applied to point contact gate, while gap between tips of gates is ~ 100 nm. Vertical scale is greatly exaggerated as shown in scale bar. After Waugh, Ph.D. thesis (1994).

In zero magnetic field the modes are spin-degenerate, so the total number of transport channels is $N_{ch} = 2N_{modes}$. The minimum k-vector for a given mode is inversely proportional to W, so the minimum energy of a mode increases as W decreases; hence, the number of modes accessible to electrons at the Fermi energy decreases with W.

Such a constriction in a 2DEG is known as a quantum point contact. A versatile way to form such a constriction in a 2DEG is with a split gate on the surface of the heterostructure with a narrow space between the two halves, the width of which is a few times the Fermi wavelength ($\lambda_F \sim 40$ nm), as shown in Figure 4.2. When a sufficiently large negative voltage is applied to the gate, the electron gas is depleted everywhere except in the gap between the halves of the gate. As a larger negative voltage is applied, this gap narrows. Hence the split gate forms a point contact of variable width, and the width is controlled by the voltage on the gate (V_{qpc}). When the conductance of this structure G_{qpc} is measured at low temperature (about 1K or lower), it exhibits a series of steps [van Wees *et al.*, 1988] – the conductance is quantized in units of $2e^2/h$, as shown by the data from one of our samples in Fig. 4.3.

Each subband has the same conductance, which is $2e^2/h$ for a pair of spin-degenerate subbands (e^2/h for a single subband with the spin degeneracy lifted by an applied magnetic field); hence the conductance of such a constriction is quantized. This is because in one dimension, the product of the density of states ρ_n and the group velocity v_n for the n^{th} mode is the same for all n, independent of the form of the confining potential:

$$\rho_n v_n = \left(\frac{1}{\pi \frac{dE_n(k)}{dk}} \right) \left(\frac{2\pi}{h} \frac{dE_n(k)}{dk} \right) = \frac{2}{h} \tag{4.2}$$

Thus the current carried by the n^{th} mode is

$$I_n = Ve^2 \rho_n v_n = \frac{2e^2}{h} \tag{4.3}$$

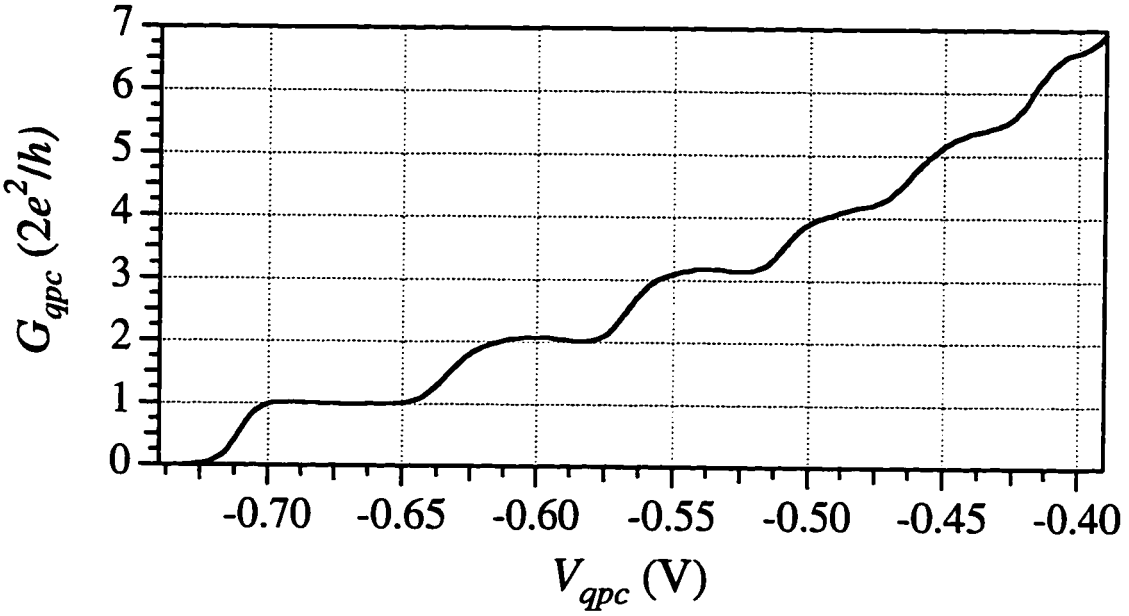

Figure 4.3 Conductance G_{qpc} of a split-gate quantum point contact as a function of voltage on the gate V_{qpc}. Note the plateaux at $G_{qpc} = 2ne^2/h$ for integer n.

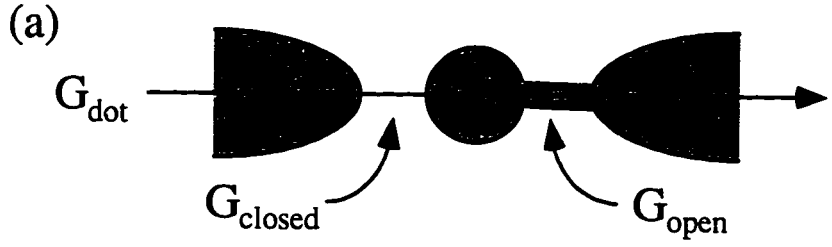

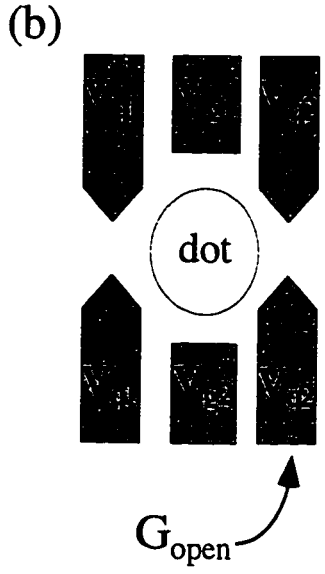

Figure 4.4 (a) Schematic of sample configuration used in the experiments described in this chapter, with one tunnel barrier weakly tunneling (G_{closed}) and one strongly tunneling (G_{open}). The conductance G_{open} is varied (and is set at a very small value for control experiments) while G_{closed} is kept at approximately 0.01 e^2/h. (b) Schematic of sample gates. Sample is formed with two point contacts and two side gates; the point contacts are adjusted to give the desired tunnel conductances to the leads, while side gates are used to confine the electron gas and control the dot potential.

and the total conductance of the constriction is

$$G = \sum_n \frac{I_n}{V} = \frac{2e^2}{h} N_{modes} \tag{4.4}$$

Note that Eq. (4.2) contains the factor of 2 for spin degeneracy in the density of states ρ_n. Thus the conductance quantum is sometimes defined[3] as $g_Q = 2e^2/h$, and we will report tunneling conductances throughout this thesis in units of $2e^2/h$.

Additional subtleties are important in the conductance of actual devices. The coupling of modes in the constriction to modes in the wide regions of the 2DEG depends on the exact shape of the constriction, and there is additional scattering resistance if the 2DEG in the constriction is not free of defects. Thus conductance quantization is only good to a few percent in the best samples. Finally, at temperatures such that the phase coherence length is longer than the path needed to travel through the constriction (typically 0.3 K and lower), additional structure arises due to quantum interference which depends on the shape of the constriction, neighboring gates, and the impurity potential. However, the transverse mode model explains the essential features of quantum point contact conductance.

When a point contact is closed down so that the energy of the lowest transverse mode is considerably higher than the Fermi energy, the point contact conductance is considerably less than $2e^2/h$, and is said to be pinched off. The point contact in this conductance regime forms a tunable tunnel barrier. Its conductance can then be described in terms of the transmission coefficient t or the reflection coefficient r of the lowest (spin-degenerate) transport mode from the barrier:

$$G = \frac{2e^2}{h} t = (1 - r) \frac{2e^2}{h} \tag{4.5}$$

[3]The conductance quantum is also often defined as $g_Q = e^2/h$ because the Hall conductance is quantized in units of e^2/h in strong magnetic fields.

The experiments described in this chapter use split-gate point contacts as tunable tunnel barriers to explore the evolution of Coulomb blockade in quantum dot systems as transport through one quantum point contact is increased from near-zero to many modes. Ordinary Coulomb blockade experiments in semiconductor quantum dots, such as those described in Chapter 2, use quantum point contacts to connect the dot(s) to external leads and to neighboring dots, and keep those point contacts well pinched off so that only weak tunneling is present.

4.3 Coulomb Oscillations in the Presence of Strong Tunneling

In this section we present measurements of zero-bias conductance in a single quantum dot with strong tunneling between the dot and one lead. Two samples were used, the sample shown in Fig. 1.6 (KC7EE) and a nominally identical sample made with a different piece of the same GaAs/AlGaAs wafer (KC7HH). The two samples differed only slightly in their characteristics. Since the measurements required only one quantum dot, and each sample provided two, measurements were made on each of the four available dots. As discussed in Chapter 2, the gates not needed to form the dot were grounded.

The sample geometry is shown in Fig. 4.4. In discussing these results, we will always refer to the lead adjacent to the weakly tunneling point contact as the "closed" lead and the conductance through this point contact as G_{closed}. The lead adjacent to the strongly tunneling point contact is called the "open" lead and the conductance of the point contact G_{open}.[4] To study the dependence of the oscillations on the conductance between the dot and one of its leads, we fixed G_{closed} to be much less than g_Q, and varied G_{open} from much less than g_Q to $5g_Q$.

[4]This may seem a slight misnomer in the control experiments in which the conductance G_{open} is also small, but hopefully it is still clear.

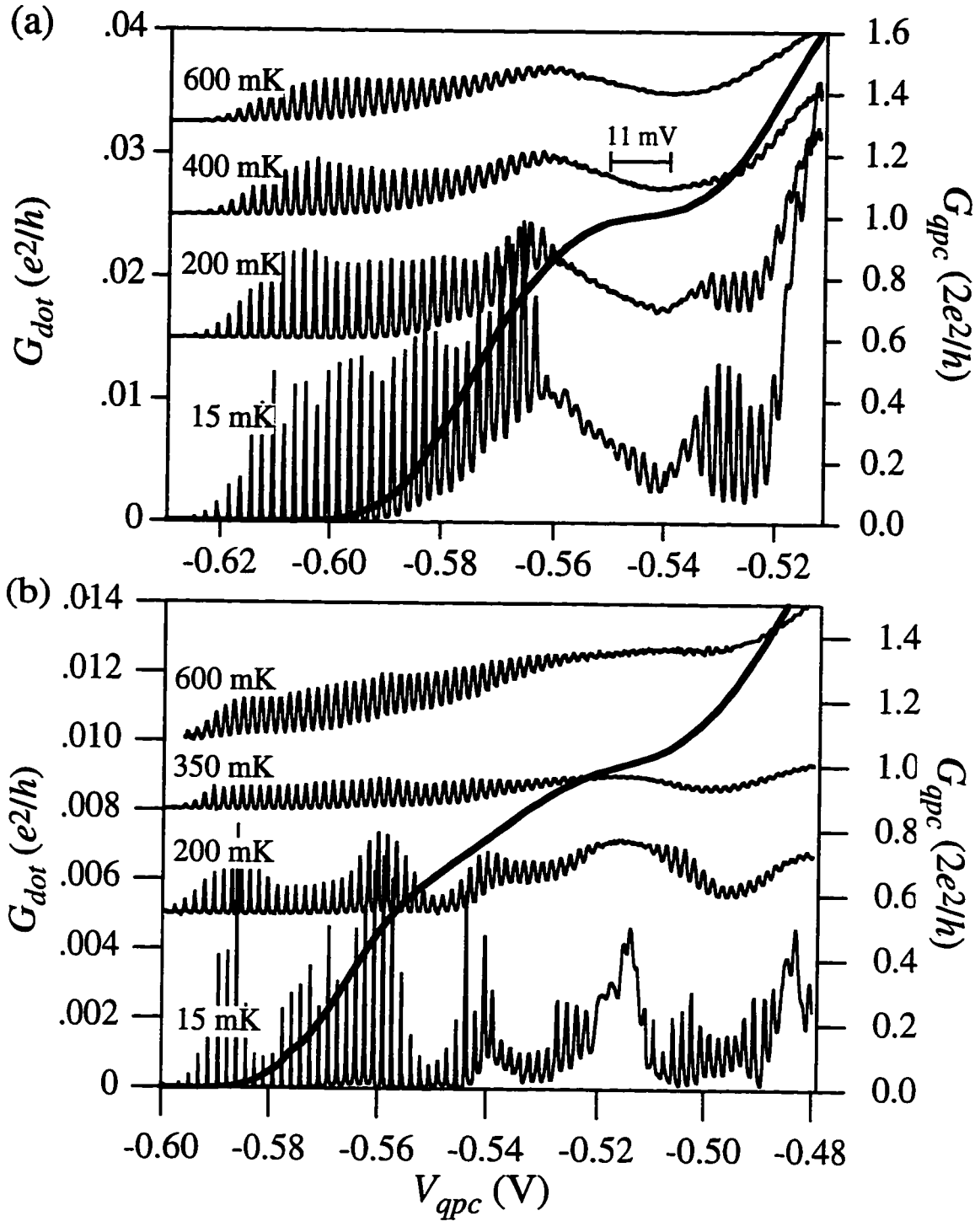

Figure 4.5 Two measurements of dot conductance G_{dot} as a function of open point contact voltage V_{q2} at a series of mixing chamber temperatures ($T_{electron}$ ~ 70 mK for T_{mix} ~ 15 mK). Traces are offset vertically for clarity; baseline at far left of each trace is at zero. Also shown (heavy line, right axis) is the conductance of the open point contact conductance G_{q2} (measured as described in the text). (a) is measured from sample KC7HH, (b) from sample KC7EE. In (a) at 400 mK the 11 mV bar indicates the width of the region in which oscillations are suppressed.

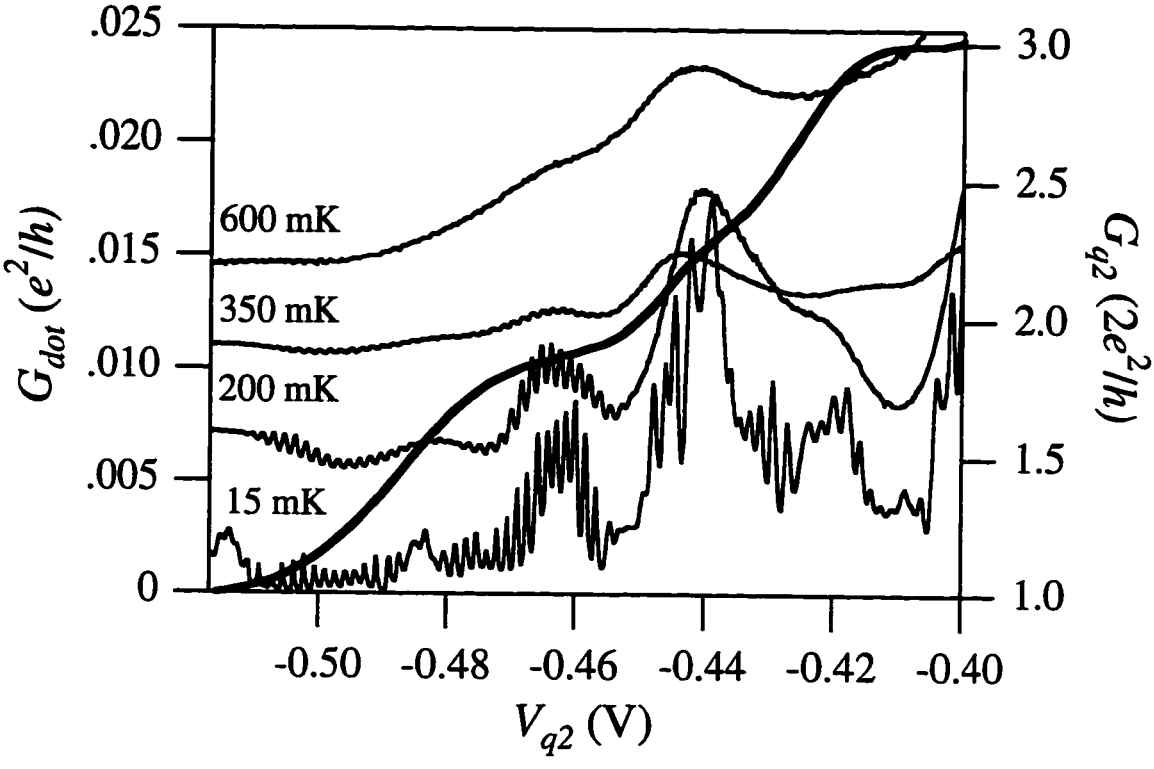

Figure 4.6 Dot conductance G_{dot} as a function of open point contact voltage V_{q2} at a series of mixing chamber temperatures (lowest electron gas temperature is about 70 mK), for the same sample as shown in Fig. 4.5(b) at higher G_{q2} values. Traces are vertically offset for clarity as in Fig. 4.5(b). Also shown (heavy line, right axis) is the conductance of the open point contact conductance G_{a2}.

4.3.1 Zero-Bias Conductance as a Function of Open Lead Conductance

Figure 4.5 shows measurements of conductance through the dot, G_{dot}, at four different temperatures as a function of the voltage V_{q2} on the gates which control the open point contact conductance G_{open}. Traces measured at different temperatures are offset vertically for clarity; the baseline at the far left of each trace is zero conductance. Also shown is G_{open} measured by energizing only the point contact gates V_{q2} and shifting the measurement in V_{q2} according to a procedure which will be described below. Results from KC7HH and KC7EE are shown in (a) and (b) respectively. In this measurement the point contact gate acts as a capacitively coupled gate as well as controlling G_{open}, so we see Coulomb oscillations. The Coulomb oscillations are strongly suppressed for $G_{open} \approx g_Q$, as predicted by theory. Surprisingly, at base temperature (T_{fridge} = 15 mK), e-periodic oscillations return for $G_{open} > g_Q$ and persist to $G_{open} > 5g_Q$ ($G_{open} = g_Q$ to $3g_Q$ shown in Fig. 4.6, higher G_{open} not shown). The period of the oscillations remains essentially constant over the entire range of G_{open}. This suggests that for $G_{open} > g_Q$, $t < 1$ for the lowest subband.

In Figure 4.5(a), at T = 400 mK, the oscillations return and persist only to somewhat below $G_{open} \sim 2g_Q$, and for T = 600 mK the oscillations do not return above $G_{open} \sim g_Q$. Analogous behavior is seen in 4.5(b), although different temperatures were studied. We obtain similar data from several samples, although the oscillation envelope varies from sample to sample, and in some samples the feature at $G_{open} \sim g_Q$ is more difficult to distinguish because it is more difficult to determine V_{g2} at which $G_{open} \sim g_Q$ (as will be discussed shortly).

Figure 4.6 shows the continuation of Fig. 4.5(b) for larger G_{open}. We see the e-periodic oscillations continue to $G_{open} \sim 3g_Q$. In this range, small e-periodic oscillations are superposed on a background which oscillates with period ~100 mV and larger amplitude. These larger oscillations probably come from quantum interference, perhaps the analog of Fabry-Perot oscillations for electrons exiting the dot through the open lead (for a discussion

of such oscillations in other nanostructures, see Katine [1996]). Ballistic transport effects in this device are plausible because the mean free path of electrons in this wafer is 5.4 μm [Katine, 1996], while the device size is only 0.8 x 0.5 μm.

One difficulty with interpreting the measurements of Figs. 4.5 and 4.6 should be noted: there is some error in determining the open lead conductance G_{open}. We know from measuring the conductance of a point contact G_{qpc} with or without neighboring gates energized that the primary effect of applying voltages to neighboring gates is to shift the entire conductance vs. gate voltage characteristic ($G_{qpc}(V_{qpc})$) to less negative gate voltage. Thus our goal is to determine the appropriate shift due to the presence of other gates. We measure the point contact conductance G_{q2} with V_{g1} and V_{g2} set at values used in the experiment and the other point contact energized just to depletion. We then shift $G_{q2}(V_{q2})$ to somewhat less negative V_{q2}. We assume the shift should be roughly twice the size of the shift caused by energizing just V_{g1} and V_{g2}. We refine this approximation by comparing the point contact characteristic to a measurement of $G_{dot}(V_{q2})$ like those shown in Fig. 4.5. We assume that at V_{q2} such that we see well-developed Coulomb oscillations in Fig. 4.5 with amplitude approximately 0.01 e^2/h, the conductance of the point contact should be roughly twice that of the peak conductance, 0.02 e^2/h (1 $M\Omega^{-1}$).[5] This criterion only determines the shift to within a few mV, however, so the exact conductance is hard to determine.[6]

Similar measurements performed by van der Vaart *et al.* [1993] showed Coulomb oscillations disappearing at $G_{open} = gQ$, but did not show the return of oscillations.[7] The most likely reason for the difference is that we see oscillations when $t_n \neq 1$ for the highest

---

[5]If the conductance of the dot were just the series conductance of the two point contacts, and the other point contact were set to 0.01 e^2/h, this relationship would be exact. However, since the overlap matrix elements between lead states and dot states affect the height of the conductance peaks, and there are also interference-type effects at work, the peak amplitude is only roughly related to the conductance of the point contacts.

[6]Further discussion of determining the conductance of one point contact in a larger device is given in Chapter 5.

[7]van der Vaart *et al.* do not show any measurements of dot conductance above $G_{open} = gQ$, though the discussion suggests they either do not expect or do not observe oscillations for $G_{open} > gQ$.

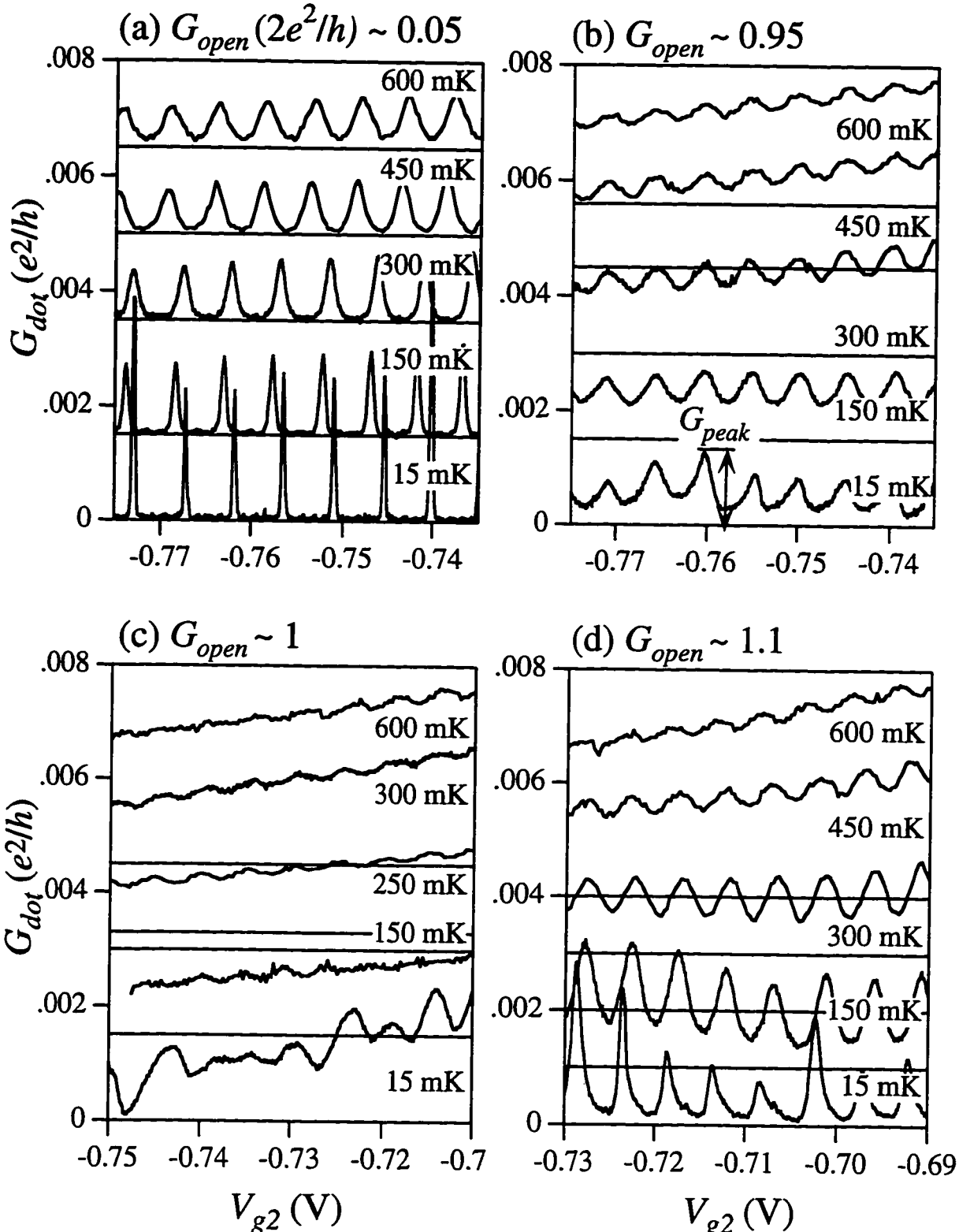

Figure 4.7 Dot conductance G_{dot} vs. gate voltage V_{g2} at a series of temperatures for each of four fixed values of G_{open}: (a) 0.05, (b) 0.95, (c) 1, (d) 1.1. Note the suppression of oscillations in (c) at $G_{open} = 1$ and their return in (d) for $G_{open} > 1$. Traces are offset vertically for clarity (peak heights G_{peak} as defined in (b) are reported in Fig. 4.8); the horizontal axis for each trace is shown where $G_{dot} = 0$ for that trace.

mode n. The point contact characteristics shown in van der Vaart *et al.* [1993] have extremely sharp steps and flat plateaus; thus above $G_{open} = g_Q$ it is plausible that the regions of V_{qpc} in which $t_n \neq 1$ are extremely narrow in their sample. When the second mode is introduced, the overall conductance increases strongly, so it would be hard to observe oscillations if they were only present for a narrow range of gate voltage. By contrast, many of of the point contacts in our samples show narrow plateaus and rise gradually in between.

We examined the temperature dependence of the absolute heights of the e-periodic oscillations, this time keeping G_{open} fixed at one of a series of values and sweeping gate V_{g2}. Figure 4.7 shows plots of G_{dot} vs. side gate voltage V_{g2} measured with sample KC7HH for a series of temperatures at the four values of G_{open} indicated. Traces are offset vertically for clarity (axes corresponding to zeros for successive traces are also shown). During each of these measurements V_{qpc} was held constant. We see that for G_{open} either less or greater than g_Q, well-defined e-periodic oscillations persist to temperatures above 300 mK; however, for $G_{open} \sim g_Q$, the oscillations are significantly suppressed at T = 150 mK and greater. The oscillations for $G_{open} << 1$ are sharp like those shown in Chapter 2; as G_{open} increases, the oscillations become broader and the valley conductance rises, as expected for lifetime-broadened oscillations. There is substantial variation in the oscillation envelope in the base temperature measurements, but at 150 mK and above, the peak heights are approximately uniform, as expected for $T \sim \delta E$ and greater. For G_{open} near or greater than 1, the absolute magnitude of conductance on the peaks, G_{peak} (indicated in Fig. 4.7(b)), decreases as temperature increase.[8]

Figure 4.8 shows peak heights G_{peak} (as defined in Fig. 4.9(b)) averaged from three peaks plotted vs. temperature for the data of Figure 4.7(a), (b), and (d), and for $G_{open} \sim 1.74\ g_Q$. Error bars in this plot indicate the range of the peak heights measured.

[8]This is difficult to see in Fig. 4.9 because of the need to offset the individual traces vertically, but the peak heights are plotted in Fig. 4.10.

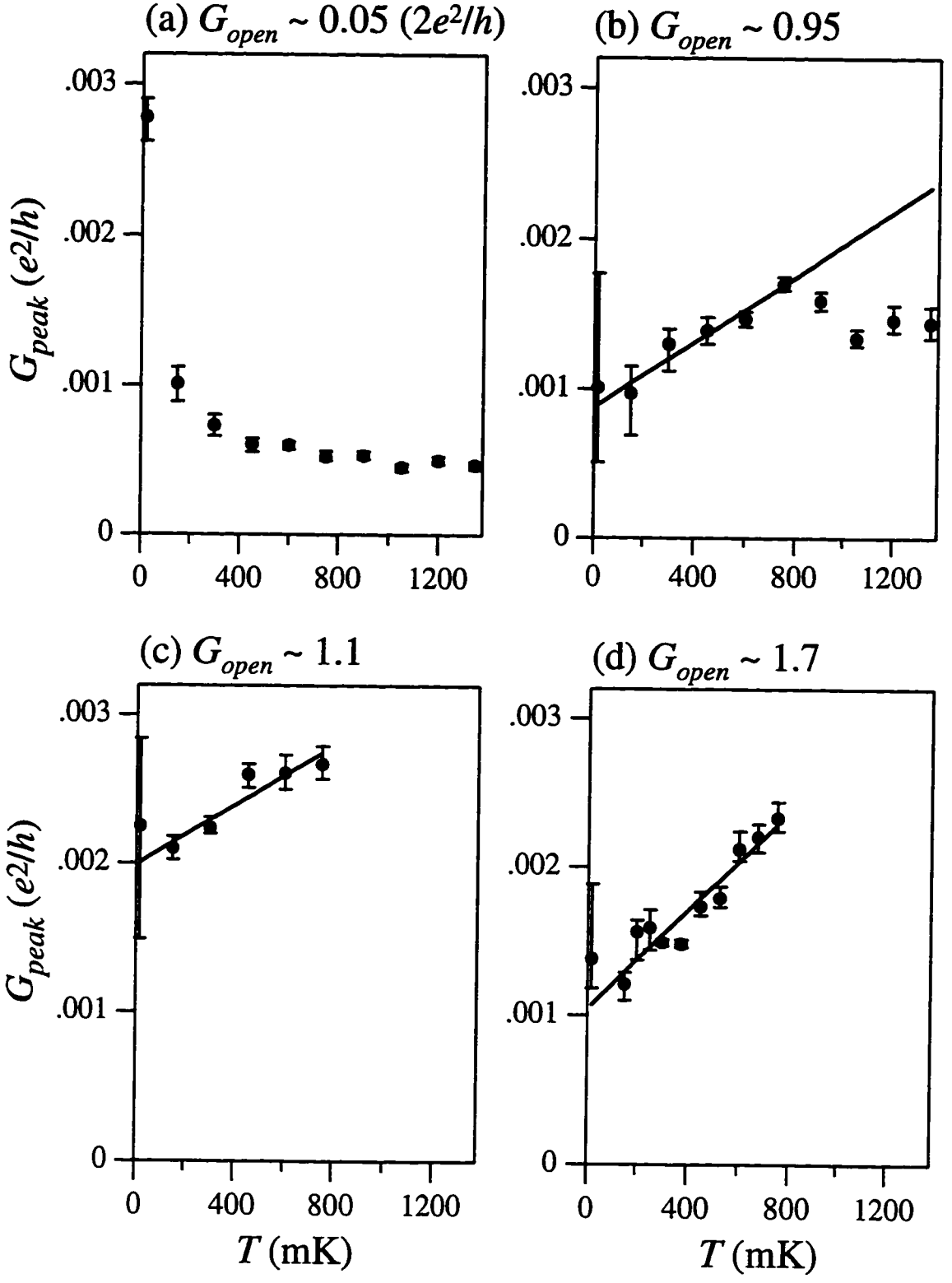

Figure 4.8 Peak heights G_{peak} vs. temperature from data of Fig. 4.7; G_{open} ~ 1 is not shown since no peaks are visible, and G_{open} ~ 1.7 is added. Theory predicts G_{peak} proportional to T.

Figure 4.8 (a) (G_{open} ~ 0.05) shows what we expect for a well-defined dot; the peak heights are greatest at base temperature, at which tunneling occurs through a single level, and drop quickly as temperature is increased, becoming basically independent of temperature when $T >> \delta E$ (see discussion of Fig. 2.5). For G_{open} ~ 0.95, 1.1, and 1.7, at 15 mK there is substantial variation in G_{peak} (hence large error bars) and then for 150 mK and greater the peak heights increase in roughly linear fashion (dipping down again for T > 750 mK for G_{open} ~ 0.95).

The theory outlined in the next section predicts $G_{peak} \propto T$ for $r << 1$. We do see roughly linear temperature dependence of G_{peak} ; however, the relevant temperature range of the measurement ($\delta E < T < E_C$) is very small and thus it is difficult to draw firm conclusions. Furthermore, the temperature dependence in this range does not extrapolate to $G_{peak}(T = 0) = 0$, as theory would predict.

We devised another measure of the temperature dependence of Fig. 4.7, given in Fig. 4.9. We define the threshold temperature for the oscillations as the temperature at which the amplitude of the oscillations is less than $2 \times 10^{-4}\ e^2/h$. (This threshold amplitude was chosen to be slightly above the minimum valley conductance of the measurements, $5 \times 10^{-5}\ e^2/h$.) We see that the threshold temperature for the oscillations decreases slowly and smoothly from 1.2 K for very low G_{open} to 300 mK for G_{open} ~ 2.1 g_Q, except for a sharp dip at $G_{open} \approx g_Q$. This threshold temperature is intended to show the maximum temperature for which oscillations can be observed, proportional to a rescaled charging energy [for a similar conception of quantum dots in the presence of strong tunneling, see Molenkamp *et al.*, 1995, and Flensberg, 1993 a, b].

To further confirm the disappearance of oscillations at one mode, we repeated the measurement of Fig. 4.7(c) (with sample KC7EE) but examined a wider range of V_{g2}, as shown in Fig. 4.10. We expect that cross-capacitance between V_{g2} and V_{q2} means that there will be a finite range of V_{g2} over which a particular V_{q2} setting corresponds to G_{open} = one mode. As a result, we only expect the oscillations to disappear over a finite range of

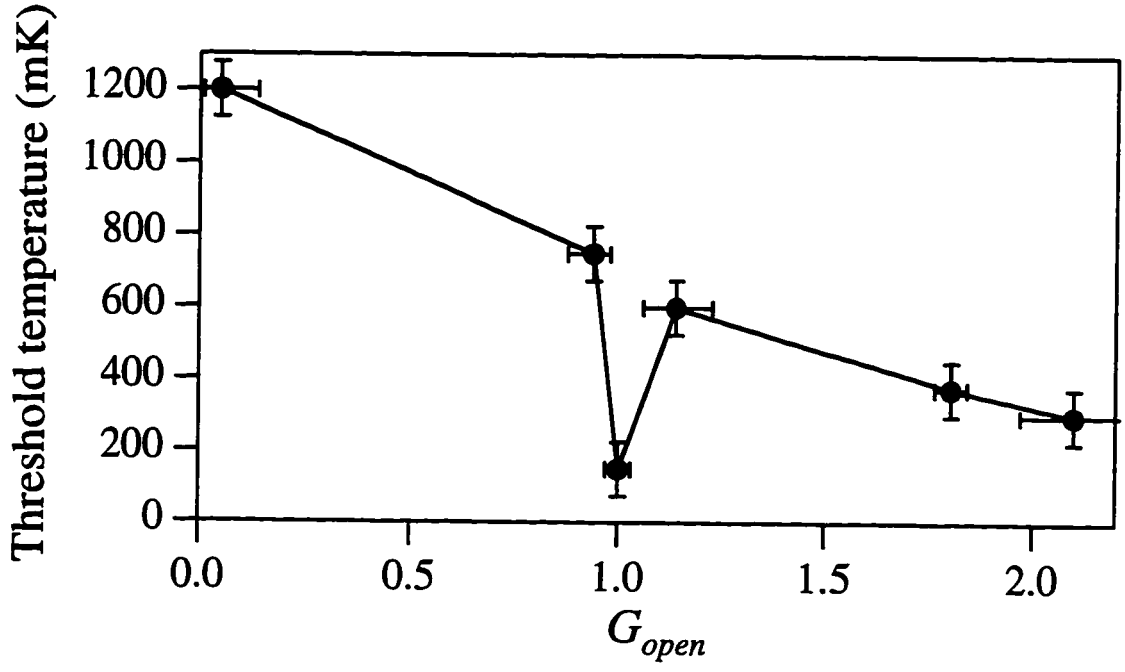

Figure 4.9 Threshold temperature of oscillations (defined in text) vs. G_{open}. Symbols are data points; line connecting them is a guide to the eye.

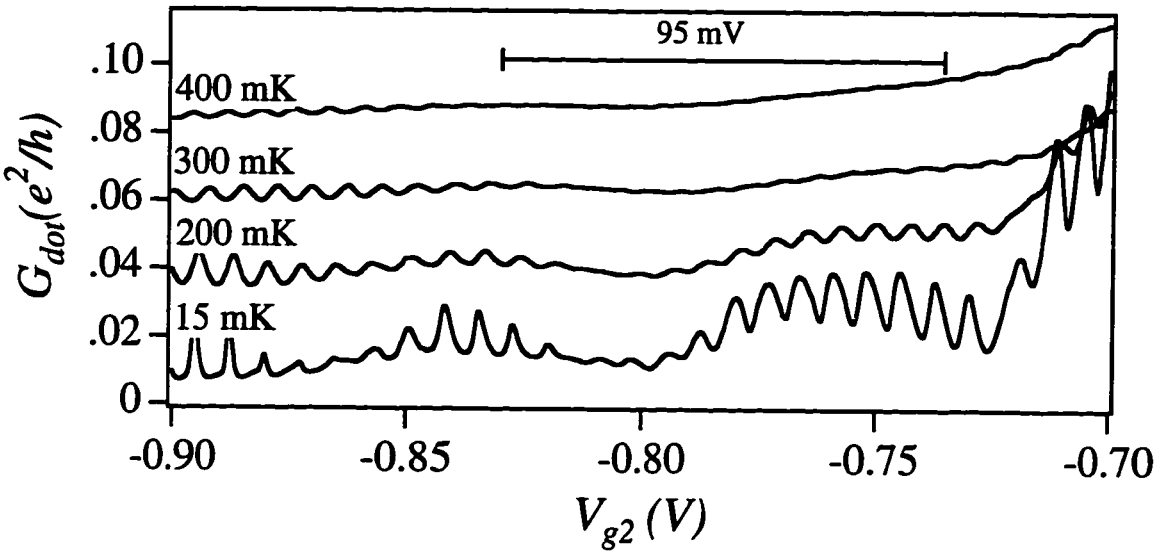

Figure 4.10 Dot conductance G_{dot} measured at four temperatures with G_{open} set at 1 mode and side gate voltage V_{g2} swept. Traces are vertically offset for clarity. Note the absence of e-periodic oscillations in the center of the graph, where V_{g2} is in the range at which G_{open} was measured. The breadth of the region with no oscillations increases with increasing temperature (it is ~95 mV wide for T = 400 mK as indicated). Oscillations return on either side of the flat region as capacitive coupling to V_{g2} changes G_{open}.

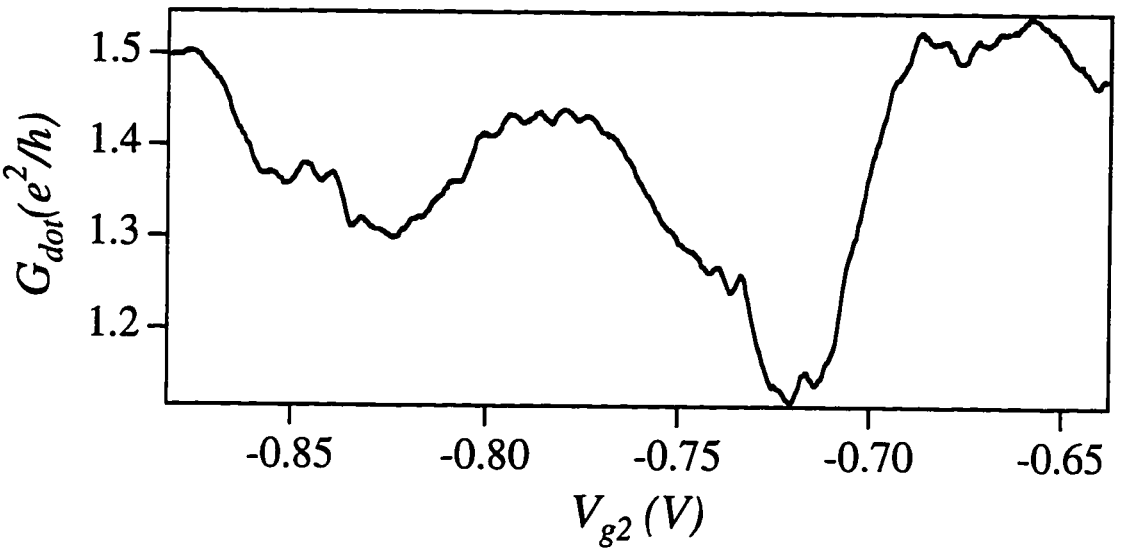

Figure 4.11 Measurement of G_{dot} with both point contacts strongly tunneling, $G_{open} \sim 2\ g_Q$ and $G_{closed} \sim 1.5\ g_Q$. Small e-periodic oscillations are superposed on a much larger background which oscillates with period ~100 mV, most likely due to quantum interference.

V_{g2} for a given V_{q2}. Coarse measurement of the cross-capacitance suggests that when sweeping V_{g2}, the oscillations should vanish over a range of V_{g2} roughly ten times wider than the V_{q2} range of suppressed oscillations in measurements made sweeping V_{q2} (such as those shown in Figure 4.5(a)). We find that the oscillations disappear over roughly 95 mV in V_{g2} for $T = 400$ mK (indicated in Fig. 4.10), whereas they disappear for 11 mV in V_{q2} at the same temperature (Fig. 4.5). The envelope variation of the measurements most likely comes from quantum interference, as discussed previously.

Finally, we determined the maximum lead conductances for which e-periodic oscillations could still be observed. We set both point contacts to conductances exceeding g_Q and measured linear conductance as a function of side gate voltage; the results are shown in Fig. 4.11. The highest conductances at which we observed e-periodic oscillations was with $G_{open} \sim 2g_Q$ and $G_{closed} \sim 1.5g_Q$. The amplitude of the e-periodic oscillations is only a few percent of the total signal, and as in Figure 4.6, they are superposed on larger background oscillations which probably come from quantum interference.

4.3.2 Theoretical Model

Matveev [1995] examined a single quantum cavity coupled through one quantum point contact to its environment, modeling the contact as a perfectly adiabatic one-dimensional channel between two wide regions of 2DEG (neglecting the finite size of the cavity, which is reasonable in the limit of small level spacing $\delta E << k_B T$). This model is equivalent to viewing the electron fluid in the channel as an elastic medium and studying its displacement.[9] Matveev calculated the correction to the cavity ground state energy as a function of the transmission coefficient t for electrons tunneling between the cavity and the lead, as t approached 1. His central result is that for $t = 1$, the ground state energy is gate voltage-independent; thus if there is at least one mode fully transmitting between a dot and its environment, the Coulomb blockade should vanish. Furthermore, he finds that for t

[9]For a technical discussion of this study, the reader is referred to the original paper by Matveev; this thesis only seeks to summarize the relevant results.

even slightly less than one, the average charge on the cavity oscillates with gate voltage period $C_g V_g/e$. Hence e-periodic oscillations should be visible for all $t < 1$.

These results were then applied to transport through a single dot configured as shown in Fig. 4.4, in which the left lead is weakly tunneling and the right lead is strongly tunneling lead, namely, $|r_L| \sim 1 \, (t_L << 1)$ and $|r_R| << 1 \, (t_L \sim 1)$ [Furusaki and Matveev, 1995].[10] They find that the strong tunneling through the right barrier renormalizes the conductance through the weak-tunneling left barrier, because the two 1D systems (the two point contacts connecting the leads to the dot) are electrostatically coupled through the dot. The essential physical concept is an analog of Anderson's orthogonality catastrophe: in a system of many particles, the N-electron ground state is nearly orthogonal to the $N+1$-electron ground state because there are many different parameters all with slightly different values. Hence the matrix elements for transport (i.e. $N \rightarrow N+1$) are suppressed by the lack of overlap between the N and N+1 ground states.

The result for the dot conductance is

$$G(X) = \frac{\pi^2 k_B T G_L}{8e^{\gamma} E_C} \left[1 - \int_{-\infty}^{\infty} dE \frac{\Gamma_R(X)}{E^2 + \Gamma_R^2(X)} \frac{1 + (E/\pi k_B T)^2}{\cosh^2(E/2k_B T)} \right] \tag{4.6}$$

with $$X \equiv \frac{C_g V_g}{e} \quad \text{and} \quad \Gamma_R(X) \equiv \frac{8e^{\gamma}}{\pi^2} E_C |r_R|^2 \cos^2(\pi X) \tag{4.7}$$

The key feature of this result is the temperature dependence of the peak conductance G_{peak} (defined in Figure 4.7(b)). On a peak (corresponding to half-integer X), the term in brackets on the right side of Eq. (4.6) evaluates to a constant, so that

$$G_{peak} \propto T \tag{4.8}$$

[10]They also consider a single dot with the same (strong) tunneling rate in both leads. Measurements on this configuration have been performed with Carol Livermore and will not be discussed in this thesis.

Again, these results assume (1) continuous level spacing δE (equivalent to the temperature regime $\delta E << k_B T$), (2) a perfect one-dimensional channel in the point contact, and (3) good screening inside the quantum dot so that Coulomb charging can be described in terms of the capacitive charging energy e^2/C_Σ. In all cases the charging energy is assumed to be much greater than the temperature. Assumption (1) applies to our samples at moderate temperatures (T~400 mK and greater), though not at the lowest temperatures we attain. Assumption (2) is likely to apply, since the potential at the level of the 2DEG formed by a voltage on a split gate is very smooth [Katine *et al.*, 1994]. Any deviations from smoothness would have to come from disorder in the impurity potential. Finally, since the Thomas-Fermi screening length (~ 200 Å in a 2DEG) is much smaller than our dots, screening is certainly good.

As discussed previously, we confirm the prediction that oscillations should vanish at $G_{open} = g_Q$. We are unable to verify the prediction Eq. (4.8) because the temperature range over which we can measure peak heights is small.

4.3.3 Nonequilibrium Conductance

We measured the differential conductance of the asymmetric dot in the nonlinear regime ($V_{ds} \neq 0$) in the same fashion as reported in Ch. 2. Figure 4.12(a) shows $G_{dot}(V_{ds}, V_g)$ in logarithmic grayscale (black is high conductance and white low) for the asymmetric dot with G_{open} slightly under 1 mode. When G_{open} is increased to ~ 1 mode or greater, the differential conductance becomes insensitive to V_g, and so in Figs. 4.12(b) and (c) we show one measurement of $G_{dot}(V_{ds})$ at fixed V_g for G_{open} ~ 1 mode and G_{open} somewhat greater than one mode. In Fig. 4.12(a), a parallelogram structure similar to Fig. 2.11 is visible in $G_{dot}(V_{ds}, V_g)$, but the regions corresponding to the regions of Coulomb blockade have low but finite conductance, rather than being truly blockaded. Application of a very small bias voltage (~50 μV) is enough to promote current flow, although there still exist peaks in the conductance at the Coulomb steps.

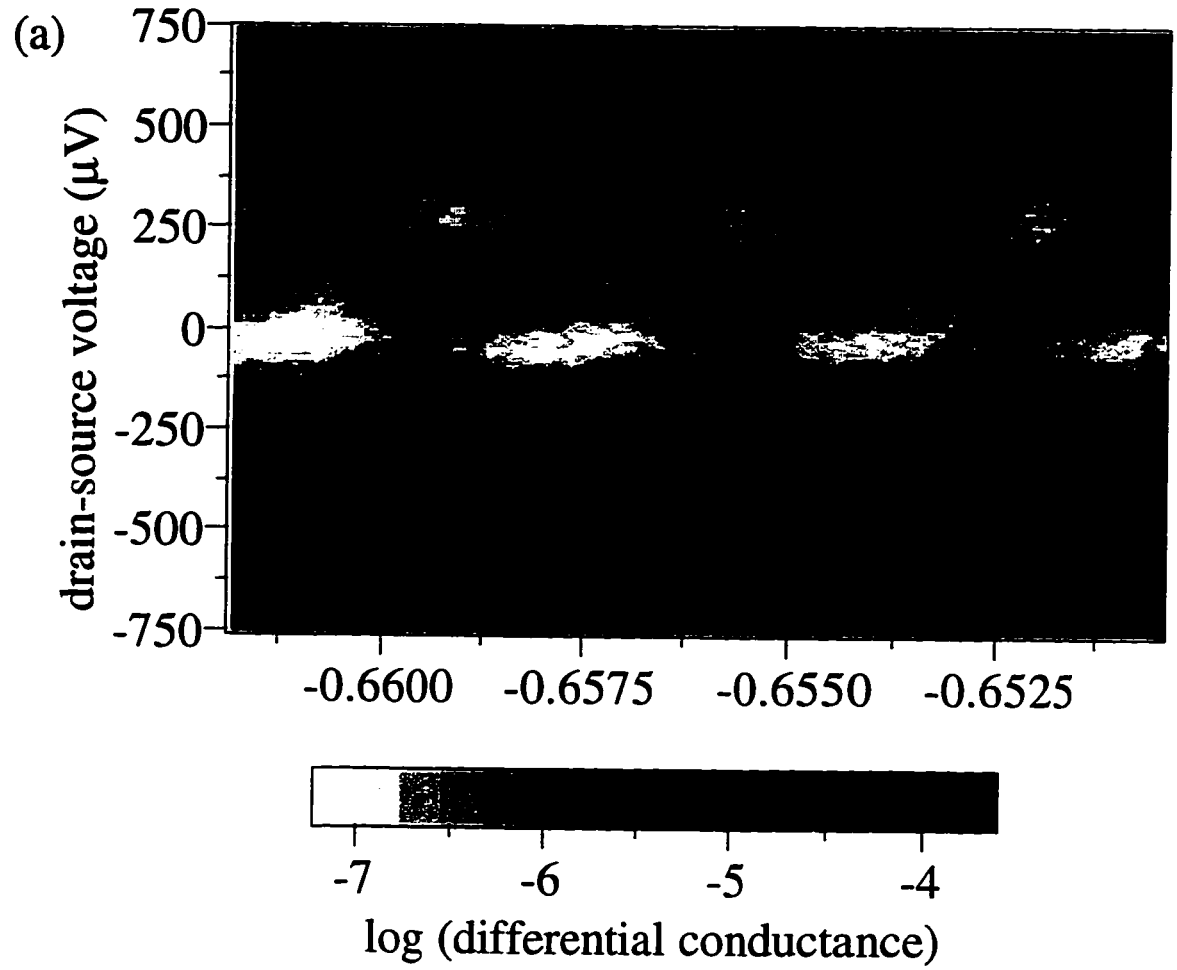

Figure 4.12 (a) Differential conductance $G_{dot}(V_{ds}, V_g)$ of the single dot with $G_{open} \sim 0.9\ g_Q$. G_{dot} is shown in logarithmic inverted grayscale. A semblance of the Coulomb blockade structure is present here but disappears entirely for (b) and (c).

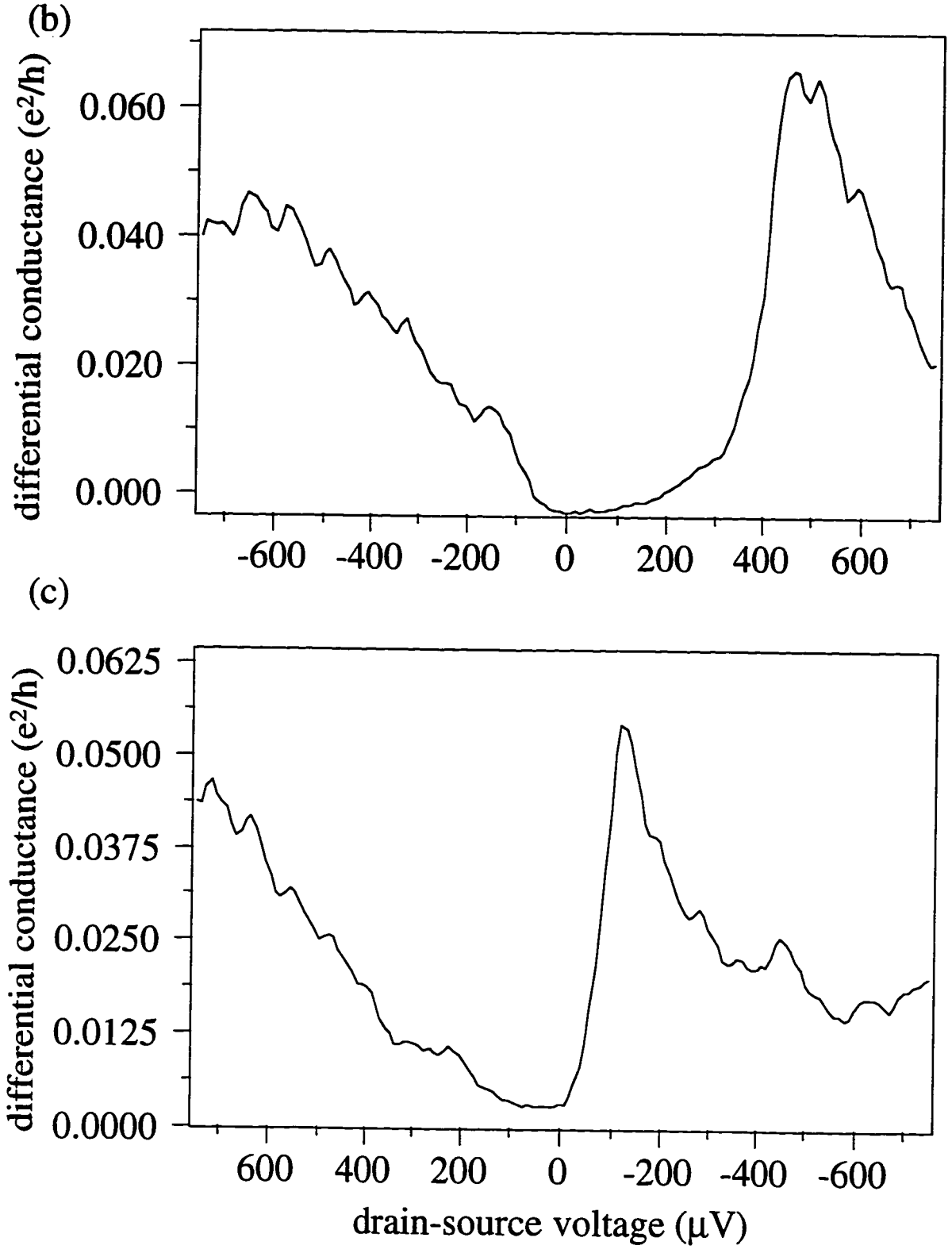

Figure 4.12(b), (c) Differential conductance $G_{dot}(V_{ds})$ of the single dot with G_{open} (b) ~ g_Q, (c) ~1.1 g_Q. G_{dot} is no longer periodic in V_g.

With G_{open} ~ 1 mode, shown in Fig. 4.12(b), as mentioned previously, the V_{g2} dependence vanishes entirely. The differential conductance does increase with finite bias voltage to a peak on either side of zero, but there is no region of suppressed conductance. Finally, with G_{open} somewhat greater than 1 mode, as shown in 4.12(c), the nonlinear conductance becomes asymmetric, with a peak at 100 μV for all V_{g2} but a peak at greater negative gate voltages Presumably this asymmetry comes about because one point contact is transmitting rather than the other. We do not see a return to the behavior of G_{open} less than 1 mode, in contrast to the linear conductance measurements.

4.4 Interpretation

These results have many possible interpretations, and we have not yet distinguished among them unambiguously. The work reported in this chapter, then, is in a sense unfinished, waiting for another student to think of and perform an experiment which would clearly identify an explanation. We describe here the two interpretations which seem most likely.

The simplest possible explanation of the equilibrium conductance results is that when there is more than one mode in the open point contact, the reflection coefficient for transport through the first mode is not zero. Within this explanation, we consider two explanations for a possible increase of r. In a single-particle model, as the constriction conductance is increased, introducing the second subband into the channel, intersubband scattering due to disorder might increase abruptly due to the increase in the density of states.[11] This model, however, does not explain why the reflection coefficient would go to zero at $G_{open} = g_Q$. Another possibility is the following: if the presence of partially occupied higher subbands enhanced electron-electron scattering in the lowest subband, or if electrons in the lowest subband scattered from electrons in the partially occupied subband in the channel, we would expect both $r = 0$ at $G_{open} = g_Q$ and $r > 0$ for $G_{open} > g_Q$.

[11] A similar effect has been predicted in arrays of narrow Si inversion lines by Das Sarma and Xie [1987].

It is also possible that these e-periodic oscillations are not Coulomb oscillations. Then there would be no need to explain how single-electron charging can happen in the presence of fully transmitting modes of transport between the dot and the lead. Ralph has suggested[12] that by analogy to Friedel oscillations [Kittel, 1987], the phase accumulated by an electron as it travels through the dot could be proportional to the average charge on the dot. Thus, over the range of V_{g2} in which the average charge on the dot changes by one electron, the phase accumulated by transport electrons would undergo a complete cycle and thus one cycle of interference would occur.

4.5 Summary

We have observed e-periodic conductance oscillations vanish at $G_{open} \sim g_Q$ and reappear for increased G_{open}. This suggests that $t < 1$ for the lowest transverse mode in the presence of partially occupied higher subbands. We have also documented the temperature dependence of the peak heights and the oscillation amplitudes. Finally, in the nonlinear conductance, blockaded structure vanishes at $G_{open} \sim g_Q$ and does not appear to return for greater G_{open}.

[12]D. C.. Ralph, private communication.

CHAPTER 5
ENERGETICS AND TRANSPORT OF TUNNEL-COUPLED QUANTUM DOTS[1]

5.1 Introduction

Single quantum dots have been studied for some time now, and a great deal of rich physics has been discovered in the process [for a review see Kouwenhoven and McEuen, 1996]. A next logical direction is the study of multiple dots, and in particular, interactions between dots. To carry on an analogy with atoms, if a single quantum dot can be thought of as an "artificial atom," [Kastner, 1993] then it is logical to examine "artificial molecules". There are many reasons to do so. Not only is the basic physics which describes such systems of interest, but systems of coupled dots have many potential applications in "single electronics," electronic devices controlled by the position of single electrons, and in advanced computing strategies in which the quantum mechanical interactions between electrons are used for computation [Lloyd, 1993; Bennett, 1995].

Many advances have been made in controlling the transport of single charges through complex systems via electrostatic interactions. The single-electron pump [Pothier *et al.*, 1991; Martinis *et al.*, 1994], single-electron turnstile [Geerligs *et al.*, 1990], Coulomb blockade electrometer [Lafarge *et al.*, 1991; Visscher *et al.*, 1994], and single charge trap [P.D. Dresselhaus *et al.*, 1994] are a few examples. These devices have generally been fabricated in metal systems. Less work has been done studying the interplay between electrostatic and quantum mechanical interactions in coupled semiconductor quantum dots. Split-gate semiconductor quantum dots are uniquely suited to studying such interactions, because the researcher is able to control the strengths of tunnel barriers individually.

---

[1]Parts of this chapter have appeared in *Surface Science* (C. H.. Crouch *et al.*, 1996) and have been submitted to *Applied Physics Letters* and *Physical Review B*.

This chapter is devoted to studying the interactions between two tunnel-coupled quantum dots in series as the tunneling rate between the dots is changed. If one thinks of two coupled dots as a diatomic molecule, we investigate the process of bond formation between the constituent atoms as the strength of interaction is increased. We use the Coulomb blockade of transport to probe the ground and excited state energies of the system as the interaction strength is increased. In particular, we determine the characteristics of the double dot which were described in Chapter 2 for the single dot, namely the differential conductance in the nonlinear regime and the temperature dependence of the zero-bias conductance. The equilibrium measurements probe the ground state of the system while the nonequilibrium measurements probe the Coulomb gap and low-lying excited states.

The device used in these experiments, KC7EE,[2] is shown in Fig. 5.1. Figure 5.1 (a) is an scanning electron micrograph of the device studied (the same device is shown in Figure 1.6). Figure 5.1(b) shows the wiring pattern of the device, which consists of three independent point contacts, one pair of side gates which are electrically connected to voltage V_{g3}, two independent side gates connected to voltages V_{g1} and V_{g2}, and the two ohmic contacts indicated. These gates allow us to form the device shown schematically in (c), two islands in series between the two leads. Each dot is coupled capacitively to a neighboring gate; the voltage applied to the gate controls the dot's electrostatic potential. In the experiments presented here, V_{g1} and V_{g2} are varied and V_{g3} is held constant to confine the electron gas. When the interdot tunnel conductance g_{int} is low, the numbers of electrons N_1 and N_2 on the individual dots are well-defined, and interactions between the dots are primarily electrostatic. As the interdot tunnel conductance increases, charge can be shared between the two dots, as electrons are shared between atoms to form a molecular bond; then N_1 and N_2 are no longer individually quantized, but their sum $N_{tot} = N_1 + N_2$ is still

[2]A few measurements of the Coulomb gap collapse were made using two dots of sample KC3Q, a triple quantum dot sample with the same size dots as KC7EE. KC3Q was made by Fred Waugh and is described as sample A in Waugh [1994].

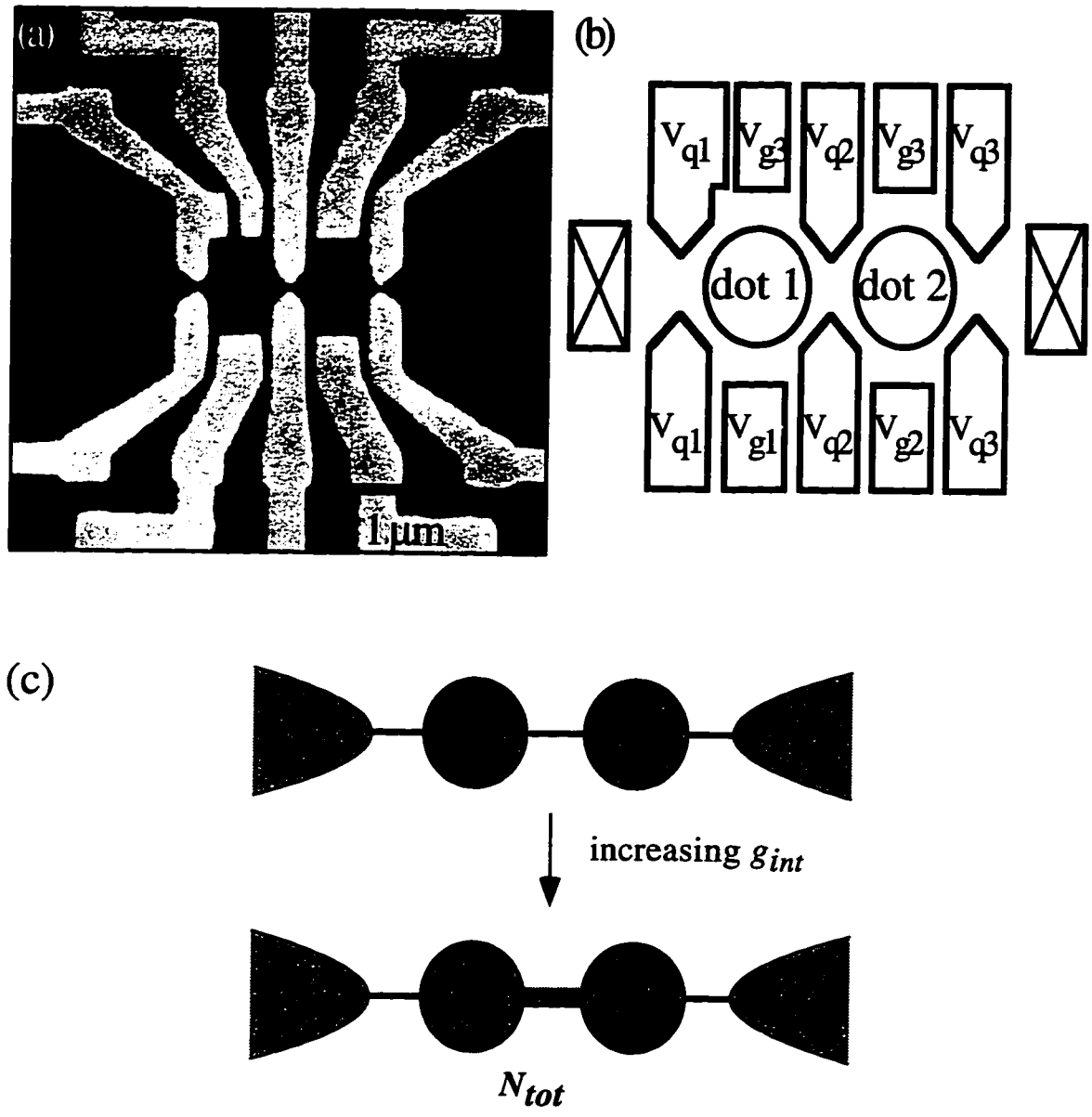

Figure 5.1 (a) SEM micrograph of the device used for most of the measurements of this chapter. Bright areas are metal gates; dark areas are the surface of the GaAs/AlGaAs wafer. (b) Wiring diagram of the device (also showing dots). Gates with a common symbol (representing an applied voltage) are electrically connected. Crossed boxes are ohmic contacts. (c) Schematic of series double quantum dot and transformation with increasing interdot tunneling g_{int} from two isolated dots to a single composite dot. ($N_{tot} = N_1 + N_2$.)

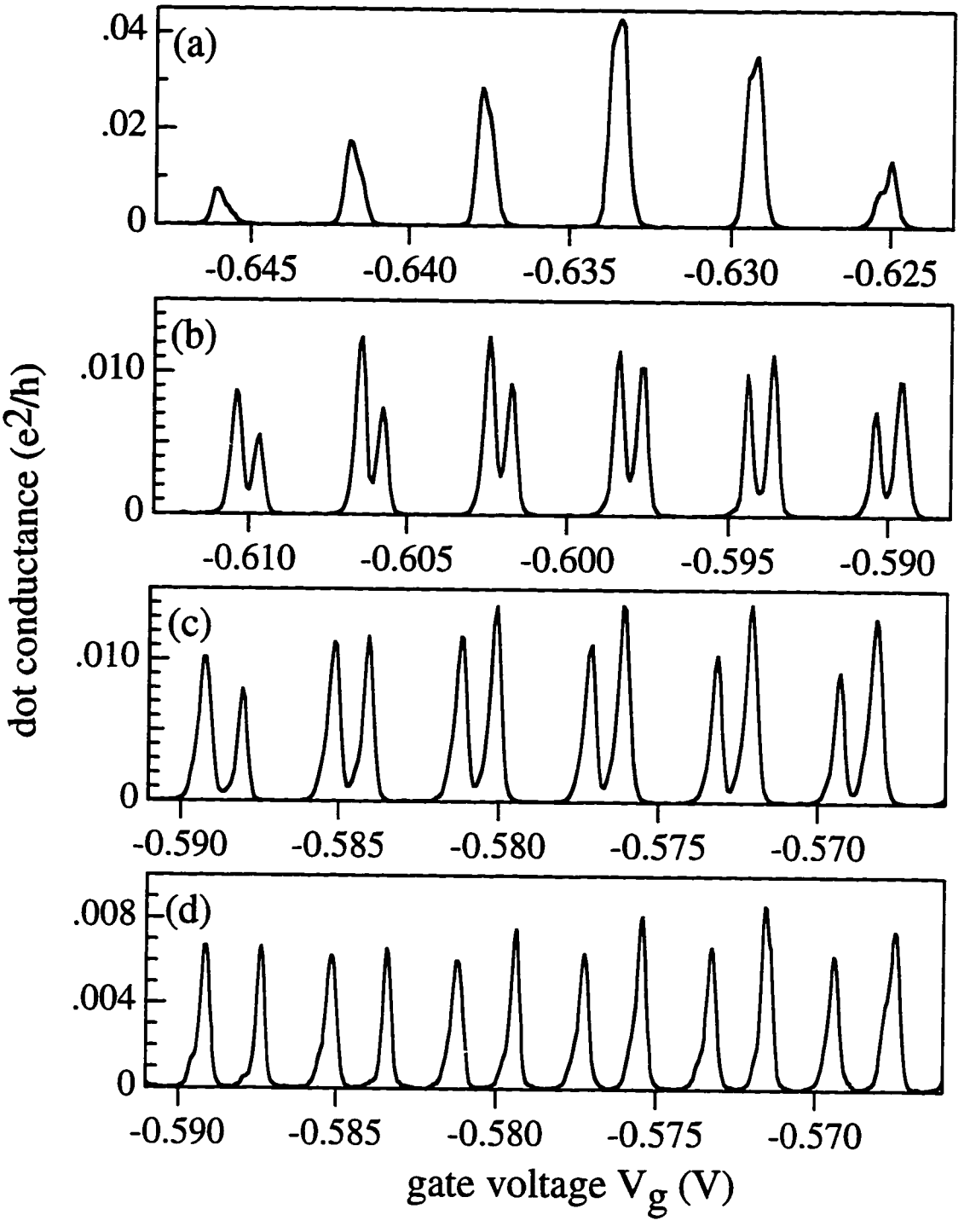

Figure 5.2 Base temperature (T_{mix} = 15 mK) double dot conductance peaks for various values of interdot conductance illustrating the increase of peak splitting from very small g_{int} to $g_{int} \sim 1$. Interdot conductances g_{int} (in units of $g_Q = 2e^2/h$) and fractional peak splittings f (defined in Eq. 5.14) are (a) $g_{int} = 0.19, f = 0.08$, (b) $g_{int} = 0.57, f = 0.34$, (c) $g_{int} = 0.69, f = 0.52$, (d) $g_{int} = 0.95, f = 0.90$.

well-defined as long as the conductance between the dot and the leads is kept low. Figure 5.1(c) schematically shows the transition from two isolated dots to one composite dot as g_{int} increases.

Prior to the work described in this thesis, Waugh *et al.* [1995] found that the zero-bias conductance of a double quantum dot at low temperature displayed sharp peaks similar to the single dot conductance peaks, but these peaks were split in two with a separation that depended on the rate of interdot tunneling. Such a family of traces is shown in Fig. 5.2. Each trace is measured at base temperature (T_{mix} = 15 mK, T_e ~ 70 mK) by sweeping V_{g1} = V_{g2} with a fixed value of g_{int} and measuring the equilibrium conductance G_{dot}. We see that as the interdot conductance g_{int} is increased from $0.19g_Q$ to $0.95g_Q$ ($g_Q = 2e^2/h$, as defined in Ch. 4), conductance peaks which initially resemble the single-dot conductance peaks shown in Fig. 2.2 split in two; the splitting increases as g_{int} increases until the peaks are no longer clearly paired; and the conductance for g_{int} near 1 resembles that of a single dot of twice the size of the individual dots. The origin of this splitting is indicated in Figure 5.3, which shows the free energy for various charge configurations (N_1, N_2) of the double dot as a function of $V_g = V_{g1} = V_{g2}$. The ground state of the double dot with $V_{g1} = V_{g2}$ has $N_1 = N_2$. If an extra electron is added to one dot, so that one dot has one electron more than the other, this creates a dipole moment between the dots which costs energy. With no coupling between the dots, as shown in Fig. 5.3 (a), states with $N_1 \neq N_2$ are much higher in energy than states with $N_1 = N_2$. This means that the linear conductance of the uncoupled double dot looks like that of the single dot, as shown in Fig. 5.3 (b), but with conductance peaks at V_g values such that two electrons are added.

The excess energy of states with $N_1 \neq N_2$ is lowered by an amount E_{int} by introducing interdot interactions, either capacitive or quantum mechanical, as shown in Figs. 5.3(c) and (e). Transport can then take place by adding one electron at a time at the gate voltages where different number states intersect, splitting what was formerly one conductance peak into two, as shown in (d) and (f). The voltage splitting ΔV_s (shown in

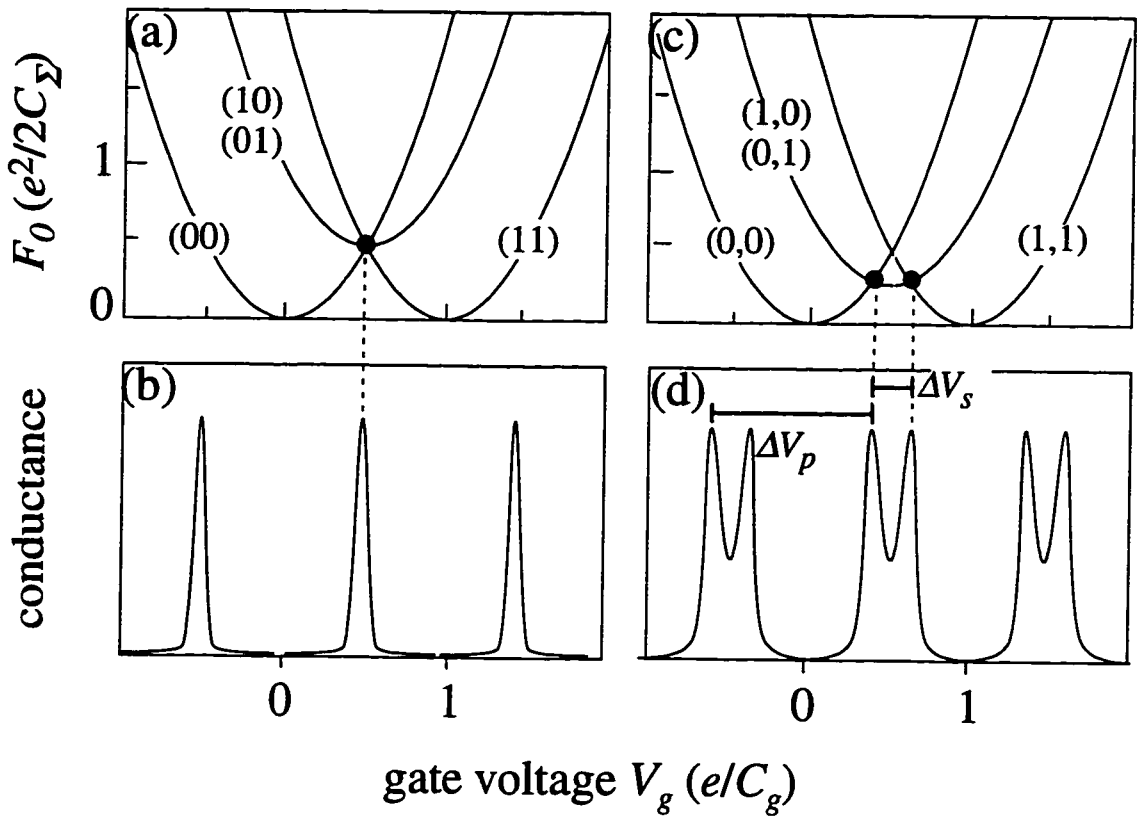

Figure 5.3 (a), (c), (e) Double dot zero-bias energy vs. gate voltage $V_g = V_{g1} = V_{g2}$ shown for (a) no interdot coupling, (c) finite interdot capacitance, (e) finite interdot tunneling. In (a) and (c) the number of electrons (N_1, N_2) on each dot is well defined; with finite interdot tunneling (e) only the total number of electrons $N_{tot} = N_1 + N_2$ is well-defined. (b), (d), (f) Corresponding zero-bias conductance through the double dot as a function of gate voltage. ΔV_s, peak splitting in volts; ΔV_p, period of split peaks in volts; E_{int}, interaction energy from interdot tunneling which lowers energy of states with $N_1 \neq N_2$. After Waugh, Ph.D. thesis [1994].

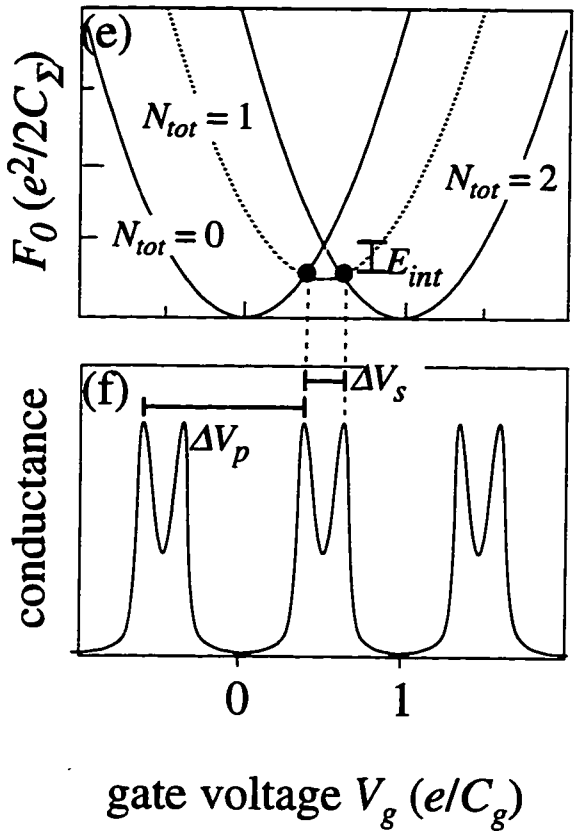

Figure 5.3 (a), (c), (e) Double dot zero-bias energy vs. gate voltage $V_g = V_{g1} = V_{g2}$ shown for (a) no interdot coupling, (c) finite interdot capacitance, (e) finite interdot tunneling. In (a) and (c) the number of electrons (N_1, N_2) on each dot is well defined; with finite interdot tunneling (e) only the total number of electrons $N_{tot} = N_1 + N_2$ is well-defined. (b), (d), (f) Corresponding zero-bias conductance through the double dot as a function of gate voltage. ΔV_s, peak splitting in volts; ΔV_p, period of split peaks in volts; E_{int}, interaction energy from interdot tunneling which lowers energy of states with $N_1 \neq N_2$. After Waugh, Ph.D. thesis [1994].

Fig. 5.3(d) and (f)) depends on the strength of the coupling, while the period of the double peaks ΔV_p is unaffected by coupling. If the coupling is capacitive, the numbers of electrons on each dot N_1 and N_2 are still well-defined. With finite tunnel coupling, N_1 and N_2 are no longer required to be integers, but N_{tot} is still a good quantum number since tunneling between the dot and leads is weak.

Such peak splitting had been previously observed in metal double-island systems [Geerligs *et al.*, 1991]; however, in metal systems tunneling rates are generally fixed, and so they observed a fixed peak splitting. The work of Waugh *et al.* [1995, 1996] demonstrated that tunneling could also lower the energy of states with odd numbers of electrons. Other groups have studied double dot systems from other angles, looking at resonant tunneling through single-particle states in mismatched dots [van der Vaart *et al.*, 1995; Dixon *et al.*, 1996], and in one case with very tiny dots, hybridization between single-particle states of the two dots [Blick *et al.*, 1996]. Transport with fixed and variable interdot coupling in parallel double dot systems [Hofmann *et al.*, 1995; Adourian *et al.*, 1996; Molenkamp *et al.*, 1995] has also been studied.

The work presented in this thesis examines the dependence of the energy of the double dot system on charge sharing due to adjustable interdot tunneling. This chapter begins by presenting, in section 5.2, theoretical models of the double dot. Results on the temperature dependence of split conductance peaks are given in 5.3, followed by measurements of the nonequilibrium conductance in 5.4. Analysis of the nonequilibrium measurements includes a self-consistent calculation of the Coulomb gap in the presence of interdot tunneling (section 5.4.4), based on the work of Golden and Halperin [1996a, b]. Finally, section 5.5 presents evidence that as the interdot tunneling rate increases, the interdot capacitance remains essentially constant, confirming the primary role of tunneling in the interactions we observe.

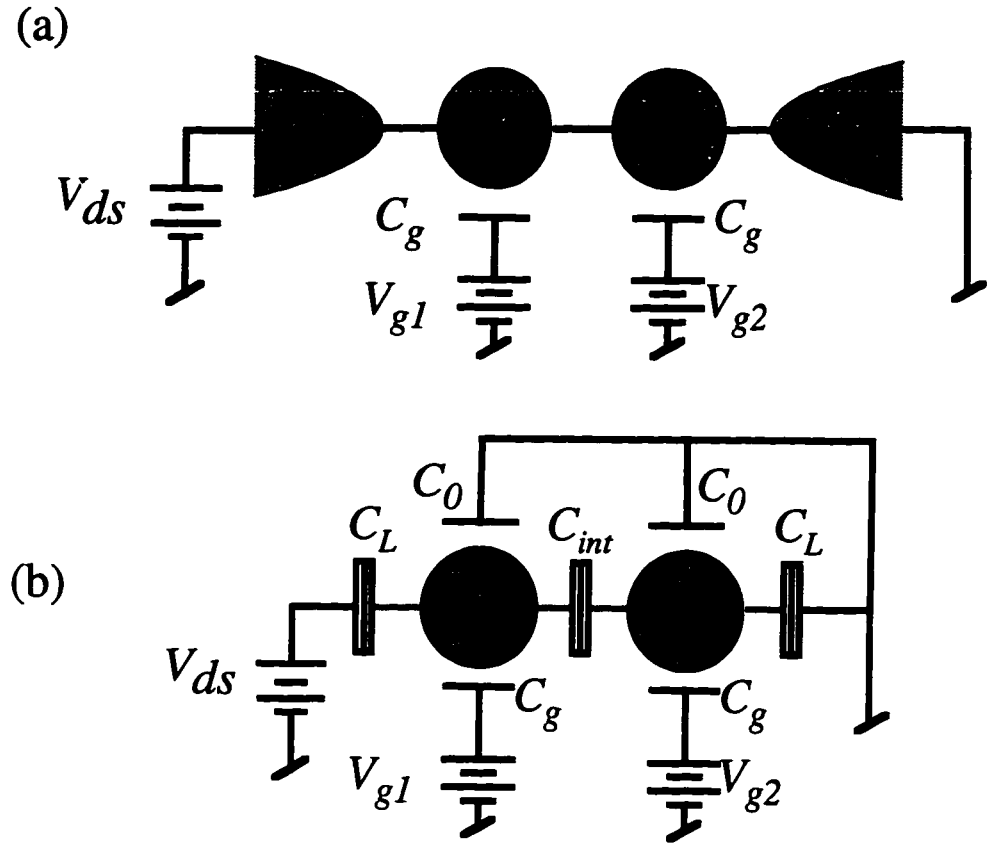

Figure 5.4 (a) Schematic of series double quantum dot. Here the two gate voltages are shown as independent; for the experiments of this thesis (except App. A) they are set to the same value. (b) Equivalent circuit with capacitances C_g from each dot to the neighboring gate, C_L from each dot to the neighboring lead, C_{int} between dots, and C_0 to ground. Split boxes connecting dots to each other and to the leads represent tunnel junctions. The numbers of electrons (N_1, N_2) on the dots in the circuit must be quantized.

5.2 Models of Double Dot Transport

5.2.1 Double Dot Electrostatic Energy

To understand transport through two quantum dots in series, we begin by determining the total electrostatic energy, and then add quantum effects. The total electrostatic energy F of two quantum dots in series is determined by the same procedure as used to determine the energy of the single dot; this energy consists of the energy stored in the capacitors and the work done by the batteries to establish the charge configuration, as in section 2.2.1.[3] We begin with the equivalent circuit shown in Fig. 5.4(b), and we consider electron configurations (N_1, N_2) which denote N_1 electrons on the left dot and N_2 electrons on the right dot. For simplicity we assume the dots have equal capacitances C_L to the neighboring leads. We also assume $C_{g1} = C_{g2} = C_g$.[4]

We find that the electrostatic potentials ϕ_1 and ϕ_2 of the two islands are

$$\phi_1 = \frac{C_L V_{ds} + C_g(V_{g1} + \alpha V_{g2}) - e(N_1 + \alpha N_2)}{C_\Sigma(1-\alpha^2)} \tag{5.1a}$$

and

$$\phi_2 = \frac{\alpha C_L V_{ds} + C_g(\alpha V_{g1} + V_{g2}) - e(\alpha N_1 + N_2)}{C_\Sigma(1-\alpha^2)} \tag{5.1b}$$

with $\alpha \equiv C_{\text{int}} / C_\Sigma$, $C_\Sigma \equiv C_g + C_0 + C_L + C_{int}$, and other quantities defined in Fig. 5.4. From this result and Eqs. (2.2) and (2.3) we obtain the double dot electrostatic energy

$$\begin{aligned} F(N_1, N_2, N_t) = \frac{e^2}{2C_\Sigma}\frac{1}{(1-\alpha^2)}\Bigg[&(x_1 - N_1)^2 + (x_2 - N_2)^2 + \left(\frac{C_L V_{ds}}{e}\right)^2 + 2(x_1 - N_1)\left(\frac{C_L V_{ds}}{e}\right) \\ &+2\alpha(x_2 - N_2)\left(\frac{C_L V_{ds}}{e}\right) + 2\alpha(x_1 - N_1)(x_2 - N_2)\Bigg] \\ &+\frac{1}{2}\left[2N_t e V_{ds} - C_L {V_{ds}}^2 - C_{g1}{V_{g1}}^2 - C_{g2}{V_{g2}}^2\right] \end{aligned} \tag{5.2}$$

---

[3] It is more arduous because there are more terms involved, but in principle it is no more difficult.

using the dimensionless gate voltage parameter

$$x_i \equiv \frac{C_{gi}V_{gi}}{e} \tag{5.3}$$

As with the single dot calculations, N_t is the total number of electrons supplied to the circuit by the battery. If we consider just the terms in 5.2 which depend on N_1 and N_2, we obtain a simplified free energy,

$$F_0(N_1,N_2,N_t) = \frac{e^2}{2C_\Sigma}\frac{1}{(1-\alpha^2)}\left[(x_1-N_1)^2+(x_2-N_2)^2+\left(\frac{C_LV_{ds}}{e}\right)^2+2(x_1-N_1)\left(\frac{C_LV_{ds}}{e}\right)\right.$$
$$\left.+2\alpha(x_2-N_2)\left(\frac{C_LV_{ds}}{e}\right)+2\alpha(x_1-N_1)(x_2-N_2)\right]+N_{tot}eV_{ds} \tag{5.4}$$

The free energy can also be written in terms of the total charge on the double dot N_{tot} and the difference n in charge between the two dots:

$$F_0(N_{tot},n) = \frac{e^2}{4C_\Sigma}\frac{1}{(1-\alpha)}[\Phi_{tot}-N_{tot}]^2+\frac{e^2}{C_\Sigma}\frac{1}{(1+\alpha)}\left[\frac{\rho}{2}-n\right]^2+N_{tot}eV_{ds} \tag{5.5}$$

using the definitions

$$\Phi_{tot} \equiv \frac{C_g(V_{g1}+V_{g2})}{e}+\frac{C_LV_{ds}}{e} \tag{5.6a}$$

$$\rho \equiv \frac{C_g(V_{g1}-V_{g2})}{e}+\frac{C_LV_{ds}}{e} \tag{5.6b}$$

$$N_{tot} \equiv N_1+N_2 \tag{5.6c}$$

---

[4]It is certainly possible to do the calculation without these approximations, but since they describe the sample studied, it is simpler to use them.

$$n \equiv N_1 - N_2 \tag{5.6d}$$

In the case of zero bias voltage, (5.4) simplifies to

$$F_0(N_1,N_2;V_{ds}=0)=\frac{e^2}{2C_\Sigma}\frac{1}{\left(1-\alpha^2\right)}\left[(x_1-N_1)^2+(x_2-N_2)^2+2\alpha(x_1-N_1)(x_2-N_2)\right] \tag{5.7}$$

and the "center-of-mass" form (5.5) to

$$F_0(N_{tot},n)=\frac{e^2}{4C_\Sigma}\frac{1}{(1-\alpha)}\left[\Phi_{tot}-N_{tot}\right]^2+\frac{e^2}{C_\Sigma}\frac{1}{(1+\alpha)}\left[\frac{\rho}{2}-n\right]^2 \tag{5.8}$$

(with the same definitions (5.3) and (5.6) but with $V_{ds}=0$).

In the next section we will explore the consequences of Eq. (5.7). Throughout this thesis, unless otherwise specified, we will assume $C_{g1} = C_{g2}$; the case of slightly mismatched C_{g1} and C_{g2} will be discussed briefly in section 5.2.5. In our samples, $C_{g1} = C_{g2}$ to within a few percent. We will not, however, always assume $V_{g1} = V_{g2}$.

5.2.2 Double Dot Zero-Bias Conductance – Capacitive Circuit Model

Consider initially the case $V_{g1} = V_{g2} = V_g$ and $V_{ds} = 0$. The free energy F_0 from (5.7) becomes

$$F_0(N_1,N_2)=\frac{e^2}{2C_\Sigma}\frac{1}{\left(1-\alpha^2\right)}\left[(x-N_1)^2+(x-N_2)^2+2\alpha(x-N_1)(x-N_2)\right] \tag{5.9}$$

As previously discussed, Figure 5.3(a) shows plots of this free energy as a function of gate voltage for various electron configurations (N_1, N_2). As with the single dot, the energy of each configuration is parabolic in gate voltage. However, there exist two kinds of configurations: those with $N_1 = N_2$ ("even" or "unpolarized" states) and those with $N_1 =$

$N_2 \pm 1$ ("odd" or "polarized" states).[5] The lowest-energy point of the odd states is higher in energy than that of the even states. This comes from the energy cost of interdot charging when $N_1 \neq N_2$. Without interdot coupling, either capacitive or quantum mechanical, the ground state of the system is always even, as shown in Fig. 5.3(a). The equilibrium conductance is thus a sequence of peaks which resemble the single dot peaks, shown schematically in Fig. 5.3(b). Each peak, however, corresponds to changing both N_1 and N_2 by one.

If $C_{int} \neq 0$, the energies of the odd states are reduced because the interdot charging energy is reduced. Lowering the odd parabolas in Fig. 5.3(a) means that now the odd parabolas intersect with the neighboring even ones separately, rather than at the point of degeneracy of the even parabolas. As shown in Fig. 5.3(d), the conductance peaks split and occur at positions

$$V_g = \frac{e}{C_g}\left[N + \frac{1}{2}\left(1 \pm \frac{\alpha}{1+\alpha}\right)\right] \tag{5.10}$$

The separation of the two parts of a split peak is given by

$$\Delta V_s = \frac{e}{C_g}\left(\frac{\alpha}{1+\alpha}\right) = \frac{e}{C_g}\left(\frac{C_{\text{int}}}{C_\Sigma + C_{\text{int}}}\right) \tag{5.11}$$

while successive split peaks are still centered on half-integer values of dimensionless gate voltage so that the voltage period of the split peaks, ΔV_p, is still e/C_g.

We now generalize to the case $V_{g1} \neq V_{g2}$, in order to see the entire picture of how single-electron charging occurs. A measurement of conductance as a function of both V_{g1} and V_{g2}, changing each one separately over some range, is referred to as the charging diagram of the system. This charging diagram can be determined qualitatively from the

---

[5]There also exist even more unbalanced configurations, $N_1 = N_2 \pm n$ with $n > 1$, but those are so much greater in energy than the configurations we consider that we can ignore them.

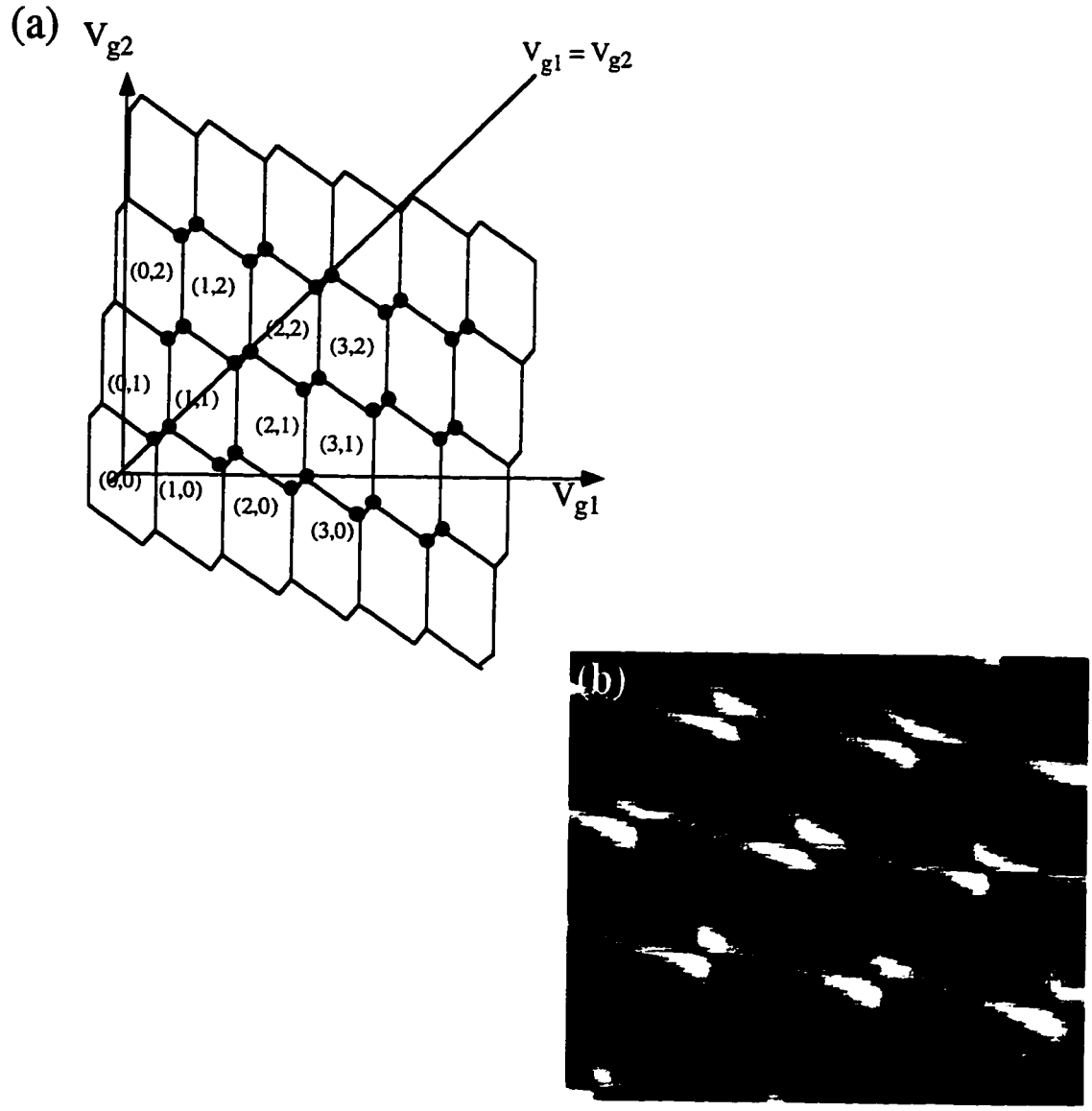

Figure 5.5 (a) Double dot charging diagram for double dot with matched gate capacitances ($C_{g1} = C_{g2}$). Each six-sided cell represents a region in which the double dot is stable with charge configuration (N_1, N_2); on the boundaries between cells, charge is free to flow between the configurations of the two cells. Current can flow through the series double dot in the circuit model when the charge state of both dots changes, namely, at the points marked with black dots; thus a measurement of conductance vs. these two gate voltages should only show peaks at these points in the absence of charge sharing between dots. For matched gate capacitances, points of current flow lie along the line $V_{g1} = V_{g2}$. (b) Measurement of double dot zero-bias conductance vs. V_{g1} and V_{g2} for g_{int} = 0.65 g_Q, from Livermore *et al.* (1996b). Conductance is represented in grayscale (white is high conductance). We see conductance along boundaries as well as at the triple points. Additional such measurements appear in Appendix A.

electrostatic energy (5.7), and is shown in Fig. 5.5. Each of the six-sided cells is a region in which the ground state is the indicated charge configuration (N_1, N_2), and hence the Coulomb blockade prevents transport through the double dot. Each cell boundary corresponds to sets of voltages (V_{g1}, V_{g2}) at which the configurations in the two cells separated by that boundary are degenerate. However, for the series double dot, the Coulomb blockade is only lifted when the number of electrons on each dot can separately change by one; thus transport in the circuit model is blocked except at the points where three cells meet ("triple points") indicated by the solid circles. Conductance observed elsewhere in the charging diagram would require inelastic cotunneling (previously discussed in 2.2.4), and would be much lower in magnitude.

We can see the conductance peaks of Fig. 5.2 described earlier in this diagram by looking along the line $V_{g1} = V_{g2}$; the triple points fall along this line, and they fall in pairs with separation determined by C_{int}. If $C_{int} = 0$, the charging diagram collapses into a set of parallelograms with each pairs of triple points collapsing to one point.

5.2.3 Effect of Interdot Tunneling

Within the circuit model, the only interdot interaction considered is capacitive. However, any interaction which reduces the energy of odd states relative to the even states by reducing the energy of frustrated charge configurations will also produce linear conductance peak splitting. This is represented schematically in Figure 5.3(e). In split-gate samples, such as those studied in this thesis, the interdot capacitance C_{int} is small and varies little over a wide range of point contact gate voltage [Stopa, 1996]. By contrast, the tunneling rate varies greatly and quantum interactions due to interdot tunneling can be substantial. In this section we will discuss the breakdown of charge quantization that results from interdot tunneling and review calculations [Matveev *et al.*, 1995, 1996a, b; Golden and Halperin, 1996a, b] of how the interaction energy E_{int} (shown in Fig. 5.3(f)) depends on the magnitude of the interdot tunneling for the case $V_{g1} = V_{g2}$.

Before describing the mathematical results of the theory, which are somewhat detailed, we summarize the essential results.[6] Matveev *et al.* [1996a, b] and Golden and Halperin [1996a, b] find, for the case $V_{g1} = V_{g2}$, that as g_{int} increases from zero to g_Q, the peak splitting ΔV_s grows from a minimum value (due to capacitive splitting) to $\Delta V_p/2$, so that at $g_{int} = g_Q$, the split peaks are no longer paired but resemble the conductance of a large composite dot, just as we observe. The splitting saturates at $\Delta V_p/2$ when g_{int} reaches g_Q.[7] Furthermore, in this model, the magnitude of the peak splitting depends only on the total interdot conductance g_{int}, not on the individual tunneling rates between individual states on the dots, and they determine a mathematical relationship between peak splitting and g_{int}. This makes for straightforward comparison to experiment.

As determined by Golden and Halperin [1996a, b] and Matveev, Glazman, and Baranger [1995; 1996a, b], the problem of two weakly tunnel-coupled dots in series can be mapped onto the problem of a single dot coupled to a single lead [Matveev, 1995] using the center-of-mass form (5.8) of the electrostatic energy of the zero-bias double dot. For the double dot system studied in these experiments, N_{tot} is always a good quantum number because coupling to the leads is weak. Thus the effect of fluctuations on N_{tot} need not be considered. The ground state of the system with N_{tot} electrons can thus be determined from the "reduced Hamiltonian" in which only the n-dependence is considered. In the next few paragraphs we will outline the Golden/Matveev approach in somewhat more detail.

A quantum mechanical treatment of the series double dot requires a Hamiltonian which includes the effects of tunneling. The Hamiltonian used by Golden and Halperin is

$$H = H_0 + H_T = K + V + H_T \tag{5.12}$$

with

---

[6]Those not interested in the details of the calculation can then skip to the beginning of the next section.
[7]This is the logical corollary to Matveev's [1995] prediction that Coulomb blockade should vanish for a single dot once the tunnel conductance from the dot to one lead reaches g_Q; once there is one mode of transport between the two dots, there is no longer interdot charging.

$$K = \sum_{i=1,2} \sum_{\sigma} \sum_{k} \varepsilon_{ik\sigma} \hat{n}_{ik\sigma}$$

the kinetic energy of the double dot system,

$$H_T = \sum_{\sigma} \sum_{k_1 k_2} \left(t_{k_1 k_2} c^{\dagger}_{2k_2\sigma} c_{1k_1\sigma} + h.c. \right)$$

the tunneling Hamiltonian, and V the electrostatic energy of the system. In this Hamiltonian i is the dot index, σ is the channel index, referring to different spins and different modes in the point contact connecting the two dots, and k is the wavevector for momentum degrees of freedom. (Both groups solve this problem for arbitrary number of channels N_{ch} in the point contact connecting the dots. We will give results for $N_{ch} = 2$ since our experiments are done with zero magnetic field and up to one mode in the point contact, so that there are two channels for the two possible spins.) For V we return to Eq. (5.8), but, as described above, only consider the n-dependent part since N_{tot} is an eigenvalue of the system. We thus use the reduced potential

$$V_{red} = \frac{e^2}{C_{\Sigma}(1+\alpha)} \left[\hat{n} - \frac{\rho}{2} \right]^2 \tag{5.13}$$

with

$$\rho \equiv \frac{C_g \left(V_{g1} - V_{g2} \right)}{e}$$

$$\hat{n} \equiv N_1 - N_2$$

Finally, we treat $H_0 \equiv K + V_{red}$ as the Hamiltonian of the unperturbed problem and H_T the perturbation, and calculate the effect of H_T. In the case $V_{g1} = V_{g2}$, peak splitting comes primarily from the reduction of energy of odd states due to H_T; a small amount of splitting

which comes from the interdot capacitance is contained in V_{red}.

Examining the unperturbed part of the Hamiltonian (5.12) with (5.13) substituted for V, we see that it is the same as the Hamiltonian for a single dot if N_{tot} is even. Thus n has integer expectation values in the unperturbed problem, which is that of a single dot with dimensionless gate voltage $\rho/2$, charging energy $e^2/C_\Sigma(1+\alpha)$, and number of electrons $\hat{n}$. We infer that the energy of the N_{tot} even, $\rho = 0$ ground state will be the same as the even double dot ground state with $V_{g1} = V_{g2}$, while the energy of the N_{tot} even, $\rho = 1$ state will be (approximately) the same as the odd double dot ground state with $V_{g1} = V_{g2}$. (This is discussed at greater length and explained more fully in Golden & Halperin, 1995.)

In the model just described, it is assumed that the eigenstate spacing is comparable to or less than the temperature, and that once substantial interdot tunneling is introduced, there will be many states which can tunnel; therefore, in evaluating the sums for K and H_T it is assumed that there are many relevant dot eigenstates k. In a sense this is the opposite approximation to the Hubbard model which assumes only a few eigenstates per dot. This leads to a family of approximations which enable evaluating the sums; the reader is referred to the papers of Golden and Halperin (and Matveev *et al.* for a slightly different discussion of the same problem) for the detail and only the results will be presented here.

Both authors calculate the interdot tunneling dependence of the fractional peak splitting f, defined as

$$f \equiv \frac{2\Delta V_s}{\Delta V_p} \tag{5.14}$$

where ΔV_s is the peak splitting in side gate voltage and ΔV_p is the split peak period, defined in Fig. 5.3. The energy reduction $E_{int} = \langle H_T \rangle$ of the odd states shown in Fig. 5.3(e) is related to f as follows [Golden and Halperin, 1996a]:

$$f_\rho(g_{int}) = \frac{4e^2}{C_\Sigma(1+\alpha)} \frac{E_{int}(g_{int},\rho)}{\rho^2} \tag{5.15}$$

Here g_{int} refers to the dimensionless interdot conductance $g_{int} \equiv G_{int} / (2e^2 / h)$.[8]

Golden and Halperin and Matveev *et al.* determine that for the fully symmetric double dot ($C_{g1} = C_{g2}$, $V_{g1} = V_{g2}$, $C_{\Sigma 1} = C_{\Sigma 2}$) in zero magnetic field, in the limit of weak interdot tunneling, the peak splitting depends on interdot conductance in the following fashion:[9]

$$f_\rho(g_{int}) = \frac{2g_{int}}{\pi^2\rho^2}\left[(1-\rho)\ln(1-\rho)+(1+\rho)\ln(1+\rho)\right] + 2c_\rho(1,2)\frac{{g_{int}}^2}{\rho^2} + 4c_\rho(2,2)\frac{{g_{int}}^2}{\rho^2} \tag{5.16}$$

in which $c_\rho(1,2)$ and $c_\rho(2,2)$ refer to coefficients calculated numerically from summing a great many Feynman diagrams.[10] To determine the energy shift between even and odd states and thus calculate the peak splitting for $V_{g1} = V_{g2}$, we evaluate (5.16) with $\rho = 1$:

$$f_{\rho=1}(g_{int}) \approx \frac{4\ln 2}{\pi^2} g_{int} + 0.2590{g_{int}}^2 \tag{5.17}$$

In the case of strong interdot tunneling, the double dot is treated as a single island containing a constriction which impedes the flow of charge from one side to the other. This approach uses a "bosonized" Hamiltonian to describe charge propagation through this constriction, assumed to be a perfect one-dimensional channel. Here the perturbing term in the Hamiltonian is the reflection amplitude of the barrier, and the unperturbed case is the single dot (i.e. the double dot with one perfectly transmitting channel connecting the two dots). Perturbation theory to second order in the reflection amplitude of the barrier for the $N_{ch} = 2$ case gives [Golden and Halperin, 1996]

---

[8]Both Golden and Halperin and Matveev *et al* abbreviate the interdot conductance as g rather than g_{int}.

[9]The first-order term was determined by both groups of authors in their 1995 publications; the higher-order results are presented in Golden and Halperin [1996].

[10]$c_\rho(x, y)$ refers to those terms x^{th} order in N_{ch} and y^{th} order in g_{int}.

$$f_\rho = 1 - \frac{\Delta_{str}(\rho) - \Delta_{str}(0)}{\left[\frac{e^2\rho^2}{4C_\Sigma(1+\alpha)}\right]} \tag{5.18}$$

The energy shift of the strong tunneling double dot from the single dot $\Delta_{str}(\rho)$ is calculated to be

$$\Delta_{str}(\rho) = \frac{4e^\gamma}{\pi^3}\left[\frac{e^2}{C_\Sigma(1+\alpha)}\right](1-g_{int})\cos^2\left(\frac{\pi\rho}{2}\right)\left[\ln\left[(1-g_{int})\cos^2\left(\frac{\pi\rho}{2}\right)\right]\right.$$

$$\left. -1 + \Phi_0 + \ln\left(\frac{8e^\gamma}{\pi^2}\right)\right] \tag{5.19}$$

with $\Phi_0 \approx 0.1703$ an term contributing to $\Delta_{str}(\rho)$ which must be evaluated numerically. Note that the fractional peak splitting f in this case is proportional to the normalized energy shift subtracted from 1, since the impedance between the dots decreases f from unity.

5.3 Double Dot Equilibrium Transport Measurements

5.3.1 Measurement of Base Temperature Conductance

We used two approaches to measure the equilibrium conductance of the double dot: measuring conductance traces while sweeping $V_{g1} = V_{g2}$, shown in Fig. 5.2, and measuring the full charging diagram by sweeping V_{g1} and V_{g2} independently in raster fashion. With matched dots, the $V_{g1} = V_{g2}$ measurement contains the most interesting features of the charging diagram, the conductance peaks of Fig. 5.2. The charging diagram for the sample used in this thesis was measured with Carol Livermore [Livermore *et al.*, 1996a and b]. The results will be summarized here briefly; a more thorough discussion is given in Appendix A. Other researchers have measured charging diagrams for other double dot samples with unmatched dots [Dixon *et al.*, 1995 and Blick *et al.*, 1996] and with dots in parallel [Hofmann *et al.*, 1995; Adourian *et al.*, 1996; Adourian, Ph.D. thesis].

A sample charging diagram measurement for intermediate g_{int} is shown in Fig. 5.5 (b). A primary finding of the charging diagram measurements is that transport occurs not only at the triple points but also along the boundaries of the charging diagram which separate cells with different N_{tot}, except for very low g_{int}. (More charging diagram measurements are shown in Appendix A.) This confirms the interpretation of peak splitting arising from charge sharing as the interdot tunneling increases, because the only way there can be conduction along these boundaries is if transport can occur when the charge state of the entire double dot system changes by one.

In Fig. 5.6 we show two measurements of fractional peak splitting f vs. g_{int}, along with the Golden and Halperin [1996b] prediction. Capacitive splitting is normalized out of the data according to a result of Golden and Halperin [1996a],

$$f = 1 - (1 + \alpha)(1 - f_{meas}) \tag{5.20}$$

where f_{meas} is the measured splitting and f is the normalized splitting due to g_{int} (as in Eqs. 5.1 ff, $\alpha = C_{int}/C_{\Sigma}$).[11] We see that agreement between measurement and theory in Fig. 5.6 is excellent. The central result (as first demonstrated by Waugh, 1995) is that the fractional splitting increases smoothly from zero with no interdot tunneling to complete ($f = 1$) with one mode in the center point contact ($g_{int} = 1$). This is the primary prediction of the theory. The agreement is best in Fig. 5.6(b) because the splittings were obtained by measuring the full charging diagram.

The primary uncertainty in the results of Fig. 5.6 comes from the determination of g_{int}. The quantity which we control directly is the voltage on the center point contact, and the corresponding conductance is determined indirectly. Although the conductance of the center point contact can be measured separately by energizing just that gate, its conductance changes when other gates are energized, partly from capacitive crosstalk between other

[11] We determine C_{int} by taking the limit of f_{meas} as g_{int} approaches zero and attributing that splitting to the interdot capacitance according to Eq. (5.9).

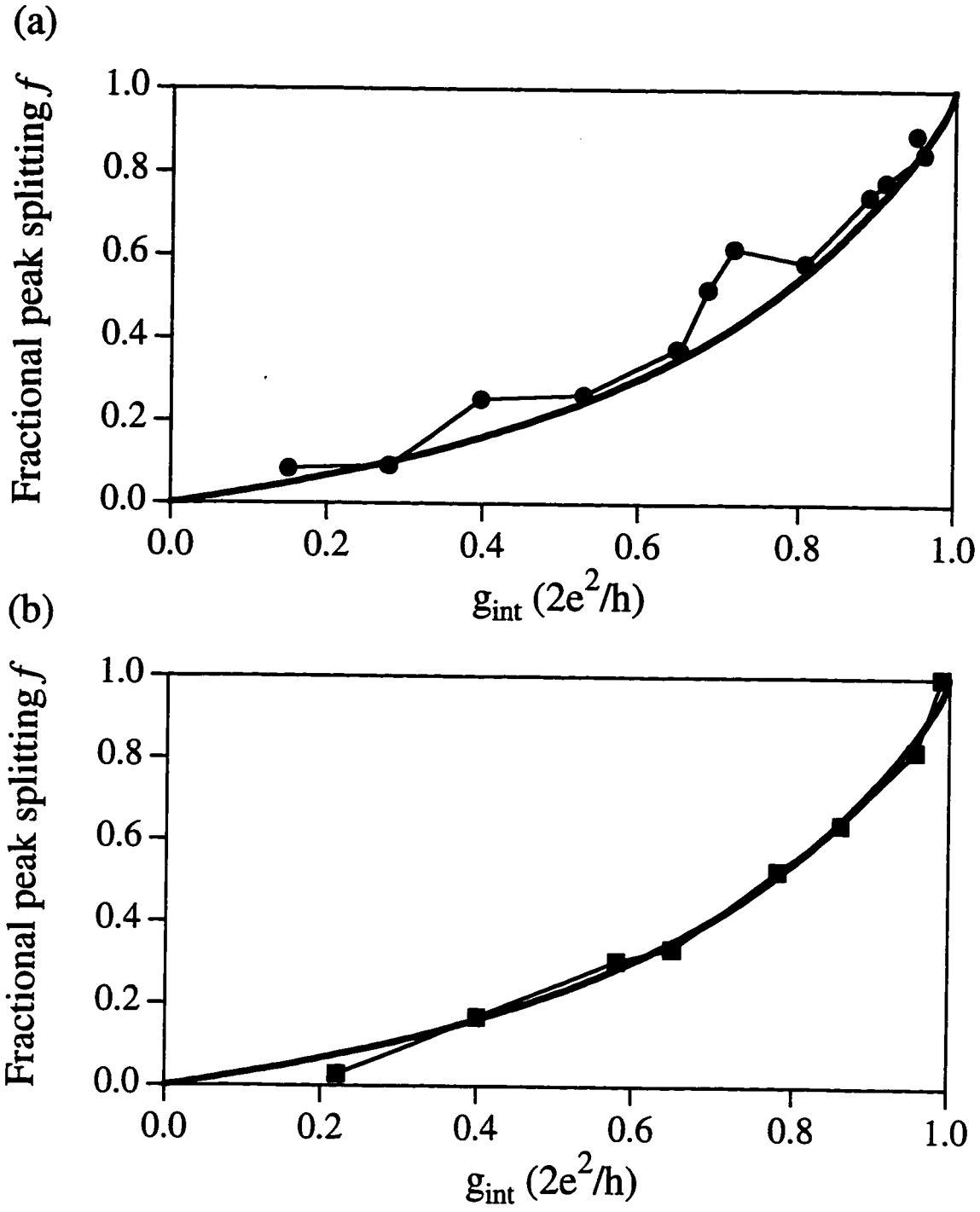

Figure 5.6 Two measurements of normalized fractional peak splitting f (solid symbols connected with lines) vs. interdot conductance g_{int}, compared to theory from Golden and Halperin, 1996b (solid line). (a) Data of Fig. 5.2 and similar measurements, used to calibrate g_{int} for the Coulomb gap measurements of section 5.4.2. (b) Data obtained from measuring the charging diagram (as discussed in Appendix A; Livermore *et al.*, 1996b) with slightly different gate voltages.

gates and the gas beneath the center point contact, and partly from ballistic transport effects such as collimation effects from the end point contacts [Beenakker and van Houten, 1989].

We determine g_{int} as follows: The primary effect of other gates on the center point contact conductance G_{qpc} as a function of point contact gate voltage V_{qpc} is to shift the entire characteristic to less negative values of V_{qpc} (as discussed in section 4.3.1). We thus assume that $G_{qpc}(V_{qpc})$ within the fully formed double dot can be found by measuring G_{qpc} with the side gate voltages V_{g1}, V_{g2}, and V_{g3} set to values used in the double dot measurements and with the end point contacts energized but transmitting many modes, and then simply shifting that measurement in V_{qpc} by some small fixed amount. This procedure is shown schematically in Figs. 5.7 (a) and (b) for the data of Figs. 5.6 (a) and (b) respectively. The solid line is the measured $G_{qpc}(V_{qpc})$ and the solid symbols are measured values of fractional peak splitting at particular values of V_{qpc}. The dashed line is the shifted G_{qpc} measurement from which g_{int} is determined; the shift in (a) is 5 mV and in (b) is 3 mV. The shifts were chosen to give the best agreement with the theory of Fig. 5.6.

An intriguing observation is how closely the splitting f as a function of $Vqpc$ mirrors $G_{qpc}(V_{qpc})$. Figure 5.7 (c) shows the measured point contact conductance from (b) shifted further to best overlay the peak splitting data; agreement is remarkable. This makes it tempting to determine g_{int} simply by overlaying the point contact conductance and the peak splitting data. However, the shifts required to do this are much larger (15 mV for the data of (c)). We expect the shift should be very small since the only difference between the center point contact in the double dot experiments and in the measurements shown in Fig. 5.7 is that in the double dot experiments, somewhat more negative voltages are applied to the outer point contacts.

5.3.2 Measured Temperature Dependence of Conductance Peaks

We measured the temperature evolution of split peaks for a variety of interdot tunneling rates. Figure 5.8 shows an illustrative subset of the data (each panel of the figure

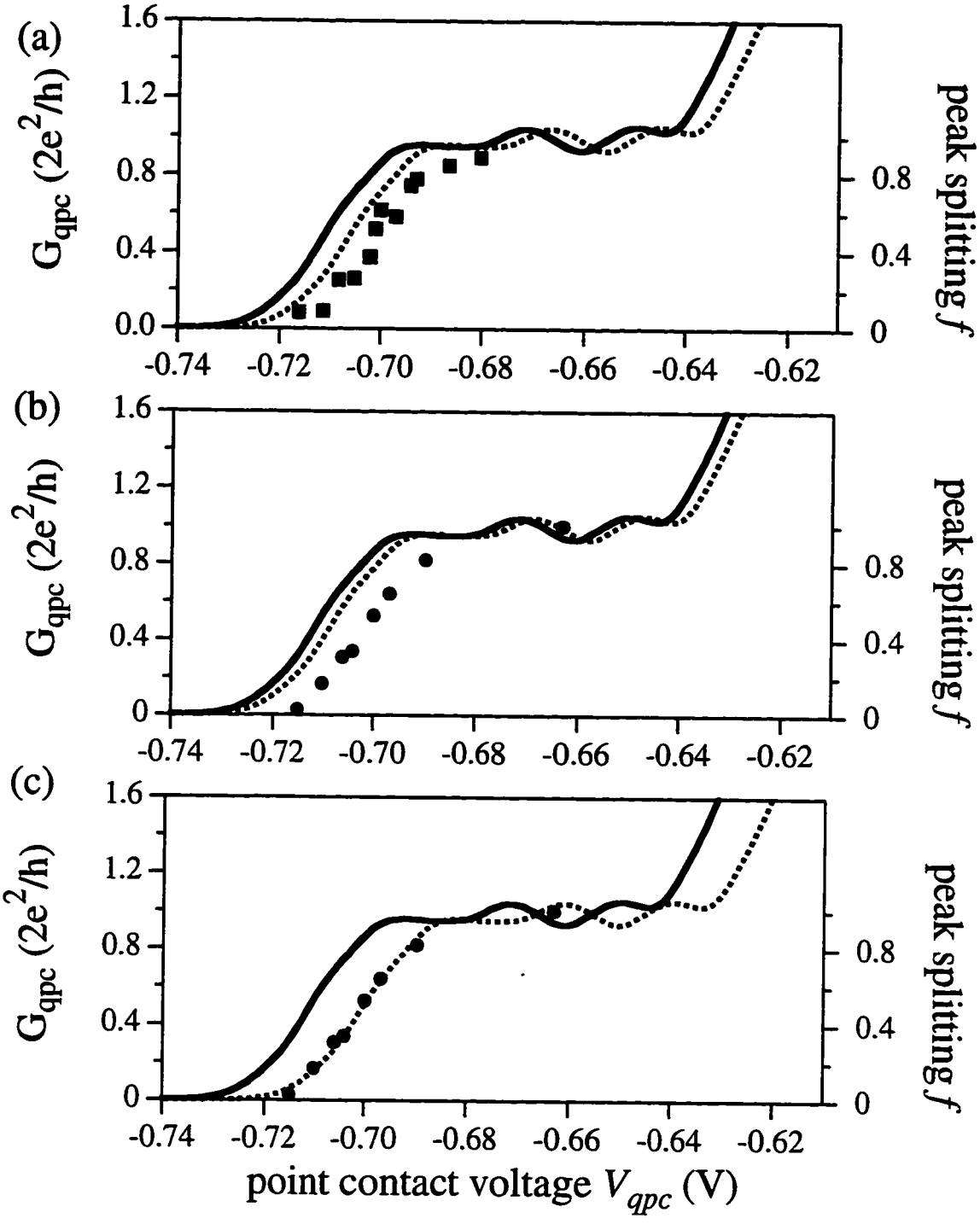

Figure 5.7 (a), (b) Determining center point contact conductance from fractional peak splitting for data shown in Fig. 5.6 (a) and (b) respectively. Solid line, measured center point contact conductance with two outer point contacts energized just to depletion and plungers energized to voltages used in experiments. Symbols, measured fractional peak splitting vs. center point contact gate voltage. Dotted line, center point contact shifted in gate voltage for best fit to $f(g_{int})$ as described in text (shift is 5 mV for (a) and 3 mV for (b)). (c) Overlay of point contact conductance on splitting data from (b); an additional 8 mV shift is required.

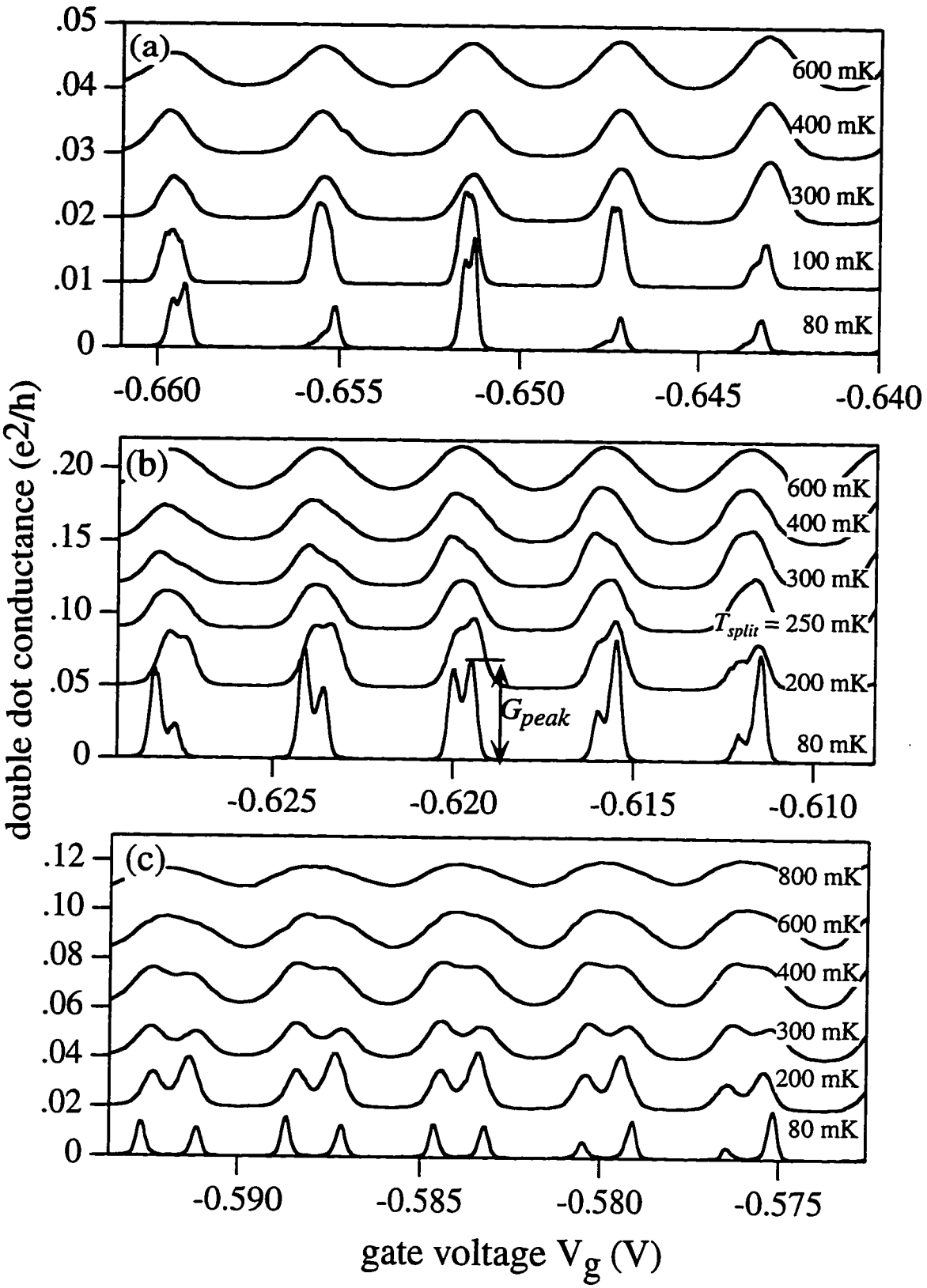

Figure 5.8 (a)-(c) Double dot conductance peaks shown at a series of temperatures for three different g_{int} = (a) 0.15, (b) 0.49, and (c) 0.78. Traces are vertically offset for clarity and horizontally offset to align peaks as discussed in the text. Temperature at which splitting disappears, T_{split}, is illustrated in (b) as is the peak height G_{peak}.

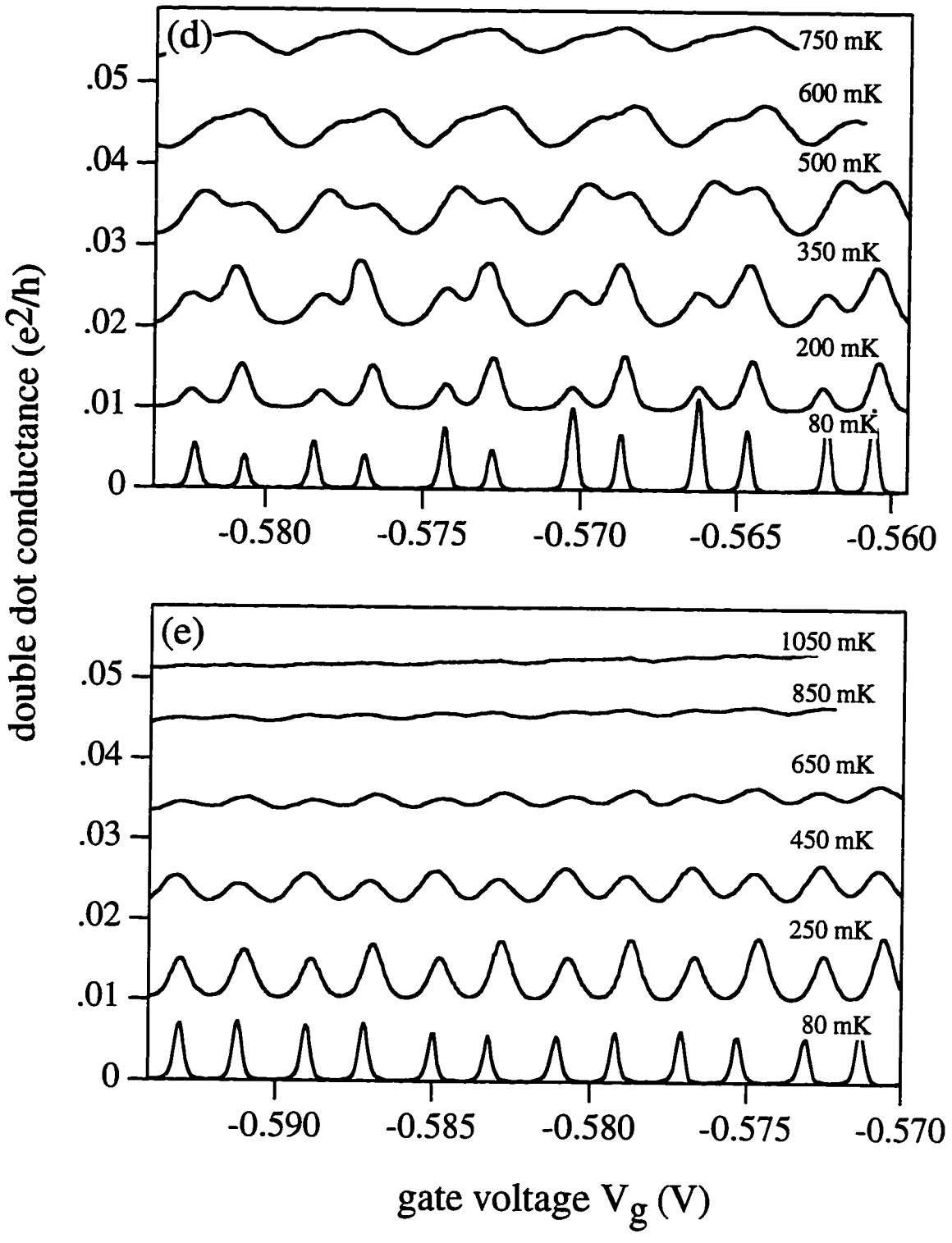

Figure 5.8 (d)-(e) Double dot conductance peaks measured at a series of temperatures for g_{int} = (d) 0.92 and (e) 0.99. Traces are vertically offset for clarity and horizontally offset to align peaks as discussed in the text. Only a subset of the temperatures for which data were taken are shown.

contains traces measured with the same g_{int}; traces taken at different temperatures are vertically offset for clarity, with the baseline of each trace roughly zero, and shifted by a fraction of a period in gate voltage to align the peaks). We see that as temperature increases, the peaks broaden, filling in the split regions, and become shorter, just as with the single dot peaks in the weak tunneling regime (section 2.2.4). The temperature at which the splitting disappears and the split peak becomes one broad peak increases as the splitting increases. Panel (e), which shows peaks with $f = 0.97$, shows that this nearly full splitting does not become obscured until 1050 mK, at which point any modulation of the conductance is barely visible.

As shown in Fig. 5.8(b), we define T_{split} to be the temperature at which the splitting just disappears (very slight splitting is visible for T just below T_{split}) In Table 5.1, we compare T_{split} to the interaction energy E_{int} determined from f using Eq. (5.15), for each g_{int}. We see that T_{split} follows E_{int}; with the best agreement for smaller g_{int}.

In Chapter 2, the shape and width of the single dot conductance peaks indicated that tunneling was taking place into a well-isolated dot. The simplest model for the shapes of the double dot peaks shown in Fig. 5.8 is to consider the double dot with interdot tunneling as a single object into which electrons can tunnel. We then expect that split peaks should

Table 5.1: Interaction Energy E_{int} and Temperature Dependence

g_{int}	E_{int}	T_{split}
0.24	103 mK	150 mK
0.49	284 mK	250 mK
0.78	633 mK	600 mK
0.92	1 K	0.7 K
0.99	1.27 K	1.05 K

simply be two peaks, each with the same shape as a single dot peak, but falling very close together. Thus we can define a "double peak" which is two adjacent peaks with shape and width given by Eq. (2.22) or (2.25) (depending on the relative size of the temperature and the level spacing) and with positions separated by the peak splitting ΔV_S. If an electron tunneling into the double dot instead tunneled first into one dot and then the other, we would expect this to change the shape of the peaks. The fit corresponding to Eq. (2.22) is

$$G = G_{01}\cosh^{-2}\left(\frac{V_g - V_{g01}}{w(T)}\right) + G_{02}\cosh^{-2}\left(\frac{V_g - V_{g02}}{w(T)}\right) \tag{5.21}$$

with $$w(T) \equiv \frac{2.5 C_\Sigma k_B T}{e C_g} \tag{5.22}$$

The fit corresponding to Eq. (2.25) is identical except that the coefficient in $w(T)$ is 2 instead of 2.5. The parameters in fitting to (5.21) are G_{01} and G_{02} (the heights of the two peaks), V_{g01} and V_{g02} (the V_g positions of the two peaks), and $w(T)$, the peak width.[12]

Fits to the double peak shape (5.21) were performed for all temperatures and splittings measured; representative data and fits (g_{int} = 0.78, T = 100 mK, 250 mK, and 400 mK) are shown on a logarithmic scale in Fig. 5.9. There is excellent agreement between the measured shape and the fit for $T < T_{split}$; for $T > T_{split}$ such results are not shown because the fits become very poor and frequently fail to converge (presumably because with five parameters it is possible to come up with any of a variety of possibilities which look like a single somewhat distorted peak).

The temperature dependence of the widths determined from these fits is exactly as expected. Figure 5.10 shows the widths as a function of temperature for g_{int} = 0.78, 0.92, and 0.99 (there were too few temperature points for the two small splittings); in all cases the widths are linear in temperature with essentially the same slope. The slopes of the best

[12]Fitting with six parameters, in which each of the paired peaks were allowed to have different widths, did not give appreciably different results for the widths of the paired peaks.

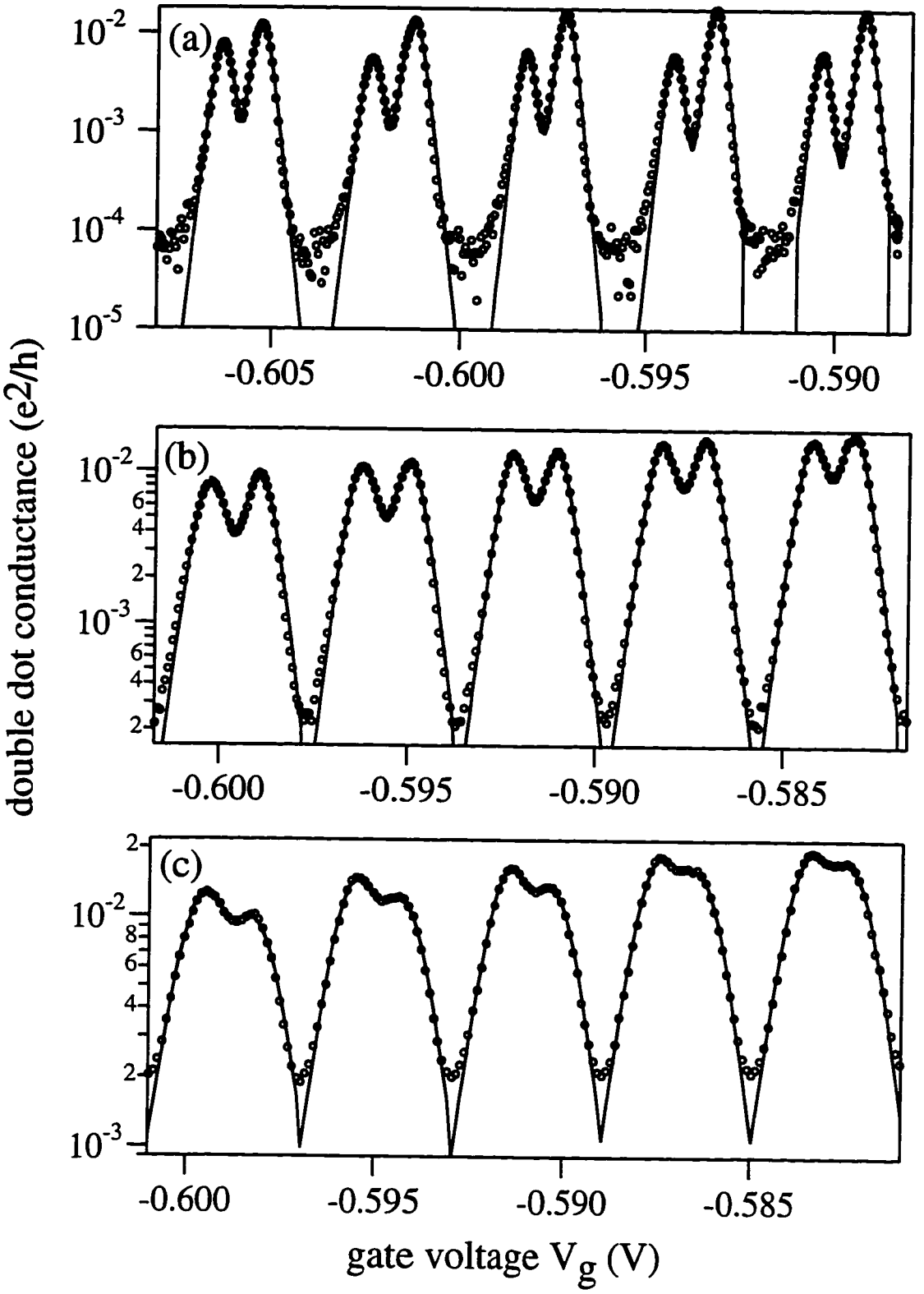

Figure 5.9 Double dot conductance (logarithmic scale) for $g_{int} = 0.78$, fit to the thermally broadened double peak shape (Eq. (5.21)) for temperatures (a) 100 mK, (b) 250 mK, and (c) 400 mK. Open symbols are data points; line is the fit.

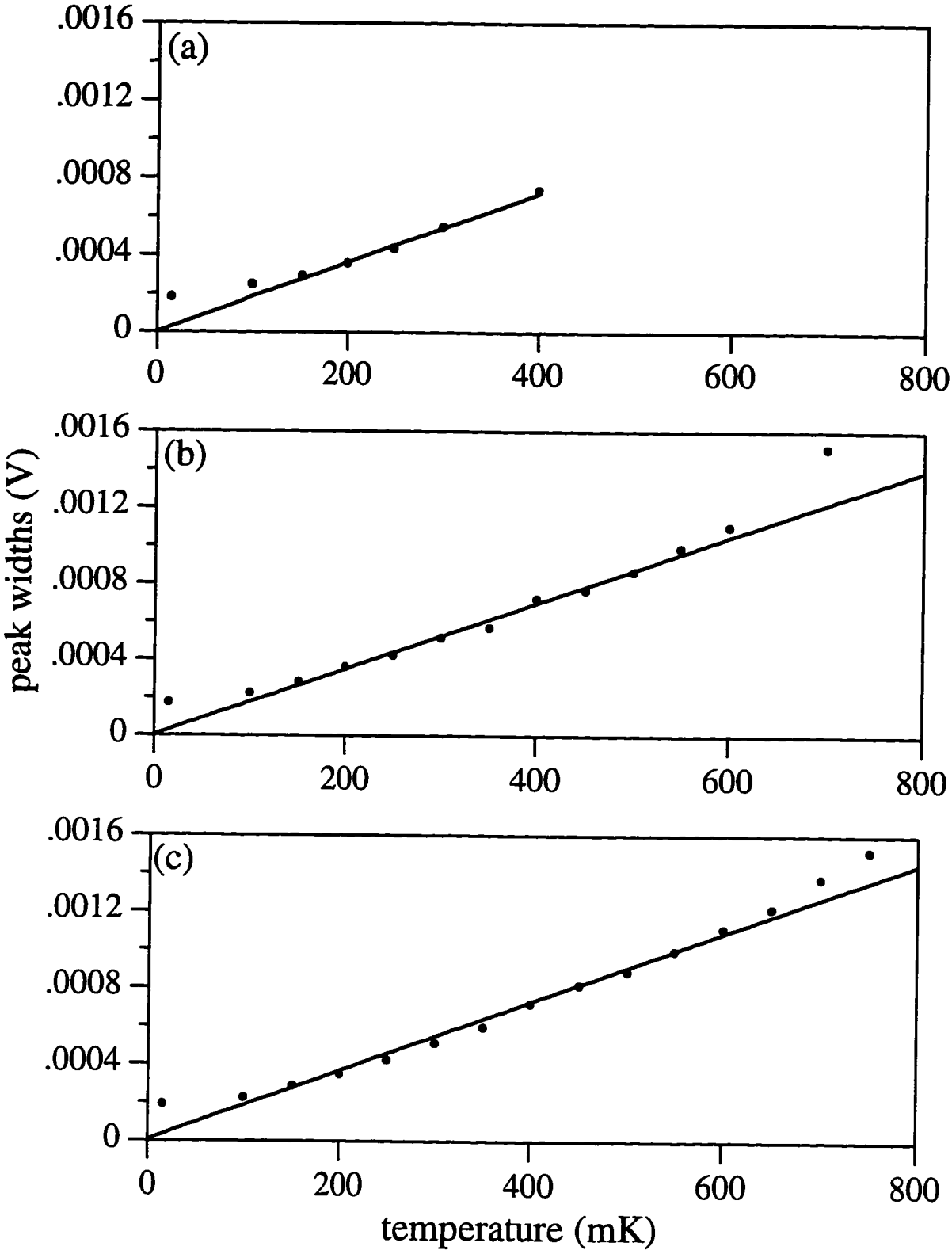

Figure 5.10 Double dot conductance peak widths $w(T)$ vs temperature obtained from fits like those in Fig. 5.9 for g_{int} = (a) 0.78, (b) 0.92, and (c) 0.99. Solid circles represent data, lines the best fit to $w(T)$ as described in the text.

fit lines in Fig. 5.10 (a) to (c) are 1.8 x 10^{-3} mV/mK, 1.7 x 10^{-3} mV/mK, and 1.8 x 10^{-3} mV/mK respectively, in very good agreement with the expected value of 1.9 x 10^{-3} mV/mK for (5.22) (assuming that many levels are involved in transport). The fits to $w(T)$ were performed with the points from 150 mK to the highest temperature for which good peak shape fits were obtained; the lowest temperature widths were omitted since they probably reflect transport through a few but not many levels, which would most likely have a somewhat different temperature dependence. In Fig. 5.10 (b) and (c) the highest temperature widths are somewhat larger than the fit predicts; this reflects the fits becoming poorer due to merging peaks.

We also examined the temperature dependence of the heights of the peaks G_{peak} (defined in Fig. 5.8 (b)), shown on a logarithmic scale in Fig. 5.11. There is no clear trend of G_{peak} with temperature except that the heights are greatest at base temperature and initially drop off more or less sharply as T increases. Theories discussed in the next section predict power-law behavior for the peak heights for moderate or strong tunneling; it is possible that the higher temperature peak heights measured for g_{int} = 0.78 and 0.99 follow power-law behavior. However, the temperature range of the measurement is too small to draw definitive conclusions. We do not expect the theories of the next section to apply for T < δE, the level spacing for a single dot of the double dot, because the theories assume continuous level spacing. Since δE ~ 400 mK and $e^2/2C_\Sigma$ ~ 1.35 K, there is no more than a fourfold range in temperature to explore.

5.3.3. Double Dot Conductance Peak Shape and Amplitude: Theory

The peak heights and shapes have been studied theoretically by Matveev *et al.* (1995; 1996a, b); a few relevant results will be presented here. The discussion divides naturally into the cases of weak, intermediate, and strong tunneling. The primary result is that the peak heights have a power law dependence on temperature in all cases except for the fully symmetric double dot with very weak tunneling; either slight asymmetry in the

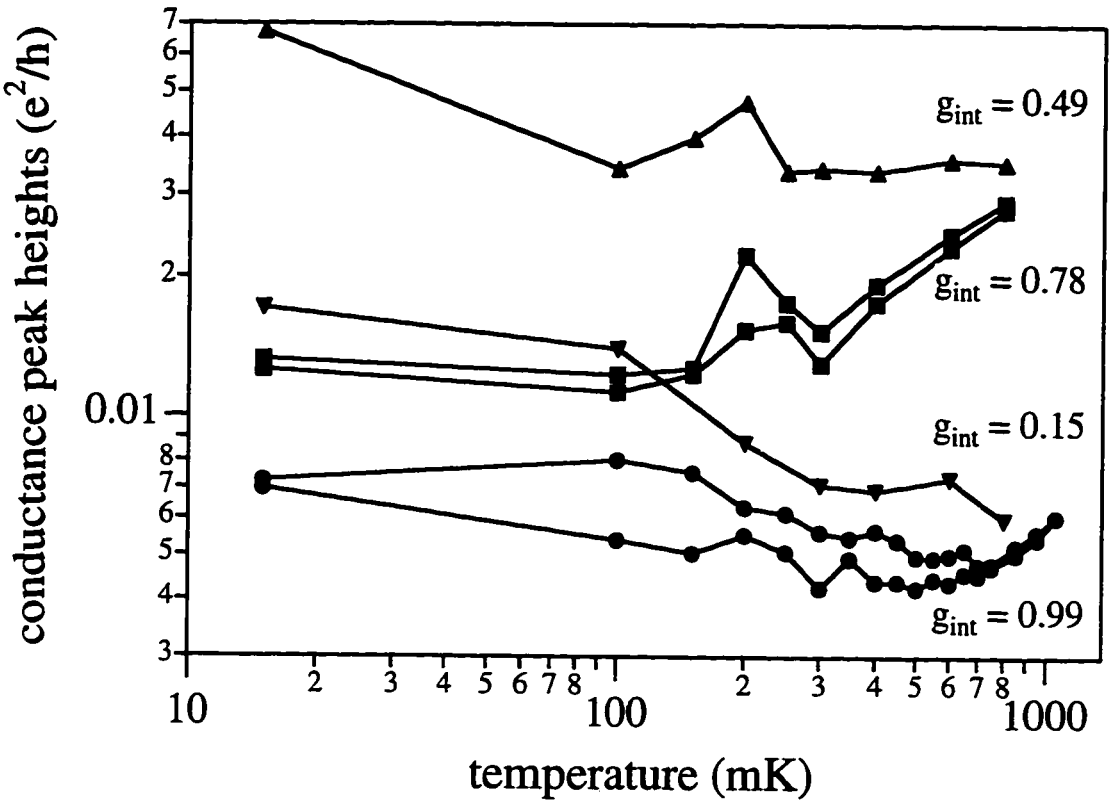

Figure 5.11 Double dot conductance peak heights G_{peak} from data of Fig. 5.8 vs temperature on a logarithmic scale for g_{int} = 0.15 (triangles), 0.49 (inverted triangles), 0.78 (squares), and 0.99 (solid circles). Pairs of data points with the same symbol represent the heights of the two halves of a split peak.

weak-tunneling case, or increased tunneling, leads to this power law behavior. (For a perfectly symmetric double dot with weak tunneling, the peak heights are temperature-independent.) The power law exponent varies from case to case. In the case of weak tunneling with asymmetry, the peak height is predicted to be proportional to T^2:

$$G_{peak}(g_{int} \to 0) \propto \frac{g_{\mathrm{int}} G_R}{6}\left(\frac{T}{\Delta}\right)^2. \tag{5.23}$$

The parameter Δ reflects the charging energy E_C and the asymmetry of the capacitances,

$$\Delta \equiv 2E_C\left(\frac{C_{g1} - C_{g2}}{C_{g1}}\right). \tag{5.24}$$

In the case of strong tunneling, the peak conductance is a power law with a variable exponent:

$$G_{peak}(g_{int} \to 1) \propto T^{\eta} \tag{5.25}$$

where the exponent η depends on the geometry of the system,

$$\eta \equiv \frac{(1 \pm |\lambda|)^2}{4} \quad \text{with} \quad \lambda \equiv \frac{C_{\Sigma 1} - C_{\Sigma 2}}{C_{\Sigma 1} + C_{\Sigma 2} - 2C_{int}}. \tag{5.26}$$

Finally, although the intermediate strength tunneling case is not as straightforward to solve as the two limits, Matveev *et al.* determine that in the case of nearly symmetric geometries ($\lambda << 1$) the power-law temperature dependence of the peaks persists, this time with exponent $\eta = 5/4$.

Peak shapes are also presented in Matveev *et al.* (1996b), and the reader is referred to that work for further details. For weak interdot tunneling, the predicted shape is the double peak shape; with strong interdot tunneling, the peak shape is a more complicated

function[13] but numerically does not differ substantially from the double peak shape. Their predicted shape would be difficult to distinguish from the double peak shape unless all the parameters involved were known very precisely [Matveev, personal communication]. Since there are many parameters involved, none of which are known as precisely as would need to be, in this thesis we only consider the double peak shape. As discussed in the previous section, although we examine the peak heights for power law behavior, the temperature range available is too small to draw definitive conclusions.

5.3.4 "Mismatched" Double Dot Transport

Although this thesis focuses on studying the properties of two identical (or nearly so) dots in series, there are interesting phenomena to be observed in systems of two dots which are different; also, because our samples are not perfect, we see the effects of slight differences between the dots. Several groups have studied double dots in which the individual dots are not identical, both theoretically [Ruzin *et al.*, 1992] and experimentally [Waugh *et al.*, 1995; Kemerink and Molenkamp, 1994], and observe stochastic Coulomb blockade. (For these studies, interdot coupling is kept weak.) For a thorough discussion of intentional studies of stochastic Coulomb blockade, the reader is referred to the Ph.D. thesis of Fred Waugh [1994] and the references mentioned previously. Stochastic Coulomb blockade with negligible interdot tunneling is like a doubly periodic beating process; if there are two different size dots or two different capacitances by which gate voltages are coupled to the dots, without charge sharing between the dots, each dot must cycle through the Coulomb blockade with a different gate voltage period, and since the overall blockade is only lifted if it is lifted for each dot, the conductance peaks are extremely sparse.

For identical dots with slightly mismatched gate capacitances, the axes of the charging diagram shown in Fig. 5.5 are multiplied by different constants; the period of the diagram as projected along the V_{gi} axis is proportional to C_{gi}, so if $C_{g1} \neq C_{g2}$, the period

[13]This function involves gamma functions of imaginary arguments.

will be different along the two axes. Figure 5.12 shows such a charging diagram. As a result, we see that uniformly (and minimally) split peaks lie along the line $V_{g1} = C_{g2}V_{g2}/C_{g1}$ rather than $V_{g1} = V_{g2}$. Without interdot tunneling, we would expect conductance peaks to be sparse as $V_{g1} = V_{g2}$ is swept; however, as shown in the charging diagram measurements in Fig. 5.5(b) and Appendix A, in the presence of moderate to strong interdot tunneling, conductance occurs along the boundaries of the diagram, not just the triple points, so the pattern of measured conductance will simply be the sequence of intersections between the line $V_{g1} = V_{g2}$ and the diagram boundaries.

If we measure linear conductance with $V_{g1} = V_{g2}$, we obtain a modulated pattern of split peaks as in Fig. 5.13. As we expect from looking at the charging diagram (Fig. 5.12), the peaks go from widely to narrowly split and then back to widely split. Furthermore, Matveev *et al.* [1996b] have simulated the conductance for a series double dot with a small asymmetry between the dots (and small interdot conductance), and find that the more widely split peaks should be shorter while the more narrowly split peaks are taller, as in our data. This measurement thus confirms that charge sharing allows current to flow whenever N_{tot} can change. However, in most experiments, we minimize this sort of modulation by choosing the side gate voltages carefully, so that we measure between four and ten split peaks in a row with essentially the same splitting and comparable height.[14,15]

5.4 Double Dot Nonequilibrium Transport

As with the single dot (section 2.3), we study the nonequilibrium properties of the double dot in order to learn about the charging energy and the excitations of the system.

---

[14]Peak height is a less reliable way to determine how well matched the dots are, since the heights vary for other reasons as discussed in Ch. 2.

[15]Choosing the side gate voltage ranges is referred to in the Westervelt group as "tuning" the sample, and it is a lengthy and tedious process even for a double dot (lasting from two to four days for a new sample depending on the sample, and requiring repetition upon thermal cycling, though usually previous thermal cycles offer clues). It becomes even more complicated for more dots, and presumably if samples with four or more dots are to be studied, the person studying them will have to figure out some way to use feedback to "auto-tune" the device (or otherwise will require both infinite patience and inordinate good fortune).

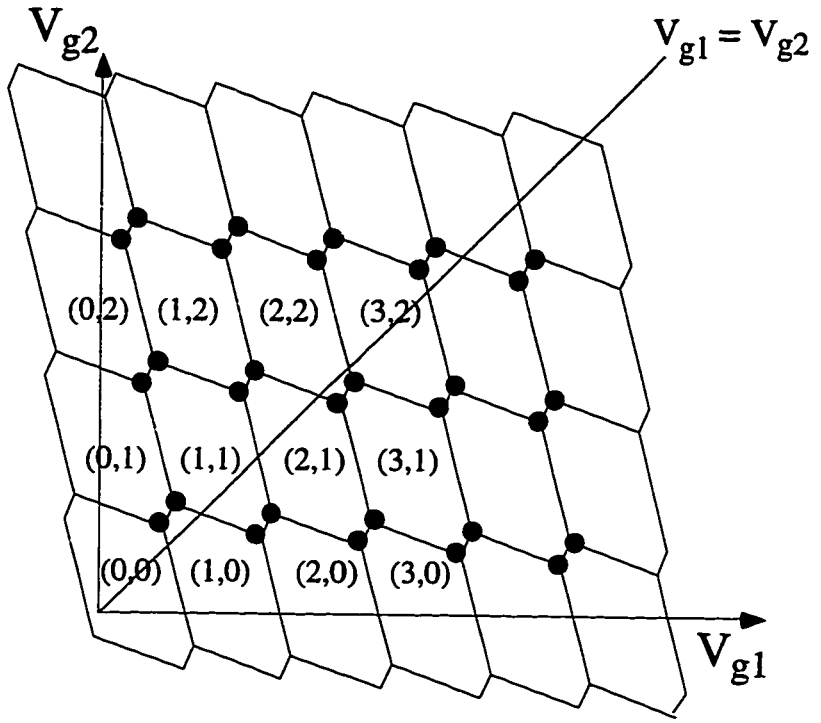

Figure 5.12 Double dot charging diagram for double dot with slightly mismatched gate capacitances ($C_{g1} \neq C_{g2}$). Note that triple points no longer lie along the line $V_{g1} = V_{g2}$. In the circuit model, one would expect only very occasional conductance peaks, while interdot tunneling allows conductance on cell boundaries across which N_{tot} changes.

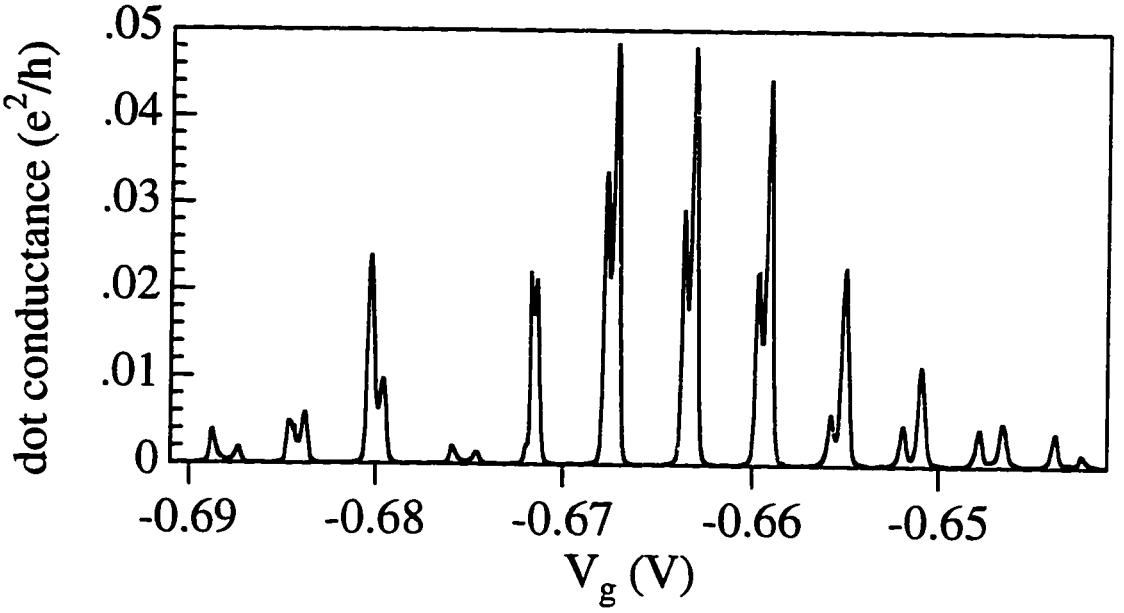

Figure 5.13 Double dot conductance peaks with slightly mismatched dots; a pronounced beating pattern, consistent with predictions of Matveev *et al.* [1996b], rather than the sparse "stochastic Coulomb blockade" expected from the circuit model, is observed.

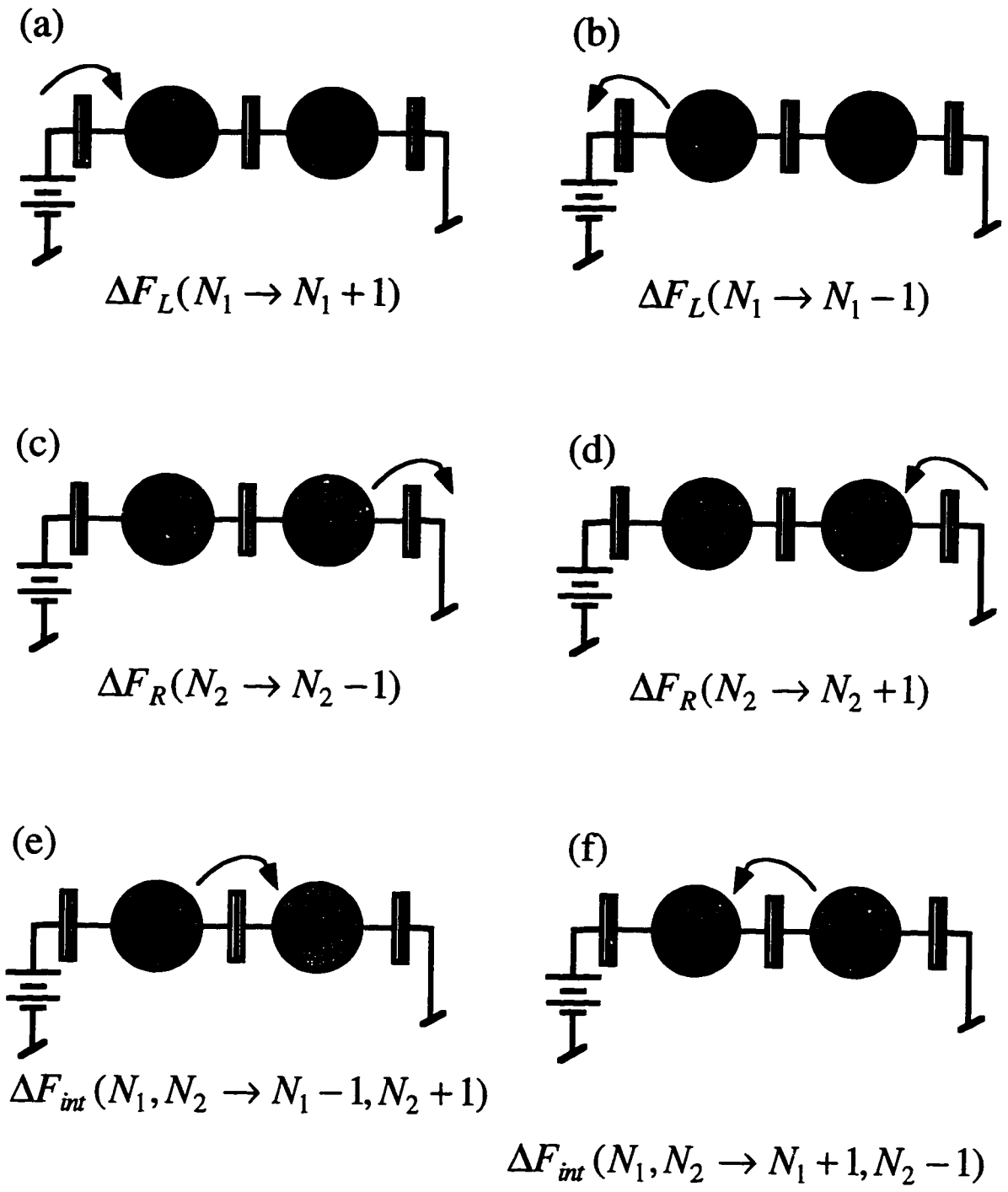

Figure 5.14 Tunneling events corresponding to the circuit model free energy changes given in Eqs. 5.27. Arrows represent tunneling, with one electron moving from the tail of the arrow to the head. In all cases the starting charge configuration of the double dot is N_1 electrons on the left dot and N_2 on the right dot. For clarity, the only circuit elemnts shown are the tunnel junctions and the battery supplying the bias voltage, but the full equivalent circuit of Figure 5.4 is used to calculate the free energy changes.

Again we will measure the differential conductance G_{dot} as a function of both V_{ds} and V_g; we will examine the dependence of the Coulomb gap ΔV_{gap} on interdot tunneling to probe the interaction energy E_{int}.

5.4.1 Finite-Bias Differential Conductance (Capacitive Circuit Model)

To study the double dot nonlinear conductance as a function of V_{ds} and V_g, we begin by determining the circuit model prediction, assuming $V_{g1} = V_{g2} = V_g$. We use the double dot free energy Eq. (5.4) to determine the regions in (V_{ds}, V_g) space in which the Coulomb blockade applies. The calculation is more involved than for the single dot because there are six ways tunneling can occur from a given starting charge configuration, shown in Fig. 5.14. Upon calculating the necessary free energies for all possible changes of electronic configuration of the double island system, we determine that, as with the single dot, after the first tunneling event happens, all subsequent tunneling events needed to transport charge all the way through the system are energetically favored.[16] Thus, determining $G_{dot}(V_{ds}, V_g)$ is a matter of determining the conditions under which any of the first tunneling events can happen.

Using the same approach as that used to obtain Eqs. (2.28), we find that the free energy changes associated with the six tunneling events of Fig. 5.14 are

$$\Delta F_L(N_1 \to N_1 + 1) = \frac{e^2}{C_\Sigma(1-\alpha^2)}\left[\frac{1}{2} + (N_1 + \alpha N_2) - \left(\frac{C_L V_{ds}}{e} + \frac{C_g V_g(1+\alpha)}{e}\right)\right] + eV_{ds}$$

$$\Delta F_L(N_1 \to N_1 - 1) = \frac{e^2}{C_\Sigma(1-\alpha^2)}\left[\frac{1}{2} - (N_1 + \alpha N_2) + \left(\frac{C_L V_{ds}}{e} + \frac{C_g V_g(1+\alpha)}{e}\right)\right] - eV_{ds}$$

$$\Delta F_R(N_2 \to N_2 - 1) = \frac{e^2}{C_\Sigma(1-\alpha^2)}\left[\frac{1}{2} - (\alpha N_1 + N_2) + \left(\frac{\alpha C_L V_{ds}}{e} + \frac{C_g V_g(1+\alpha)}{e}\right)\right]$$

[16]These calculations are not presented in this thesis because they are routine and tedious, but they can be obtained from the author if necessary.

$$\Delta F_R(N_2 \to N_2+1) = \frac{e^2}{C_\Sigma(1-\alpha^2)}\left[\frac{1}{2}+(\alpha N_1+N_2)-\left(\frac{\alpha C_L V_{ds}}{e}+\frac{C_g V_g(1+\alpha)}{e}\right)\right]$$

$$\Delta F_{\text{int}}\left((N_1,N_2)\to(N_1-1,N_2+1)\right) = \frac{e^2}{C_\Sigma(1+\alpha)}\left[1-(N_1-N_2)+\frac{C_L V_{ds}}{e}\right]$$

$$\Delta F_{\text{int}}\left((N_1,N_2)\to(N_1+1,N_2-1)\right) = \frac{e^2}{C_\Sigma(1+\alpha)}\left[1+(N_1-N_2)+\frac{C_L V_{ds}}{e}\right]$$

(5.27a-f)

We then note that there are two cases to consider for the starting electron configuration, $N_1 = N_2$ and $N_1 = N_2 \pm 1$. Thus, in order to calculate the double dot nonlinear conductance phase diagram analogous to Fig. 2.4, we need to work out the region of stability corresponding to each starting configuration.

Figure 5.15 shows the set of parallelograms of Coulomb blockade (the "Coulomb blockade characteristic") for the double dot for small C_{int}. In the following paragraphs we will calculate this diagram. We expect that in the limit of $C_{int} = 0$, the Coulomb blockade characteristic will consist of a series of parallelograms similar to the single-dot ones, in which the ground state has $N_1 = N_2$, and that as C_{int} increases from zero, some sort of split structure with ground state $N_1 = N_2 \pm 1$ will develop between the parallelograms. Consider first the behavior of the $N_1 = N_2$ ground state. Examining the zero-bias calculations, we see that the even ground state exists over a range of dimensionless gate voltage ($x = C_g V_g/e$)

$$N-\frac{1}{2(1+\alpha)} < x < N+\frac{1}{2(1+\alpha)} \tag{5.28}$$

If we substitute $N_1 = N_2 = N$ into Equations (5.27) and change to dimensionless variables (x, y) with $y = C_\Sigma V_{ds}/e$, we obtain the following conditions for stability of the (N, N)

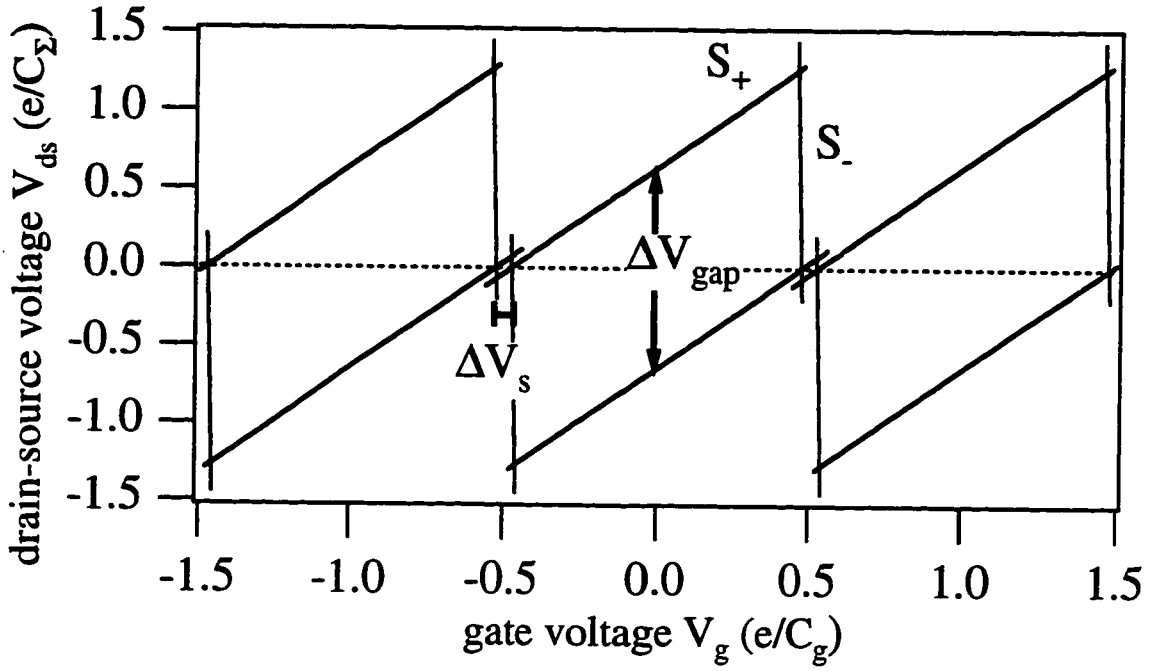

Figure 5.15 Thresholds for double dot conductance as a function of V_{ds} and V_g with the origin of V_g set to zero, calculated using the circuit model and the capacitances of our double dot samples. Parallelograms enclosed by threshold lines are areas of Coulomb blockade; current is allowed to flow in area outside parallelograms. The dotted line indicates $V_{ds} = 0$. The Coulomb gap as defined in this thesis, ΔV_{gap}, and the raw peak splitting ΔV_s are marked. The positive slope S_+ and the negative slope S_- are indicated by labeling the thresholds which have those slopes. This plot is also known as the "Coulomb blockade characteristic."

ground state:

$$y > \left(\frac{1+\alpha}{1-\alpha^2-\gamma}\right)\left[x-\left(N+\frac{1}{2(1+\alpha)}\right)\right] \tag{5.29a}$$

$$y < \left(\frac{1+\alpha}{1-\alpha^2-\gamma}\right)\left[x-\left(N-\frac{1}{2(1+\alpha)}\right)\right] \tag{5.29b}$$

$$y > -\left(\frac{1+\alpha}{\alpha\gamma}\right)\left[x-\left(N-\frac{1}{2(1+\alpha)}\right)\right] \tag{5.29c}$$

$$y < -\left(\frac{1+\alpha}{\alpha\gamma}\right)\left[x-\left(N+\frac{1}{2(1+\alpha)}\right)\right] \tag{5.29d}$$

with $\alpha \equiv C_{int} / C_\Sigma$ and $\gamma \equiv C_L / C_\Sigma$ as previously defined. These four conditions, with Eq. 5.28, outline the large parallelograms in (V_{ds}, V_g) space shown in Fig. 5.15.[17]

As with the single dot Coulomb blockade characteristic, the size and slopes of the sides of the parallelograms is determined by the capacitances of the system. Unfortunately, for the double dot, there is no simple relationship between the size of the Coulomb blockade characteristic and the charging energy. We thus parametrize the double dot Coulomb blockade in the following fashion: On looking at Fig. 5.15, we see that the height of the major parallelograms is constant over a wide range of gate voltage, decreasing only at the ends. This height corresponds to the region of Coulomb blockade in a single I-V characteristic measured at constant gate voltage, and is often referred to as the "Coulomb gap." In the electrostatic model, this gap is determined entirely by the capacitances of the system. For the purposes of this thesis, we define ΔV_{gap} to be the quantity shown in Fig. 5.15 – the height between parallel sides of the parallelograms in the region where that

[17]The conditions corresponding to (5.27e, f) are always satisfied when these four conditions are satisfied for the even ground state, so they do not act as constraints.

height is constant. We can calculate the gap from the stability conditions (5.29a) to (d) by noting that for $x = N$, the gap is positioned symmetrically about $y = 0$, and thus

$$\Delta V_{gap} = 2\left|V_{thresh}(x = N)\right| \tag{5.30}$$

where V_{thresh} refers to the threshold voltage for current flow, the V_{ds} position of the Coulomb blockade boundary. The absolute value signs are needed since there is both a negative V_{ds} and a positive V_{ds} boundary. Using (5.29) we determine that for the purely capacitive model,

$$\Delta V_{gap} = \frac{e}{C_\Sigma\left(1-\alpha^2-\gamma\right)} \tag{5.31}$$

Likewise the slopes S_+ and S_- indicated in Fig. 5.15 can be determined from the conditions (5.29). We find

$$S_+ = \frac{C_g\left(C_\Sigma + C_{int}\right)}{C_\Sigma{}^2 - C_{int}{}^2 - C_\Sigma C_L} \tag{5.32}$$

$$S_- = \frac{C_g\left(C_\Sigma + C_{int}\right)}{C_{int}C_L} \tag{5.33}$$

What about the regions between the large parallelograms in Fig. 5.15? In those regions the ground state is polarized, with $N_1 = N_2 \pm 1$. These regions correspond to x values

$$N + \frac{1}{2(1+\alpha)} < x < N + 1 - \frac{1}{2(1+\alpha)} \tag{5.34}$$

Here the energetics of the transport process are a little more complicated, since at zero bias the states $(N, N + 1)$ and $(N + 1, N)$ are degenerate. We must consider positive and negative bias separately, because finite bias lifts this degeneracy.

Examining Eqs. (5.27e) and (f), we see that positive bias will immediately cause the ($N + 1$, N) state to convert to the (N, $N + 1$) state, and likewise negative bias will convert the (N, $N + 1$) state to the ($N + 1$, N) state. So consider transport from the ($N + 1$, N) state with positive applied bias voltage. There are two possible transport pathways for positive bias starting from ($N + 1$, N), shown in Fig. 5.16(a) and (b). The region in which the (N, $N + 1$) state is stable against these pathways taking place are:

$$y < \left(\frac{1+\alpha}{1-\alpha^2-\gamma}\right)\left[x-\left(N+\frac{1}{2(1+\alpha)}\right)\right] \tag{5.35a}$$

$$y < -\left(\frac{1+\alpha}{\alpha\gamma}\right)\left[x-\left(N+1-\frac{1}{2(1+\alpha)}\right)\right] \tag{5.35b}$$

(Note that each equation has the same letter as the corresponding process shown in Fig. 5.16.) Likewise if we begin from (N, $N + 1$) with negative applied bias voltage, there are two other possible transport pathways (Fig. 5.16(c) and(d)), and the region stable against these processes is

$$y > -\left(\frac{1+\alpha}{\alpha\gamma}\right)\left[x-\left(N+\frac{1}{2(1+\alpha)}\right)\right] \tag{5.35c}$$

$$y > \left(\frac{1+\alpha}{1-\alpha^2-\gamma}\right)\left[x-\left(N+1-\frac{1}{2(1+\alpha)}\right)\right] \tag{5.35d}$$

Note that the conditions (5.35a) and (5.35c) have the same boundary but the opposite sign as the conditions (5.29a) and (5.29d), and (5.35b) and (5.35d) are the same boundary and opposite sign as the conditions (5.29b) and (5.29c) for $N + 1$. Thus the small parallelograms are bounded by the same lines as the large parallelograms, but the enclosed area is on the opposite side of the lines.

We thus obtain the charging diagram shown in Fig. 5.15. The Coulomb blockade

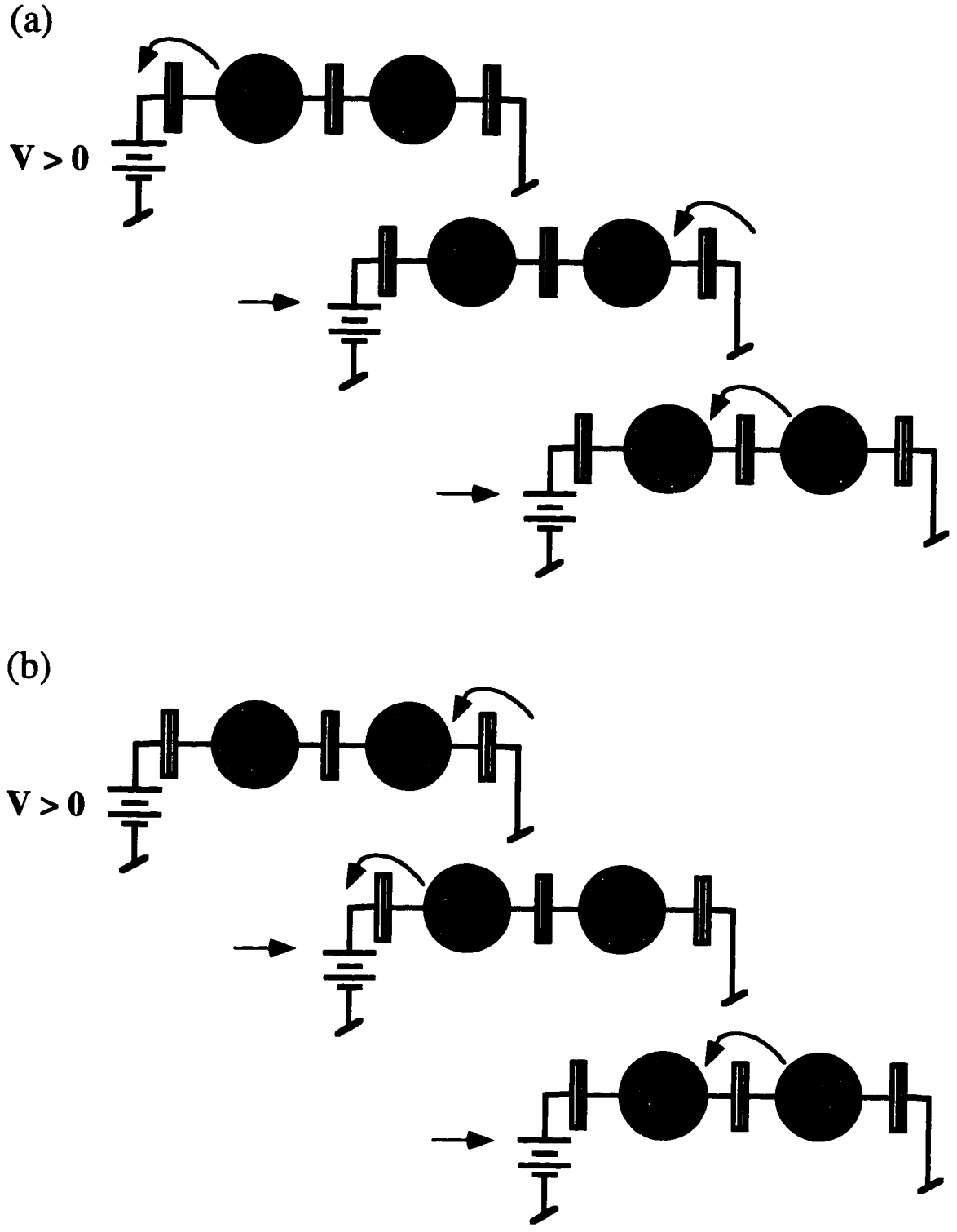

Figure 5.16 Transport pathways allowed from the polarized ground state in the circuit model, used to calculate the conditions (5.35) which give part of the Coulomb blockade characteristic shown in Fig. 5.15. Arrows represent tunneling events; each dot is labeled with the number of electrons on that dot before the represented tunneling event occurs.

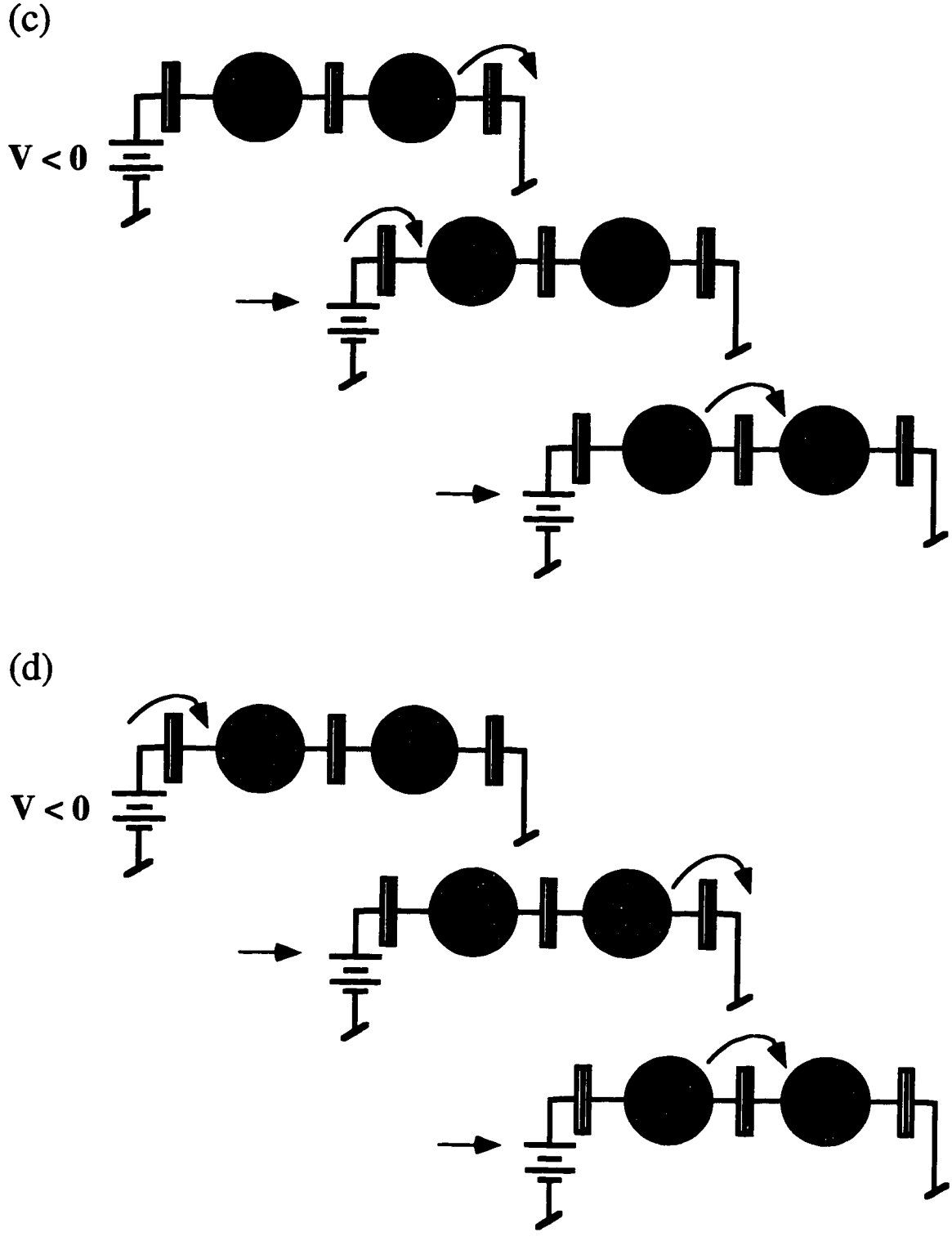

Figure 5.16 Transport pathways allowed from the polarized ground state in the circuit model, used to calculate the conditions (5.35) which give part of the Coulomb blockade characteristic shown in Fig. 5.15. Arrows represent tunneling events; each dot is labeled with the number of electrons on that dot before the represented tunneling event occurs.

characteristic evolves in the same fashion as the linear conductance peaks: the places where conductance occurs at zero bias split into two and a smaller version of the Coulomb blockade characteristic develops between them. The experiments to be described investigate how the complete nonlinear conductance phase diagram, and the Coulomb gap in particular, evolve with increasing interdot conductance.

5.4.2 Measured Differential Conductance: Coulomb Gap Collapse

The measured nonequilibrium differential conductance $G_{dot}(V_{ds}, V_g)$ for representative values of interdot tunneling g_{int} is shown in Figure 5.17. Differential conductance is represented with a logarithmic inverted grayscale (black is high, white low, as indicated on the color bar in Fig. 5.17). Values of g_{int} are determined from the center point contact voltage and the analysis shown in Fig. 5.6(a). We see that 5.17(a), the measurement with smallest g_{int}, has large main parallelograms of Coulomb blockade and very small secondary ones. As g_{int} increases, the pattern of the data evolve as follows: The height and width of the main parallelograms of Coulomb blockade decrease, and the secondary parallelograms grow in both height and width, until there are no longer distinguishable "main" and "secondary" parallelograms when there is a full mode of transport between the dots. Instead, the charging diagram in this case resembles that of a single dot of twice the total capacitance and twice the gate capacitance. Figure 5.17 (d) shows a slight asymmetry within a pair of parallelograms because there is not quite one mode between the dots.[18]

We can summarize the information contained in the entire family of measurements by examining the dependence of the Coulomb gap ΔV_{gap} (as defined in Fig. 5.15 and Eq. 5.30) on interdot tunneling rate. Figure 5.18 shows two such plots; 5.18(a) gives data acquired in early 1996 using the fast data-taker (section 3.4.2) with sample

[18]Quirks of KC7HH made it difficult to get exactly one mode between the dots. Previous measurements with a different device but without the raster method of taking data found that a full mode between the dots leads to indistinguishable parallelograms.

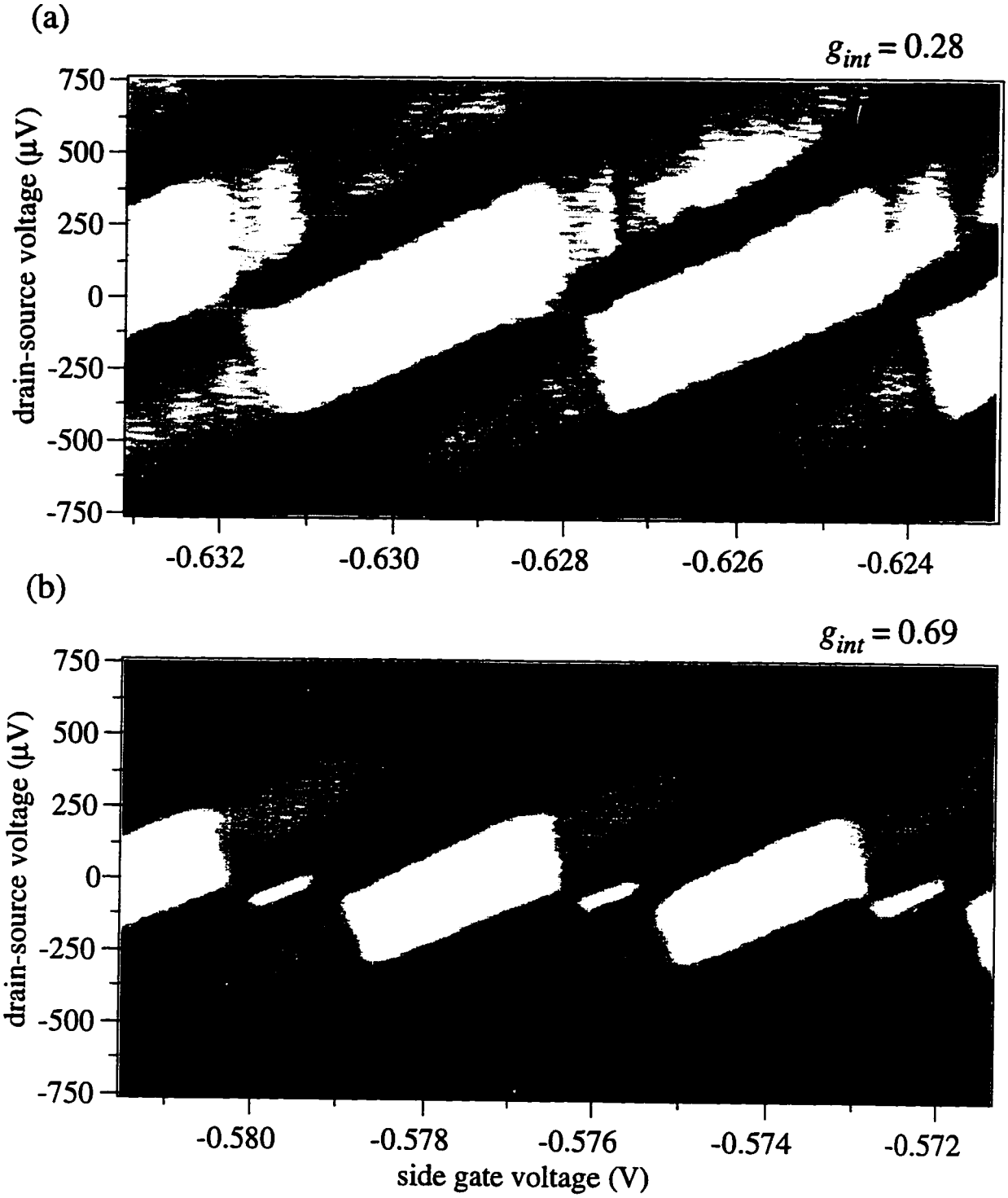
(a)
$g_{int} = 0.28$
750
500
250
0
-250
-500
-750
drain-source voltage (μV)
-0.632
-0.630
-0.628
-0.626
-0.624
(b)
$g_{int} = 0.69$
750
500
250
0
-250
-500
-750
drain-source voltage (μV)
-0.580
-0.578
-0.576
-0.574
-0.572
side gate voltage (V)
-8.0
-7.0
-6.0
-5.0
-4.0
log(differential conductance)

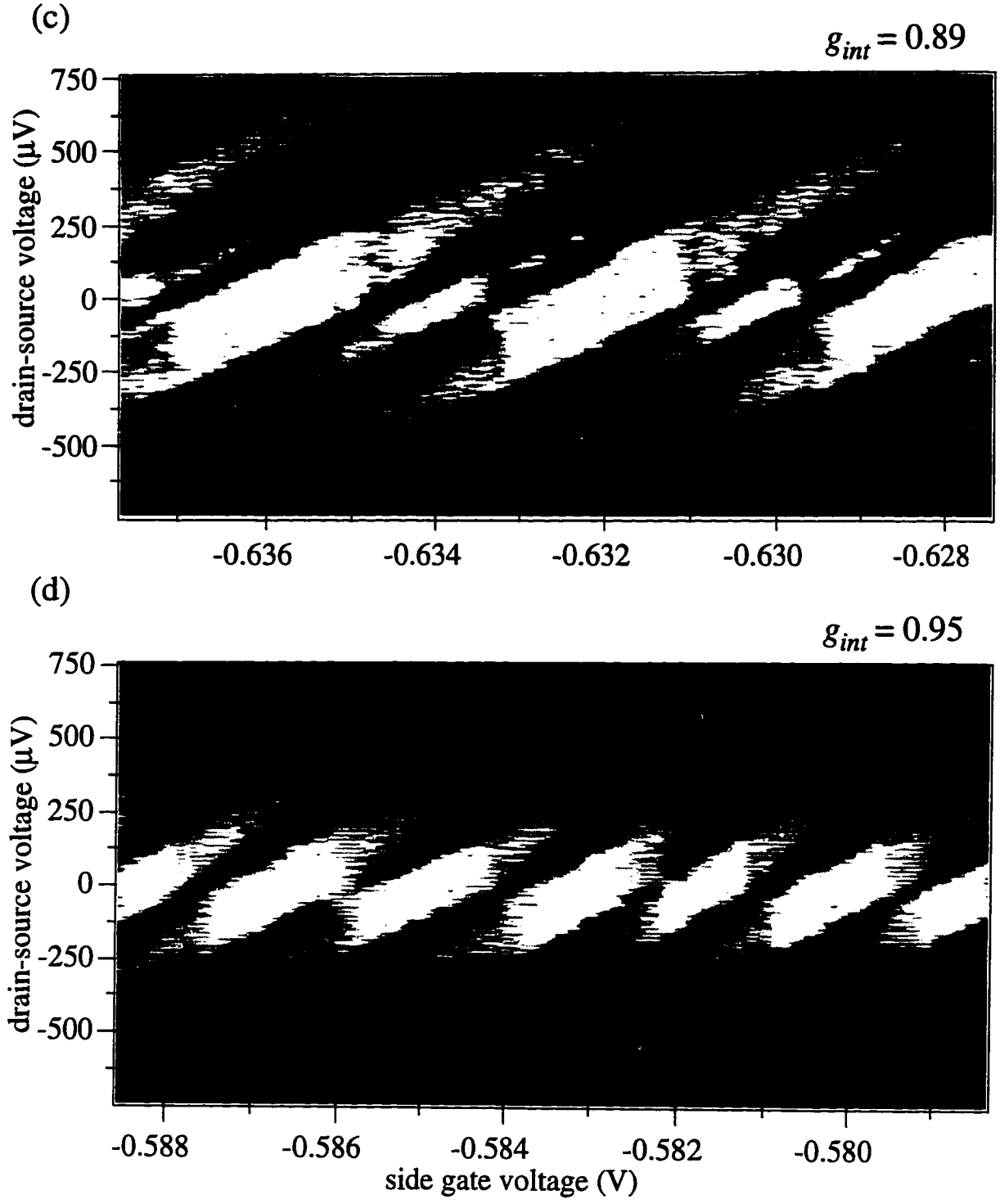

Figure 5.17 Measured differential conductance (represented with logarithmic inverted grayscale) as a function of drain-source voltage V_{ds} and side gate voltage $V_g = V_{g1} = V_{g2}$ for g_{int} = (a) 0.28, (b) 0.69, (c) 0.89, and (d) 0.95. A representative color bar is shown on the previous page.

KC7EE, and (b) shows the data obtained in December 1994 without the fast data-taker (hence fewer points) with sample KC3Q. Because sample KC3Q had better-matched point contacts, it was possible to fix g_{int} at exactly 1 mode.[19] We can see that the shape of ΔV_{gap} vs. g_{int} is the same in both cases. (The data of 5.18(b) must be rescaled be combined with those of 5.18(a) because the capacitances of the two samples are slightly different, thus making comparison inappropriate; but the capacitances are sufficiently similar that if plotted on the same graph, the two datasets nearly overlap.)

Figures 5.18(a) and (b) also show two sets of theoretical curves. The solid lines are a self-consistent calculation of the gap performed by this author using charge fluctuation theory as formulated by Golden and Halperin; the details of this calculation appear in the next section. The dotted line in 5.18 (a) shows the general behavior of the gap from a Hubbard model calculation for a double dot modeled as two sites, each of which contains a single spin-degenerate level [Kotlyar, private communication, 1996]. Although the exact shape of the gap behavior depends on a number of assumptions made about the properties of the double dot, the general prediction is that the gap will depend on the tunneling rate in the following manner [Kotlyar, private communication, 1996]:

$$\Delta V_{gap} \propto 1 - \sqrt{g_{\text{int}}} \tag{5.36}$$

The dotted line thus indicates the form of this prediction. The open squares at $g_{int} = 0$ correspond to the capacitive circuit model gap for the double dot with our measured capacitances, and the open triangles at $g_{int} = 1$ correspond to the circuit model gap for a single dot with total capacitance $2(C_{\Sigma} - C_{int})$ and our measured dot-to-lead capacitances.

Comparing theory and experiment in Fig. 5.18, we see that the charge fluctuation theory calculation is in good agreement with our data. The Hubbard model calculation, by contrast, gives the wrong curvature for the dependence of the gap on g_{int}. More

[19]Unfortunately, sample KC3Q did not survive top-loading for follow-up measurements.

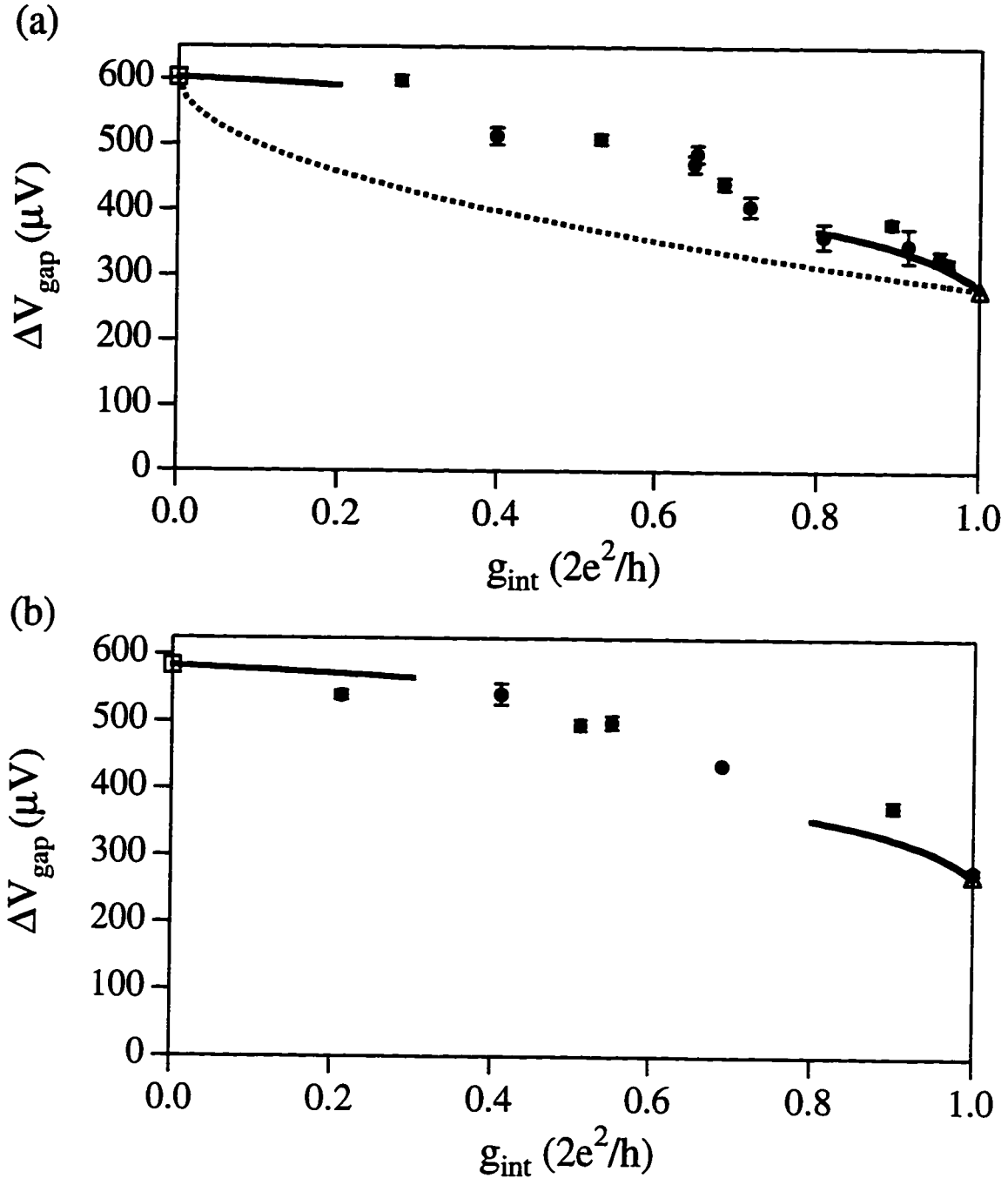

Figure 5.18 (a) Coulomb gap ΔV_{gap} measured from sample KC7EE (filled circles with error bars) vs. g_{int}, compared to self-consistent calculation of ΔV_{gap} described in Sec. 5.4.3 (solid line), Hubbard model calculation (dotted line), circuit model gap for double dot of our capacitances (open square), and circuit model gap for single dot of twice the total capacitance (open triangle). (b) Same measurement with sample KC3Q and without fast data-taking method.

sophisticated calculations [Kotlyar and Das Sarma, 1996], with multiple states on a site which allow the electrostatic energy as well as the interdot tunneling rate to vary as g_{int} is changed, come closer to reproducing the shape of the data; such a calculation seems to involve additional adjustable parameters, however, and it does not seem appropriate (as discussed in section 5.5) to allow the electrostatic energy to vary substantially.

The reader may note in Fig. 5.17 that although the sizes of the parallelograms changes substantially, the slopes of the sides do not change significantly. Since the slopes are determined in the orthodox theory by the capacitances of the system, and since there is no obvious way that adding tunneling would change the shape (except if the tunneling interaction depended on gate voltage), the slopes should be consistent with the measured capacitances and vary no more than the capacitances could be expected to vary. Using (5.32) and (5.33) and our measured capacitances, we expect

$$S_+ = 0.155$$

$$S_- = -9.9$$

We measure slopes which agree with these calculated numbers within the accuracy of the measurements (in particular it is difficult to measure the negative slope accurately since that boundary is less well defined). In this range of C_{int}, the slopes are fairly insensitive to the value of C_{int}; C_{int} = 100 aF gives a slope which cannot be distinguished within the error of the measurement. Thus the slopes are consistent with our picture of the interdot capacitance remaining constant, although they do not serve as proof of that picture.

A final observation to be made: unlike the single-dot measurements shown in Fig. 2.14, there is no evidence of single-particle states in Fig. 5.17. As discussed in Ch. 2, the dots in this sample are large enough that the single-particle states of the individual dots are not separated much. Most likely we do not see single-particle states in the double dot because mixing the single particle states of each dot produces a group of more closely spaced double dot states.

5.4.3 Self-Consistent Calculation: Adaptation of the Equilibrium Model

The many-body theories summarized so far [Matveev *et al.*, 1996a, b; Golden and Halperin 1996a, b] predict equilibrium conductance only. However, these theories can be used to determine the Coulomb gap in a self-consistent fashion, if we assume that there is no difference between inducing a potential difference between the dots via two different gate voltages and inducing such a potential difference via a drain-source bias. In this section we present this author's adaptation of the Golden and Halperin [1996a, b] formulation of charge fluctuation theory to calculate the Coulomb gap for tunnel-coupled quantum dots with $V_g = V_{g1} = V_{g2}$.

We recall the definition of the Coulomb gap (5.30). In section 5.4.1 we calculated the Coulomb gap based on purely electrostatic free energy expressions. We can also determine the threshold voltage for current flow in a more general fashion: the threshold voltage is that voltage which satisfies $\Delta F = 0$ for tunneling which leads to current flow (as in Eqs. (5.27)). To determine the effect of charge fluctuations on the Coulomb gap, we recall Eq. (5.30):

$$\Delta V_{gap} = 2\left|V_{thresh}(x = N)\right|$$

We want to calculate V_{thresh}, the threshold voltage for current flow, in the same fashion as in section 5.4.1, but we will calculate it self-consistently, including the tunneling contribution to the total energy.

Consider again the model Coulomb blockade (V_{ds}, V_g) dependence shown in Fig. 5.15. The large parallelograms are associated with an even N_{tot} ground state; thus the gap ΔV_{gap} comes from the condition

$$F(N_{tot}+1) - F(N_{tot}) = 0 \tag{5.37}$$

with N_{tot} even. If we include the tunneling contribution to the free energy, we have

$$F(N_{tot}+1) = F_0(N_{tot}+1) - E_{int}(g, 1+\rho) \tag{5.38}$$

$$F(N_{tot}) = F_0(N_{tot}) - E_{int}(g,\rho) \tag{5.39}$$

where F_0 refers to the purely electrostatic energy (5.5) with $x_1 = x_2$, N_{tot} is the (even) number of electrons in the ground state, and E_{int} is the amount by which the double dot free energy is lowered by interdot tunneling, from Eq.(5.15).[20]

To determine $\Delta F_0 = F_0(N_{tot} + 1) - F_0(N_{tot})$, we consider the relations 5.30 which give the energy changes associated with the tunneling events shown in Fig. 5.14. We wish to evaluate this energy change at dimensionless gate voltage $x = N$ with one of the conditions corresponding to one of the positive-sloped boundaries of the parallelograms in Fig. 5.15, so that $|V_{thresh}| = \Delta V_{gap}/2$ as in Eq. (5.35). Thus we use the condition (5.27a) corresponding to the tunneling event in Fig. 5.14(a). Substituting $x = N$ and simplifying Eq. (5.27a) with the notation of Eqs. (5.29), we obtain

$$\Delta F_0 = \frac{e^2}{C_\Sigma}\left(\frac{1}{1-\alpha^2}\right)\left[\frac{1}{2} + \frac{C_\Sigma V_{ds}}{e}\left(1-\alpha^2-\gamma\right)\right] \tag{5.40}$$

where again $\alpha \equiv C_{int} / C_\Sigma$ and $\gamma \equiv C_L / C_\Sigma$. We have from above,

$$E_{int}(g_{int},\rho) = \frac{e^2}{4C_\Sigma(1+\alpha)}\rho^2 f_\rho \tag{5.41}$$

For this calculation we define a normalized interaction energy

$$\tilde{E}_{int}(g_{int},\rho) \equiv \rho^2 f_\rho \tag{5.42}$$

Since we want to find the V_{ds} value V_{thresh} which satisfies $\Delta F = 0$, we can equally well determine it from a normalized energy $\Delta\tilde{F}$. Then our task becomes to determine the normalized total energy

---

[20]In (5.38), E_{int} is calculated using $1 + \rho$ because the state with $N_{tot} + 1$ electrons has an odd number of electrons; in mapping the double dot problem onto the single dot problem [Golden and Halperin, 1996a], the odd ground states (N, $N + 1$) are mapped onto the single dot state N with $\rho_{odd} = 1 + \rho$, whereas the even ground states (N, N) are mapped onto the single dot state N without any change in ρ.

$$\Delta\tilde{F} \equiv \frac{\Delta F}{e^2 / C_\Sigma(1+\alpha)} = \frac{1}{1-\alpha}\left[\frac{1}{2} + \frac{C_\Sigma V_{ds}}{e}\left(1-\alpha^2-\gamma\right)\right] - \frac{1}{4}\Delta\tilde{E}_{int} \qquad (5.43)$$

with

$$\Delta\tilde{E}_{int} \equiv \tilde{E}_{int}(g_{int}, 1+\rho) - \tilde{E}_{int}(g_{int}, \rho) \qquad (5.43)$$

We then solve for $V_{thresh} = V_{ds}$ satisfying $\Delta\tilde{F} = 0$.

Using the result (5.16) for $E_{int}(g_{int}, \rho)$ in the weak tunneling limit (with $N_{ch} = 2$), we obtain

$$\Delta\tilde{E}_{int}(g << 1) = \frac{2g}{\pi^2}\left[(2+\rho)\ln(2+\rho) - \rho\ln(-\rho) - (1-\rho)\ln(1-\rho) - (1+\rho)\ln(1+\rho)\right]$$

$$+2g^2\left[c_{1+\rho}(1,2) - c_\rho(1,2) + 2c_{1+\rho}(2,2) - 2c_\rho(2,2)\right] \qquad (5.45)$$

using the notation of (5.16). We then substitute (5.44) in (5.42) and can determine V_{thresh} self-consistently (using numerical values for the coefficients c_ρ), beginning with $V_{thresh}(g_{int} = 0) = 301\ \mu V$. The code for this calculation appears in Appendix D.

In the strong tunneling limit, we have instead (from Eqs. (5.18) and (5.19))

$$\Delta\tilde{E}_{int}(g \to 1) \approx 1 + 2\rho + 0.9189(1-g)\left\{\cos^2\left(\frac{\pi\rho}{2}\right)\left[\ln\left[(1-g)\cos^2\left(\frac{\pi\rho}{2}\right)\right] - 0.4627\right]\right.$$

$$\left. -\cos^2\left(\frac{\pi(1+\rho)}{2}\right)\left[\ln\left[(1-g)\cos^2\left(\frac{\pi(1+\rho)}{2}\right)\right] - 0.4627\right]\right\} \qquad (5.46)$$

The numbers come from evaluating the following two expressions:

$$\ln(8e^\gamma / \pi^2) + 0.1703 - 1 \approx -0.4627 \qquad \text{and} \qquad 4e^\gamma / \pi^3 \approx 0.2297.$$

Again this result is used to solve self-consistently for V_{thresh}.[21]

---

[21] In principle it should be possible to calculate the energy shift directly from $\Delta_{str}(\rho)$; however, since that energy shift is referred to a single dot rather than a double dot, it becomes rather difficult to work out how the single dot electrostatics relate to the double dot electrostatics.

5.5 Electrostatic Simulation of the Device

Michael Stopa performed self-consistent electrostatic simulations of the electron density profile of our double dot device ($V_{ds} = 0$).[22] The simulations modeled the device with Thomas-Fermi screening and low-temperature Fermi-Dirac statistics, rather than performing a full quantum mechanical calculation (such a calculation becomes intractable for even a single quantum dot the size of ours). The capacitances C_L, C_Σ, and C_{int} of the double dot and the total number of excess electrons N in one dot were calculated. In addition, the double dot capacitances were calculated as the center point contact voltage V_{qpc} was changed to lower the tunnel barrier between the dots.

The calculated and measured capacitances of the double dot are presented in Table 5.2, along with capacitances calculated by Chagarn Whan[23] treating the dots and gates as ideal conductors with the fully classical electrostatic simulation *FASTCAP*. The calculated values are in good agreement with our measured values. This suggests that the calculated number of electrons per dot, 750 to 800, is also reasonable.

The dependence of the capacitances calculated by Stopa on the center point contact voltage is shown in Fig. 5.19. All of the capacitances are essentially independent of center point contact voltage. In particular, C_{int} hardly changes (growing only from 24 to 26 aF)

Table 5.2: Measured and Calculated Capacitances of the Double Dot

capacitance	measured value	Stopa value	Whan value
C_Σ	342 ± 15 aF	290 ± 5 aF	300 aF
C_{int}	18 ± 10 aF	25 ± 2 aF	38 aF
C_L	75 ± 10 aF	45 aF	54 aF

[22]The author is grateful to Michael Stopa for performing these calculations.
[23]Whan, personal communication.

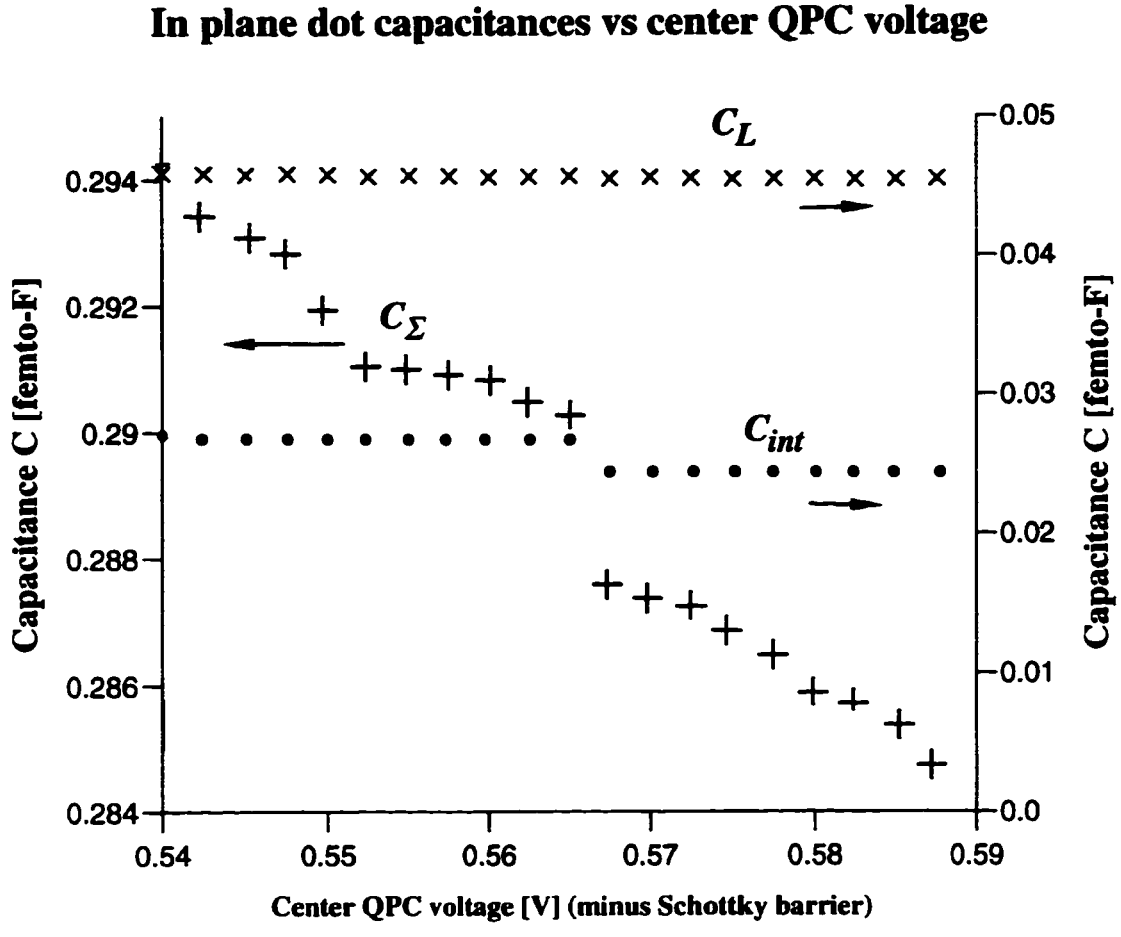

Figure 5.19 Electrostatic simulations by M. Stopa giving dependence of double dot capacitances on center point contact (QPC) voltage. Shown are the dependence of C_Σ (crosses), C_{int} (filled circles), and C_L (x's). The principal result is that all capacitances, particularly C_{int}, are insensitive to the center point contact voltage over a wide range.

even as the height of the tunnel barrier formed by the point contact approaches the Fermi level. Stopa has subsequently done quantum mechanical simulations of smaller single dots [Stopa, 1996] to study the dependence of tunnel junction capacitance on tunnel barrier height. He finds in these simulations as well that the capacitance across a point contact (whether from dot to lead or from one dot to another) does not change substantially as that point contact conductance is increased even to greater than one mode.

Whan also examined the dependence of C_{int} on the separation between the dots. Most notably, he finds that C_{int} is extremely insensitive to the separation between the dots (modeled as planar metal ellipses of length D and thickness much less than D, and separated by a distance d). As long as the dot-dot separation d is smaller than the dot size D, C_{int} barely changes as d is decreased from 0.2 D to .001 D.

5.6 Inadequacy of Capacitive Model

Conductance peak splitting in semiconductor quantum dots was initially interpreted by others [see for example van der Vaart *et al.*, Ph.D. thesis] using circuit models, and was assumed to come from dramatic growth of the interdot capacitance as the center point contact voltage was changed. This was understandable since peak splitting had first been observed in metal double island systems [Geerligs *et al.*, 1991], in which the primary coupling was capacitive. (As already discussed, in that system it was not possible to vary the strength of the coupling.) Indeed, Waugh [1994] gives circuit model simulations in which he shows that the only way that peak splitting can be produced by the circuit model is by changing the interdot capacitance, not the interdot conductance. However, the critical assumption of the circuit model is that the charge on each island must be quantized; Waugh retained this assumption in his simulations.

On examining the results of these circuit models, it becomes apparent that the capacitance must grow unphysically large to explain the amount of splitting observed. Figure 5.20 shows the fractional peak splitting f and Coulomb gap ΔV_{gap} as a function of

interdot capacitance calculated from Eqs. (5.11) and (5.31), using the measured values for the other capacitances. These calculations assume that only the interdot capacitance changes and the other capacitances in the system stay constant. We thus recast (5.11) and (5.31) slightly to show the dependence on interdot capacitance explicitly. We define $C_{\Sigma d}$ as the self-capacitance of one dot of the double dot minus the contribution from the interdot capacitance:

$$C_{\Sigma d} \equiv C_L + C_g + C_0 = C_\Sigma - C_{int} \tag{5.47}$$

Given C_{int} as determined in section 5.2.4 and C_Σ measured from a single dot, we find

$$C_{\Sigma d} = 323 \pm 15 \text{ aF}$$

We then rewrite (5.11) and (5.31) as

$$f = \frac{2C_{int}}{C_{\Sigma d} + 2C_{int}} \tag{5.48}$$

$$\Delta V_{gap} = \frac{e\left(C_{\Sigma d} + C_{int}\right)}{C_{int}\left(2C_{\Sigma d} - C_L\right) + C_{\Sigma d}^2 - C_L C_{\Sigma d}} \tag{5.49}$$

and from these relations calculate Fig. 5.20.

Although a moderate amount of peak splitting and Coulomb gap decrease can come from physically reasonable values of the interdot conductance, it is not possible to achieve the full observed splitting or gap decrease without using $C_{int} \sim 10$ fF. Such a value is physically unreasonable since it is thirty times the total capacitance of a single isolated dot. Furthermore, conformal mapping calculation of the capacitance between two coplanar semi-infinite conducting half planes shows that the capacitance grows only logarithmically as the distance between them decreases. The curvature introduced by considering disks rather

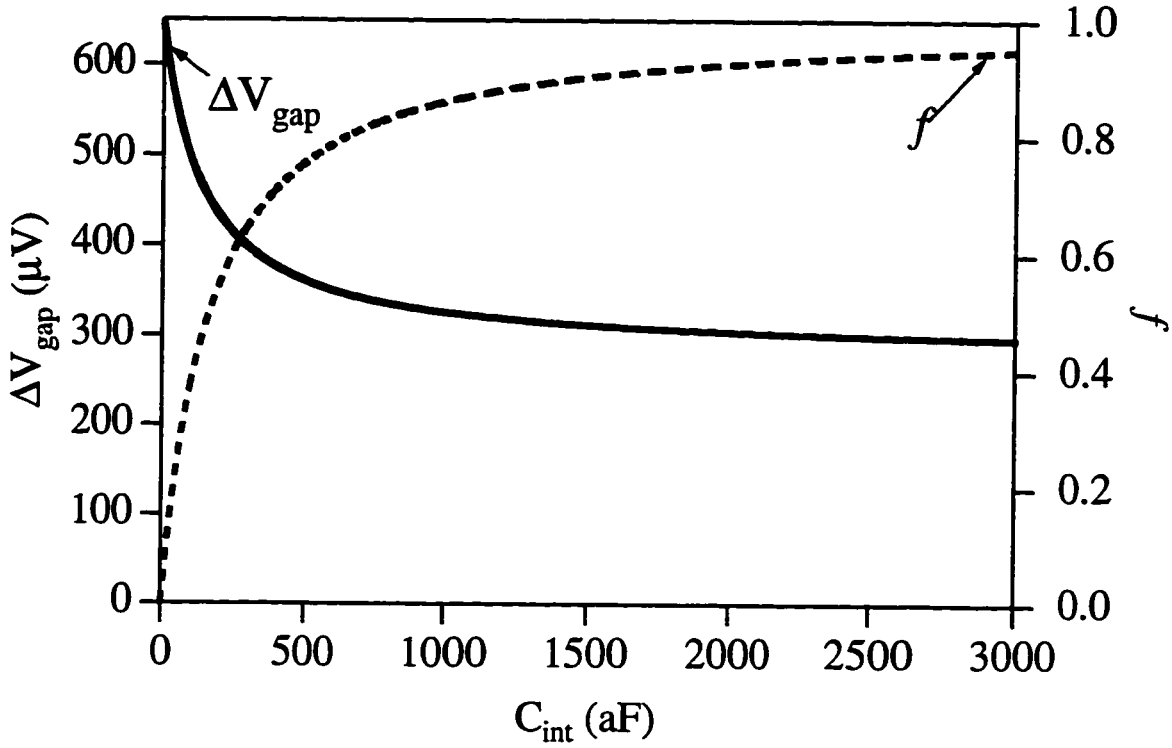

Figure 5.20 Double dot Coulomb gap (solid line, left axis) and conductance peak splitting (dashed line, right axis) vs. interdot capacitance C_{int}, calculated from the circuit model (Eqs. (5.11) and (5.31)) with all other capacitances held constant. Values for C_{int} > 3000 aF are not shown; peak splitting approaches 1 and gap approaches 280 μV asymptotically, reaching $f = 0.97$ and $\Delta V_{gap} = 290$ μV at $C_{int} = 5000$ aF.

than half-planes is expected to remove even that divergence.[24] This result is borne out by the classical electrostatic calculations of Whan described previously. Finally, the semiclassical simulations described in the previous section [Stopa, unpublished work] find no significant growth in the interdot capacitance – not even to values which would lead to 20% splitting, much less full splitting.

Given that growth of tunnel conductance between the dots explains the limiting behavior exactly (for $g_{int} = 0$ and $g_{int} = 1$), we find the breakdown of charge quantization in the individual dots of the double dot an excellent explanation of our results.

5.7 Summary

This chapter presents several measurements of how tunneling between two quantum dots in series reduces their interaction energy, as manifested through splitting of conductance peaks and collapse of Coulomb gap. All of these measurements together make a strong case that tunneling into the double dot with moderate to strong interdot tunneling present is like tunneling into a single quantum object.

[24]This calculation has been performed both by John M. Golden and Fred Waugh.

CHAPTER 6
CONCLUSIONS

The results presented in this thesis demonstrate that tunneling has a significant impact on the energetics and transport properties of single and coupled quantum dots. The capacitive circuit model, which describes transport very effectively in the limit of weak tunneling throughout the system, breaks down because the total charge on any one dot is no longer quantized in the presence of significant tunneling. Instead, a model which explicitly includes charge sharing between sites via tunneling describes the results.

In particular, we have demonstrated, through nonlinear conductance measurements and temperature studies of zero-bias conductance, that as the tunneling between two dots in series is increased, the two-dot system goes from two independent dots, each of which must have an integer number of electrons on it, to a composite object in which charge is shared between what were originally two distinct sites. One electron can be added at a time to this composite object, and the energetics of adding this single electron depends on the rate of tunneling present between the two original dots.

So how do these results bear on the motivation for studying quantum dots discussed at the beginning of thesis, namely understanding better the nature of tunneling interactions in many-body systems, and possibilities for single electronics and quantum computing? The results of this thesis provide strong confirmation that tunneling between a large number of states on each site (as opposed to tunneling between single states, as described by Hubbard models) is the source of the breakdown of charge quantization. This thesis does not bear directly on development of applications. It does, however, make clear how controllable this process is in the model system studied, in which there are only two dots and a separate voltage controls each main component of the device. The ability to control the strength of interdot interactions would undoubtedly be useful in more complex single-electron circuitry or in quantum computing. Less labor-intensive techniques would have to be developed for finding the best operating parameters in more complex devices,

however.

There remain some unanswered questions which could be interesting for future students to pursue. First, it is not clear why the single dot excitation spectrum presented in Chapter 2 (Fig. 2.14) shows such insensitivity to side gate voltage (and hence to the number of electrons). It would be interesting to study this further in dots of different size (does the regularity vanish with much smaller dots?) and to study the magnetic field dependence of the spectrum (does it remain regular in small magnetic fields? Do the observed states split into two in the presence of a moderate field?). It would also be good to examine in dots of less symmetric design (does this same regularity persist?).

The results of Chapter 4 on the single dot with strong tunneling to one lead also suggest future work. It would be good to devise an experiment which could distinguish whether the *e*-periodic oscillations observed with $G_{open} > 1$ mode are due to quantum interference or single-electron charging. Such an experiment could use magnetic fields or samples with designs chosen to probe different possible ballistic electron trajectories. Different point contact designs could be studied to see if the shape of the point contact gates affects the results. It is somewhat more difficult to imagine what experiment would conclusively demonstrate what is doing on, since the results shown here vary in certain features from sample to sample.

A remaining question in the work reported here is: is the transport through the double quantum dot phase-coherent? It certainly seems likely; the double dot temperature studies of Ch. 5 indicate that electrons most likely tunnel into the entire double dot, rather than into one dot and then the other, and single quantum dot experiments suggest that transport through single dots with weak tunneling to the leads is phase-coherent [Yacoby *et al.*, 1994]. An experiment which could conclusively demonstrate the coherence (or lack thereof) of transport, such as by placing the double dot in an electron interferometer, would be significant.[1]

---

[1] Kouwenhoven and McEuen [1996] also view the question of coherence in double dot transport as one of

There are many new directions which future students of coupled quantum dots could investigate. Extending these studies to more complex coupled dot structures is clearly a good strategy. Such work will require innovations in technique, both fabrication of more complex samples and searching gate voltage parameter space to find the correct voltages to apply to all the gates. It will also require clear thinking about what multidot structures would be most interesting to examine and what transport signatures would be significant in the midst of the highly complicated energetics of a multidot structure with many degrees of freedom. Structures designed to test quantum computing strategies, and structures which draw upon existing "single electronics" designs but study the ways their properties change in the presence of strong tunneling, would clearly be interesting. Extending the "artificial molecule" analogy and testing structures which are known in nature to show interesting electronic properties (such as aromatic and highly conjugated structures) would also be interesting. Finally, mixing ballistic transport effects and the sort of experiments described in this thesis could lead to some fascinating physics, though these experiments would be something more of a stretch, requiring very high-quality material, and being less likely to actually work. Quantum dots could be designed which selected for transport through particular eigenstates (corresponding to ballistic orbits) and then dots could be coupled together to examine interactions between these particular states. (Some work examining charging in open ballistic microstructures has already been reported in the Ph.D. thesis of Jordan Katine [1996].)

The results of this thesis are part of a body of knowledge on coupled semiconductor quantum dots which has been accumulated by many workers over the last few years [Waugh *et al.*, 1995; van der Vaart *et al.*, 1995; Hofmann *et al.*, 1995; Molenkamp *et al.*, 1995; Dixon *et al.*, 1996; Blick *et al.*, 1996; Matveev *et al.*, 1996; Golden and Halperin, 1996; Adourian *et al.*, 1996; Livermore *et al.*, 1996]. It is the hope of this author that these

---

the significant open questions in this field.

results will stimulate further questions to be answered on the interplay between classical and quantum interactions in many-body systems.

APPENDIX A
MEASUREMENT OF DOUBLE DOT CHARGING DIAGRAM

The text of this chapter has been accepted for publication in *Science*. It describes measurements of the double dot charging diagram, explained briefly in 5.2.4, which were performed in collaboration with Carol Livermore using the same sample, measurement apparatus, and cryogenics described in the rest of the thesis.

The Coulomb blockade in coupled quantum dots

C. Livermore, C.H. Crouch, and R.M. Westervelt
Division of Applied Sciences and Department of Physics
Harvard University, Cambridge, Massachusetts 02138

K.L. Campman and A.C. Gossard
Materials Department
University of California, Santa Barbara, California 93106

Individual quantum dots are often referred to as "artificial atoms". Two tunnel-coupled quantum dots may be considered an "artificial molecule". We report low temperature measurements of a series double quantum dot with adjustable interdot tunnel conductance fabricated in a GaAs/AlGaAs heterostructure. The Coulomb blockade is used to determine the ground state charge configuration within the "molecule" as a function of the total charge on the double dot and the interdot polarization induced by electrostatic gates. As the tunnel conductance between the two dots is increased from near zero to $2e^2/h$, the measured conductance peaks of the double dot exhibit pronounced changes in agreement with many body theory.

Quantum dots in semiconductors are small islands of electrons which are governed by the interplay of quantum mechanical and electrostatic effects. Often quantum dots are referred to as "artificial atoms" (1) because electronic states within closed dots are quantized, permitting spectroscopic measurements (2). Multiple quantum dots coupled by electronic tunneling are then "artificial molecules", which can be made in many configurations with adjustable interdot tunneling rates. Coupled dot structures can be used to make electronic circuits governed by quantum mechanics as well as electromagnetics. Recent experiments (3-12) and theory (13-19) have investigated the behavior of coupled dot systems in different configurations.

In this report, we use the Coulomb blockade as a spectroscopic tool to probe the ground state configuration of charge in two tunnel-coupled quantum dots with adjustable interdot tunneling. These measurements are the first to control independently the induced charge on each dot and the interdot tunneling rate in order to cover the full three dimensional parameter space and allow explicit comparison with theory. Previous work (3, 8, 10) has tested aspects of the theory by sampling two dimensional cuts through the parameter space. The data below present a unified picture of how the coupled dot system evolves from the weak tunneling regime, in which capacitive coupling is dominant, to the strong tunneling regime, in which interdot tunneling dominates, including the effects of interdot polarization. The data are in excellent agreement with recent many body theory (13-16) which describes how the quantization of charge within quantum dots is relaxed as interdot tunneling increases.

Figure 1 shows a scanning electron micrograph and a schematic diagram of our coupled quantum dot device. The dots are defined in a GaAs/AlGaAs heterostructure which contains a high mobility (5×10^5 cm^2/Vs) two-dimensional electron gas (2DEG) located 57 nm beneath the surface. Electrostatic gates, which appear as light regions in Fig. 1A, are defined by electron beam lithography and Cr/Au metallization. When a negative voltage is applied to the gates, the electrons in the 2DEG beneath are depleted,

leaving two small islands of electrons connected in series to each other and to two leads through quantum point contacts. The size of the lithographic opening for each dot is 500 nm x 800 nm. The actual dot area is somewhat less due to lateral depletion; simulations show that each dot contains about 750 to 800 electrons (20). The voltage V_{p2} applied to the center point contact gate controls the interdot conductance G_{int}, and the voltages V_{p1} and V_{p3} applied to the outer point contact gates control the dot-to-lead conductances $G_{dot-lead}$. The side gate voltages V_{g1} and V_{g2} in Fig. 1B are used in the experiment described below to induce excess charge separately on the two dots; the remaining two side gates are tied together at voltage V_{g3}.

An important feature of the present experiment is that the tunnel coupling between the quantum dots can be continuously adjusted from the weak tunneling regime, in which the dots are well isolated, to the strong tunneling regime, in which the two dots effectively join into one (3). In the weak tunnel coupling regime, the numbers of electrons on each dot n_1 and n_2 are quantized, and Coulomb blockade theory applies to each dot individually as studied previously (7, 9, 11, 12). In the strong tunneling regime, n_1 and n_2 are not individually well defined, and the coupled dot system enters the interesting regime in which it acts as an artificial molecule. Throughout this work the coupled dot system is well isolated from the leads ($G_{dot-lead} << 2e^2/h$) and the total number of electrons $n_{tot} = n_1 + n_2$ is quantized; we use the Coulomb blockade for the entire coupled dot system to probe its ground state energy.

The energetics of the double dot in the weak tunneling limit are described by standard Coulomb blockade theory (21). Figure 2A shows a circuit diagram for the double dot including the relevant capacitances which control the charging energy in this limit: $C_{g1} = 34 \pm 2$ aF and $C_{g2} = 35 \pm 2$ aF are the capacitances to side gates 1 and 2, $C_{int} = 18 \pm 7$ aF is the interdot capacitance, and $C_\Sigma = C_{\Sigma 2} = C_{\Sigma 1} = C_{01} + C_{g1} + C_{int} = 342 \pm 15$ aF is the total capacitance of each dot to ground. These values were determined using the nonlinear current-voltage characteristics of the two dots as described in (4). The total electrostatic

energy $U(V_{g1},V_{g2})$ of the double dot system is controlled by the two gate voltages V_{g1} and V_{g2}:

$$U=\frac{1}{2C_{\Sigma}(1-\alpha^2)}\left[\left(C_{g1}V_{g1}-n_1e\right)^2+\left(C_{g2}V_{g2}-n_2e\right)^2+2\alpha\left(C_{g1}V_{g1}-n_1e\right)\left(C_{g2}V_{g2}-n_2e\right)\right] \quad (1)$$

where $\alpha \equiv C_{int}/C_{\Sigma}$. For given n_1 and n_2, the energy surface $U(V_{g1},V_{g2})$ is a paraboloid. The ground state charge configuration is determined by the values n_1 and n_2 which minimize the total electrostatic energy. The ground state energy plotted in Fig. 2B is an array of paraboloids corresponding to different charge configurations (n_1,n_2). At low temperatures, the charging energy U presents a barrier to tunneling: the Coulomb blockade. Conduction through two dots in series occurs only when both n_1 and n_2 can change simultaneously, at the intersections of three paraboloids indicated in Figs. 2B and 2C by dots (for example (n_1,n_2) = (1,1), (1,2) and (2,1)) (7). The characteristic electrostatic energy scale is the charging energy of a single dot. For this experiment this is $e^2/2C_{\Sigma}$ = 230 μeV, smaller than the Fermi energy E_F = 10 meV, but larger than the average energy level spacing $\Delta E \equiv 2E_F/n_1 \equiv 30\mu eV$ and the electron gas temperature $T_e \equiv 7.5$ μeV, determined from the widths of conductance peaks.

The configuration of quantized electronic charges in coupled dot systems plays an essential role in coupled dot energetics. For balanced gate voltages $V_{g1} = V_{g2}$ the induced charges $C_{g1}V_{g1}$ and $C_{g2}V_{g2}$ on each dot are equal, and the lowest energy configurations have equal numbers of electrons on each dot so that $n_{tot} = n_1 + n_2$ is even. If one additional electron is added, making the total number of electrons odd, charge quantization requires that this electron reside on one dot or the other in the limit of weak interdot tunneling, so that the double dot is polarized with an electric dipole moment. This polarization results in additional electrostatic energy. If the gate voltages are adjusted with $V_{g1} \neq V_{g2}$ to induce a polarized charge configuration with $n_1 \neq n_2$, one finds analogous

situations in which charge quantization results in unpolarized configurations $n_1 = n_2$ with excess energy. In general, quantization of charge on individual dots of coupled dot systems results in frustrated configurations in which the actual charge differs from that induced by the gate voltages, producing excess electrostatic energy.

Tunneling between dots relaxes the requirement for charge quantization on each dot and changes both the coupled dot ground state energy and the selection rules for charge transport. The condition for quantization of charge in many body systems is of fundamental interest and has been studied theoretically (22-25). Matveev (23) has studied a single quantum dot connected to its environment by a quantum point contact with tunnel conductance G_p near one mode. He finds that as G_p approaches $G_p = 2e^2/h$, the periodic oscillations of the charging energy with dot charge decrease continuously, and that charge quantization is completely destroyed when $G_p = 2e^2/h$. In tunnel-coupled double dots, tunneling reduces the excess electrostatic energy associated with charge quantization, as for the frustrated configurations described above, by allowing electrons to be shared between dots. Many body theory of tunnel coupled double dots (13-16) predicts that the excess energy of such frustrated charge configurations is controlled by the interdot tunnel conductance G_{int}, and decreases continuously from a maximum at $G_{int} = 0$ to zero at $G_{int} = 2e^2/h$. For dot geometries such as in Fig. 1, this transition is driven entirely by the change in interdot conductance because the classical interdot capacitance remains approximately constant (20, 26). Interdot tunneling also relaxes the selection rules for charge transport through a series double dot because added electrons are shared by both dots.

We use the Coulomb blockade of electrons on the entire coupled double dot system to study the evolution of the ground state charge configuration as the interdot tunnel conductance G_{int} is varied. To carry out the experiment, the sample was cooled in a He dilution refrigerator to base temperature, and the conductance through the double dot was measured with low noise lockin techniques using a small ac bias voltage (10 μV_{rms}) to

probe the ground state. The outer point contact conductances were set in the weak tunneling regime ($G_{dot\text{-}lead} << 2e^2/h$), while the interdot conductance was set to a series of values between $G_{int} \cong 0$ and $G_{int} \cong 2e^2/h$. At each value of interdot conductance, the series conductance G_{dot} of the double dot was recorded while the side gate voltages V_{g1} and V_{g2} were swept in a raster pattern, using a computerized data acquisition system. The interdot conductance was separately calibrated vs. gate voltage V_{p2} by measuring the point contact conductance with all the gates energized and the outer point contacts open.

Figure 3 shows a series of images of the measured double dot conductance G_{dot} vs. side gate voltages V_{g1} and V_{g2} for interdot conductances increasing from (A) $G_{int} = 0.22$ G_o to (F) $G_{int} = 0.98$ G_0 with $G_0 \equiv 2e^2/h$. In each panel the color scale represents $\log(G_{dot})$, with yellow indicating high conductance and black low conductance approaching the noise level. The images in Fig. 3 show the evolution of the Coulomb blockade for the double dot system from weakly coupled dots in Fig. 3A to a single large dot in Fig. 3F. Figure 3A shows conductance at an array of points as predicted by Coulomb blockade theory for capacitively coupled separate dots, as in Fig. 2C. As shown, these points are at the intersection of hexagons defined by the charge configuration (n_1,n_2) of individual dots; the small splitting is caused by the interdot capacitance. The diagram is compressed along the diagonal compared with Figure 2C due to cross-capacitance between each side gate and the opposite dot. For larger interdot conductances in Figs. 3B to 3F, the pattern changes dramatically and is no longer described by the Coulomb blockade theory of individual dots. At $G_{int} = 2e^2/h$ in Fig. 3F, the conductance pattern becomes an array of lines corresponding to the Coulomb blockade for a single large dot. These lines separate regions defined by integer values of the total double dot charge n_{tot}, which increases with average gate voltage $V_{av} = (V_{g1} + V_{g2})/2$. The conductance pattern in Fig. 3F is insensitive to polarization induced by differences in gate voltage $\Delta V = V_{g1} - V_{g2}$, because the dots have joined into one.

The evolution of the images in Fig. 3 between the weak and strong tunneling limits shows how the relaxation of charge quantization via interdot tunneling changes the transport properties of tunnel-coupled quantum dots. For weak interdot tunnel conductance, the numbers of electrons n_1 and n_2 on the two dots are quantized, and current only flows when the Coulomb blockade is simultaneously lifted on both dots. Two independent conditions will be satisfied only at a point in the (V_{g1}, V_{g2}) plane; the measured conductance peaks form an array of points where the Coulomb blockade is simultaneously lifted for both dots. As interdot tunnel conductance increases from $G_{int} = 0$ to $G_{int} = 2e^2/h$, the conditions that both n_1 and n_2 are quantized relax to one single condition that the total charge $n_{tot} = n_1 + n_2$ must be quantized. Any one condition will be satisfied along a line in the (V_{g1}, V_{g2}) plane, and the observed conductance occurs along lines where the Coulomb blockade is lifted for the entire double dot in the strong tunneling limit. Between those two extremes, the conductance steadily grows out from the points in Fig. 3A along the boundaries between configurations with different total charge n_{tot}, and the shape of these boundaries changes from the zig-zag pattern for weak tunneling to straight lines for Fig. 3F.

The splitting between the lines of conductance in Fig. 3 measures the modification of double dot energetics by interdot tunneling predicted by theory (13-16), and thus determines an analog of the molecular binding energy. The minimum splitting ΔV_s in gate voltage occurs along the V_{av} direction, as shown in Fig. 3. As interdot tunnel conductance increases from $G_{int} \cong 0$ to $G_{int} \cong 2e^2/h$, this splitting increases from $\Delta V_s \cong 0$ to $\Delta V_s \cong \Delta V_p/2$ where ΔV_p is the period of the array in Fig. 3A along the V_{av} direction. Figure 4 plots the measured fractional splitting $F = 2\Delta V_s/\Delta V_p$ vs. the interdot conductance G_{int}, measured separately (27). Also plotted are the fractional splitting predicted by Golden and Halperin (15) in the weak and strong tunneling limits (solid lines) with an interpolation (dashed line); Matveev et al. (16) find similar theoretical results. As shown, the data and

theory are in excellent quantitative agreement, providing additional confirmation of the physical picture presented above.

The double dot conductance pattern is in detailed agreement with charge quantization theory (13-16) outlined above. From the evolution of the conductance pattern in Fig. 3 alone, it is clear that the transition from isolated dots to a single large dot is strongly correlated with interdot conductance and is complete at $G_{int} = 2e^2/h$, in agreement with theory (13-16). The lines of conductance in Fig. 3 follow the intersection of energy surfaces for tunnel coupled double dots with different total charge n_{tot} and directly measure the deformation in the double dot energy surface $U(V_{g1},V_{g2})$ due to interdot tunneling. The splitting due to this deformation shown in Fig. 4 is in quantitative agreement with many body theory (13-16). Additional quantitative comparisons between theory and experiment have been made for certain special cases. In the strong tunneling limit appropriate for Fig. 3E, the shapes of the zig-zag boundaries (5) are in good agreement with theory (13). The full conductance pattern shown in Fig. 3 goes beyond current theory and provides an experimental basis for future work on the energetics of tunnel coupled quantum dots.

References

1. M. A. Kastner, *Rev. Mod. Phys.* **64**, 849 (1992).
2. R. C. Ashoori, *Nature* **379**, 413 (1996).
3. F. R. Waugh, M. J. Berry, D. J. Mar, R. M. Westervelt, K. C. Campman, A. C. Gossard, *Phys. Rev. Lett.* **75**, 705 (1995).
4. C. H. Crouch, C. Livermore, F. R. Waugh, R. M. Westervelt, K. L. Campman, A. C. Gossard, *Surface Science* **361/362**, 631 (1996).
5. C. Livermore, C. H. Crouch, R. M. Westervelt, K. L. Campman, A. C. Gossard, to be published in *Superlattices and Microstructures* (1996).

6. A. S. Adourian, C. Livermore, R. M. Westervelt, K. L. Campman, A. C. Gossard, to be published in *Superlattices and Microstructures* (1996).

7. See, for example, F. Hofmann, T. Heinzel, D. A. Wharam, J. P. Kotthaus, G. Bohm, W. Klein, G. Trankle, G. Weimann, *Phys. Rev. B* **51**, 13872 (1995).

8. N. C. van der Vaart, S. F. Godijn, Y. V. Nazarov, C. J. P. M. Harmans, J. E. Mooij, L. W. Molenkamp, C. T. Foxon, *Phys. Rev. Lett.* **74**, 4702 (1995); N. C. van der Vaart, Ph.D. thesis (1995).

9. L. W. Molenkamp, K. Flensberg, M. Kemerink, *Phys. Rev. Lett.* **75**, 4282 (1995).

10. R. H. Blick, R. J. Haug, J. Weis, D. Pfannkuche, K. v. Klitzing, K. Eberl, *Phys. Rev. B* **53**, 7899 (1996).

11. D. Dixon, L. P. Kouwenhoven, P. L. McEuen, Y. Nagamune, J. Motohisa, N. Sakaki, *Phys. Rev. B.* **53**, 12625 (1996).

12. M. Kemerink, L. W. Molenkamp, *Appl. Phys. Lett.* **65**, 1012 (1994).

13. K. A. Matveev, L. I. Glazman, H. U. Baranger, *Phys. Rev. B* **54**, 5637 (1996).

14. J. M. Golden, B. I. Halperin, *Phys. Rev. B* **53**, 3893 (1996).

15. J. M. Golden, B. I. Halperin, *Phys. Rev. B*, in press (1996).

16. K. A. Matveev, L. I. Glazman, H. U. Baranger, *Phys. Rev. B* **53**, 1034 (1996).

17. I. M. Ruzin, V. Chandrasekhar, E. I. Levin, L. I. Glazman, *Phys. Rev. B* **45**, 13 469 (1992).

18. G. Klimeck, G. Chen, S. Datta, *Phys. Rev. B* **50**, 2316 (1994).

19. C. A. Stafford, S. D. Sarma, *Phys. Rev. Lett.* **72**, 3590 (1994).

20. M. Stopa, private communication (1995).

21. H. Grabert, M. H. Devoret, Eds., *Single Charge Tunneling*, vol. 294 (Plenum, New York, 1992) and references therein.

22. G. Falci, G. Schon, G. T. Zimanyi, *Phys. Rev. Lett.* **74**, 3257 (1995).

23. K. A. Matveev, *Phys. Rev. B* **51**, 1743 (1995).

24. K. A. Matveev, *Sov. Phys. JETP* **72**, 892 (1991).

25. L. I. Glazman, K. A. Matveev, *Sov. Phys. JETP* **71**, 1031 (1990).

26. F. R. Waugh, M. J. Berry, C. H. Crouch, C. Livermore, D. J. Mar, R. M. Westervelt, K. L. Campman, A. C. Gossard, *Phys. Rev. B* **53**, 1413 (1996).

27. The interdot conductance G_{int} was measured with all gates energized and the outer two point contacts open. In order to account for the change in G_{int} caused by placing the outer two point contacts in the tunneling regime, the calibration of G_{int} vs. gate voltage was shifted by a small amount $\Delta V_{p2} = 3.0$ mV. The small splitting due to interdot capacitance $C_{int} = 18$ aF was added to the theory plot as described in (14).

28. We thank K.A. Matveev, J.M. Golden, B.I. Halperin, and M. Stopa for helpful discussions and A. Adourian, M.A. Eriksson, J. Hergenrother, J.A. Katine, J.G. Lu, and D. Ralph for experimental assistance. This work was supported at Harvard by NSF grant NSF-DMR-95-01438, by ONR grant N00014-95-1-0866, and in part by the MRSEC program of the NSF under award DMR-94-00396 and at UCSB under grant AFOSR F 49620-94-1-0158. C. Livermore and C.H. Crouch acknowledge support from the NSF Graduate Fellows Program and C.H. Crouch from the AT&T Graduate Research Program for Women.

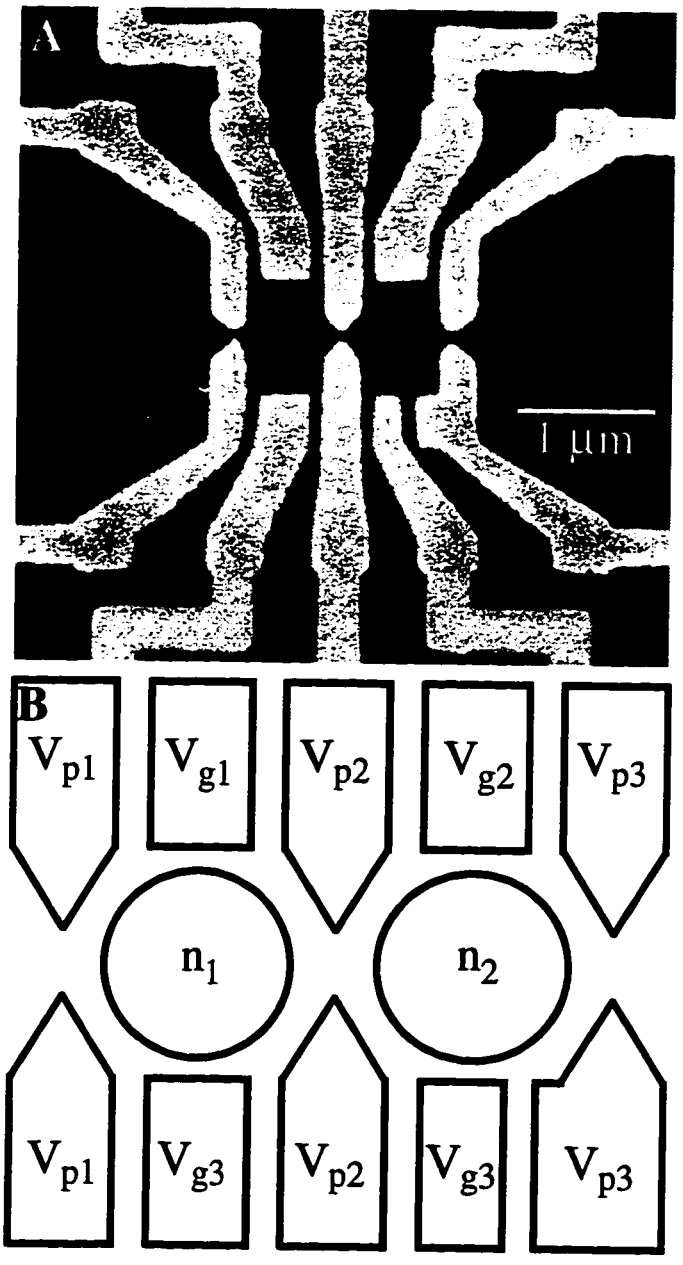

Figure A.1 (A) SEM micrograph of the series double dot device. Light regions are Cr/Au gates on the surface of a GaAs/AlGaAs heterostructure (dark area). (B) Schematic of device and wiring. All ten gates are energized to form the double dot. Gates labeled V_{g1} and V_{g2} are side gates used to control the excess charge on each dot. Gates labeled V_p are point contact gates used to separately control the dot-lead conductances and the interdot conductance. Identically labeled gates are wired together.

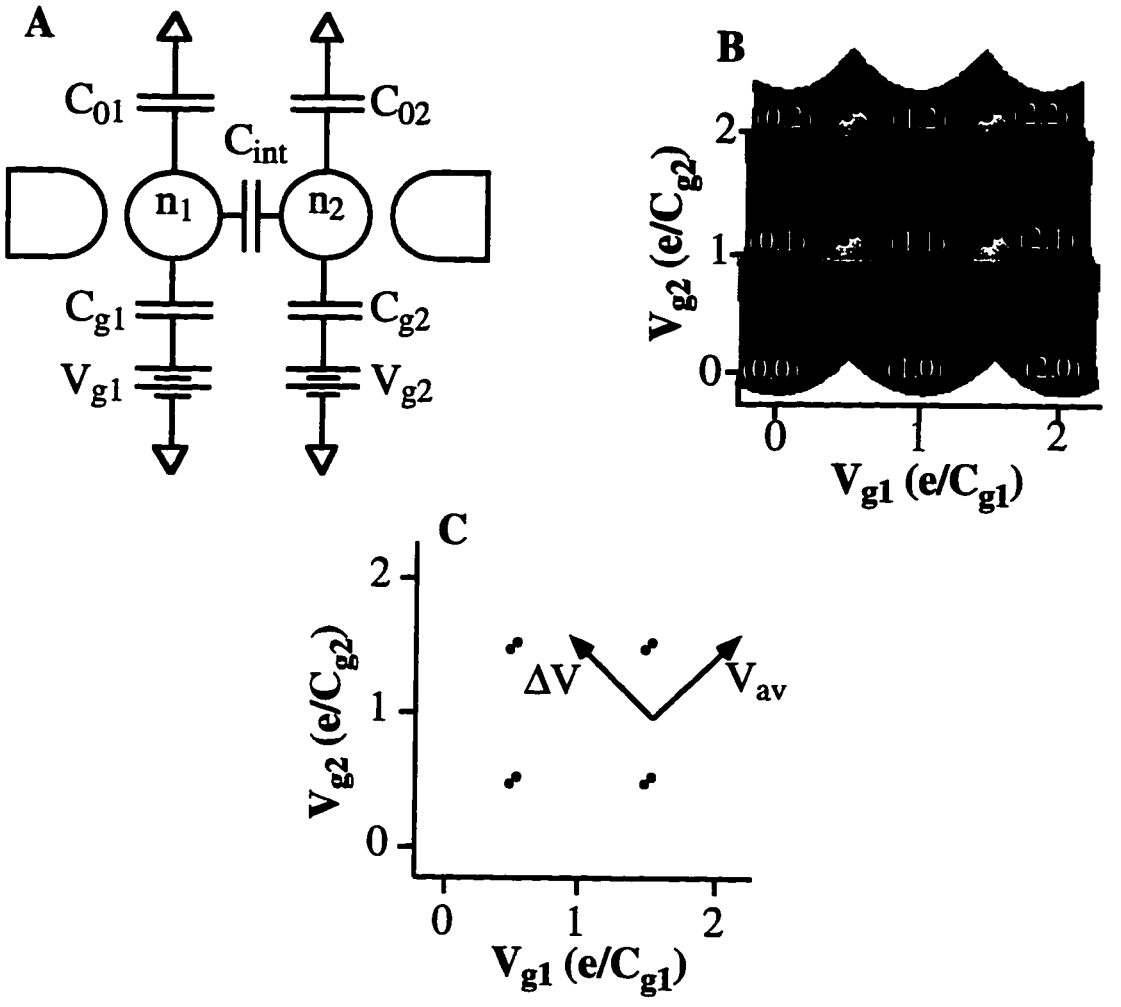

Figure A.2 (A) Simplified diagram of capacitive circuit model. Capacitances C_{g1} and C_{g2} represent capacitance from side gates to dots. Capacitance C_{int} represents a capacitive interaction between dots. Dot-lead capacitances and capacitances to constant voltage surface gates are included as part of the capacitances C_{01} and C_{02} to ground. (B) Grayscale plot of the minimum energy surface as a function of side gate voltages calculated from the capacitive model. Dark regions are minima of the energy paraboloids for given occupation numbers (n_1, n_2). Bright lines are intersections of paraboloids corresponding to different charge states. Bright vertices marked with dots are intersections of three paraboloids; these are the only places at which the Coulomb blockade is lifted and current may flow. (C) Diagram indicating the points at which current may flow in the capacitive model (dots). The direction of increasing average potential is shown by the arrow labeled V_{av}, while increasing potential difference is indicated by the arrow labeled ΔV. The slight separation of the pairs of dots in the V_{av} direction comes from C_{int} and is calculated using its measured experimental value.

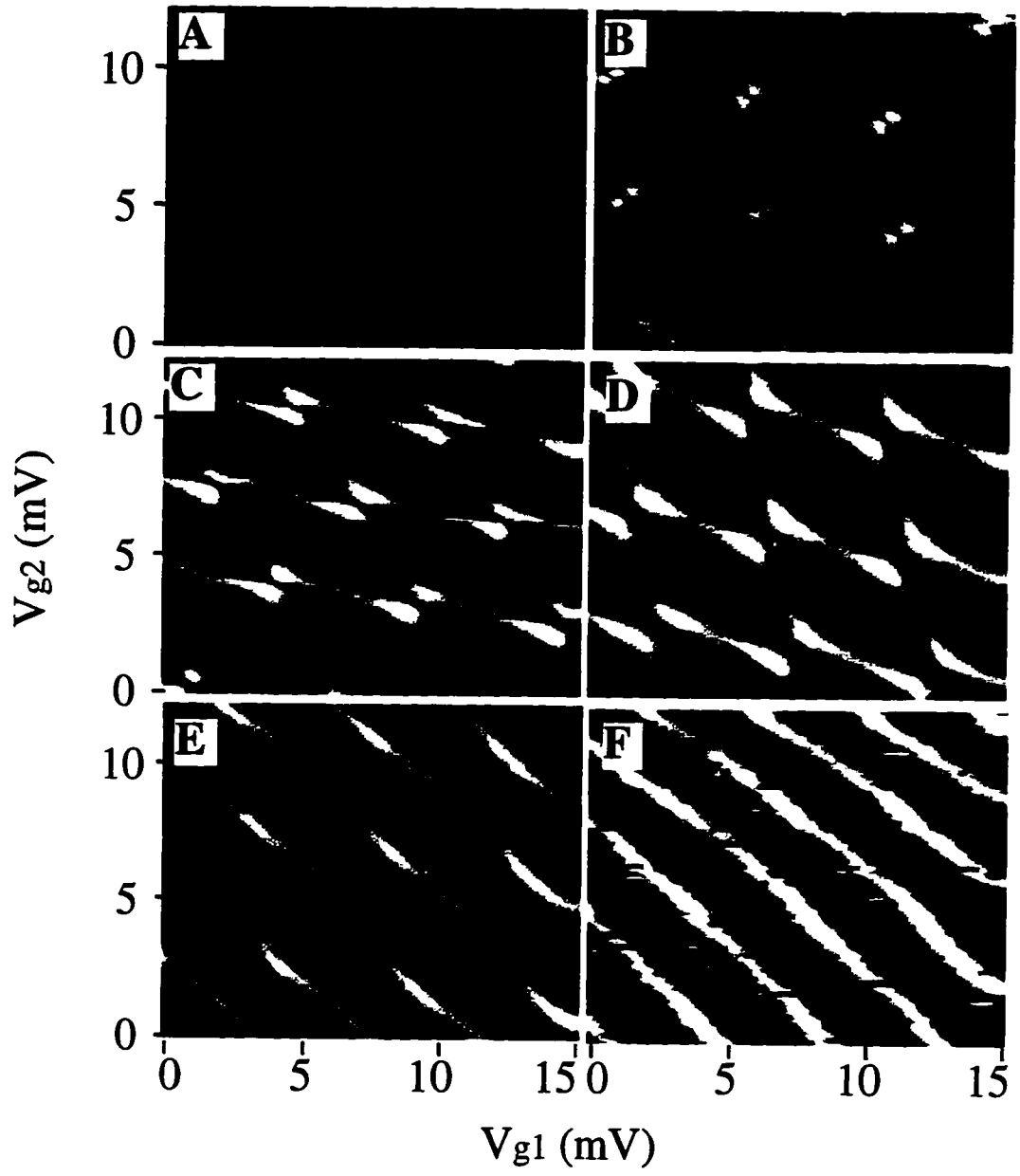

Figure A.3 Logarithm of double dot conductance as a function of gate voltages V_{g1} and V_{g2}, which are offset to zero. White indicates high conductance; black represents low conductance. Panels are arranged in order of increasing interdot conductance G_{int}. Interdot conductances are (A) $G_{int} = 0.22\ G_0$, (B) $G_{int} = 0.40\ G_0$, (C) $G_{int} = 0.65\ G_0$, (D) $G_{int} = 0.78\ G_0$, (E) $G_{int} = 0.96\ G_0$, and (F) $G_{int} = 0.98\ G_0$ where $G_0 = 2e^2/h$. Panel F is thresholded to a higher value of conductance than the earlier panels to accommodate a higher background conductance.

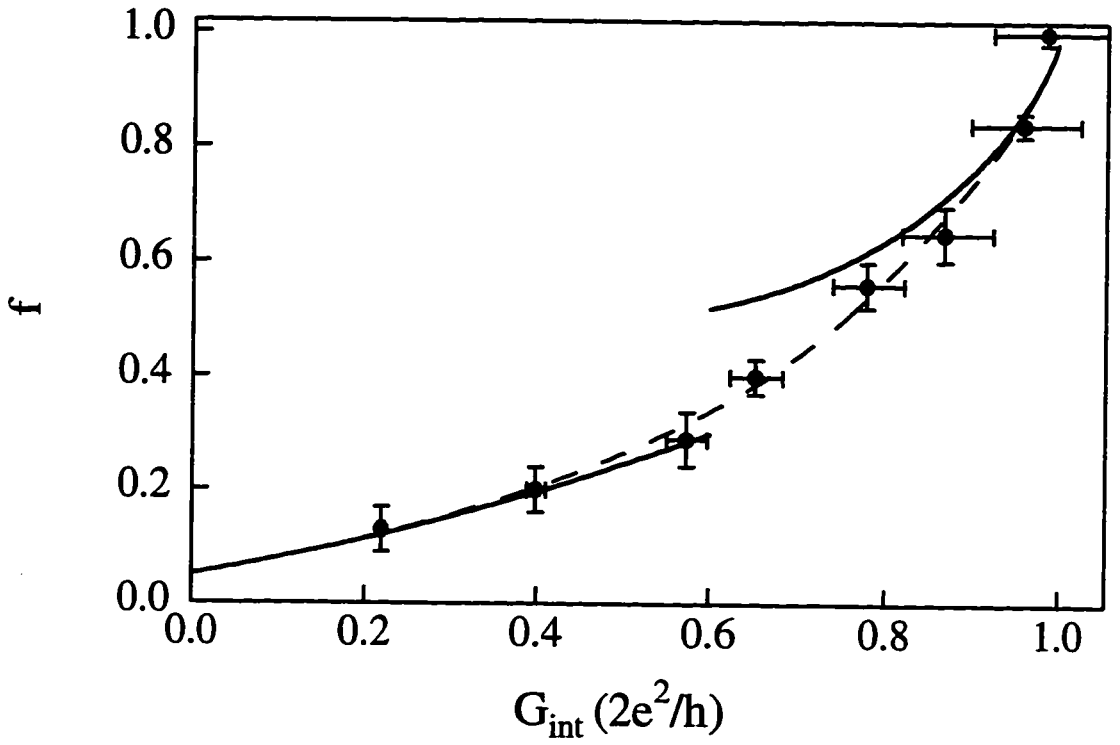

Figure A.4 Measured fractional splitting f (solid circles), theoretical fractional splitting (solid lines), and theoretical interpolation (dotted line) plotted as a function of interdot tunnel conductance G_{int}. Theoretical splitting includes both splitting due to interdot tunneling and the small splitting due to interdot capacitance.

APPENDIX B
ELECTRON BEAM LITHOGRAPHY

Over the last six years, the Westervelt group has developed a great deal of expertise in making nanostructures with ebeam lithography. The basic procedures have been well recorded in several theses [Berry, 1994; Yang, 1995]. However, the group is constantly learning new things about lithography, and in order to make sure that all we learn is preserved, Jordan Katine, Aram Adourian, and I have each included our own insights on the process in our theses. This appendix is simply my own procedure sheet which I use for e-beam lithography; since perhaps the most important aspect of good lithography is doing everything the same way every time, anyone who wishes to learn from my experience will learn most from seeing the whole procedure rather than isolated "hints". Note that this procedure sheet assumes you already know the very basic elements of sample mounting, SEM use, etc., so for a beginner it should be used in conjunction with the standard procedure sheet which Yuan Lu has made available.

A few general principles which are specific to writing small structures (such as coupled quantum dots):

1) As already stated, develop a procedure which you follow the same way every time. The SEM seems to be somewhat hysteretic, and it is more important than appears logical to do things in the same order, place the sample at the same height, use the same beam current, etc., every time in order to achieve reproducible results. (This is generally true but particularly important for structures which have little tolerance for error.)
2) Accurate focus is critical, far more so than accurate doses. As a rule of thumb, if the fine focus on one side of the chip differs from that on the other by more than about 50 units (who knows what those units actually are), your writing will only turn out well if you are lucky enough that the average focus really is the correct focus where you write. My best writing sessions have had fewer than 20 units difference from side to side,

and on one glorious day, I had exactly the same focus (within the 5 to 10-unit scatter which is normal for multiple measurements on the same side) on both sides.

3) The most likely causes of a tilted chip are, in order of decreasing likelihood: tilt of the sample mount within the sample holder, carbon paint under the chip causing the sample not to be flat on the mount, PMMA on the underside of the chip causing the same. Ways to deal with all three of these are discussed in the procedure list.

4) If the chip is flat, but the silver paint goes down gloppy, runny, and in large streaks rather than in tiny, dry flecks, focusing with this silver paint will be difficult.

5) There are enough things which you can forget, enough variability in the SEM performance from one day to the next, and enough things which a previous user can leave set up wrong on the SEM which you don't think to check, that it is best (though not essential) to start by writing a test pattern (which includes the entire device, because things can go wrong at large magnification), removing it with the detector off and the beam blanked but on, developing it, and examining the developed PMMA both under an optical microscope and the SEM. Once this has been examined, if all is well, you can immediately remove the test, insert your real sample (or if you're really brave, you can mount the real sample on the same mount as the test piece), and write the real sample. Most of the setup time is saved on the second writing – all you have to do is refocus, check the stigmation (which only rarely needs to be corrected substantially), and write. Likewise, if you have time, patience, and material, it is good to write several samples after you have confirmed that everything is working properly (or if something was wrong, after you have corrected for it). You can then develop and evaporate metal on only one, and if it turns out well, develop and evaporate on the others, saving yourself time in the future. Furthermore, if something goes wrong in the evaporation but it appears that the writing was fine, you can do another evaporation immediately rather than having to write again.

Note that once you get good at it, it takes about an hour (or slightly less) to remove a sample, develop it, inspect it under the optical microscope, remount it, inspect it under the SEM, and then load the new sample for writing. It will take longer if the new sample then has to be mounted onto the same mount, so it is helpful to have multiple interchangeable sample mounts.

6) There is almost always a way to get around most user mistakes. If you write the finest layer or the finest two layers with the wrong magnification or dose, move over fifty microns and start over. If a macroscopic part of your pattern didn't develop (because of C paint on the chip or some defect in the layer), you may be able to remove the intervening PMMA with a scalpel or press indium onto the chip surface in the gap after metallization. Nevertheless, mistakes are easier to deal with when one can start over (as in the first example), and it is best to anticipate possible errors and avoid them.

Sample preparation

1. It is best if the chip has smooth, square edges and corners; uneven edges and misshapen corners make it harder to orient the sample properly under the SEM and also make the chip difficult to handle without dropping it.
2. Make sure that the PMMA layer is even in the critical areas. For some samples, unevenness at the edges is not a problem. Small defects in the layer are very unlikely to be a problem for fine features (since the fine features are extremely tiny) but if they look likely to interrupt larger features (such as arms which go to gate pads), it is best to measure where they are under an optical microscope, figure out whether they will interrupt larger features, and if so, figure out if it is possible to shift the pattern to avoid such interruption. If avoidance is not possible, you can either chance it and see whether it works, or wash off the PMMA and start over.

Sample mounting

1. Use a brass SEM mount with a hole drilled in the top surface (off to the side so it doesn't interfere with mounting samples) for measuring beam currents.
2. Be careful to get the chip on the mount lying as flat as possible. Apply carbon paint to the two opposite edges in quick succession. (I generally do this by putting a dab of paint on each side close to but not touching the sample, then using a sharpened applicator to push paint into contact with the sample, without actually touching the sample with the applicator. Whatever you find easiest, practice several times with junk chips.) Use as little paint as possible to avoid paint oozing underneath the sample. After the paint has dried, hold the sample mount tilted under a low-power optical microscope in order to see for certain if the edge of the sample is flush with the sample mount surface. If not, carefully remove the sample from the surface of the mount and try again.
3. Check the consistency of the carbon paint before applying it; if too runny, it will go under the chip, but if too thick, it will be hard to push the paint toward the sample and hard to make the bond.
4. Avoid getting carbon paint on the surface of the chip if possible. Paint on the corners will obscure them, making it difficult to orient the chip. However, the primary danger of paint on the surface is that it will get into the exposed areas upon developing and metal will not stick to them.
5. Put Ag paint on sample mount for stigmation and focusing. Be sure not to put silver paint anywhere you might write (among other things, if the beam strikes silver paint while writing, it can scatter and selectively expose the PMMA in unexpected places), but be sure to get it on the level part of the PMMA rather than the edge. In general put silver paint as close as you dare to where you will actually write. Think about the large parts of your device when thinking about where not to put silver paint.
6. My technique for applying Ag paint to sample (PMMA layer):

   Break applicator to get a feathery point (help it with a scalpel if necessary).

Dip applicator in thickened Ag paint on the sides of the bottle (paste-like stuff).

Dry applicator on piece of filter paper, which should get lots of paint on the paper, and place paper and applicator under lamp to dry for 15 minutes or so. Test the applicator for dryness by smearing it on the filter paper and watching what comes off; then rub it in the dried globs of paint.

Hold the applicator parallel to the chip surface, with the tip above the area where you want paint flecks. Tap the applicator gently with your fingers (do not touch the surface of the PMMA). If everything is dry and you started with paint with lots of bits of Ag rather than just solvent, flakes of Ag will come loose onto PMMA.

Inspect under visual microscope to confirm presence of flecks.

Be careful not to scratch the PMMA (that's why you don't actually touch the chip surface). Scratches can usually be distinguished from paint under the high-power Nomarski microscope but will look shiny under low-power microscopes.

7. Don't dry the chip under the lamp for more than 45 minutes – carbon paint will crack. Ideally you mount the sample several hours before writing so that you can dry the sample under the lamp for only a few minutes, then let it dry the rest of the way at room temperature. It is very important that both silver and carbon paint be solvent-free, both for the vacuum in the SEM and because neither can do its job properly if there is significant solvent present.
8. Measure the location of the silver paint under the Nomarski high-power microscope. Then draw a picture of the sample on the mount indicating the locations of silver paint and carbon paint (as well as other landmarks on the mount and the orientation of the chip). Take this picture with you to write – it's very helpful in focusing to be able to start out focusing knowing where the paint is.

<u>Electron beam writing: Preparation</u>

1. Make sure instrument is in appropriate standby conditions (checklist taped to SEM chassis). In particular, make sure that Tilting Correct and Scan Rotation are both off--

either one even minimally activated will cause severe writing problems. Also make sure that the unmarked silver height adjustment knob (to the lower left of the loading port) is in the middle of its travel.

2. Place sample mount in sample holder and make sure that neither the screw which holds the sample mount in place or the plug that supports it from underneath pushes the mount away from level. The plug underneath can be removed – the sample mount will actually sit perfectly well in the holder without it, and it tends to be more level this way – but if you do this you should make sure you always do this, so that the sample height in the mount is the same every time. Be careful to turn the mount in the holder so that the chip edges are square with the insertion rod (which means they will be square with the x-y translation of the sample holder inside the SEM).
3. Check that the insertion rod is greased well (if not, the vacuum seal can fail as the rod slides into the chamber). Then load sample holder, making certain that it fits smoothly onto the dovetails in the SEM. Note that if the sample holder falls off the dovetails, it can be recovered by opening up the chamber, at the cost of a couple of hours. Yuan or an experienced group member should open up the chamber.
4. Move specimen out of the way--ideally move in the direction which will take the chip furthest away but still leaves you on the sample mount. Note that x = 19.1, y = 38.8 is located on the sample holder (not the brass sample mount, but the holder). Yuan recommends this position for saturating the filament because it gives a good, bright image and you know you are not endangering your sample.
5. Bring up brightness on both screens. Load appropriate conditions from memory. Adjust working distance if necessary manually (and then change it in the conditions). Most quantum dot patterns are written at 35 keV, working distance 15. Set scan rate to TV and mode to linescan (either on EOS p. 3 or on buttons).
6. Check that the filament button is turned fully counterclockwise (off), then turn on accelerating voltage.

7. Make sure detector is on (it's supposed to just come on when the voltage is turned on, I think, but it doesn't always do so). Set magnification to about 200x (it probably doesn't really matter) and CL to about 12 or 13. Adjust brightness and contrast until you can see a line on both screens (the room needs to be fairly dark). Turn filament up slowly (the whole process should take about a minute) until the second maximum in brightness (corresponds to vertical position of line) is reached, then back off very slightly. Typically saturation corresponds to about 220 on the filament current meter and clock position 11:00 on the filament knob.
8. Preliminary gun alignment adjustment: At CL 12 or 13, adjust x & y tilt to get maximum current (as read on PCD cup). Then go to CL 3 and adjust x & y shift to maximize current. Return to CL 12/13 and readjust shift (should not need much adjusting at all). After changing condenser lens, press Lens Clear, until the tilt and the shift have each been properly adjusted. Then check that they are still OK (and do fine adjustment if necessary) without using Lens Clear. Hereafter avoid Lens Clear entirely (like the plague).
9. Do a preliminary focus with the height adjustment knob referred to in point 1. Choose some consistent means of doing so; I find it convenient to focus on the surface of the sample mount (not the holder, since the two will be substantially dissimilar if the plug is removed from the bottom of the holder) so that relatively little focus will be needed with the electronic focus knob later. The key point is to start out with the electronic focus always corresponding to the same actual height of the sample, and since the height adjustment knob lacks markings, this must be done by focusing on something.
10. Let the beam continue to warm up so that it will have been on for 45 minutes to an hour before you start trying to do fine alignment (steps 11 and 12). This is a convenient time to see if you need to do anything to your patterns. If absolutely necessary, the sample holder can be inserted without the sample and the filament saturated, then removed with the beam blanked in order to insert the sample later. (This is useful if one is running

behind and does not have the sample mounted at the time that one's SEM session begins.) Double-check tilt and shift when the beam has finished warming up.

11. Center objective aperture: Find a place on the sample mount where there are some features at about 500x magnification (scratches or large streaks of silver paint are handy for this). Press Wobble button and adjust the two controls (I think that the one which faces the user is the side-to-side control and the one perpendicular to it is the vertical control). Repeat at about 10,000x and (if desired) at 20,000x (this last one probably doesn't make much difference).
12. Set stigmation: Find a piece of silver paint on the sample mount which has a reasonable amount of detail visible at 20,000x (and typically CL 13 or 14). Focus it and adjust x & y stigmators. The key to a well-stigmated image is that edges are crisp: so try to find a piece of silver paint with a fair amount of edge detail. Repeat stigmation up to about 80,000x if writing fine features. The final stigmation usually is best set on the chip surface, so don't be too perfectionist about the high magnification on the sample mount, but the better the stigmation you can get off the chip, the less you end up exposing the PMMA.
13. Repeat gun alignment, wobble, and stigmation (these things are interdependent) until all have stabilized at a good image. Normally each will only need to be done once and then fine-tuned slightly a second time.
14. Bring magnification down to about 500x, set CL to 14 or 15, and locate sample. Rotate sample as needed to bring it square with x- and y-translators.

To do this: Use a finger to mark where one edge intercepts the edge of the screen. Move sample so that the length of the edge travels through the field of view, noting whether the point of interception moves. Determine from this which way the sample is tilted and turn sample rotation knob (not scan rotation) in the same sense that the sample should be turned, turning it far enough that the sample edge intercept with the screen edge moves about halfway between where it started and where it ended. Repeat as needed

until sample moves squarely with x- and y-translators. If the sample mount has been set in the proper orientation within the holder originally, only a degree or two of rotation should be needed.

15. Increase magnification to a few thousand and record positions of corners, and calculate desired starting position for writing (usually chip center). Make a diagram in the lab book.

16. Set condenser lens to 15 and locate Ag paint on chip. Increase magnification to 20,000x and find a small piece of Ag paint for focusing (this is where the measured locations are helpful!). The best paint for focusing is small (probably not visible at less than a few thousand magnification, does not fill the screen at less than 60,000x or more) and very bright, and has sharp edges. Determine focus and record both focus and condenser lens at which focus was measured. Increase magnification to 60,000x and repeat (may even want to go to 80,000x depending on how good an image you want). Locate several other pieces of Ag paint and repeat. In particular, it's important to measure the focus at two extremes of the chip, but far enough in from the edge that the PMMA layer is basically level.

While still at the condenser lens used to determine the focus, set the focus for writing with either the average focus (usual, since generally paint is placed at both extremes of the chip equally far from the critical area) or the focus nearest the critical area. Record desired focus at the condenser lens and magnification at which it was measured, and do not change focus hereafter. If focus is accidentally changed, it must be reset at the appropriate condenser lens, because numerical focus values are dependent on condenser lens (the SEM software automatically changes focus when the condenser lens is changed to compensate for this dependence).

Since this compensation is not perfect, one should focus at or as close as possible to the condenser lens used to write the finest features, so if it is possible to focus at condenser lens 16, that is desirable. I generally find I can get a much better focus with 15.

16. Move sample out of the way (perhaps go a little beyond a corner) and prepare runfiles and measure beam currents. For the finest features to reproduce properly, it is best to use the same beam current every time. The beam current at the highest magnification can be fixed to the desired value by changing the fine condenser lens setting (move cursor to that place on the menu, then use +/- keys to change the value) and monitoring the value of the current as measured in a hole bored in the sample mount (to be discussed later). Then, keep this fine CL setting throughout the writing session, and change the coarse setting to the appropriate setting to measure the currents for coarser features. This procedure is only necessary for the finest beam current setting (typically CL 16); the higher currents can be measured in the PCD cup, because a small lack of reproducibility is not as important.

To measure beam currents in a hole on the sample mount:

Center hole in sample mount on screen. Go to 100,000x magnification (whatever will make it clear that the whole beam is going into the mount). Toggle white switch from "alarm" to "AEM" mode (switch is located next to NPGS control switch). This switch brings an ammeter into the current path from the sample mount to ground. The same meter which displays the PCD cup-measured currents will now show current through the sample. This current is consistently lower than the amount measured by the PCD cup, and appears to reproduce from run to run and filament to filament, whereas the PCD cup is more sensitive to the particulars of the filament. Allow current reading to stabilize over a minute or two before recording value.

17. Put PCD cup in place, turn brightness down on screens and on detector, and change to NPGS control. (Sometimes a bright spot appears on the screen when changing control switch, hence the precautions.) Set beam blanking to external and move sample into desired location for writing. Enter appropriate beam currents into runfiles and double-check that all parameters are set properly (for example, pauses appear before layers if that is desired, area doses and center-to-center point distances are correct). Set

magnification and condenser lens appropriately for first layer. Remove PCD cup and start!

While writing:

1 Always turn computer screen off before writing.

2. Always check magnification and condenser lens setting before writing.

3. To write at magnification less than 90x requires the scan speed to be set to slow (20) rather than TV. Pressing the button marked "slow" once in the scan controls switches to this speed (there are other slow speeds too). There are a different set of shifts with the slow scan speed, so again, develop a standard procedure for when to switch to the slow speed and measure the shifts appropriately. Writing goes faster at the higher magnifications if the scan speed there is faster, so I recommend switching just before writing high-magnification stuff. Putting in the PCD cup while pressing the button is comforting since typically the beam spot on the screen flashes, though it doesn't seem to actually affect the sample – just be sure to remove the PCD cup before resuming writing! Then, after writing, you must increase the magnification before you can switch back to fast scan rate, or bizarre things will happen (including the display screen going completely blank and seeming unresponsive to commands until the scan speed is restored to slow).

After writing:

1. Move the sample out of the way.

2. Restore CL to 16, magnification to about 500x.

3. Put PCD cup in.

4. Restore SEM control, turn beam blanking off.

5. Remove PCD cup – you should see an image of wherever you think you are on the sample mount!

Writing multiple samples:

1. Generally beam currents should not change much. It's worth double-checking them with the PCD cup since that only takes a moment. This of course means that you need to look at the current reading on the PCD cup as well as in the hole in the sample mount when measuring the current of the finest condenser lens setting.
2. Writing multiple samples is fastest if two chips are mounted on the same mount. You then just have to be extra-careful that you are always conscious of where you are on the chip and not inadvertently exposing one of the samples.
3. Samples can be removed from the SEM while the voltage is on *as long as the detector is turned off.* Also be certain that the insertion rod is well oiled so that the vacuum seal holds well while inserting and removing samples. (This is not general information for all SEM users, however; Yuan prefers that only experienced users do this, since if the chamber is accidentally vented with the filament on, the filament breaks.) Since removing the sample requires dragging it directly under the beam, it is also a good idea to blank the beam and insert the PCD cup before putting the sample in place to be removed. On replacing the next sample, don't forget that the working distance will need to be changed again.

Viewing developed PMMA

1. Though it seems counterintuitive, the best contrast is actually obtained with 35 keV at condenser lens 16 (even though 15 keV is better for viewing metallized structures; sometimes condenser lens 15 can be helpful in initially locating the pattern).
2. Proper stigmation is critical, so if starting a new session (rather than reinserting a just-written sample) be sure to put silver paint on the sample or at least on the mount.
3. The biggest challenge is finding the written regions: so it is easiest to view PMMA if there is a broad line connected to the pattern which runs off the edge. You can then focus on the edge at low magnification, move to where the part which runs off the edge should be, and focus on that line, then follow it to the finer parts.

4. The second biggest challenge is that the contrast (at least for me) is counter-intuitive; the developed regions are darker than the undeveloped PMMA. It is easy to confuse foreground and background in the initial focusing.
5. When viewing the very finest parts of the pattern, bear in mind that prolonged exposure will damage them. Switching in the PCD cup or switching beam blanking on while viewing can be a good strategy because the image on the screen will linger for a while.
6. Use the averaged screen and spend a while adjusting brightness and contrast on a noncritical area so that everything is set just right before viewing the critical regions.

APPENDIX C
OXFORD MODEL 200
DILUTION REFRIGERATOR OPERATION

Most of the information needed to operate the Oxford Model 200 $^3He/^4He$ dilution refrigerator is contained in the manual, specifically the version kept in a black binder which has handwritten notes added by many different users.[1] (One of these days someone should find the original word processing file and update it.) This appendix is simply a compilation of some additional things which I learned about the fridge during my two years of operating it, things which are too complex to simply add as a handwritten note in a margin. A copy of this appendix will be added to the black binder awaiting the day when the manual will be updated.

C.1 Top Loading Considerations

One feature of the Model 200 which is wonderful when it works and extremely aggravating when it does not is that it is top-loading. Over the last two years, Carol Livermore and I have learned a number of things about what makes for a good or bad top-load. The most striking and non-intuitive things we've learned are recorded here. First of all, the liquid helium precooling of the top-loading siphon and slug is critical to the success of a top-load (if success is defined as not boiling off all the mixture), but there are many things that can go wrong. The most surprising failure modes proved to be related to the threaded copper endpiece of the top-loading siphon. The only thermal contact the slug has to the siphon is by screwing onto this piece. A cursory inspection of the copper endpiece when attached to the siphon would lead anyone to believe that the copper endpiece screws tightly onto the siphon and thus must be in good thermal contact with the siphon. However, after a series of disastrous top-loads in which the mixing chamber was

[1] Jack Hergenrother deserves primary credit for writing most of the notes and corrections; over time, Jia Lu, Carol, and I have added a few, and I'm sure other users will continue to do so.

consistently heated up to 4 K (or even warmer), Jack Hergenrother, Jia Lu, and we discovered that this was not to be taken for granted – there is a gap between the end of the siphon and the copper end piece, so the only thermal contact provided was by the threads. Furthermore, the threads had become rather mangled by the set screw which holds the copper endpiece in place on the siphon, and they were also dirty, further increasing the thermal resistance. The solution: stuff a small wad of copper wool inside the copper endpiece to fill the gap, touch up the threads (courtesy of Louis DeFeo in the McKay machine shop), and clean them well. Also be sure before top-loading that the threads on the copper endpiece and the matching threads inside the hole on the end of the slug are clean (clean with isopropyl alcohol or acetone and methanol and blow dry) and that no grease from handling the greased top-loading siphon gets on them.

Carol and I had a rather exciting unload once when we pulled up the siphon expecting to find a slug on the end, and found no slug. This happened when the threads on the tip of the copper endpiece became sufficiently worn that they no longer held the slug well. To solve this problem, we had Louis DeFeo make a new endpiece. He made two, so there is a second spare endpiece, which is kept, along with the drawings and the die and tap for the left-handed thread, in Carol Livermore's drawer in McKay 209. To avoid such excitement in the future, the threads on the endpiece should always be inspected before top-loading, and Louis can touch them up if they are getting a little crumpled but are still serviceable. One problem is that it seems that the Westervelt and Tinkham slugs are slightly different, and thus attach to both siphon and tailpiece slightly differently.

In general, precooling the siphon for top-loading is a rather finicky process, requiring the siphon to be properly pumped out (which can fail when removing it from the valve used to pump on it), all the fittings on the siphon assembly to attach properly to the helium delivery siphon (also very finicky – I recommend greasing the O-rings each time and sighting along the entire assembly to be sure that it is basically straight and not strained in any fashion), and the circulation process to go smoothly. For unknown reasons, it

seems that circulating LHe at excessive pressure (> 4 psi) or for too long (> 25 minutes with slug on the end, > 15 minutes without slug) can cause the siphon to go soft (probably an O-ring freezes somewhere). If the siphon becomes frosted anywhere other than at the crosspiece where it mates to the LHe delivery system, probably the stick has gone soft, and the top-load should be aborted (even if you don't care about warming up the mixing chamber, if you try to lower the frosted stick, it will probably freeze and get stuck; you also risk getting ice into the IVC and compromising the vacuum seal through which the stick slides). It is worth being very picky about the top-loading and unloading process and making sure that all the indications are positive (and monitoring the pressure on the LHe bath, since regulators have been known not to do their job well!) before proceeding, since it will generally take at least an hour to recondense the mixture if it all boils off, not to mention additional time for the fridge to cool back to base temperature.

Finally, we have sometimes wondered if samples which proved to be "blown up" (i.e. destroyed by static electricity) when we measured them met that fate in the toploading process. We discovered that the toploading siphon is actually electrically isolated from the fridge body (which made sense when we thought about it, because there are O-ring seals at every connection), and thus it is conceivable that in dry weather, as the siphon slides into the fridge, the whole assembly builds up some static charge, and then when the slug touches the electrical contacts at the bottom (which are grounded to the fridge body during top-loading), it encounters a substantial potential difference, leading to a large electrical shock. To protect the sample against this possibility, we connected one end of a very long grounding wire to the fridge body and the other end to the crosspiece where the shaft of the top-loading siphon and the LHe circulation assembly cross. It is slightly awkward to hold the grounding wire in place on the crosspiece while turning the siphon to load or unload a sample, but not impossible. While it's not clear whether this grounding wire was responsible, we have not had any samples blow up since in four or five top-loads.

C.2 Electrical connections

C.2.1 Sample wiring

Anyone who uses the Model 200 should know that lead 7 on the tailpiece is connected to pin 15 of Fischer connector #3 (the rightmost connector which carries the signal wires). This was done somewhere back in dark history of the fridge because there is a short between lead 7 and the microwave filters; so lead 7 is diverted to connect to lead 15 somewhere below the microwave filters. As a result, lead 7 does not have any microwave filtering on it. First, it is important simply to know this (so as not to panic when it appears that whatever gate is attached to lead 7 is not connected). Secondly, it appears that if lead 7 is connected to the ohmic contacts of the sample, the fridge will not cool quite to base temperature (the loss is slight, with base being about 30 mK rather than 15 mK), and possibly the sample is somewhat noisier. (It is always difficult to distinguish whether noise is coming from the sample itself or from the variable background noise of the environment, and since it required a thermal cycle to change the wiring, it's not straightforward to compare results obtained with and without lead 7 on the ohmic contacts.) However, it seems that lead 7 functions perfectly well when attached to a surface gate (and the fridge achieves expected base temperature), so fridge users should not go to any length to avoid using lead 7, at least for GaAs/AlGaAs split-gate devices. (If one or more leads are not needed for an experiment, however, then by all means lead 7 should be the one not used.)

C.2.2 Sample slug

One frustration of working with the Model 200 is that its sample slug is not compatible with the sample mounting systems of the other cryostats used by the Westervelt group. Past users from the group have mounted their samples on D-shaped pieces of PC board ("D"s) and connected sample to PC board and PC board to fridge slug by means of

indium and gold wire.[2] (The wires on the fridge slug are soldered to another piece of PC board with blobs of indium soldered to the ends.) It seems nearly impossible (or at least beyond the creativity of this author) to devise a simple way to connect a wire-bondable sample mount to this slug. The situation is as follows: It is not possible to fit one of the sockets used in the Kelvinox 100 and the ^{3}He evaporation refrigerator into the slug such that the plane of the sample would be perpendicular to the axis of the slug,[3] even if the socket were substantially shaved down. A piece of the socket which is small enough to fit (i.e. a corner) has been tested, but does not grip the chip carrier tightly enough for reliable electrical connection. Thus using a standard socket does not seem possible.

The next possibility considered was making a custom mount for just a chip carrier (a carrier is shown schematically in Fig. 3.4(b)). The simplest possibility seemed to be to solder wires to half of a chip carrier, connect those wires to male Microtech connectors, and attach female Microtechs to the wires on the slug. The sample could then be wire-bonded to the chip carrier while the Microtechs were attached to a grounded pair of Microtechs, and then the carrier could be connected to the slug. Unfortunately, the Microtechs proved very difficult to handle, because unlike the sample mount used by the Tinkham group in which the Microtechs are supported by a piece of PC board, these were simply "free-standing" and were difficult to grip and align. Furthermore, the solder joints holding the wires into the Microtechs, most likely weakened by the jerking which they received in the connecting process, proved fairly unreliable; we loaded the one sample which was mounted in this fashion four times and each time one or two connections (different ones each time) proved bad.

There are a number of possibilities which remain but which we did not take the time to try. If the main goal is to wire-bond the sample to the next layer of connections, but one

---

[2]The similarity to chewing gum and string has not been lost on this author, as in "held together with bubble gum and string."

[3] The field from the 7 T magnet is parallel to the axis of the slug, and the usual reason to use the magnetic field is to put the sample in the quantum Hall regime, namely, in a strong magnetic field perpendicular to the plane of the 2DEG.

is willing to continue attaching that layer to the slug with gold wire and indium, then the obvious solution is to use a PC board D as at present, but have gold pads electrically connected to each indium blob and wire-bond the sample to the D. This would eliminate the painstaking hand wiring of the sample, which would be an improvement. The only tricky issue would be finding space for both gold pads and indium blobs such that there was room for the wire bonder wedge to make wire bonds without getting stuck in the indium, but also such that the gold pads were well positioned for making contact to the sample. (Unfortunately soldering indium to the pads after wire bonding seems a rather risky alternative, although in the midst of the failures with the first chip carrier mount I did solder to wires which were electrically connected to the sample a number of times, to no apparent ill effect. The possibility of getting indium solder on the sample is also a substantial risk.) This solutions does not make the sample transferable to the other fridge or the ^{3}He evaporation refrigerator, but that seems unlikely since it is not possible to fit even a whole chip carrier in perpendicular to the slug axis without hollowing out the entire slug.

To eliminate indium and gold wire entirely, some more elaborate system involving Microtech connectors or some custom-built connector (analogous to the dip sockets used for IC's) would be required. One could imagine making a piece of PC board to attach to the D by means of soldered copper wires before mounting the sample; the D could then be oriented perpendicular to the slug axis and the other piece laid on the flat part of the slug, with the wires turning the corner. The second piece of PC board could be connected to the slug with Microtechs in the same manner as the Tinkham group header system (which has generally proved successful). One could also imagine designing some sort of custom PC board mount which half a chip carrier could be pressed into (like an IC), and connecting that PC board to the rest of the slug with soldered wires. (Thus the PC board mount would be a permanent part of the slug and only the chip carrier would be removed.) This solution would possibly make samples portable into other systems, although the leads which would need to be used on the half chip carrier might not all correspond to leads which are

connected on the sockets in the other dewars. Since both of these solutions required more work than we had time for (the first because gold plated PC board takes a while, the second because it was unclear how to design such a mount which would be reliable at low temperatures), neither has been tried.

C.2.3 Temperature controller

A frustration which may be particular to GaAs/AlGaAs users is that the automatic resistance bridge temperature controller does not work (it does not reliably keep the mixing chamber to the set value, but typically overheats or overcools it). Carol and I have not made a thorough effort to fix this for two reasons: First of all, the cooling power of the fridge is steady enough that if the mixing chamber heater is set to some carefully selected value, it is pretty straightforward with about five minutes of manual controlling (which always has to precede auto-controlling anyway) to get the fridge to the desired temperature, and then just leaving the heater at that value generally is sufficient for temperature stability within a couple of mK over the ten to fifteen minutes that our measurements make. (This is true for temperatures below about 750 mK; once the fridge gets warmer, it is more persnickety. We have successfully controlled manually to temperatures as warm as 1350 mK, but it requires more continuous attention to keep the fridge temperature steady above about 750 mK, probably because it seems to require circulating without the booster pump.) So, we have not bothered to mess with it much since we can do without it. Furthermore, the one time that we seemed to have gotten the auto-controller to work (sort of), the measurement we made was very noisy, so we concluded that the auto-controller was an unacceptable source of electrical noise.

It should not be too difficult to figure out what is wrong with the auto-controller and either fix it, if the problem is in the cables, or conclude that the problem is in the controller and replace it (or borrow the one from the Kelvinox 100 to double-check). I've just never had the time to do it, given that the time involved in manually controlling is not too great. Whether the electrical noise introduced by the auto-controller is a symptom of the

problem or reflects bad design is not clear to me. It would be very nice to have a working controller, however, because then the experimenter could be free from keeping an eye on the temperature during measurements and could do more productive things.

C.3 Maintenance

C.3.1 Utility diffusion pump

Another adventure in dealing with the fridge was having the small utility diffusion pump fail while maintaining outward signs of functioning. Presumably the reason it failed was that it had been on without being backed for the better part of a week when the small rotary pump usually used to back it was being used to pump on the 1K pot. However, it still made the appropriate crackling sounds, deceiving us into thinking it was working. When three top-loads in a row had failed by the stick frosting up, I was certain that the problem was the stick going soft, but thought it likely that there was actually a leak in the stick (or in the valve used to pump it out so that when the valve was closed the stick leaked). Jack Hergenrother finally guessed that the problem was that the stick was not actually getting pumped out; this was verified when we pumped out the stick with a pump cart and had a successful topload.

Unfortunately, since the Penning gauge which is supposed to monitor the pressure at the head of the utility diffusion pump failed long ago, what should have been an easy problem to catch was made difficult because we'd gotten used to relying on the sound of the oil crackling and the backing pressure to tell us if the pump was working. When we attached a borrowed gauge to measure that pressure, we found that it was only pumping to 10^{-2} torr – essentially the roughing pump was just pumping through the diffusion pump. Even more unfortunately, we had used this pump to pump on the IVC while doing three failed and one successful top-load, and we discovered a couple of days later that indeed an enormous amount of junk had cryopumped into the IVC during that time, when the fridge began behaving strangely (this will be described shortly).

The final mystery with this pump was that it was never obvious what was wrong with it (other than that it would not pump). We drained the oil out; the full 75 ml charge was there and was not even noticeably discolored. We leak-checked the pump (in a sense) by pumping on it with a pump-cart, and were able to pump to the pump cart's base pressure (low 10^{-6} torr). We concluded that the problem must have been the oil because once we put in new oil, the pump worked reasonably well again (pumping to low 10^{-5} torr range). We attributed this somewhat degraded base pressure to the warmth of the cooling water, which would mean that the oil would not condense as effectively on the pump walls (it was summertime, and the cooling water used on the Model 200 is just municipal water, since the fridge was installed before the chilled water system was put into McKay).

C.3.2 Gas in the IVC

Another strange experience I have had a number of times with the Model 200 (though presumably this could happen to any fridge) is that when air gets into the IVC, it can take days for this to show up as a loss of base temperature or general malfunctioning. In February 1996, the fridge began to unaccountably warm up two days after doing a top-load, and over the course of a few hours reached 4 K and stayed there. On connecting the utility diffusion pump to the IVC, we saw that there was a lot of stuff in it (high backing pressure, ~0.5 mbar, which persisted for thirty minutes or so). Pumping out the IVC overnight with the baffles open and the fridge briefly warmed up a little above 4K (by toploading a slug which was only radiatively precooled) solved that problem.

C.3.3 Leaks

In June 1996, a leak developed through Fischer connector #3 (the one to which the sample switcher box attaches). For three days, every time we filled the 1K pot, the mixture all boiled off. However, pumping on the IVC did not reveal any significant pressure (though that may have been because the diff pump was out of commission and we had to use a turbo pump cart in which we actually monitored the IVC pressure rather than a

backing pressure). We thus concluded there was liquid in the IVC and warmed up the fridge to 6 K or so (this time by turning all the heaters to their maximum power, filling the 1K pot and ceasing pumping on it, and opening the baffles) to pump out the IVC (again having baffles open is critical to effective pumping). We did this twice, pumping out the IVC for twelve hours or so, and each time thinking that we'd solved the problem. The first time that the problem recurred, we assumed the problem was because we'd used the pump cart and pumped through the manifold which connects the IVC and OVC lines, which is fairly low conductance; we figured we just hadn't pumped long enough given the diminished pumping power. By this time we had fixed the utility diffusion pump and were able to use it (again there was not much rise in backing pressure even with the fridge warm). After the second time of pumping out overnight, we were able to fill the 1K pot without incident, but then upon transferring LHe into the bath the next morning, the mixture boiled off again. At this point, we realized that we had to warm the fridge up at least to 77K and pump out the IVC and leak-check it. Upon warming to 77K we found that the leak was even worse, and at room temperature it was impossible to pump down the IVC. It finally occurred to someone that the Fischer connector might be leaking, and indeed it was. It's not clear whether the leak worsened over time or whether it didn't appear as bad at first because while cold the cryopumping action of the IVC compensated for the leak.

C.3.4 1K pot valve

For eighteen months (November 1994-May 1996) we operated the fridge with the 1K pot main fill valve not working very well (to open it when the fridge was cold required removing the threaded cap which was supposed to open and close it and using Vise-grip pliers to simply pull it up to the end of its travel; closing it was just a matter of pushing it back down). We initially thought that we would have to open up the fridge to fix it. However, in April 1996 when we did have the fridge open, we realized that all that was needed was to undo the set screws which held it in place and pull out the long needle assembly (which is about four feet long). We had feared that the tip of the needle was

mangled, but it was in perfect condition. We then cleaned it thoroughly and replaced the O-rings, and because the shaft had been covered with grease and metal filings (which we surmised came from the threaded cap), thought we'd solved the problem. However, when we replaced it and checked to see if the valve was closing properly (by pumping out the pot and then watching its pressure with the valve closed and the pump disconnected), we saw there was a substantial leak (> 20 mbar/minute) from the pot to the main bath. The problem turned out to be that the head of the assembly (the part which forms the vacuum seal up at the top of the fridge) was slightly misaligned on the shaft (presumably somehow all the jerking around with pliers had bent it). Louis DeFeo adjusted the assembly so that everything was properly centered (it had only been out of true by about .01 inch, but the shaft is four feet long, so that put the needle way out of place!) and also polished the head, which was somewhat scarred, on the lathe. One or both of those two treatments solved the problem, and the needle valve now opens and closes with very little effort.

C.4 Ways to improve the fridge

Recommendations for anyone who has time to overhaul the fridge in significant ways (rather than just keeping it functioning):

1) Redo the cooling water system for the utility diffusion pump and booster pump so that they are cooled by the McKay chilled water system rather than municipal water. When running the fridge in warm weather, I've noticed that the return line from the pumps is hot to the touch. The utility diffusion pump only achieved a base pressure of about 1×10^{-5} torr (measured by borrowing the high-vacuum gauge from the Tinkham group's turbo pump cart) even after an oil change in this warm weather, which Steve thought could be attributed to the cooling water not being sufficiently cold. The pump seemed to do better when the booster was shut off and thus the water was only cooling the utility pump.

2) Ask the machinists whether there is any way to redo the fittings on the top-loading siphon and helium delivery siphon so that the circulation of LHe through them is a

less tenuous process. Presently the system is very finicky, as will be apparent to anyone the first time he or she tries to assemble it!

3) Also see whether there is any way to improve the valve used to pump out the insulating vacuum space in the top-loading siphon. This valve occasionally fails when it is closed and the stick is pulled out of it, causing the stick to go soft and the top-load to then fail (by the stick frosting up).

4) Replace the Penning gauge which measures the pressure at the head of the utility diffusion pump.

5) Fix the automatic temperature controller (and eliminate the noise it introduces into our measurements if fixing it does not also alleviate the noise).

6) Rebuild the slug to close up the primary opening through which radiation can come (as discussed in Chapter 3).

7) Improve the sample mounting system in the slug (as discussed in C.2.2).

C.5 Acknowledgements and thanks

(I wanted to say more about this than there was room for in the main acknowledgements, since many people use this fridge and work together very closely.)

Jack Hergenrother has contributed enormously to both the mechanical functioning of the fridge and the smooth (or as smooth as can be expected) process of sharing responsibility and use of the fridge. I have been very impressed with Jack's willingness to give of his time and expertise even once he was no longer a primary user of the fridge. He has also modeled graciousness and patience in coordinating the use of the fridge between the two groups; sharing so significant a piece of equipment is tricky at best at times when everyone wants it, and he has sought to keep the process not only fair but amicable. From being willing to be called at home with questions the first time I was running the fridge to his capable coordination of the last disassembly and reassembly, Jack has been an

indispensible colleague and coworker, and has gone beyond expectations to serve the rest of us.

All the rest of the fridge users have also been part of the smoothness of the process, in their willingness to lend a hand when either actual hands or troubleshooting was needed, and their willingness to be flexible with the uncertainties of experimental physics. I also am grateful to Steve Shepard for helping with problems with vacuum systems even though the fridge is technically not under his jurisdiction.

Louis DeFeo and the machinists in the Gordon McKay machine shop are outstanding. I have always found them to be helpful when I've gone to them with some mechanical object or vacuum system which is not working for some unclear reason. I highly recommend taking advantage of their expertise and thanking them often!

APPENDIX D

CODE FOR THE SELF-CONSISTENT CALCULATION

The following code is written to be included in an Igor Pro (version 3.0 or more recent) experiment as a procedure. To run it also requires tables of the parameters C12 and C22, which I have not included because these tables have 1000 rows; however, these tables can be obtained from John Golden or from Catherine Crouch (saved in the Igor experiment Ch. 5: ddIV analysis 3/11/96). There are two different routines, one which finds the threshold voltage in the weak tunneling limit (FindVthreshlow) and one which finds it in the strong tunneling limit (FindVthreshhigh). The numbers are obtained using the capacitances of sample KC7EE (the same calculation was performed with slightly different numbers reflecting the different sample capacitances for sample KC3Q).

```
Function FindVthreshlow(Vsoln, coeff12, coeff22)
    Wave Vsoln, coeff12, coeff22
    Variable/D rho, rhotest, g, Vthresh
    Variable gindex
    rho=-0.140
    rhotest=0
    gindex=0
    do
        g=gindex*0.01
        do
            Vthresh=-3.011719235e-04 + 2.881981224e-05*g*((2+rho)*ln(2+rho)-rho*ln(-1* rho-(1-rho)
                *ln(1-rho)-(1+rho)*ln(1+rho)) +2.844401504e-04*g^2* (coeff12(1+rho)-coeff12(abs(rho))
                +2*coeff22(1+rho)-2*coeff22(abs(rho)))
            rhotest=468*Vthresh
            rho=0.5*(rho+rhotest)
        while (abs(rhotest-rho)>0.0001)
        Vsoln[gindex]=Vthresh
        gindex=gindex+1
    while (gindex<101)
End


Function FindVthreshhigh(Vsoln)
    Wave Vsoln
    Variable/D rho, rhotest, g, Vthresh,arg0,arg1
    Variable gindex
    rho=-0.140
    rhotest=0
    gindex=0
    do
```

```
        g=gindex*0.01
        do
            arg0=1.570796327*rho
            arg1=arg0 + 1.570796327
            Vthresh= -1.4027e-04 + 1.1533e-04*(1-g)*((cos(arg0))^2*(ln((1-g)*(cos(arg0))^2)-0.4627)-
                (cos(arg1))^2*(ln((1-g)*(cos(arg1))^2)-0.4627))
            rhotest=468*Vthresh
            rho=0.5*(rho+rhotest)
        while (abs(rhotest-rho)>0.0001)
        Vsoln[gindex]=Vthresh
        gindex=gindex+1
    while (gindex<100)
End
```

REFERENCES

Adourian, A. S., Livermore, C., R. M. Westervelt, K. L. Campman, and A. C. Gossard (1996a). "Single-electron charging in parallel coupled quantum dots," to appear in *Microstructures and Superlattices.*

Adourian, A. S. (1996b). "Single-electron transport in parallel coupled quantum dot nanostructures," Ph.D. thesis, Harvard University.

Altshuler, B. L., P. A. Lee, and R. A. Webb, eds. (1991). *Mesoscopic Phenomena in Solids* (North-Holland Elsevier Science Publishers B. V., Amsterdam).

Ashcroft, N. W., and N. D. Mermin (1976). *Solid State Physics* (Saunders College, Philadelphia), 689.

Ashoori, R. C., H. L. Stormer, J. S. Weiner, L. N. Pfeiffer, K. W. Baldwin, and K. W. West (1993). "N-electron ground state energies of a quantum dot in magnetic field," *Phys. Rev. Lett.* **71**, 613.

Averin, D. V., and K. K. Likharev (1991). "Single Electronics: A Correlated Transfer of Single Electrons and Cooper Pairs in Systems of Small Tunnel Junctions," in *Mesoscopic Phenomena in Solids*, eds. B. L. Altshuler, P. A Lee, and R. A. Webb (Elsevier), p. 173-271.

Averin, D. V., and K. K. Likharev (1992). "Possible applications of the single charge tunneling," in *Single Charge Tunneling*, ed. H. Grabert and M. H. Devoret (Plenum Press, New York), 311.

Averin, D. V., A. N. Korotkov, and K. K. Likharev (1991). "Theory of single-electron charging of quantum wells and dots," *Phys. Rev. B* **44**, 6199.

Bakhvalov, N. S., G. S. Kazacha, K. K. Likharev, and S. I. Serdyukova (1989). "Single-electron solitons in one-dimensional tunnel structures," *Sov. Phys. JETP* **68**, 581.

Baskey, J. H. (1994). "Transport and capacitance measurements of electron multilayers in wide parabolic quantum wells," Ph. D. thesis, Harvard University.

Beenakker, C. W. J., and H. van Houten (1989). *Phys. Rev. B* **39**, 10445.

Beenakker, C. W. J. (1991). "Theory of Coulomb-blockade oscillations in the conductance of a quantum dot," *Phys. Rev. B* **44**, 1646.

Beenakker, C.W. J., and H. van Houten (1991). "Quantum transport in semiconductor nanostructures," in *Solid State Physics*, vol. 44, ed. H. Ehrenreich and D. Turnbull (Academic Press, San Diego), 1.

Bennett, C.(1995). "Quantum Information and Computation," *Physics Today* **48** (10), 24.

Berry, M. J. (1994). "Mesoscopic transport and quantum chaos in ballistic quantum billiards," Ph. D. thesis, Harvard University.

Berry, M. J., J. H. Baskey, R. M. Westervelt, and A. C. Gossard (1994a). *Phys. Rev. B* **50**, 8857.

Berry, M. J., J. A. Katine, R. M. Westervelt, and A. C. Gossard (1994b). "Influence of shape on electron transport in ballistic quantum dots," *Phys. Rev. B* **50**, 17721.

Berry, M. J., J. A. Katine, C. M. Marcus, R. M. Westervelt, and A. C. Gossard (1994c). "Weak localization and conductance fluctuations in a chaotic quantum dot," *Surf. Sci.* **305**, 495.

Black, C. T. (1996). Ph.D. thesis, Harvard University.

Blick, R. H., R. J. Haug, J. Weis, D. Pfannkuche, K. von Klitzing, K. Eberl (1996). "Single-electron tunneling through a double quantum dot: the artificial molecule," *Phys. Rev. B* **53**, 7899.

Blick, R. H., R. J. Haug, K. von Klitzing, K. Eberl (1996). "Photon-assisted tunneling through a double quantum dot," *Surf. Sci.* **361/362**, 595.

Brody, T. A., J. Flores, J. B. French, P. A. Mello, A. Pandey, and S. S. M. Wong, (1981). *Rev. Mod. Phys.* **53**, 385.

Bruus, H., and A. D. Stone (1994). "Quantum chaos in a deformable billiard: applications to quantum dots," *Phys. Rev. B* **50**, 18275.

Bryant, G. W. (1993). "Electrons in coupled vertical quantum dots: interdot tunneling and Coulomb correlation," *Phys. Rev. B* **48**, 8024.

Büttiker, M. (1986). "Four-terminal phase-coherent conductance," *Phys. Rev. Lett.* **57**, 1761.

Büttiker, M. (1988a). "Coherent and sequential tunneling in series barriers," *IBM J. Res. Develop.* **32**, 63.

Büttiker, M. (1988b). "Symmetry of electrical conduction," *IBM J. Res. Develop.* **32**, 317.

Büttiker, M., Y. Imry, R. Landauer, and S. Pinhas (1985). "Generalized many-channel conductance formula with application to small rings," *Phys. Rev. B* **31**, 6027.

Chang, A. M., H. U. Baranger, L. N. Pfeiffer, K. W. West, and T. Y. Chang (1996). "Non-Gaussian distribution of Coulomb blockade peak heights in quantum dots," *Phys. Rev. Lett.* **76**, 1695.

Cleland, A. N., J. M. Schmidt, and J. Clarke (1992). "Influence of the environment on the Coulomb blockade in submicrometer normal-metal tunnel junctions," *Phys. Rev. B* **45**, 2950.

Crouch, C. H., C. Livermore, F. R. Waugh, R. M. Westervelt, K. L. Campman, and A. C. Gossard, "Coulomb gap of coupled quantum dots with adjustable interdot tunneling," *Surf. Sci.* **361/362**, 631.

Crouch, C. H., C. Livermore, R. M. Westervelt, K. L. Campman, and A. C. Gossard (1996a). "Coulomb oscillations in partially open quantum dots," to appear in *Microstructures and Superlattices.*

Crouch, C. H., C. Livermore, R. M. Westervelt, K. L. Campman, and A. C. Gossard (1996b). "Coulomb gap collapse in tunnel-coupled quantum dots," submitted to *Appl Phys. Lett.*

Das Sarma, S., and X. C. Xie (1987). "Calculated transport properties of ultrasubmicrometer quasi-one-dimensional inversion lines," *Phys. Rev. B.* **35**, 9875.

Datta, S., and M. J. McLennan (1990). "Quantum transport in ultrasmall electronic devices," *Rep. Prog. Phys.* **53**, 1003.

Dresselhaus, P. D., L. Ji, S. Han, J. E. Lukens, and K. K. Likharev (1994). "Measurement of single electron lifetimes in a multijunction trap," *Phys. Rev. Lett.* **72**, 3226.

Dingle, R., H. L. Stormer, A.C. Gossard, and W. Wiegman, *Appl. Phys. Lett.* **7**, 665 (1978).

Dixon, D., L. P. Kouwenhoven, P. L. McEuen, Y. Nagamune, J. Motohisa, and H. Sakaki (1996). "Linear and nonlinear transport through coupled quantum dots," *Surf. Sci.* **361/362**, 636.

Dixon, D., L. P. Kouwenhoven, P. L. McEuen, Y. Nagamune, J. Motohisa, and H. Sakaki (1996). "Influence of energy level alignment on tunneling between coupled quantum dots," *Phys. Rev. B* **53**, 12625.

Edwards, H. L., Q. Niu, and A. L. deLozanne (1993). "A quantum dot refrigerator," *Appl. Phys. Lett.* **63**, 714.

Field, M., C. G. Smith, M. Pepper, D. A. Ritchie, J. E. F. Frost, G. A. C. Jones, and D. G. Hasko (1993). "Measurements of Coulomb blockade with a noninvasive voltage probe," *Phys. Rev. Lett.* **70**, 1311.

Flensberg, K. (1993). *Phys. Rev. B* **48**, 11156.

Flensberg, K. (1994). *Physica B* **203**, 432.

Folk, J. A., S. R. Patel, S. F. Godijn, A. G. Huibers, S. M. Cronenwett, C. M. Marcus, K. L. Campman, and A. C. Gossard (1996). "Statistics and parametric correlations of Coulomb blockade peak fluctuations in quantum dots," *Phys. Rev. Lett.* **76**, 1699.

Foxman, E. B., P. L. McEuen, U. Meirav, N. S. Wingreen, Y. Meir, P. A. Belk, N. R. Belk, and M. A. Kastner (1993). "Effects of quantum levels on transport through a Coulomb island," *Phys. Rev. B* **47**, 10020.

Foxman, E. B., U. Meirav, P. L. McEuen, M. A. Kastner, O. Klein, P. A. Belk, and D.

M. Abusch (1994). "Crossover from single-level to multilevel transport in artificial atoms," *Phys. Rev. B* **50**, 14193.

Fulton, T. A., and G. J. Dolan (1987). "Observation of single-electron charging in small tunnel junctions," *Phys. Rev. Lett.* **59**, 109.

Furusaki, A., and K. A. Matveev (1995). "Coulomb blockade oscillations of conductance in the regime of strong tunneling,"*Phys. Rev. Lett.* **75**, 709 (1995).

Geerligs, L. J., V. F. Anderegg, P. A. M.Holweg, J. E. Mooij, H. Pothier, D. Esteve, C. Urbina, M. H. Devoret (1990). "Frequency-locked turnstile device for single electrons," *Phys. Rev. Lett.* **64**, 2691.

Geerligs, L. J., V. F. Anderegg, and J. E. Mooij (1990). "Tunneling time and offset charging in small tunnel junctions," *Physica B* **165/166**, 973.

Giaever, I., and H. R. Zeller (1968). "Superconductivity of small tin particles measured by tunneling," *Phys. Rev. Lett.* **20**, 1504.

Glattli, D. C., C. Pasquier, U. Meirav, F. I. B. Williams, Y. Jin, and B. Etienne (1991). "Co-tunneling of the charge through a 2-D electron island," *Z. Phys. B - Condensed Matter* **85**, 375.

Golden, John M., and Bertrand I. Halperin (1996a). "Relation between barrier conductance and Coulomb blockade peak splitting for tunnel-coupled quantum dots," *Phys. Rev. B* **53**, 3893.

Golden, John M., and Bertrand I. Halperin (1996b). "Higher-order results for the relation between channel conductance and the Coulomb blockade for two tunnel-coupled quantum dots," to appear in *Phys. Rev. B.*

Grabert, H., and M. H. Devoret, eds. (1992). *Single Charge Tunneling*, NATO ASI Series B, Vol. 294 (Plenum: New York).

Gruner, G., and A. Zawadowski (1974). "Magnetic impurities in non-magnetic materials," *Rep Prog. Phys.* **37**, 1497.

Hergenrother, J. M. (1995). "Parity effects and charge transport in the single-electron

transistor," Ph.D. thesis, Harvard University.

Hofmann, F., T. Heinzel, D. A. Wharam, J. P. Kotthaus, G. Bohm, W. Klein, G. Trankle, and G. Weimann (1995). "Single electron switching in a parallel quantum dot," *Phys. Rev. B* **51**, 13872.

Jalabert, R. A., A. D. Stone, and Y. Alhassid (1992). "Statistical theory of Coulomb blockade oscillations: quantum chaos in quantum dots," *Phys. Rev. Lett.* **68**, 3468.

Johnson, A. T., L. P. Kouwenhoven, W. de Jong, N. C. van der Vaart, C. J. P. M. Harmans, and C. T. Foxon (1992). "Zero-dimensional states and single-electron charging in quantum dots," *Phys. Rev. Lett.* **69**, 1592.

Kastner, M. (1992). "The single-electron transistor," *Rev. Mod. Phys.* **64**, 849.

Kastner, M. (1993). "Artificial atoms," *Physics Today* **46(1)**, 24.

Katine, J. A., M. J. Berry, R. M.Westervelt, and A. C. Gossard (1994). *Superlattices and Microstructures* 16, 211.

Katine, J. A. (1996). "Electronic quantum interference in ballistic microstructures," Ph. D. thesis, Harvard University.

Kemerink, M., and L. W. Molenkamp (1994). "Stochastic Coulomb blockade in a double quantum dot," *Appl. Phys. Lett.* **65**, 1012.

Kittel, C. (1987). *Quantum Theory of Solids*, Second Revised Printing (New York: John Wiley & Sons).

Klimeck, G., G. Chen, and S. Datta (1994). "Conductance spectroscopy in coupled quantum dots," *Phys. Rev. B* **50**, 2316.

Kotlyar, R., and S. Das Sarma, preprint (1996).

Kouwenhoven, L. P., F. W. J. Hekking, B. J. van Wees, and C. J. P. M. Harmans (1990). "Transport through a finite one-dimensional crystal," *Phys. Rev. Lett.* **65**, 361.

Kouwenhoven, L. P., N. C. van der Vaart, A. T. Johnson, W. Kool, C. J. P. M. Harmans, J. G. Williamson, A. A. M. Staring, and C. T. Foxon (1991). "Single

electron charging effects in semiconductor quantum dots," *Z. Phys. B--Condensed Matter* **85**, 367.

Kouwenhoven, L. P., A. T. Johnson, N. C. van der Vaart, D. J. Maas, and C. J. P. M. Harmans (1992). "Quantized current in a quantum dot turnstile," *Surf. Sci.* **263**, 405.

Kouwenhoven, L. P., S. Jauhar, K. McCormick, D. Dixon, P. L. McEuen, Y. V. Nazarov, N. C. van der Vaart, and C. T. Foxon (1994). "Photon-assisted tunneling through a quantum dot," *Phys. Rev. B* **50**, 2019.

Kouwenhoven, L. P. (1995). "Coupled quantum dots as artificial molecules," *Science* **268**, 1440.

Kouwenhoven, L. P., and P. L. McEuen (1996). "Single-Electron Transport Through a Quantum Dot," in *Nano-Science and Technology*, ed. G. Timp (AIP Press, New York).

Kulik, I. O., and R. I. Shekhter (1975). "Kinetic phenomena and charge discreteness effects in granulated media," *Sov. Phys. JETP* **41**, 308.

Kulkarni, A. K., and J. T. Lukowski (1986). "Effect of annealing process parameters on the properties of AuGe ohmic contacts to GaAs," *J. Appl. Phys.* **59**, 2901.

Lafarge, P., H. Pothier, E. R. Williams, D. Esteve, C. Urbina, and M. H. Devoret (1991). *Z. Phys. B* **85**, 327.

Landauer, R. (1957). "Spatial variation of currents and fields due to localized scatterers in metallic conduction," *IBM J. Res. Dev.* **1**, 223.

Landauer, R. (1988). "Spatial variation of currents and fields due to localized scatterers in metallic conduction," *IBM J. Res. Dev.* **32**, 306.

Lent, C. S., P. D. Tougaw, and W. Porod (1993). "Bistable saturation in coupled quantum dots for quantum cellular automata," *Appl. Phys. Lett.* **62**, 714.

Livermore, C., C. H. Crouch, R. M. Westervelt, K. L. Campman, and A. C. Gossard (1996a). "Conductance peak splitting in charge-polarized coupled quantum dots," to appear in *Microstructures and Superlattices*.

Livermore, C., C.H. Crouch, R.M. Westervelt, K.L. Campman, and A.C. Gossard (1996b). "The Coulomb gap in coupled quantum dots", to appear in *Science*.

Lloyd, S. (1993). "A potentially realizable quantum computer," *Science* **261**, 1569.

Mar, D. J. (1994). "Cryogenic field-effect transistors for the study of semiconductor nanostructures," Ph. D. thesis, Harvard University.

Marcus, C. M., A. J. Rimberg, R. M. Westervelt, P. F. Hopkins, and A. C. Gossard (1992). "Conductance fluctuations and chaotic scattering in ballistic microstructures," *Phys. Rev. Lett* **69**, 506.

Marcus, C. M., R. M. Westervelt, P. F. Hopkins, and A. C. Gossard (1993). "Phase breaking in ballistic quantum dots: experiment and analysis based on chaotic scattering," *Phys. Rev. B* **48**, 2460.

Martinis, J. M., M. H. Devoret, and J. Clarke (1987). "Experimental tests for the quantum behavior of a macroscopic degree of freedom: the phase difference across a Josephson junction," *Phys. Rev. B* **35**, 4682.

Martinis, J. M., and M. Nahum (1993). "Effect of environmental noise on the accuracy of Coulomb-blockade devices," *Phys. Rev. B* **48**, 18316.

Martinis, J. M., M. Nahum, and H. D. Jensen (1994). "Metrological accuracy of the electron pump," *Phys. Rev. Lett.* **72**, 904.

Matveev, K. A. (1995). "Coulomb blockade at almost perfect transmission," *Phys. Rev. B* **51**, 1743.

Matveev, K. A., L. I. Glazman, and H. U. Baranger (1996a). "Tunneling spectroscopy of quantum charge fluctuations in the Coulomb blockade," *Phys. Rev. B* **53**, 1034.

Matveev, K. A., L. I. Glazman, and H. U. Baranger (1996b). "Coulomb blockade of tunneling through a double quantum dot," *Phys. Rev. B* **54**, 5637.

Matveev, K. A., L. I. Glazman, and H. U. Baranger (1996c). "Theory of Coulomb blockade of tunneling through a double quantum dot," *Surf. Sci.* **361/362**, 623.

McEuen, P. L., E. B. Foxman, U. Meirav, M. A. Kastner, Y. Meir, and N. S. Wingreen

(1991). "Transport spectroscopy of a Coulomb island in the quantum Hall regime," *Phys. Rev. Lett.* **66**, 1926.

McEuen, P. L., E. B. Foxman, J. Kinaret, U. Meirav, and M. A. Kastner (1992). "Self-consistent addition spectrum of a Coulomb island in the quantum Hall regime," *Phys. Rev. B* **45**, 11419.

Meir, Y., N. S. Wingreen, and P. A. Lee (1991). "Transport through a strongly interacting electron system: theory of periodic conductance oscillations," *Phys. Rev. Lett* **66**, 3048.

Meir, Y., N. S. Wingreen, and P. A. Lee (1993). "Low-temperature transport through a quantum dot: the Anderson model out of equilibrium," *Phys. Rev. Lett.* **70**, 2601.

Meirav, U., P. L. McEuen, M. A. Kastner, E. B. Foxman, A. Kumar, and S. J. Wind (1991). "Conductance oscillations and transport spectroscopy of a quantum dot," *Z. Phys. B - Condensed Matter* **85**, 357.

Meirav, U., M. A. Kastner, and S. J. Wind (1990). "Single-electron charging and periodic conductance resonances in GaAs nanostructures," *Phys. Rev. Lett.* **65**, 771.

Meurer, B., D. Heitmann, and K. Ploog (1992). "Single-electron charging of quantum-dot atoms," *Phys. Rev. Lett.* **68**, 1371.

Molenkamp, L. W., K. Flensberg, and M. Kemerink (1995). "Scaling of the Coulomb energy due to quantum fluctuations in the charge on a quantum dot," *Phys. Rev. Lett.* **75**, 4282.

Nagamune, Y., H. Sakaki, L. P. Kouwenhoven, L. C. Mur, C. J. P. M. Harmans, J. Motohisa, and H. Noge (1994). "Single electron transport and current quantization in a novel quantum dot structure," *Appl. Phys. Lett.* **64**, 2379.

Ott, Henry W. (1976). *Noise Reduction Techniques in Electronic Systems* (New York: John Wiley & Sons).

Pasquier, C., U. Meirav, F. I. B. Williams, and D. C. Glattli (1993). "Quantum limitation on Coulomb blockade observed in a 2D electron system," *Phys. Rev. Lett.* **70**, 69.

Pothier, H., P. Lafarge, P. F. Orfila, C. Urbina, D. Esteve, and M. H. Devoret (1991). "Single electron pump fabricated with ultrasmall normal tunnel junctions," *Physica B* **169**, 573.

Ralph, D. C., and R. A. Buhrman (1994). "Kondo-assisted and resonant tunneling in a single charge trap: a realization of the Anderson model out of equilibrium," *Phys. Rev. Lett.* **72**, 3401.

Richardson, Robert C., and Eric N. Smith (1988). *Experimental Techniques in Condensed Matter Physics at Low Temperatures* (Addison-Wesley).

Rimberg, A. J. (1992). "Magnetotransport in uniform and modulated electron gases in wide parabolic quantum wells," Ph. D. thesis, Harvard University.

Ruzin, I. M., V. Chandrasekhar, E. I. Levin, and L. I. Glazman (1992). "Stochastic Coulomb blockade in a double-dot system," *Phys. Rev. B* **45**, 13469.

Sakamoto, T., S. W. Hwang, F. Nihey, Y. Nakamura, and K. Nakamura (1994). "Coulomb blockade of two quantum dots in series," *Jpn. J. Appl. Phys.* **33**, 4876.

Scott-Thomas, J. H. F., S. B. Field, M. A. Kastner, H. I. Smith, and D. A. Antoniadis (1989). "Conductance oscillations periodic in the density of a one-dimensional electron gas," *Phys Rev Lett* **62**, 583.

Shih, Y.-C., M. Murakami, E. L. Wilkie, and A. C. Callegari (1987). "Effects of interfacial microstructure on uniformity and thermal stability of AuNiGe ohmic contact to n-type GaAs," *J. Appl. Phys.* **62**, 582.

Stafford, C. A., and S. Das Sarma (1994). "Collective Coulomb blockade in an array of quantum dots: a Mott-Hubbard approach," *Phys. Rev. Lett.* **72**, 3590.

Staring, A. A. M., H. van Houten, and C. W. J. Beenakker (1992). "Coulomb-blockade oscillations in disordered quantum wires," *Phys. Rev. B* **45**, 9222.

Staring, A. A. M., J. G. Williamson, H. van Houten, and C. W. J. Beenakker (1991). "Coulomb-blockade oscillations in a quantum dot," *Physica B* **175**, 226.

Stopa, M. (1993). "Coulomb oscillations and semiconductor quantum dot self-consistent

level structure," *Phys. Rev. B* **48**, 18340.

Stopa, M. (1996). "Quantum dot self-consistent electronic structure and the Coulomb blockade," preprint.

Sun, Y.-S., and G. Kirczenow (1994). "Energy level locking in quantum conductors," *Phys. Rev. Lett.* **72**, 2450.

Tewordt, M, H. Asahi, V. J. Law, R. T. Syme, M. J. Kelly, and G. A. C. Jones (1992). "Resonant tunneling in coupled quantum dots," *Appl. Phys. Lett.* **60**, 595.

Thornton, T. J., M. Pepper, H. Ahmed, D. Andrews, and G. J. Davies, *Phys. Rev. Lett.* **56**, 1198 (1986).

Tighe, T. S. (1993). Ph.D. thesis, Harvard University.

Tinkham, M. (1996). *Introduction to Superconductivity*, 2nd. ed (New York: McGraw-Hill).

van der Vaart, N. C., S. F. Godijn, Y. V. Nzarov, C. J. P. M. Harmans, J. E. Mooij, L. W. Molenkamp, and C. T. Foxon (1995). "Resonant tunneling through two discrete energy states," *Phys. Rev. Lett.* **74**, 4702.

van der Vaart, N. C. (1995). "Single electron transport and quantum confinement in semiconductor nanostructures," Ph.D. thesis, Delft University of Technology.

van der Vaart, N. C., A. T. Johnson, L. P. Kouwenhoven, D. J. Maas, W. de Jong, M. P. de Ruyter van Steveninck, A. van der Enden, C. J. P. M. Harmanss, and C. T. Foxon (1993). "Charging effects in quantum dots at high magnetic fields," *Physica B* **189**, 99 (1993).

van Houten, H., C. W. J. Beenakker, and A. A. M.Staring (1992). "Coulomb-blockade oscillations in semiconductor nanostructures," in *Single Charge Tunneling* (Plenum Press, NY), eds. H. Grabert and M. Devoret, 167.

van Houten, H., and C. W. J. Beenakker (1996). "Quantum point contacts," *Physics Today* **49** (7), 22.

van Wees, B. J., H. van Houten, C. W. J. Beenakker, J. G. Williamson, L. P.

Kouwenhoven, D. van der Marel, and C.T. Foxon (1988). "Quantized conductance of point contacts in a two-dimensional electron gas," *Phys. Rev. Lett.* **60**, 848.

Visscher, E. H., S. M. Verbrugh, J. Lindeman, P. Hadley, and J. E. Mooij (1994). "Fabrication of multilayer single-electron tunneling devices," *Appl. Phys. Lett.* **66**, 305.

Wang, L., J. K. Zhang, and A. R. Bishop (1994). "Microscopic theory for conductance oscillations of electron tunneling through a quantum dot," *Phys. Rev. Lett.* **73**, 585.

Washburn, S., and R. A. Webb (1992). "Quantum transport in small disordered samples from the diffusive to the ballistic regime," *Rep. Prog. Phys.* **55**, 1311.

Waugh, F. R. (1994). "Novel architectures and devices for computing," Ph.D. thesis, Harvard University.

Waugh, F. R., M. J. Berry, D. J. Mar, R. M. Westervelt, K. L. Campman, and A. C. Gossard (1995). "Single-electron charging in double and triple quantum dots with tuneable coupling," *Phys. Rev. Lett.* **75**, 705.

Waugh, F. R., M. J. Berry, C. H. Crouch, C. Livermore, D. J. Mar, R. M. Westervelt, K. L. Campman, and A. C. Gossard (1996). "Measuring interactions between tunnel-coupled quantum dots," *Phys. Rev. B* **53**, 1413.

Wilkinson, P. B., T. M. Fromhold, L. Eaves, F. W. Sheard, N. Miura, and T. Takamasu (1996). "Evidence for periodic 'scar' patterns in the wavefunctions of a chaotic quantum well," *Surf. Sci.* **361/362**, 696.

Weis, J., R. J. Haug, K. von Klitzing, and K. Ploog (1992). "Competing channels in single-electron tunneling through a quantum dot," *Phys. Rev. Lett.* **71**, 4019.

Yang, Scott (1995). "Mesoscopic transport in a deformable quantum ring," Ph. D. thesis, Harvard University.

Yacoby, A., M. Heiblum, D. Mahalu, and H. Shtrikman (1994). "Coherence and phase-sensitive measurements in a quantum dot," *Phys. Rev. Lett.* **73**, 3149.

Zheng, H. Z., H. P.Wei, D. C. Tsui, and G. Weimann, *Phys. Rev. B.* **34**, 5635 (1986).